

Jorge Romero Pascual



Nanomaterials and devices for energy storage and conversion

Supervised by:

Prof. Eugenio Coronado Miralles

Dr. Gonzalo Abellán Sáez



PhD Thesis

Nanoscience and Nanotechnology

Valencia, october 2019

Nanomaterials and devices for energy storage and conversion



VNIVERSITAT DE VALÈNCIA

Instituto de Ciencia Molecular (ICMol)

TESIS DOCTORAL

Jorge Romero Pascual

Doctorado en Nanociencia y Nanotecnología

Dirigida por:

Prof. Eugenio Coronado Miralles

Dr. Gonzalo Abellán Sáez

Valencia, octubre de 2019



VNIVERSITAT
DE VALÈNCIA



PARC CIENTÍFIC

ICMOL
Institut de Ciència Molecular




EXCELENCIA
MARÍA
DE MAEZTU

D. EUGENIO CORONADO MIRALLES, Profesor Catedrático del Departamento de Química Inorgánica de la Universidad de Valencia, y D. GONZALO ABELLÁN SÁEZ, Investigador Ramón y Cajal del Instituto de Ciencia Molecular (ICMol) la Universidad de Valencia.

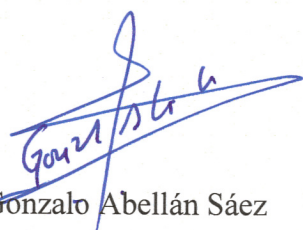
CERTIFICAN:

Que la presente Tesis Doctoral, titulada: “**Nanomaterials and devices for energy storage and conversion**”, ha sido desarrollada por JORGE ROMERO PASCUAL, bajo la dirección de ambos en el Instituto de Ciencia Molecular (ICMol), autorizando mediante este escrito la presentación de la misma para optar al grado de Doctor.

En Paterna, a 18 de octubre de 2019.



Dr. Eugenio Coronado Miralles
Co-director



Dr. Gonzalo Abellán Sáez
Co-director y tutor

*A mis padres,
A mi hermana,
A Valen...*

...a la memoria de mi abuelo

Table of Contents

Table of Contents

<i>Abbreviations</i>	5
Chapter 1: Introduction	9
1.1. Introduction.....	11
1.2. Motivation.....	19
1.3. Publications during the PhD.....	24
1.4. References.....	27
Chapter 2: Nanocomposites for supercapacitors	33
2.1. Introduction.....	35
2.2. Summary of the most important results.....	37
2.3. Contribution of the author.....	41
2.4. References.....	43
Chapter 3: Supercapacitive N-doped graphene	135
3.1. Introduction.....	137
3.2. Summary of the most important results.....	140
3.3. Contribution of the author.....	144
3.4. References.....	145
Chapter 4: Nanocomposite OER catalysis	201
4.1. Introduction.....	203
4.2. Summary of the most important results.....	207
4.3. Contribution of the author.....	209

4.4. References.....	210
Appendix: Chapter 5: Material scaling and supercapacitive device assembly.....	275
5.1. Introduction.....	277
5.2. Scaling of $FeNi_3$ -Graphene nanocomposite.....	279
5.3. Scaling of the $FeNi_3$ -Graphene-NiFoam electrodes.....	284
5.4. Assembly and study of two-electrode batteries.....	287
5.4 References.....	294
Resumen de la Tesis Doctoral.....	297

Abbreviations

Abbreviations

ABF	Annular bright field
<i>ca.</i>	Circa (approximately)
CNTs	Carbon nanotubes
COF	Covalent-organic frameworks
CV	Cyclic voltamperometry
CVD	Chemical vapor decomposition
EDLC	Electrical double-layer capacitor
EELS	Electron energy-loss spectroscopy
EES	Electrochemical energy storage
ESS	Energy storage system
<i>et al.</i>	et alia (and others)
GC	Glassy carbon
HAADF	High angle annular dark field
HER	Hydrogen evolution reaction
ICP-OES	Inductively coupled plasma-optical emission spectroscopy
<i>i.e.</i>	id est (that is)
ITO	Indium doped tin oxide
LSV	Linear sweep voltammetry
MF	Magnetic field
MHD	Magnetohydrodynamic

MOF	Metal-organic frameworks
NC	Nanocomposite
NP	Nanoparticle
OER	Oxygen evolution reaction
ORR	Oxygen reduction reaction
PEIS	Potentiostatic electrochemical impedance spectroscopy
RHE	Reversible hydrogen electrode
RT	Room temperature
SC	Supercapacitors
SEM	Scanning electron microscopy
SRS	Statistical Raman spectroscopy
STEM	Scanning transmission electron microscopy
TEM	Transmission electron microscopy
TG-MS	Thermogravimetric analysis coupled with a mass spectrometer
TMDCs	Transition-metal dichalcogenides
TOF	Turnover frequency
TRL	Technology Readiness Levels
XRPD	X-Ray powder diffraction

Chapter 1

Introduction

1.1 Introduction

The shortage of energy is one of the most serious global challenges of our time. World energy consumption is increasing dramatically due to rapid population growth and economic development, resulting in higher greenhouse gas emissions and climate change. It is estimated that global energy demands will double its energy supply by 2050 and triple by the year 2100^{1,2}. To avoid environmental deterioration due to polluting energies and meet the growing demand for energy, new technological advances for clean and sustainable energy are necessary to ensure a prosperous future and economic growth. Along this front, the scientific community is developing intense research in the areas of advanced technologies for energy storage (for example, supercapacitors and batteries) and conversion (for example, photovoltaic and electrocatalytic cells). As a result, a great deal of research is driven by the growing demand for more efficient and clean energy storage and conversion for different applications, from micro or nano systems to portable electronic devices, and even to electrical vehicles and renewable energy systems³⁻⁹.

Nowadays, solar, wind, hydrothermal, geothermal, nuclear, biomass, fuel cells, high energy density batteries and supercapacitors are becoming attractive. Among them, fuel cells, batteries and supercapacitors are referred to as electrochemical energy technologies, since they depend on a common electrochemical principle, transforming chemical energy directly into electrical energy with little or no pollution. However, it is still not possible to make a generalized commercialization of electrochemical energy technologies due to problems of high cost, durability and operability, which are in turn linked to severe materials challenges¹⁰⁻¹⁴.

For instance, although the market has been revolutionized by lithium-ion batteries in their application for portable electronics, like cell phones and laptop computers, their application for automobile applications (electric vehicles and hybrid electric vehicles) is hampered by the high cost, safety problems and the power and energy density problems necessary for the cathode, anode and electrolytic materials used. Similarly, the adoption of fuel cell technologies is delayed by the high cost and durability of the platinum-based electrocatalysts and Nafion electrolyte membrane conventionally used, in addition to the complex operability.

The main objective today is the design and development of new materials that can increase efficiency, improve durability and reduce cost, making these technologies commercially viable. In this regard, nanotechnology and nanostructured materials make a great promise due to the unusual properties endowed by their low dimensions and the combination of bulk and surface properties to the overall behaviour¹⁵⁻¹⁹. However, there are wide room for the improvement of their performance. In this sense, the exploration of different synthetic approaches and innovative processes play a critical role in overall performance, obtaining control of particle composition, size, morphology and electrochemical properties²⁰⁻²⁴. Here, the key concepts and recent advances in electrochemical energy techniques are presented with particular emphasis on energy storage and conversion.

1.1.1 Energy storage

At present, there has been a growing interest in high power and high energy density storage systems due to the large increase in renewable energy demand. Energy storage systems (ESSs) are the key to deal with the intermittent nature of renewable energy sources and increase the power transmitted into the grid from systems such as wind and solar power. In addition, the appearance of electric vehicles requires that the kinetic energy of the vehicles be stored somewhere each time the vehicle slows down or stops. Although it has been successfully achieved with batteries on a low power scale, new methods to improve efficiency will require large amounts of energy that are only capable of providing other energy storage technologies, such as supercapacitors (SCs). Because of this, SCs have attracted significant attention due to their high power capabilities and long service life, which provides a very good opportunity to build more advanced hybrid ESSs²⁵.

SCs are devices with high power rates compared to batteries. Although SCs can provide a power thousands of times energy than batteries in the same volume, they cannot store the same amount of charge (from 3 to 30 times less)²⁵. This makes SCs suitable for applications where energy bursts are needed, but a large energy storage capacity is not required. SCs can also be included within a battery-based ESS, thus improving the sizing while fulfilling the power and energy requirements²⁶. The comparison of energy and power density of SCs and others ESSs can be easily observed graphically in a Ragone plot, in which the energy and power densities are represented in horizontal and vertical axes. As shown in Figure 1.1, different storage technologies are represented in a Ragone plot. However, the Ragone plot does not reflect many other performance parameters such as cost, safety and cycle life, shown in Table 1.1. As we can see, another great advantage of SCs is their cycle life, with millions of cycles thanks to their charge storage mechanism, which does not involve irreversible chemical reactions for a pure electrical double-layer capacitors (EDLCs). The main disadvantage related to the charge storage mechanism is the operating voltage of a SCs cell, which should be kept low in order to avoid the chemical decomposition of electrolytes²⁷. An additional disadvantage is the operating voltage of a supercapacitor cell, which must be kept low to avoid chemical breakdown of electrolytes.

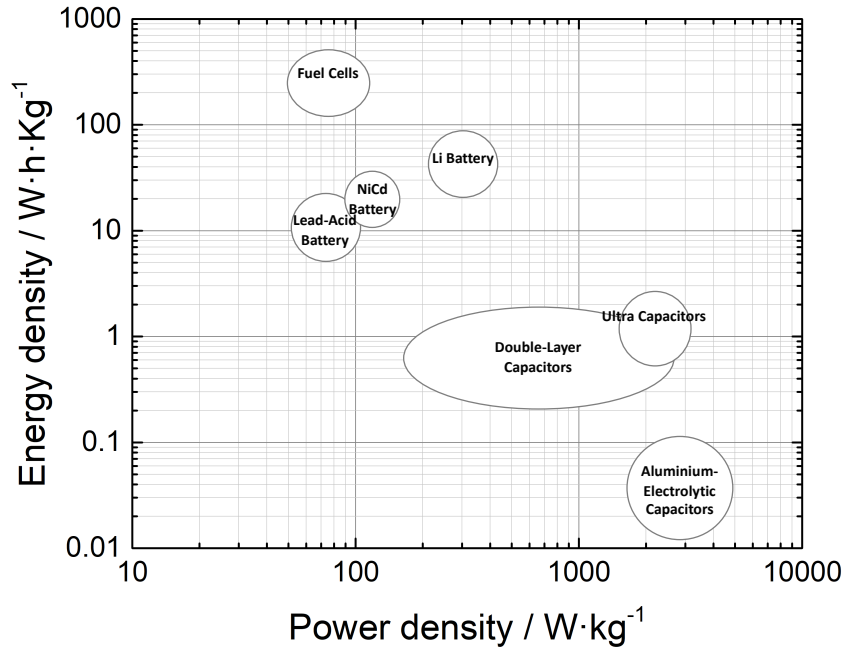


Figure 1.1. Ragone plot of principal commercial energy-storage devices (source data from US Defense Logistics Agency).

Table 1.1. Comparison table among selected electrochemical energy storage systems²⁶.

	Capacitor	Supercapacitor	Battery
<i>Specific energy ($\text{W}\cdot\text{h}\cdot\text{kg}^{-1}$)</i>	< 0.1	1 – 10	10 - 100
<i>Specific power ($\text{W}\cdot\text{kg}^{-1}$)</i>	> 10,000	500 – 10,000	< 1,000
<i>Discharge time</i>	10^{-6} to 10^{-3} s	s to min	0.3 – 3 h
<i>Charge time</i>	10^{-6} to 10^{-3} s	s to min	1 – 5 h
<i>Cycle life</i>	Almost infinite	> 500,000	About 1,000

A SC cell is formed by two electrodes (working and counter electrode) with a permeable separator between them. The electrodes can be identical (symmetrical configuration) or different (asymmetric configuration). The separator, which avoids

electrical contact between the electrodes, must be permeable to ions, to allow the transfer of ionic charge, while having high electrical resistance, high ionic conductance and low thickness to achieve the best performance²⁸. The most frequently used electrolytes in SCs are aqueous and organic electrolytes. Aqueous electrolytes usually have a low breakdown voltage, around 1 V, which is significantly lower than with organic electrolytes (around 3 V), but the conductivity of aqueous electrolytes is greater than that of organic electrolytes, which is desirable for high power devices. Also, aqueous electrolytes have low cost and ease of handling.

Depending on the storage mechanism, EDLC, pseudocapacitors or faradic capacitors and hybrid capacitors (combination of both) can be distinguished, as we can see in Figure 1.2. EDLCs are based on nanoporous materials with a very high specific surface area ($> 1000 \text{ m}^2 \cdot \text{g}^{-1}$) as active electrode materials. The electrodes are generally made of nanoporous carbon materials thanks to their availability, existing industrial production and low cost. Pseudocapacitors are based on conductive electrodes usually made of conducting polymers or metal oxides and, sometimes, on functionalized porous carbons, combining electrostatic and pseudocapacitive storage mechanisms. These materials can obtain specific capacitance values much higher than in EDLCs and the charge storage mechanism depends on the rapid redox reactions that occur on the electrode surface. However, these redox reactions can cause the electrodes to swell and shrink, resulting in poor mechanical stability and lower cycle life in pseudocapacitive materials. Finally, hybrid capacitors are the combination of an EDLC and a pseudocapacitive type electrode, which combines the properties of both systems and leads to intermediate performance in some cases (Figure 1.2).

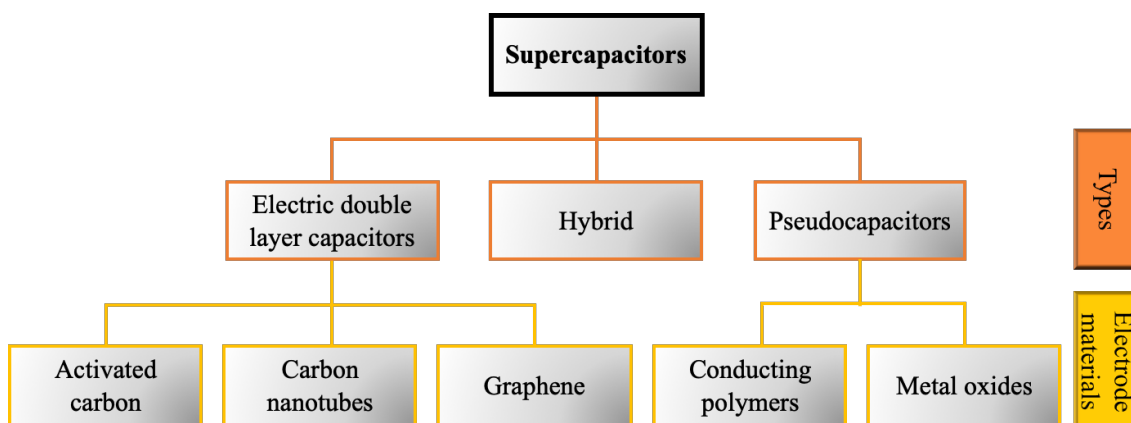


Figure 1.2. Schematic classification of different supercapacitors.

The most significant factor for evaluating the performance of supercapacitive behaviour is the specific capacitance. This value can be obtained by using two different configuration of the cells: a typical three electrode cell and a two electrode cell. The capacitance values are obtained by galvanostatic charge/discharge cycles, according to Eq. 1.1 for EDLC and Eq. 1.2 for pseudocapacitive capacitance in both electrode cells configurations.

$$C_s = \frac{I \cdot \Delta t}{m \cdot \Delta V} \quad (\text{Eq. 1.1})$$

$$C_s = \frac{2 \cdot I \cdot \int V dt}{m \cdot \Delta V^2} \quad (\text{Eq. 1.2})$$

where I is the charge/discharge current, Δt is the time for a full charge or discharge, m the weight in grams of the active material in the electrode layer and ΔV is the voltage change after a full charge or discharge. The reason for using a different equation for pseudocapacitance is that if we use the same equation as for EDLC, much of the capacity coming from redox processes is neglected.

The energy and power density of a SC is a very important factor for practical applications. The energy density, E ($\text{W} \cdot \text{h} \cdot \text{kg}^{-1}$), and the power density, P ($\text{W} \cdot \text{kg}^{-1}$), should be calculated from a two-electrode cell as an operating device according to the Eq. 1.3. and Eq. 1.4. When it is measured in a three electrode cell, it must be taken into account that it is a half cell; therefore, the value should be divided by 4²⁹.

$$E = \frac{C_s \cdot \Delta V^2}{2} \quad (\text{Eq. 1.3})$$

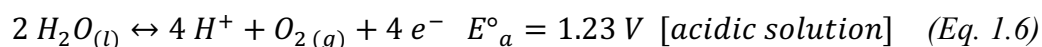
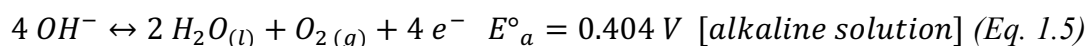
$$P = \frac{E}{\Delta t} \quad (\text{Eq. 1.4})$$

where ΔV (V) is the voltage used for the measurement and Δt (h) is the corresponding discharge time.

1.1.2 Energy conversion

Energy conversion has been considered as a solution to significantly reduce the dependency on fossil fuels. Among the several energy systems through electrochemical reactions, fuel cells, water splitting and metal air batteries are the most efficient and reliable systems. Water oxidation reaction or oxygen evolution reaction (OER) is the core reaction for all these systems to carry out their reversible process along with oxygen reduction reaction (ORR) and/or hydrogen evaluation reaction (HER)³⁰⁻³⁶.

In OER, molecular oxygen is produced via several proton/electron-coupled procedures. In acidic conditions, the reaction operates through oxidation of two water molecules (H₂O) to give four protons (H⁺) and one oxygen molecule (O₂) by losing a total of four electrons³⁷. In basic conditions, oxidation of hydroxyl groups (OH⁻) takes the lead, and they are transformed into H₂O and O₂ with the same number of electrons being involved³⁸.



An external current is required to create the potential difference of 1.23 V vs. normal hydrogen electrode (NHE) to drive the OER at pH = 0. Thus, a shift in reaction potential *i.e.* ~ 59 mV per unit pH, occurs theoretically according to Nernst equation (Eq. 1.7)³⁹:

$$E = E^\circ - \frac{R \cdot T}{n \cdot F} \ln \frac{[\text{Red}]}{[\text{Ox}]} \quad (\text{Eq. 1.7})$$

where E is the cell potential, E° is the cell potential at standard conditions, R is the ideal gas constant, T is the temperature in Kelvin, n is the number of moles of electrons involved each mole of reaction, F is the Faraday constant, $[\text{Red}]$ is the concentration of reduced molecules and $[\text{Ox}]$ is the concentration of oxidized molecules).

However, in order to avoid the impact of pH on the applied potential and keep the working voltage around 1.23 V for OER at all pHs, reversible hydrogen electrode (RHE) reference is used, which takes into account the pH shift. As we can see in Eqs. (1.5) and (1.6), generation of O₂ requires a transfer of four electrons, and kinetically favourable OER process occurs through multiple step reactions with single electron transfer at each

step³⁸. Thus, an accumulation of energy at each step makes OER kinetics very sluggish and with large overpotential to overcome, for this reason, in OER electrocatalysis it seeks to expedite the reaction and lower the potential.

At the present, noble-metal-based materials are placed at the top in stability in all pH values despite the fair activity towards OER, however, the high price and scarcity are the main problems for their practical application. Considerable research efforts have been devoted to obtaining alternative materials with a better OER activity. Very few non-precious metal oxides are stable under oxidative potentials in acidic condition⁴⁰. To overcome this limitation recent research has been focused in searching for non-precious metal-based alternatives for OER electrocatalysis in alkaline conditions, in which they are chemically stable. Some of these alternatives are carbon-based materials (*e.g.* graphene and graphene oxide, CNT, nitrogen-doped carbon, *etc.*), alloys, oxides, hydroxides and oxyhydroxides of earth abundant metals (*e.g.* Mn, Co, Ni, and Fe, *etc.*) and their combination with carbon^{41–53}. Although many high-performance non-precious metal-based catalysts have been recently developed, it has not yet been possible to find a competitive material that can replace in the industry noble-metal-based catalysts. An ideal OER electrocatalyst should have low overpotential, low Tafel slope, high stability/durability, good activity, low-cost, high earth abundance, scalability, *etc.*, parameters that will be explained below with its effects on performance.

The working electrodes/substrates play a critical role in determining the performance and influence the reaction rate due to their different structure, conductivity, degree of wettability and access of catalyst to an electrolyte. On the basis of the structure, electrode supports are divided into two categories: flat surface electrode and 3D electrode. The most common flat surface electrodes are glassy carbon (GC), Cu/Ti foil and indium doped tin oxide (ITO) substrate. They allow single-way penetration of electrolyte, that thus limiting the catalysis on surface of catalyst only. Meanwhile, while the 3D substrates like carbon cloth/paper (CC and CP) and Ni foam, allow multiple pathways for electrolyte penetration from all sides of catalyst and involve all the material in catalytic reaction. All these electrode substrates have different advantages and limitations, being the GC electrode the easiest to handle and the most widely used, but it offers a limited loading of catalyst⁵⁴. In addition, the GC electrode requires a binder to hold the catalyst material, which increases resistance, blocks active sites and prevents ion diffusion⁵⁵. On the other hand, to get rid

of the use of binders, many researches grow the catalyst directly on conductive substrates such as Ni foam, CC, CP, offering a strong electrical connection between the catalytic material and the collector. Importantly, the 3D texture of the Ni foam provides high gas density and easy electrolyte penetration and results in better catalysis. However, sometimes the absence of binders can lead to the peeling of catalyst, resulting in poor stability.

The electrolyte for OER electrocatalysis extremely influences the performance of electrode material. The OER electrocatalysis in alkaline solution is more favourable, while it is difficult in neutral electrolytes and reaches at very low performance in acidic solution. Currently, most of the research is focused on finding the OER electrocatalysts which are stable in alkaline conditions, while for the most of these materials are not stable in acidic condition due to high oxidative potential. So, an OER electrocatalysts that can work under full range of pH (0–14) is highly desirable.

The most significant factor for evaluating the performance of OER catalysts their onset potentials, but it is difficult to observe the exact value. For this reason, the value of potential at a current density of $10 \text{ mA}\cdot\text{cm}^{-2}$ is considered more reliable and commonly used, as we can see in Figure 1.3. Overpotential is the potential difference between the potentials obtained at a specific current density and 1.23 V. Generally, a catalyst that has an overpotential at $10 \text{ mA}\cdot\text{cm}^{-2}$ in the range of 300 – 400 mV is considered to be excellent catalyst for OER; however, there are very few catalysts that have overpotential much less than 300 mV.

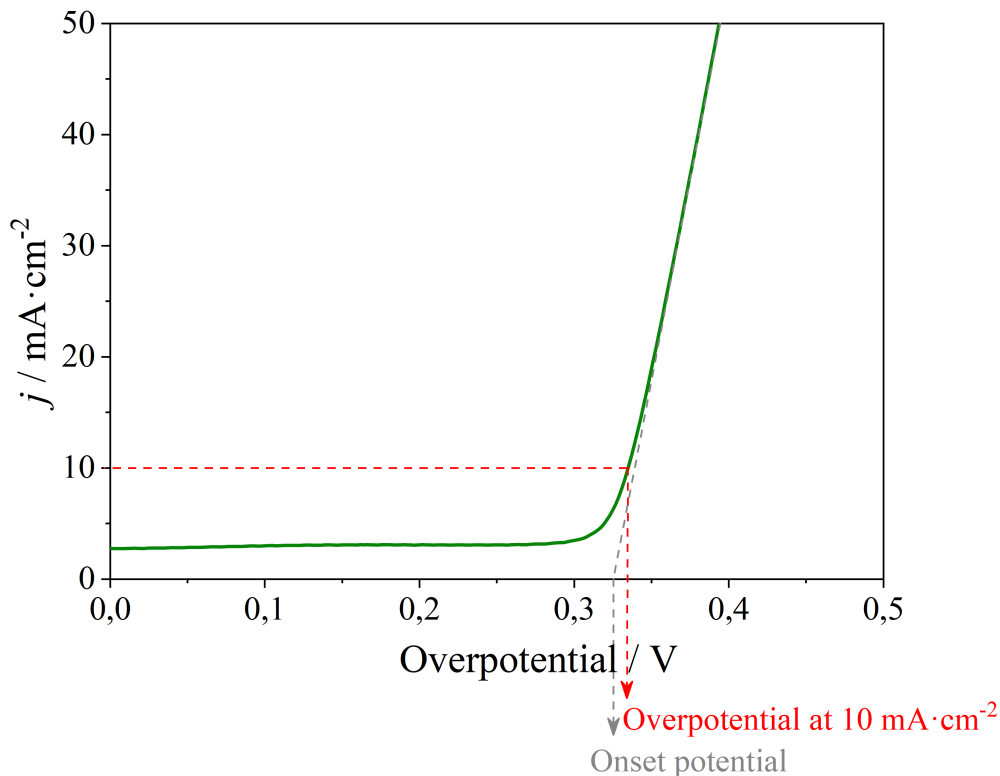


Figure 1.3. Linear sweep voltammetry (LSV) example of how to obtain the onset potential value and the overpotential at a certain current density.

Tafel analysis is used to know the kinetics and reaction mechanism and to compare the catalytic activity of different catalysts. With the Tafel slope, the sensitivity of the current response to the given voltage can also be examined using the following equation:

$$\eta = b \cdot \log\left(\frac{j}{j_0}\right) \quad (\text{Eq. 1.8})$$

where η denotes the overpotential, b represents the Tafel slope, j is the current density and j_0 is the exchange current density. The quality of good OER is that it should have a low Tafel slope and large current density.

The stability of a catalyst is a very important factor for practical applications. It depends on several factors, such as the nature of an electrolyte and its stability in basic or acidic medium and the nature of the working electrode which determines that the stability of the catalyst, and normally the active materials grown directly on it are more stable than to the pasted ones. Most of the stability tests are evaluated *via* carrying out the chronopotentiometry at a constant potential or current density.

Finally, to determine the catalytic activity of the material, the turnover frequency (TOF) is the key promoter and can be calculated using the equation:

$$TOF = \left(\frac{j \cdot A}{4 \cdot F \cdot n} \right) \quad (Eq. 1.9)$$

where j ($\text{mA} \cdot \text{cm}^{-2}$) is the current density at a particular overpotential, A is the area of the working electrode, F is the Faraday constant ($96500 \text{ C} \cdot \text{mol}^{-1}$) and n is the number of moles of the active materials. It is almost impossible to obtain an exact TOF value since in a catalyst not all elements are catalytically active, but it is still a relevant and useful parameter for comparing similar catalytic materials.

Once a material has all the properties that define a good catalyst, it can be used in different applications. The requirement of sustainable energy is increasing every day and hydrogen (H_2) as an energy source has received tremendous attention from last few decades, since its oxidation product is only water^{3,50,54–60}. Therefore, the use of hydrogen as fuel, generated from an electrolysis, can reduce the dependence on fossil fuels as well as the emission of CO_2 ⁶¹. Thus, water splitting is one of the most important applications of OER for the production of hydrogen and its use as fuel⁶².

Another application of OER is in electrochemical energy storage (EES), because of it has great potential from portable devices to electric vehicles, as well as large scale grid storage^{52,63}. Among several EES systems, the metal-air battery is the most promising, due to its high theoretical energy density, with values close to gasoline⁶¹. In addition, OER can be applied in energy conversion devices. The fuel cell is an energy conversion device that converts chemical energy into electrical energy by catalytic oxidation of the fuel^{3,64,65}. There are different types of fuel cells, being solid oxide and reversible fuel cells the most demanded, because of their ability of energy storage and fuel resurge, respectively^{66–70}. Nevertheless, the high cost of the catalyst used in various anodic and cathodic reactions of fuel cells and their poor efficiencies and stability are the main obstacles in the commercialization of fuel cells⁷¹.

1.2 Motivation

This thesis is motivated by the recent advances in energy storage and conversion. Inspired by the rapid energy demand that society demands, different materials applied to the energy sector, in storage and conversion, have gained significant attention throughout the scientific community. In this context, novel carbon-based nanocomposites and layered double hydroxides recently showed exceptional results as SCs and electrocatalysts, being cheaper than the materials currently used. In addition, the possibility of scaling these materials is a vital part for their future application in the industry.

Herein, we develop an extensive investigation on the synthesis processing and application of carbon-based nanocomposites and LDHs, using innovative approaches. This work is divided in five main chapters, composed of the state of the art of different materials applied in different energy fields, followed by a summary of the most important results and highlighting the author's main contributions to the field and the included papers.

Fundamental aspects of graphene-based nanomaterials as SCs, such as a hybrid nanocomposite consisting of FeNi₃-graphene (Chapter 2) or N-doped graphene (Chapter 3) have been thoroughly discussed. Moreover the study of NiFe layered double hydroxides (Chapter 4) and iron-carbon nanocomposites (Chapter 5) as electrocatalyst allowed us to propose new efficient alternatives to settle benchmark electrocatalysts. Last but not least, a great effort in scaling-up and prototyping (Chapter 6) helped us to bring closer to the application this class of sustainable energy materials.

Regarding the articles attached to this thesis they were selected based on the main topic they refer to. Chapter 2 includes two papers focused on an FeNi₃-Graphene nanocomposite with magnetic properties and supercapacitive behaviour: “Insights into the formation of metal carbon nanocomposites using hybrid NiFe layered double hydroxides as precursors” Romero, J., Varela, M., Assebban, M., Oestreicher, V., Jorda, J. L., Abellán, G & Coronado, E. (*submitted*); “Giant Enhancement in the Supercapacitance of NiFe–Graphene Nanocomposites Induced by a Magnetic Field” Romero, J., Prima-Garcia, H., Varela, M., Miralles, S. G., Oestreicher, V., Abellán, G., & Coronado, E. *Adv. Mater.* 31, 1970200 (2019). Chapter 3 focuses on N-doped graphene

with excellent supercapacitive behaviour: “Metal-functionalized covalent organic frameworks as precursors of supercapacitive porous N-doped graphene” Romero, J., Rodríguez-San-Miguel, D., Ribera, A., Mas-Ballesté, R., Otero, T. O., Manet, I., Licio, F., Abellán, G., Zamora, F. & Coronado, E. *J. Mater. Chem. A* 5, 4343–4351 (2017). Chapter 4 shows the excellent electrocatalytic properties for OER of an unprecedented iron-carbon nanocomposite: “Solvent-Free Synthesis of ZIFs: A Route toward the Elusive Fe(II) Analogue of ZIF-8” López-Cabrelles, J., Romero, J., Abellán, G., Giménez-Marqués, M., Palomino, M., Valencia, S., Rey, F. & Mínguez Espallargas, G. *J. Am. Chem. Soc.* 141, 7173–7180 (2019). Finally, Appendix/Chapter 5 focuses on the study of scaling process of materials and their assembly in two electrode cells as a commercial-like SC prototypes.

1.3 Publications during the PhD

Patents

1. **Romero, J.**, Prima, H., Abellán, G., Coronado, E. Method for obtaining a nanocomposite material by means of cycles of galvanostatic charge and discharge under the action of magnetic fields and material thus obtained. Patent ES2649688B1 (Spain). WO2018011445A1 (International).
2. **Romero, J.**, López, J., Mínguez, G., Coronado, E. Iron zeolitic imidazolate framework, production method thereof and nanocomposite derived from same. Patent ES2703849A1 (Spain). WO2019053312A1 (International).
3. **Romero, J.**, Oestreicher, V., Abellán, G., Coronado, E. Síntesis a demanda de láminas de LDHs nanométricas con anión interlamina en un único paso y en condiciones ambientales. (*patent in preparation*).

Articles

1. **Romero, J.**, Oestreicher, V., Assebban, M., Dolle, C., Coronado, E. & Abellán, G. *One-pot* room temperature synthesis of hybrid layers hydroxides CoNi-Sebacate as precursors for high capacitive nanocomposites. (*manuscript in preparation*)
2. Silva, A. S. D., Carrasco, J. A., Oestreicher, V., **Romero, J.**, Markus, B. G., Simon, F., Vieira, B. J. C., Waerenborgh, J. C., Abellán, G. & Coronado, E. Fundamental Insights into the Covalent Silane Functionalization of NiFe-Layered Double Hydroxides. (*submitted*)
3. **Romero, J.**, Varela, M., Assebban, M., Oestreicher, V., Jorda, J. L., Coronado, E. & Abellán, G. Insights into formation of metal carbon nanocomposites using hybrid NiFe layered double hydroxides as precursors. (*submitted*)
4. **Romero, J.**, Prima-Garcia, H., Varela, M., Miralles, S. G., Oestreicher, V., Abellán, G., & Coronado, E. Giant Enhancement in the Supercapacitance of NiFe–Graphene Nanocomposites Induced by a Magnetic Field. *Adv. Mater.* **31**, 1970200 (2019).

5. López-Cabrelles, J., **Romero, J.**, Abellán, G., Giménez-Marqués, M., Palomino, M., Valencia, S., Rey, F. & Mínguez Espallargas, G. Solvent-Free Synthesis of ZIFs: A Route toward the Elusive Fe(II) Analogue of ZIF-8. *J. Am. Chem. Soc.* **141**, 7173–7180 (2019).
6. La-Placa, M.-G., Igual-Muñoz, A. M., **Romero, J.**, Daniels, R. E., Kozhevnikov, V. N., Sessolo, M. & Bolink, H. J. Red Light-Emitting Electrochemical Cells Employing Pyridazine-Bridged Cationic Diiridium Complexes. *ECS J. Solid State Sci. Technol.* **8**, R84–R87 (2019).
7. Souto, M., **Romero, J.**, Calbo, J., Vitórica-Yrezábal, I. J., Zafra, J. L., Casado, J., Ortí, E., Walsh, A. & Mínguez Espallargas, G. Breathing-Dependent Redox Activity in a Tetrathiafulvalene-Based Metal–Organic Framework. *J. Am. Chem. Soc.* **140**, 10562–10569 (2018).
8. Morant-Giner, M., Sanchis-Gual, R., **Romero, J.**, Alberola, A., García-Cruz, L., Agouram, S., Galbiati, M., Padial, N. P., Waerenborgh, J. C., Martí-Gastaldo, C., Tatay, S., Forment-Aliaga, A. & Coronado, E. Prussian Blue@MoS₂ Layer Composites as Highly Efficient Cathodes for Sodium- and Potassium-Ion Batteries. *Adv. Funct. Mater.* **28**, 1706125 (2018).
9. **Romero, J.**, Rodríguez-San-Miguel, D., Ribera, A., Mas-Ballesté, R., Otero, T. O., Manet, I., Licio, F., Abellán, G., Zamora, F. & Eugenio Coronado. Metal-functionalized covalent organic frameworks as precursors of supercapacitive porous N-doped graphene. *J. Mater. Chem. A* **5**, 4343–4351 (2017).
10. Carrasco, J. A., **Romero, J.**, Varela, M., Hauke, F., Abellán, G., Hirsch, A. & Coronado, E. Alkoxide-intercalated NiFe-layered double hydroxides magnetic nanosheets as efficient water oxidation electrocatalysts. *Inorg. Chem. Front.* **3**, 478–487 (2016).
11. Carrasco, J. A., **Romero, J.**, Abellán, G., Hernández-Saz, J., Molina, S. I., Martí-Gastaldo, C. & Coronado, E. Small-pore driven high capacitance in a hierarchical carbon via carbonization of Ni-MOF-74 at low temperatures. *Chem. Commun.* **52**, 9141–9144 (2016).
12. Carrasco, J. A. Prima-García, H., **Romero, J.**, Hernández-Saz, J., Molina, S. I., Abellán, G. & Coronado, E. CVD synthesis of carbon spheres using NiFe-LDHs as

catalytic precursors: structural, electrochemical and magnetoresistive properties. *J. Mater. Chem. C* **4**, 440–448 (2016).

13. Abellán, G., Carrasco, J. A., Coronado, E., **Romero, J.** & Varela, M. Alkoxide-intercalated CoFe-layered double hydroxides as precursors of colloidal nanosheet suspensions: structural, magnetic and electrochemical properties. *J. Mater. Chem. C* **2**, 3723–3731 (2014).

1.4 References

1. Dunn, B., Kamath, H. & Tarascon, J.-M. Electrical Energy Storage for the Grid: A Battery of Choices. *Science* **334**, 928–935 (2011).
2. Manthiram, A., Murugan, A. V., Sarkar, A. & Muraliganth, T. Nanostructured electrode materials for electrochemical energy storage and conversion. *Energy Environ. Sci.* **1**, 621–638 (2008).
3. Ma, C., Xu, N., Qiao, J., Jian, S. & Zhang, J. Facile synthesis of NiCo₂O₄ nanosphere-carbon nanotubes hybrid as an efficient bifunctional electrocatalyst for rechargeable Zn–air batteries. *Int. J. Hydrog. Energy* **41**, 9211–9218 (2016).
4. Zhang, H., Yu, X. & Braun, P. V. Three-dimensional bicontinuous ultrafast-charge and -discharge bulk battery electrodes. *Nat. Nanotechnol.* **6**, 277–281 (2011).
5. El-Kady, M. F., Strong, V., Dubin, S. & Kaner, R. B. Laser Scribing of High-Performance and Flexible Graphene-Based Electrochemical Capacitors. *Science* **335**, 1326–1330 (2012).
6. Gao, W. *et al.* Direct laser writing of micro-supercapacitors on hydrated graphite oxide films. *Nat. Nanotechnol.* **6**, 496–500 (2011).
7. Burschka, J. *et al.* Sequential deposition as a route to high-performance perovskite-sensitized solar cells. *Nature* **499**, 316–319 (2013).
8. You, J. *et al.* A polymer tandem solar cell with 10.6% power conversion efficiency. *Nat. Commun.* **4**, 1–10 (2013).
9. Xie, K. *et al.* Iron supported C@Fe₃O₄ nanotube array: a new type of 3D anode with low-cost for high performance lithium-ion batteries. *J. Mater. Chem.* **22**, 5560–5567 (2012).
10. Yang, P. & Tarascon, J.-M. Towards systems materials engineering. *Nat. Mater.* **11**, 560–563 (2012).
11. Graetzel, M., Janssen, R. A. J., Mitzi, D. B. & Sargent, E. H. Materials interface engineering for solution-processed photovoltaics. *Nature* **488**, 304–312 (2012).
12. Su, Y.-S. & Manthiram, A. Lithium–sulphur batteries with a microporous carbon paper as a bifunctional interlayer. *Nat. Commun.* **3**, 1–6 (2012).
13. Wang, X. *et al.* Tandem colloidal quantum dot solar cells employing a graded recombination layer. *Nat. Photonics* **5**, 480–484 (2011).
14. Wang, H. *et al.* An ultrafast nickel–iron battery from strongly coupled inorganic nanoparticle/nanocarbon hybrid materials. *Nat. Commun.* **3**, 1–8 (2012).
15. Sun, Y. & Xia, Y. Shape-Controlled Synthesis of Gold and Silver Nanoparticles. *Science* **298**, 2176–2179 (2002).
16. Rolison, D. R. Catalytic Nanoarchitectures--the Importance of Nothing and the

Unimportance of Periodicity. *Science* **299**, 1698–1701 (2003).

17. Duan, X. *et al.* High-performance thin-film transistors using semiconductor nanowires and nanoribbons. *Nature* **425**, 274–278 (2003).

18. Xia, Y. *et al.* One-Dimensional Nanostructures: Synthesis, Characterization, and Applications. *Adv. Mater.* **15**, 353–389 (2003).

19. Bruce, P. G., Scrosati, B. & Tarascon, J.-M. Nanomaterials for Rechargeable Lithium Batteries. *Angew. Chem. Int. Ed.* **47**, 2930–2946 (2008).

20. Appapillai, A. T., Mansour, A. N., Cho, J. & Shao-Horn, Y. Microstructure of LiCoO₂ with and without “AlPO₄” Nanoparticle Coating: Combined STEM and XPS Studies. *Chem. Mater.* **19**, 5748–5757 (2007).

21. Long, J. W., Stroud, R. M., Swider-Lyons, K. E. & Rolison, D. R. How To Make Electrocatalysts More Active for Direct Methanol Oxidation Avoid PtRu Bimetallic Alloys! *J. Phys. Chem. B* **104**, 9772–9776 (2000).

22. Rolison, D. R. & Dunn, B. Electrically conductive oxide aerogels: new materials in electrochemistry. *J. Mater. Chem.* **11**, 963–980 (2001).

23. Xie, K. & Wei, B. Materials and Structures for Stretchable Energy Storage and Conversion Devices. *Adv. Mater.* **26**, 3592–3617 (2014).

24. Tian, N., Zhou, Z.-Y., Sun, S.-G., Ding, Y. & Wang, Z. L. Synthesis of Tetrahedral Platinum Nanocrystals with High-Index Facets and High Electro-Oxidation Activity. *Science* **316**, 732–735 (2007).

25. Miller, J. R. & Simon, P. Electrochemical Capacitors for Energy Management. *Science* **321**, 651–652 (2008).

26. Pandolfo, A. G. & Hollenkamp, A. F. Carbon properties and their role in supercapacitors. *J. Power Sources* **157**, 11–27 (2006).

27. Kötz, R. & Carlen, M. Principles and applications of electrochemical capacitors. *Electrochimica Acta* **45**, 2483–2498 (2000).

28. Sharma, P. & Bhatti, T. S. A review on electrochemical double-layer capacitors. *Energy Convers. Manag.* **51**, 2901–2912 (2010).

29. Stoller, M. D. & Ruoff, R. S. Best practice methods for determining an electrode material’s performance for ultracapacitors. *Energy Environ. Sci.* **3**, 1294–1301 (2010).

30. Wang, Z.-L., Xu, D., Xu, J.-J. & Zhang, X.-B. Oxygen electrocatalysts in metal–air batteries: from aqueous to nonaqueous electrolytes. *Chem. Soc. Rev.* **43**, 7746–7786 (2014).

31. Mahmood, N. *et al.* Chlorine-doped carbonated cobalt hydroxide for supercapacitors with enormously high pseudocapacitive performance and energy density. *Nano Energy* **11**, 267–276 (2015).

-
32. Tahir, M. *et al.* One Dimensional Graphitic Carbon Nitrides as Effective Metal-Free Oxygen Reduction Catalysts. *Sci. Rep.* **5**, 12389 (2015).
33. Huang, Z.-F. *et al.* Hollow Cobalt-Based Bimetallic Sulfide Polyhedra for Efficient All-pH-Value Electrochemical and Photocatalytic Hydrogen Evolution. *J. Am. Chem. Soc.* **138**, 1359–1365 (2016).
34. Lin, Z., Waller, G. H., Liu, Y., Liu, M. & Wong, C. 3D Nitrogen-doped graphene prepared by pyrolysis of graphene oxide with polypyrrole for electrocatalysis of oxygen reduction reaction. *Nano Energy* **2**, 241–248 (2013).
35. Lv, Z. *et al.* Fabrication of zero to three dimensional nanostructured molybdenum sulfides and their electrochemical and photocatalytic applications. *Nanoscale* **8**, 18250–18269 (2016).
36. Meng, C. *et al.* Atomically and Electronically Coupled Pt and CoO Hybrid Nanocatalysts for Enhanced Electrocatalytic Performance. *Adv. Mater.* **29**, 1604607 (2017).
37. Conway, B. E. & Liu, T. C. Characterization of electrocatalysis in the oxygen evolution reaction at platinum by evaluation of behavior of surface intermediate states at the oxide film. *Langmuir* **6**, 268–276 (1990).
38. Birss, V. I., Damjanovic, A. & Hudson, P. G. Oxygen Evolution at Platinum Electrodes in Alkaline Solutions II . Mechanism of the Reaction. *J. Electrochem. Soc.* **133**, 1621–1625 (1986).
39. Gong, M. & Dai, H. A mini review of NiFe-based materials as highly active oxygen evolution reaction electrocatalysts. *Nano Res.* **8**, 23–39 (2015).
40. McCrory, C. C. L., Jung, S., Peters, J. C. & Jaramillo, T. F. Benchmarking Heterogeneous Electrocatalysts for the Oxygen Evolution Reaction. *J. Am. Chem. Soc.* **135**, 16977–16987 (2013).
41. Tahir, M. *et al.* Efficient water oxidation through strongly coupled graphitic C₃N₄ coated cobalt hydroxide nanowires. *J. Mater. Chem. A* **4**, 12940–12946 (2016).
42. Li, Y., Hasin, P. & Wu, Y. Ni_xCo_{3-x}O₄ Nanowire Arrays for Electrocatalytic Oxygen Evolution. *Adv. Mater.* **22**, 1926–1929 (2010).
43. Zhao, Y. *et al.* Ultrafine NiO Nanosheets Stabilized by TiO₂ from Monolayer NiTi-LDH Precursors: An Active Water Oxidation Electrocatalyst. *J. Am. Chem. Soc.* **138**, 6517–6524 (2016).
44. Chen, R., Wang, H.-Y., Miao, J., Yang, H. & Liu, B. A flexible high-performance oxygen evolution electrode with three-dimensional NiCo₂O₄ core-shell nanowires. *Nano Energy* **11**, 333–340 (2015).
45. Wang, Y. *et al.* Reduced Mesoporous Co₃O₄ Nanowires as Efficient Water Oxidation Electrocatalysts and Supercapacitor Electrodes. *Adv. Energy Mater.* **4**, 1400696 (2014).
46. Meng, Y. *et al.* Structure–Property Relationship of Bifunctional MnO₂

Nanostructures: Highly Efficient, Ultra-Stable Electrochemical Water Oxidation and Oxygen Reduction Reaction Catalysts Identified in Alkaline Media. *J. Am. Chem. Soc.* **136**, 11452–11464 (2014).

47. Bergmann, A., Zaharieva, I., Dau, H. & Strasser, P. Electrochemical water splitting by layered and 3D cross-linked manganese oxides: correlating structural motifs and catalytic activity. *Energy Environ. Sci.* **6**, 2745–2755 (2013).

48. Fekete, M. *et al.* Highly active screen-printed electrocatalysts for water oxidation based on β -manganese oxide. *Energy Environ. Sci.* **6**, 2222–2232 (2013).

49. Smith, R. D. L. *et al.* Photochemical Route for Accessing Amorphous Metal Oxide Materials for Water Oxidation Catalysis. *Science* **340**, 60–63 (2013).

50. Feng, J.-X., Ye, S.-H., Xu, H., Tong, Y.-X. & Li, G.-R. Design and Synthesis of FeOOH/CeO₂ Heterolayered Nanotube Electrocatalysts for the Oxygen Evolution Reaction. *Adv. Mater.* **28**, 4698–4703 (2016).

51. Najafpour, M. M., Ehrenberg, T., Wiechen, M. & Kurz, P. Calcium Manganese(III) Oxides (CaMn₂O_{4-x}·x H₂O) as Biomimetic Oxygen-Evolving Catalysts. *Angew. Chem. Int. Ed.* **49**, 2233–2237 (2010).

52. Yang, Y., Fei, H., Ruan, G., Xiang, C. & Tour, J. M. Efficient Electrocatalytic Oxygen Evolution on Amorphous Nickel–Cobalt Binary Oxide Nanoporous Layers. *ACS Nano* **8**, 9518–9523 (2014).

53. Tahir, M. *et al.* Electrocatalytic oxygen evolution reaction for energy conversion and storage: A comprehensive review. *Nano Energy* **37**, 136–157 (2017).

54. Jiao, Y., Zheng, Y., Jaroniec, M. & Qiao, S. Z. Design of electrocatalysts for oxygen- and hydrogen-involving energy conversion reactions. *Chem. Soc. Rev.* **44**, 2060–2086 (2015).

55. Masa, J. *et al.* Amorphous Cobalt Boride (Co₂B) as a Highly Efficient Nonprecious Catalyst for Electrochemical Water Splitting: Oxygen and Hydrogen Evolution. *Adv. Energy Mater.* **6**, (2016).

56. Zhu, Y., Zhou, W., Sunarso, J., Zhong, Y. & Shao, Z. Phosphorus-Doped Perovskite Oxide as Highly Efficient Water Oxidation Electrocatalyst in Alkaline Solution. *Adv. Funct. Mater.* **26**, 5862–5872 (2016).

57. Zhang, B. *et al.* Homogeneously dispersed multimetal oxygen-evolving catalysts. *Science* **352**, 333–337 (2016).

58. Yang, X. *et al.* Highly acid-durable carbon coated Co₃O₄ nanoarrays as efficient oxygen evolution electrocatalysts. *Nano Energy* **25**, 42–50 (2016).

59. Du, P. & Eisenberg, R. Catalysts made of earth-abundant elements (Co, Ni, Fe) for water splitting: Recent progress and future challenges. *Energy Environ. Sci.* **5**, 6012–6021 (2012).

60. Narayan, S. R., Manohar, A. & Mukerjee, S. Bi-Functional Oxygen Electrodes –

- Challenges and Prospects. *Electrochem. Soc. Interface* **24**, 65–69 (2015).
61. Jahan, M., Liu, Z. & Loh, K. P. A Graphene Oxide and Copper-Centered Metal Organic Framework Composite as a Tri-Functional Catalyst for HER, OER, and ORR. *Adv. Funct. Mater.* **23**, 5363–5372 (2013).
62. Kibsgaard, J. & Jaramillo, T. F. Molybdenum Phosphosulfide: An Active, Acid-Stable, Earth-Abundant Catalyst for the Hydrogen Evolution Reaction. *Angew. Chem. Int. Ed.* **53**, 14433–14437 (2014).
63. Guo, Y. *et al.* Engineering the Electronic State of a Perovskite Electrocatalyst for Synergistically Enhanced Oxygen Evolution Reaction. *Adv. Mater.* **27**, 5989–5994 (2015).
64. Tahir, M. *et al.* Bifunctional catalysts of Co₃O₄@GCN tubular nanostructured (TNS) hybrids for oxygen and hydrogen evolution reactions. *Nano Res.* **8**, 3725–3736 (2015).
65. Zhang, J., Zhao, Z., Xia, Z. & Dai, L. A metal-free bifunctional electrocatalyst for oxygen reduction and oxygen evolution reactions. *Nat. Nanotechnol.* **10**, 444–452 (2015).
66. Shih, Z.-Y., Periasamy, A. P., Hsu, P.-C. & Chang, H.-T. Synthesis and catalysis of copper sulfide/carbon nanodots for oxygen reduction in direct methanol fuel cells. *Appl. Catal. B Environ.* **132–133**, 363–369 (2013).
67. Li, Q., Mahmood, N., Zhu, J., Hou, Y. & Sun, S. Graphene and its composites with nanoparticles for electrochemical energy applications. *Nano Today* **9**, 668–683 (2014).
68. Yu, E. H., Wang, X., Krewer, U., Li, L. & Scott, K. Direct oxidation alkaline fuel cells: from materials to systems. *Energy Environ. Sci.* **5**, 5668–5680 (2012).
69. Mahmood, N., Zhang, C., Yin, H. & Hou, Y. Graphene-based nanocomposites for energy storage and conversion in lithium batteries, supercapacitors and fuel cells. *J. Mater. Chem. A* **2**, 15–32 (2014).
70. Ren, L., Hui, K. S. & Hui, K. N. Self-assembled free-standing three-dimensional nickel nanoparticle/graphene aerogel for direct ethanol fuel cells. *J. Mater. Chem. A* **1**, 5689–5694 (2013).
71. Chang, J., Feng, L., Liu, C., Xing, W. & Hu, X. An Effective Pd–Ni₂P/C Anode Catalyst for Direct Formic Acid Fuel Cells. *Angew. Chem. Int. Ed.* **53**, 122–126 (2014).

Chapter 2

Nanocomposites for supercapacitors

2.1 Introduction

For the pressing need of facing the global warming and the finite nature of fossil fuels, the search for alternative energy sources has been intensified dramatically during the last few years^{1,2}. As a result, recently there has been a growing interest in high power and high energy density storage systems. A more widespread use of renewable sources and a better efficiency of transportation systems are two important goals to be pursued to overcome this problem. 2D layered materials like graphene and its inorganic analogues such as transition-metal dichalcogenides (TMDCs) or LDHs have taken the lead in the design of advanced nanomaterials based on their superior electrochemical performance reliant on their unique physical properties, control over their organization and efficient electronic communication due to hybridization between components^{3,4}. Energy-related applications that could benefit the most from these layered systems include flexible electronics, lithium and sodium ion batteries with efficient anodes and cathodes, SCs with high energy and power densities, and solar cells⁵.

SCs are key elements among energy storage devices and represent an avenue worth exploring due to their potential to deliver high power densities in short periods of time with high cyclability and durability⁶. SCs are mainly utilized for industrial stationary applications, automotive transportation and portable electronic applications. In supercapacitive devices, all the efforts trying to improve the energy and power densities have been devoted to modify the internal configuration of the capacitor. This includes new synthetic approaches for electrode materials, novel capacitor configurations, or tailored porous hierarchies. Even though the fast development of electrode materials for SCs has increased dramatically the performance of these devices, it is still room for further improvement⁷.

In this context, a loosely investigated approach to reach this challenge consists in the application of an external stimulus, such as a magnetic field (MF), for example⁸⁻¹⁰. For this type of application, the best types of SCs are hybrids, due to its combination of pseudocapacitance and EDLC, as we have seen in previous Chapter. These hybrid SCs combine the presence of metal oxides NPs with magnetic properties and a carbon matrix that provides better conductivity and a homogeneous arrangement of NPs. In principle, MF may affect the capacitive internal resistances since they are expected to induce

complex magnetohydrodynamic (MHD) phenomena in the electrolytes, offering a new tool for tuning the performance of SCs. Unfortunately, this effect has always remained small, despite some remarkable efforts^{11,12}.

In this Chapter we present an approach to overcome this limitation, consists of incorporating magnetic nanoparticles in the electrochemically active material, which can be easily magnetized by a MF. In this sense, we present an exhaustive *in situ* study of a low-temperature synthesis for a hierarchically structured magnetic graphene-FeNi₃ NC using hybrid NiFe-LDH nanoreactors as precursors^{13,14}. Also, we show its super capacitive properties and the influence of a MF as an external stimulus.

2.2 Summary of the most important results

The main objective in this Chapter is synthesize a nanocomposite that has a supercapacitive behaviour and magnetic properties to perform external stimuli through a MF. For this type of study the best candidate is a hybrid SCs, which has magnetic NPs and a graphitic carbon matrix to increase its conductivity and favour the redox reactions for the pseudocapacitance.

To obtain this supercapacitive hybrid material, a calcination procedure was used at 900 °C in a nitrogen atmosphere, using a NiFe-LDH-Seb as a precursor, where the NiFe-LDH provide the metals for the NPs and the sebacate (Seb) chains in the interlaminar space form the carbon matrix. For a better understanding of the formation process, different *in situ* studies were carried out. X-Ray powder diffraction (XRPD) at room temperature (RT) confirms the presence of the NiFe-LDH phase by the typical reflections planes of (006) and (009) at low angles ($2\theta = 11.14^\circ$ and 18.96° , respectively), and also, the (110) at higher angles ($2\theta = 62^\circ$)^{13,15}. Due to *in situ* XRPD measurements, we were able to observe the temperature-dependent structural changes, observing an onset LDH structure collapse at 250 °C. Meanwhile, a new weak broad peak start to appear at around $\theta = 42.5$, assigned as the (111) reflection from a *fcc* structure, suggesting the formation of small NPs of FeNi₃, < 5 nm^{16,17}. When the temperature rises up to 350 °C, all peaks associated with the LDH structure disappear, and all reflection lines from the *fcc* structure appear (JCPDS N°. 38-0419), such as $2\theta = 50.87^\circ$, 75.45° and 91.05° , that can be indexed as the (200), (220) and (331) reflections, respectively. Further, infrared spectroscopy measured *ex-situ*, employing samples calcined obtained at different temperatures in a Chemical Vapor Deposition (CVD) oven, are in good agreement with the XRPD patterns, showing a collapse of the LDH structure at the same temperature by the loss of metal-oxygen (M-O) stretching and bending modes. In addition, the growth of crystallite's size of the metallic NPs can be estimated employing the Scherrer equation, showing a growth from 5 nm to 30 nm in less than 150 °C.

In order to see the chemical changes during the formation of the NC, thermogravimetric analysis coupled with a mass spectrometer (TG-MS) under an inert atmosphere of helium was carried out, showing a first mass loss corresponding to the interlamellar water. Then, a second mass loss is observed in the 250-400 °C range, with H₂O (m/z 18) and CO₂ (m/z 44) signals, attributed to a dihydroxylation and

decomposition of the LDH and the organic linker, as in the XRPD measurements^{18,19}. Also, at around 400 °C BTX signals were observed, confirming that the graphite matrix is started to be formed. To complement the TG-MS measurements, *in situ* Raman spectroscopy was performed. Those measurements revealed in the pristine material the characteristic bands in the 750-1750 and 2750-3000 cm⁻¹ regions of alkyl chains, attributed to the sebacate molecules. These peaks are still present until they reach 350 °C, confirming the conversion of the sebacate chains to the carbon matrix.

In order to see the formation of the nanocomposite more clearly, *in situ* atomic-resolution aberration-corrected scanning transmission electron microscopy and electron energy-loss spectroscopy (STEM-EELS) at 80 kV was performed in a heating chip. RT images showed a flake-like structure consisting of plates with rough edges, typical structure of coprecipitation-LDHs. Small variations on the flake structure were observed at 300 °C, and nanometric clusters starts to be more obvious at 350 °C. Raising to 400 °C, we can observe the complete formation of the NPs with perfect nanocrystals with sizes in the few nm range.

After obtaining the NC formed by FeNi₃ NPs embedded in a carbon matrix, presents excellent performances as SC and, at the same time, it behaves as soft magnet at RT. The interplay between these two properties was studied^{14,20}. When an external MF was applied during galvanostatic charge/discharge cycles, a drastic increase of the capacitance retention and the pseudocapacitance/Faradaic contribution was observed. This specific capacitance after 1000 charge/discharge cycles reach as values up to *ca.* 1850 ± 180 F·g⁻¹ (360 mA·h·g⁻¹ in terms of faradaic battery-type). This represents an increase in the supercapacitance of *ca.* 1100% with respect to the initial value, with excellent values of energy and power density (71.31 W·h·kg⁻¹ and 9450 W·kg⁻¹) measured in three-electrode cell configuration.

For better understanding the fundamental behaviour of the magnetocapacitive FeNi₃-carbon nanocomposites, potentiostatic electrochemical impedance spectroscopy (PEIS) measurements were performed, showing an increase of the electrode's resistance and the low frequency leakage resistance with the applied MF. This was indicative that MF was responsible for the improvement in the energy storage performance of our device and suggesting that the electrolytes can foster the formation of an oxide surface around the NPs¹¹.

With respect to the degree of graphitization and homogeneity of the material, statistical Raman spectroscopy (SRS) was performed, showing an average I_D/I_G ratio of 1.2 before and 1.1 after the application of the MF. This suggests a slight decrease in the functionalization of the graphene matrix. These results are in good agreement with X-ray photoelectron spectroscopy (XPS) measurements, where C1s high resolution spectra showed a decrease in the C–O contribution after the application of the MF. Also, Ni 2p spectra showed three resolved features, attributed to metallic and divalent Ni (mainly NiO and Ni(OH)₂), and Ni satellite²⁰. Compared to pristine NC, a more pronounced Ni–O peak was presented after the magnetic cycles. Additionally, we observed that before and after performing the galvanostatic cycles in presence of the MF, the samples behave as soft magnets with small coercive fields and no significant differences in both cases. Furthermore, conductivity measurements showed an increase in the resistance of one order of magnitude upon magnetic cycling, shifting from a metal conductor behaviour to a semiconductor, confirming that the oxidation processes at the surface of the metal nanoparticles are enhanced by the MF.

As we have seen, all these techniques point toward a preferential growth of electroactive oxide layers and a better structural resilience of the graphene matrix when the charge/discharge cycles take place in presence of a MF. For a corroboration of the mechanism, we used real-space techniques sensitive to both chemistry and structure, such as STEM-EELS. After the galvanostatic cycles in presence of a MF, annular bright field (ABF) and high angle annular dark field (HAADF) images revealed the wide formation of small precipitates. The smaller particles tend to exhibit a core-shell like structure, crystalline needle-shaped clusters and other crystal-line small particles (<5 nm). EELS analysis demonstrated that all clusters and needles consisted of Ni, Fe, and O, showing a strong oxidation of the surface of the particles, which is mostly Fe oxide. Indeed, EELS fine structure showed a strong Ni–Fe segregation, with a total Ni–Fe separation with the small Fe-rich clusters heavily oxidized, while the Ni-rich clusters remain metallic and are only oxidized in the surface.

In order to clarify whether the MF metal segregation requires an electrochemical process or not, we have performed forefront in situ STEM-EELS analysis under the MF of the microscope objective lens (of the order of 2T) and temperatures between RT and 400 °C. After 15 h of exposure to the MF at RT some surface segregation occurred in the form of a noticeable density of nanometric surface clusters with an inhomogeneous composition.

Them, after being annealed *in situ* at 400 °C for 30 min, the surface clusters have increased in size, almost duplicating their volume, with an inhomogeneous oxidation reminiscent of the core-shell morphology. These results confirm the MF induced segregation process, demonstrating the importance of providing energy to the system, either in the form of thermal agitation or electrochemical potential.

2.3 Contribution of the author

2.3.1 Article 1: *“Insights into the formation of metal carbon nanocomposites using hybrid NiFe layered double hydroxides as precursors”*

In this paper we studied the formation *in situ* of a NC using a NiFe-LDH as precursor. Through different characterization techniques we have been able to observe the structural and chemical changes of the NC formation process. Since the collapse of the precursor structure to form small NP, an increase in its size as the temperature increases; until the formation of a graphitic carbon matrix around the NPs.

The author synthesized the precursor of NiFe-LDH-Seb and all NCs at different calcination temperatures, contributed in the experimental characterization and discussed the results. The author wrote the paper supervised by the other authors.

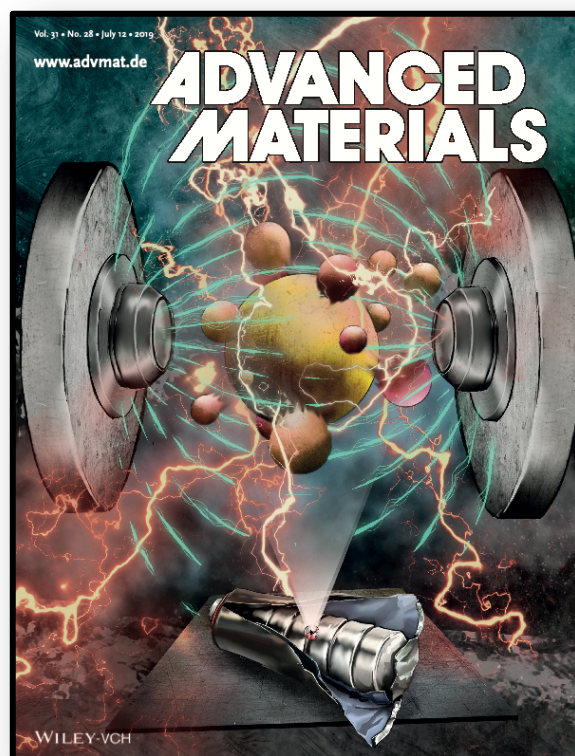
The paper was submitted to Inorganic Chemistry.

2.3.2 Article 2: *“Giant Enhancement in the Supercapacitance of NiFe– Graphene Nanocomposites Induced by a Magnetic Field”*

The main goal of this communication was to show how we can combine magnetic and supercapacitive properties of a FeNi₃-Grphene NC, and the study of the effect of this combination. With different charge and discharge galvanostatic cycles, with and without an external MF, we carefully analysed the effect of the MF, obtaining a dramatic enhancement (more than one order of magnitude) of the specific capacitance and a metal phase segregation forming electrochemical active nanometric metal clusters of Ni. Due to its excellent performance as supercapacitor, we patented these results in 2016 (WO2019053312A1: *“Method for obtaining a nanocomposite material by means of cycles of galvanostatic charge and discharge under the action of magnetic fields and material thus obtained.”*)

The author synthesized the NC, contributed to the experimental characterization, performed all electrochemical experiments and studies and collaborated in the writing of the paper and the patent.

Note about the paper: Article 2 was selected to be the cover of its respective issue:



2.4 References

1. Lewis, N. S. & Nocera, D. G. Powering the planet: Chemical challenges in solar energy utilization. *Proc. Natl. Acad. Sci.* **103**, 15729–15735 (2006).
2. Gray, H. B. Powering the planet with solar fuel. *Nat. Chem.* **1**, 7–7 (2009).
3. Nicolosi, V., Chhowalla, M., Kanatzidis, M. G., Strano, M. S. & Coleman, J. N. Liquid Exfoliation of Layered Materials. *Science* **340**, 1226419 (2013).
4. Wang, H. & Dai, H. Strongly coupled inorganic–nano-carbon hybrid materials for energy storage. *Chem. Soc. Rev.* **42**, 3088–3113 (2013).
5. Bonaccorso, F. *et al.* Graphene, related two-dimensional crystals, and hybrid systems for energy conversion and storage. *Science* **347**, 1246501 (2015).
6. Beguin, F. & Frackowiak, E. *Supercapacitors: Materials, Systems, and Applications*. (John Wiley & Sons, 2013).
7. Wang, G., Zhang, L. & Zhang, J. A review of electrode materials for electrochemical supercapacitors. *Chem. Soc. Rev.* **41**, 797–828 (2012).
8. Monzon, L. M. A. & Coey, J. M. D. Magnetic fields in electrochemistry: The Lorentz force. A mini-review. *Electrochem. Commun.* **42**, 38–41 (2014).
9. Monzon, L. M. A. & Coey, J. M. D. Magnetic fields in electrochemistry: The Kelvin force. A mini-review. *Electrochem. Commun.* **42**, 42–45 (2014).
10. Olsson, F. K. *et al.* Heteroepitaxy of InP on Silicon-on-Insulator for Optoelectronic Integration. *ECS Trans.* **3**, 23–29 (2007).
11. Zhu, J. *et al.* Magnetic field induced capacitance enhancement in graphene and magnetic graphene nanocomposites. *Energy Environ. Sci.* **6**, 194–204 (2012).
12. Zhu, J. *et al.* Magnetocapacitance in magnetic microtubular carbon nanocomposites under external magnetic field. *Nano Energy* **6**, 180–192 (2014).

13. Abellán, G., Coronado, E., Martí-Gastaldo, C., Ribera, A. & F. Sánchez-Royo, J. Layered double hydroxide (LDH)–organic hybrids as precursors for low-temperature chemical synthesis of carbon nanoforms. *Chem. Sci.* **3**, 1481–1485 (2012).
14. Abellán, G., Coronado, E., Martí-Gastaldo, C., Ribera, A. & Otero, T. F. Magnetic Nanocomposites Formed by FeNi₃ Nanoparticles Embedded in Graphene. Application as Supercapacitors. *Part. Part. Syst. Charact.* **30**, 853–863 (2013).
15. Coronado, E. *et al.* Spontaneous Magnetization in Ni–Al and Ni–Fe Layered Double Hydroxides. *Inorg. Chem.* **47**, 9103–9110 (2008).
16. Lu, X., Liang, G. & Zhang, Y. Synthesis and characterization of magnetic FeNi₃ particles obtained by hydrazine reduction in aqueous solution. *Mater. Sci. Eng. B* **139**, 124–127 (2007).
17. Liu, X. G. *et al.* (Fe, Ni)/C nanocapsules for electromagnetic-wave-absorber in the whole Ku-band. *Carbon* **47**, 470–474 (2009).
18. Conterposito, E. *et al.* Structural Characterisation of Complex Layered Double Hydroxides and TGA-GC-MS Study on Thermal Response and Carbonate Contamination in Nitrate- and Organic-Exchanged Hydrotalcites. *Chem. – Eur. J.* **21**, 14975–14986 (2015).
19. Carrasco, J. A. *et al.* Alkoxide-intercalated NiFe-layered double hydroxides magnetic nanosheets as efficient water oxidation electrocatalysts. *Inorg. Chem. Front.* **3**, 478–487 (2016).
20. Abellán, G., Prima-García, H. & Coronado, E. Graphene enhances the magnetoresistance of FeNi₃ nanoparticles in hierarchical FeNi₃–graphene nanocomposites. *J. Mater. Chem. C* **4**, 2252–2258 (2016).

Article 1

*Insights into the formation of metal carbon nanocomposites
using hybrid NiFe layered double hydroxides as precursors*

Submitted

Insights into the formation of metal carbon nanocomposites using hybrid NiFe layered double hydroxides as precursors.

*Jorge Romero*¹, *María Varela*^{2*}, *Mhamed Assebban*^{1,3}, *Victor Oestreicher*¹, *Jose L. Jordá*⁴,
Gonzalo Abellán^{1,3*}, *Eugenio Coronado*^{1*}

¹ Instituto de Ciencia Molecular (ICMol), Universidad de Valencia, Catedrático José Beltrán 2, 46980, Paterna, Valencia, Spain.

² Universidad Complutense de Madrid, Instituto Pluridisciplinar & Departamento de Física de Materiales, Madrid 28040, Spain.

³ Department of Chemistry and Pharmacy and Joint Institute of Advanced Materials and Processes (ZMP), University Erlangen-Nürnberg, Henkestr. 42, 91054 Erlangen and Dr.-Mack Str. 81, 90762 Fürth, Germany.

⁴ Instituto de Tecnología Química (UPV-CSIC), Universitat Politècnica de València, Consejo Superior de Investigaciones Científicas, Avenida de los Naranjos s/n, 46022, Valencia, Spain.

KEYWORDS: NiFe, layered double hydroxides, nanocomposites, *in situ* microscopy, hybrid materials,

ABSTRACT: The low-temperature formation mechanism of NiFe-carbon nanocomposites synthesized using hybrid sebacate intercalated layered double hydroxides (LDHs) as precursors has been deciphered by means a combined study using complementary *in situ* (temperature-dependent) techniques. Specifically, studies involving X-ray powder diffraction, thermogravimetry coupled to mass spectroscopy (TG-MS), statistical Raman spectroscopy (SRS), aberration-corrected scanning transmission electron microscopy and electron energy-loss spectroscopy (STEM-EELS) have been carried out. The experimental results confirm the early formation of FeNi₃ NPs at *ca.* 200–250 °C, preceding the concerted collapse of the starting NiFe-LDH laminar structure in just 50 °C (from 350 to 400 °C). At the same time, the catalytic interactions between the metallic atoms and the sebacate molecules permit the concomitant formation of a graphitic carbon matrix leading to the formation of the final FeNi₃-carbon nanocomposite. Furthermore, *in situ* temperature-dependent experiments in the presence of the intrinsic magnetic field of the STEM-EELS, allow observing the complete metal segregation of Ni and Fe even at 400 °C. These results provide fundamental insights into the catalytic formation of carbon-based nanocomposites using LDHs as precursors, and pave the way for the fine-tuning of their properties, with special interest in the field of energy storage and conversion.

1. INTRODUCTION

The demand of energy storage has increased exponentially in the last few years, forcing to look for new highly efficient and low-cost alternative materials to substitute those currently employed in conventional Li-ion batteries.^{1,2} In this sense, carbon-based supercapacitors (SCs) represent one of the most important alternatives in electrochemical energy storage due to their high energy and power densities, straightforward processability, and promising cycling life. SCs obtain their capacitance mainly due to the electrical double layer capacitance (EDLC), but currently several efforts are devoted to improve their energy and power densities through hybridization, including metal nanoparticles (NPs) to obtain a second source of capacitance by redox reactions of the metals, which is known as the faradic capacitance or pseudo-capacitance.³ As it has been recently reported by our group, a promising method to obtain these types of hybrid SCs consists of using Layered Double Hydroxides (LDHs) endowed with organic molecules in their interlaminar space as precursors.⁴⁻⁸ Indeed, our synthetic approach involves the facile low-temperature thermal decomposition of hybrid sebacate-intercalated catalytic Ni^{II}Fe^{III}-LDHs –synthesized using a conventional co-precipitation method– leading to hybrids consisting of FeNi₃–nanoparticles embedded in a carbon nanoform matrix. These materials behave as soft magnets at room temperature and exhibit excellent performances as supercapacitors, which can be dramatically improved by *ca.* 1100% in a second step in the presence of an external magnetic field as small as 4000 G.⁹ It was assumed that the periodic distribution of catalytic centres at the atomic scale inherent to LDH layers and the intimate contact between these layers and the carbon precursors in a constricted media might explain the appearance of carbon nanoforms and reduced metal nanoparticles. However, no direct experimental evidence of the catalytic process has been reported so far. Moreover, the issue about whether the metal reduction and the carbon graphitisation

processes are concomitant or not remains an open question. Indeed, when using hexagonal NiFe-LDHs (synthesized using ammonia releasing reagents,¹⁰ as catalysts, and ethylene as a carbon source –by means of chemical vapor deposition (CVD)–, a mixture of platelets consisting of NiFe₂O₄, NiO and FeNi₃ phases and carbon nanotubes is obtained,¹¹ in contrast to the formation of metallic NPs embedded in a graphitic matrix. Thus, current experimental evidences prevent understanding the catalytic process, and therefore an *in situ* experimental investigation using complementary techniques sensitive to both chemistry and structure would be strongly required to shed light on this interesting process. To tackle this challenge, we thoroughly analysed the formation of the nanocomposites by temperature-dependent powder X-ray diffraction, temperature-dependent statistical Raman spectroscopy, thermogravimetry coupled to mass spectroscopy, FT-IR, XPS, and last but not least, using real-space techniques such as in-operando temperature-dependent atomic-resolution aberration-corrected scanning transmission electron microscopy and electron energy-loss spectroscopy (STEM-EELS) at 80 kV.

Altogether we have been able to observe when and how different changes occur, seeing the structural conversion and the formation of metallic NPs embedded in a graphitic matrix at very low calcination temperatures. The formation of FeNi₃ NPs starts between 200–250 °C, and the concomitant collapse of the layered structure and the formation of the carbon nanoforms occur in around 50 °C (from 350 to 450 °C).

EXPERIMENTAL SECTION

Chemicals

All chemicals reagents $\text{Ni}(\text{NO}_3)_2 \cdot 6\text{H}_2\text{O}$, $\text{Fe}(\text{NO}_3)_3 \cdot 9\text{H}_2\text{O}$, $\text{HO}_2\text{C}(\text{CH}_2)_8\text{CO}_2\text{H}$ (sebacic acid), NaOH , and ethanol (Aldrich, Fluka, Alfa-Aesar) were used as received without further purification. Ultrapure water was obtained from a Millipore Milli-Q equipment.

Synthesis of the NiFe-LDH-Seb

The precursor NiFe-LDH–Seb was prepared following the general method described previously by our group, using sebacic acid/ NaOH .^{6,12}

Physical Characterization

Metallic atomic composition of bulk samples was determined by means of electron probe microanalysis performed in a Philips SEM-XL30 equipped with an EDAX microprobe. Carbon, nitrogen, and hydrogen contents were determined by microanalytical procedures by using a LECO CHNS-932. X-ray powder diffraction (XRPD) patterns were obtained with a Malvern Panalytical Empyrean diffractometer using the copper $K\alpha$ radiation ($\text{Cu-K}\alpha = 1.54178 \text{ \AA}$). Attenuated total reflectance Fourier-transform infrared (ATR-FTIR) spectra were collected in an Agilent Cary 630 FTIR spectrometer in the $4000\text{--}650 \text{ cm}^{-1}$ range in absence of KBr pellets. X-ray photoelectron spectroscopy (XPS) measures were recorded in a Thermo Scientific™ K-Alpha™ X-ray Photoelectron Spectrometer. Al $K\alpha$ x-ray radiation was employed as X-ray source. For all the elements more than 100 spectra were recorded employing a step of 0.1 eV with a focused spot higher than $50 \text{ }\mu\text{m}$. XPS data were analyzed with Thermo Advantage v5.9912 software. Raman spectroscopic characterization was carried out on a Horiba LabRAM Aramis confocal Raman

microscope ($\lambda_{\text{exc}}=532$ nm) with a laser spot size of *ca.* 1 μm (Olympus LMPlanFl 100, NA 0.80). The incident laser power was kept as low as possible to avoid structural sample damage: 0.17–1.8 mW. Spectra were obtained with a CCD array at -70 °C —grating: 600 grooves per mm. Spectra were obtained from a 20 x 20 μm area with 1 μm step size. Sample movement was carried out by an automated XY-scanning table. Scanning transmission electron microscopy and electron energy-loss spectroscopy (STEM-EELS) observations were carried out in a JEOL ARM200cF equipped with a spherical aberration corrector, a cold field emission gun and a Gatan Quantum EEL spectrometer, operated at 80 and 200 kV. The intensity of the magnetic field within the objective lens pole piece gap is of the order of 1 T. *In situ* heating experiments were carried out using a DENSSolutions Lighting D9 double tilt holder. EELS compositional maps were obtained by fitting EEL spectrum images to reference spectra via multiple linear least square (MLLS) fits.

2. RESULTS AND DISCUSSION

The precursor used in this work is a NiFe-LDH with sebacate molecules in the interlaminar space (NiFe-LDH-Seb) and a experimental Ni:Fe ratio of 3:1, synthesized by coprecipitation method under controlled heating conditions at 80 °C for 4 days, following a previously reported procedure^{6,12}.

In order to evaluate the formation of the nanocomposite (NC), we have monitored the change in the crystallinity of the initial NiFe-LDH-Seb by *in situ* X-ray powder diffraction (XRD) as a function of the temperature under nitrogen atmosphere. Figure 1(a) shows the evolution of the XRD patterns of the NiFe-LDH-Seb sample starting from room temperature until reaching 500 °C. The XRD pattern measured at room temperature displays broad and small diffraction lines confirming the presence of the NiFe-LDH phase forming very small crystalline domains. The peaks at $2\theta = 11.14^\circ$ and 18.96° can be assigned to the reflections (006) and (009), and provide information about the c parameter of the unit cell, which is related to the interlayer distance. An additional broad signal at higher angles, close to $2\theta = 60^\circ$, is assigned to the reflection (110) and can provide information a parameter of the unit cell, related to the minimal distance between the cations within the layer. So, values of the lattice parameters a and the basal spacing ($c/3$) were calculated to be 3.07 Å and 15.9 Å, respectively, in good agreement with values determined in previous report⁵.

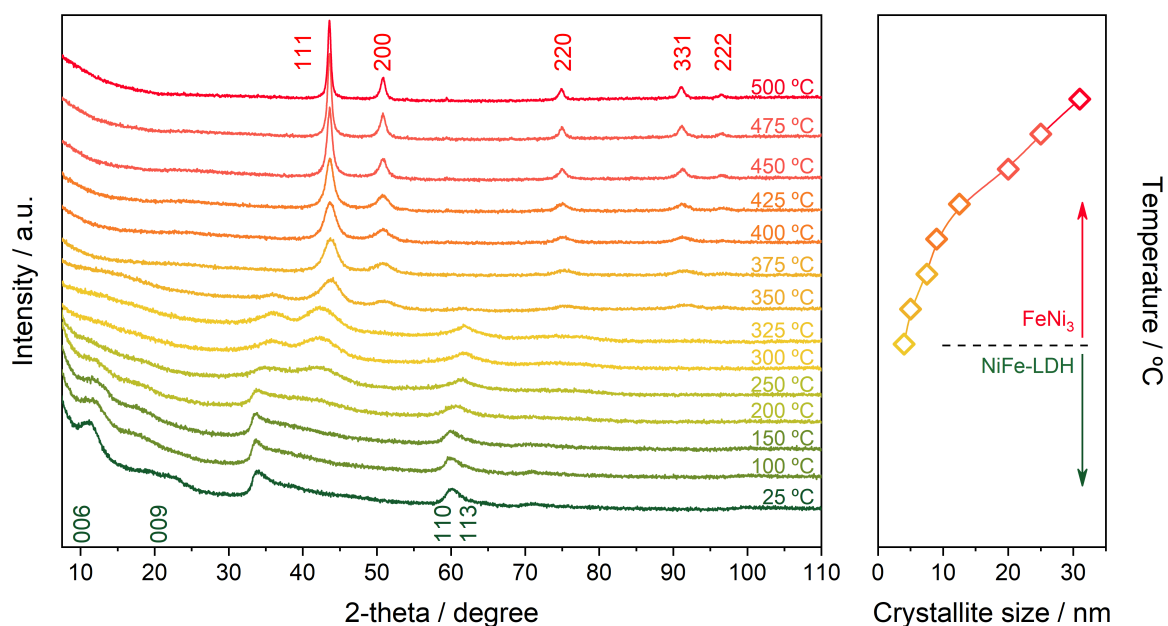


Figure 1. (a) *In situ* X-Ray powder diffraction patterns of the NiFe-LDH-Seb sample as a function of the temperature. The measurements were carried out in a heating chamber under nitrogen atmosphere. (b) Crystallite size calculated using the Scherrer equation applied to the diffraction peak corresponding to the (111) plane (Eq.1).

The evolution of the XRPD patterns suggests that the LDH structure remains unchanged until 200 °C indicating that the basal space of the sample was not significantly affected by the removal of interlamellar water molecules (*vide infra*), which generally occurs in this range of temperatures. This means that in our sample, the double anchoring point of sebacate anions impose the interlayer distance, in contrast to other LDH hybrids endowed with interlamellar anions connected by only one anchoring point, in which heating induces remarkable changes in the basal spacing¹³.

As soon the temperature reaches 250 °C, the reflection lines from the LDH structure are progressively becoming smaller and broader, suggesting its collapse and consumption.

Meanwhile, a new peak starts to emerge at around $\theta = 42.5$, which can be assigned to the (111) reflection coming from a *fcc* structure, proper to the NiFe metallic alloy. Next, a drastic structural transformation takes place between 250 and 350 °C, as new diffraction lines start to appear while the ones corresponding to the LDH phase start to vanish, suggesting the massive transformation of the crystalline LDH phase in a new one. These peaks observed at $2\theta = 50.87^\circ$, 75.45° and 91.05° are indexed to the (200), (220) and (331) reflections, respectively, and are characteristic of the *fcc* structure of FeNi₃ alloy (JCPDS N°. 38-0419)^{14,15}. Up to 375 °C the reflections from the *fcc* structure of FeNi₃ are becoming narrower and more intense, indicative of an enhancement in the crystallinity as well as a growth in the crystallite size. In fact, the growth of crystallite size can be estimated employing the Scherrer equation (Eq. 1):

$$\tau = \frac{K \cdot \lambda}{\beta \cdot \cos\theta} \quad (\text{Eq. 1})$$

where τ is the mean size of the ordered (crystalline) domains at a fixed θ value; K is a dimensionless shape factor with a value of 0.89; λ is the X-ray wavelength; β is the line broadening at half the maximum intensity (FWHM) in radians; and θ is the Bragg angle to the corresponding peak. Indeed, the evolution of the calculated crystallite size values as a function of temperature (Figure 1(b)) shows that, the initially formed FeNi₃ particles consisted mainly of nanoparticles smaller than 5 nm in size. Then, as the sample is further heated, the nanoparticles grow in size leading to the formation of bigger particles reaching 30 nm at 500 °C most probably through an Ostwald ripening process.

Average FTIR spectra (of at least 10 single point spectrum) of the NiFe-Seb-LDH sample were carried out ex-situ after each heat treatment at different temperatures in a CVD oven under inert nitrogen atmosphere (Figure SI 2). The measurements depict at least two steps in the transformation of NiFe-LDH Seb into NC. In the 25–200 °C range the loss of interlayer water can be clearly followed by the broad band at around 3400 cm^{-1} decrease. This signal is attributed to O–H stretching modes of water molecules, which gradually decreases in intensity until it disappears completely at 300 °C, indicating the complete loss of interlayer water. Additionally, the collapse of the LDH structure and its transformation into metallic NPs is distinctly evidenced by the marked disappearance of the metal-oxygen (M-O) stretching and bending modes (600 cm^{-1})¹⁶ in the 200–300 °C, in good agreement with above-discussed XRPD data. Finally, the diminution of asymmetric/symmetric stretching modes attributed to C-O confirms the loss of RCOO- groups.

In order to gain more information about the thermal behavior of the NiFe-LDH-Seb sample and the corresponding chemical changes, thermogravimetric analysis coupled to mass spectrometry (TG–MS) measurements was carried out¹⁷. Figure 2a depicts the mass loss of the sample upon heating up to 500 °C, which consists of a two-stage process: a first mass loss of 5% below 170 °C attributed to the loss of interlamellar and surface adsorbed water molecules ($m/z=18$) and a second mass loss of *ca.* 30% from 220 to 400 °C (attributed to dehydroxylation and decomposition/pyrolysis of the sebacate anion)^{16,17}. The second mass loss indicates that the sebacate anion decomposes in a relatively well-defined manner (step) and releases fragments that correspond to formaldehyde ($m/z=30$) and CO_2 ($m/z=44$). The release of formaldehyde, peaking at around 250 °C, is explained by the reduction of the carboxyl group of the sebacate anion. Afterwards, the emission of formaldehyde decreases as a result of the beginning of the dehydroxylation process, which is indicated by the emission of water molecules ($m/z=18$), and

subsequently CO₂ is being released instead. Further heating to nearly 350 °C marks a steep mass loss accompanied by an abrupt increase in the emission of H₂O and CO₂ as well as a fragment corresponding to benzene (m/z=78). The production of the latter hints towards a catalytic reaction involving Ni and/or Fe metal centers which are by now (at 350 °C) reduced to their metallic form as indicated by the XRD and FTIR data discussed above.¹⁸ Raman spectroscopy has been also used to further understand the evolution of the sebacate molecules as a function of temperature under N₂ atmosphere (Figure 2b)¹⁹. The mean spectra of the pristine NiFe-LDH-Seb at room temperature measured using a laser with a 532 nm excitation wavelength, displays large features in the 2750–2950 cm⁻¹ region ascribed to asymmetric and symmetric stretching of C-H bond, whilst the bands in 750–1750 cm⁻¹ region are attributed the deformation and twisting of the CH₂ within alkyl chain of the sebacate molecules²⁰. The characteristic peaks of M-O species are detected at 622 and 671 cm⁻¹, though the intensity of the signals is quite low. Upon heating, no significant changes can be observed up to 200 °C, then the intensity of the sebacate signals start to decrease (in concordance with FTIR) while at the same time new bands at 1354 and 1581 cm⁻¹ characteristic of a graphitic material rise (*i.e.*, D and G), indicating the conversion of the organic chains from sebacate molecules into a new graphitic structure. The D and G bands become more evident as we continue heating up to 350 °C. This observation fits perfectly well with the benzene signal detected by TG-MS and sheds light into the chemical transformation that takes place within the interlamellar gallery of the NiFe-LDH-Seb. Furthermore, we correlated these results with X-ray photoelectron spectroscopy in order to analyse the oxidation state of the different components in the surface of the material. Along this front, XPS confirms the formation of graphitic carbon at 400 °C (Figure 2c). Moreover, XPS allows to corroborate the appearance of metallic iron at 300 °C, in concordance with the *in situ* XRPD, however the presence of metallic nickel, highlighted by

the signal centered at 852.7 eV, is only appreciable when the temperature rises 400 °C. It is to be noted that, as a result of the configuration of the Raman chamber not being completely airtight, trace amounts of oxygen penetrated inside and caused the thermal transformations to occur at temperatures lower than in the case of XRD, FTIR and XPS measurements, as well as inducing some combustion of the organic molecules thus making challenging to measure with confidence at temperatures higher than 400 °C.

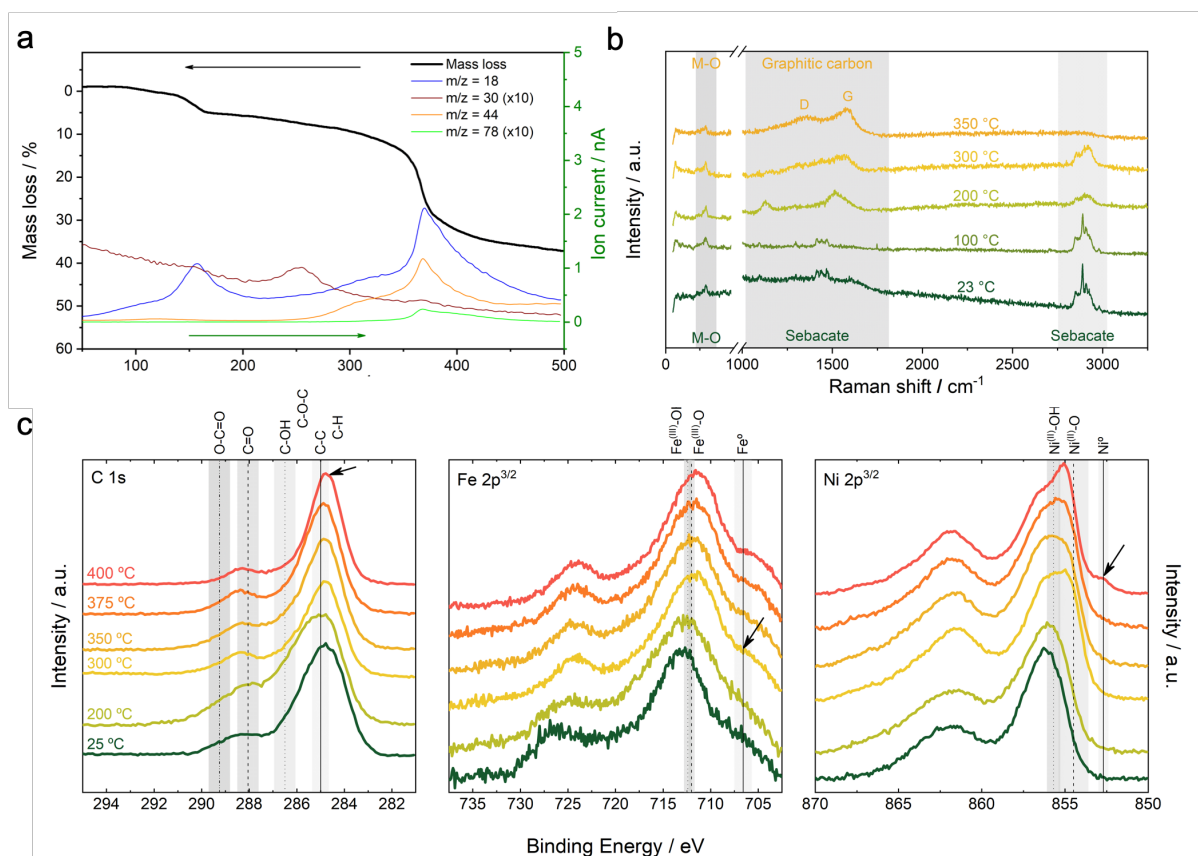


Figure 2. (a) TG-MS analysis using a heating rate of 10 °C/min under helium. (b) *in situ* Raman spectroscopic characterization in a heating chamber under inert atmosphere. (c) XPS high-

resolution spectra of the C 1s, Fe 2p^{3/2} and Ni 2p^{3/2} of the pristine material and the *ex situ* calcinations samples at different temperatures.

To sum up, XRD, FTIR, TG-MS, Raman and XPS characterization confirms that heat treatment of the NiFe-LDH-Seb under inert atmosphere results in a collapse and shrinkage of the inorganic layered structure and growth of graphitic carbon in the confined space between the layers. While the exact mechanism is still unknown, it is quite evident that it involves a concomitant decomposition of the sebacate and further catalytic graphitization of the carbon matrix, resulting the *in situ* carbothermal reduction of Ni²⁺ and Fe³⁺ species, which form FeNi₃ nanoparticles. The previous results suggest that the formation of catalytic FeNi₃ NPs starts before the collapse of the layered structure (around 250–350°C) leading afterwards to the formation of the FeNi₃-carbon nanocomposite, however, we do not count with a direct experimental evidence. This process can be similar to what happens during the CVD synthesis of carbon nanotubes (CNT) using carbon feedstock, where metal catalyst particles play two key roles, namely: i) decomposition of the carbon feedstock (hydrocarbon) and ii) catalytic nucleation/growth of the emerging CNT. In a similar way, another study has reported the formation of graphitic nanostructures via metal-induced catalyzed graphitization using nickel, cobalt, or iron²¹.

In order to further clarify the formation of the nanocomposite, the precise moment when the layered structure collapses and to determine the involved dynamic processes, we have performed *in situ* electron microscopy analysis at temperatures ranging between room temperature and 400 °C. Specifically, we analyzed the NiFe-LDH by real-space techniques, sensitive to both structure and chemical composition, namely atomic-resolution aberration-corrected scanning transmission electron microscopy and electron energy-loss spectroscopy (STEM-EELS) at 80 kV. For this

acceleration voltage, the magnetic field within the objective lens pole piece is slightly above one Tesla.

Simultaneously acquired low magnification annular bright field (ABF) and high angle annular bright field (HAADF) images of the as-prepared NiFe-LDH sample (Figure SI 3-4) show a flake-like structure consisting of partially curved plates with rough edges with lateral length in the tens of nanometers range, typical of LDH materials prepared by coprecipitation method^{5,6}. High-resolution images in Figure SI 5 depict the local crystallinity within the material with the expected in-plane hexagonal crystal symmetry. Compositional maps obtained from EELS measurements reveal the chemical composition of the flake and show a rather even lateral distribution of the constituent metals, namely Fe and Ni, as well as C and O.

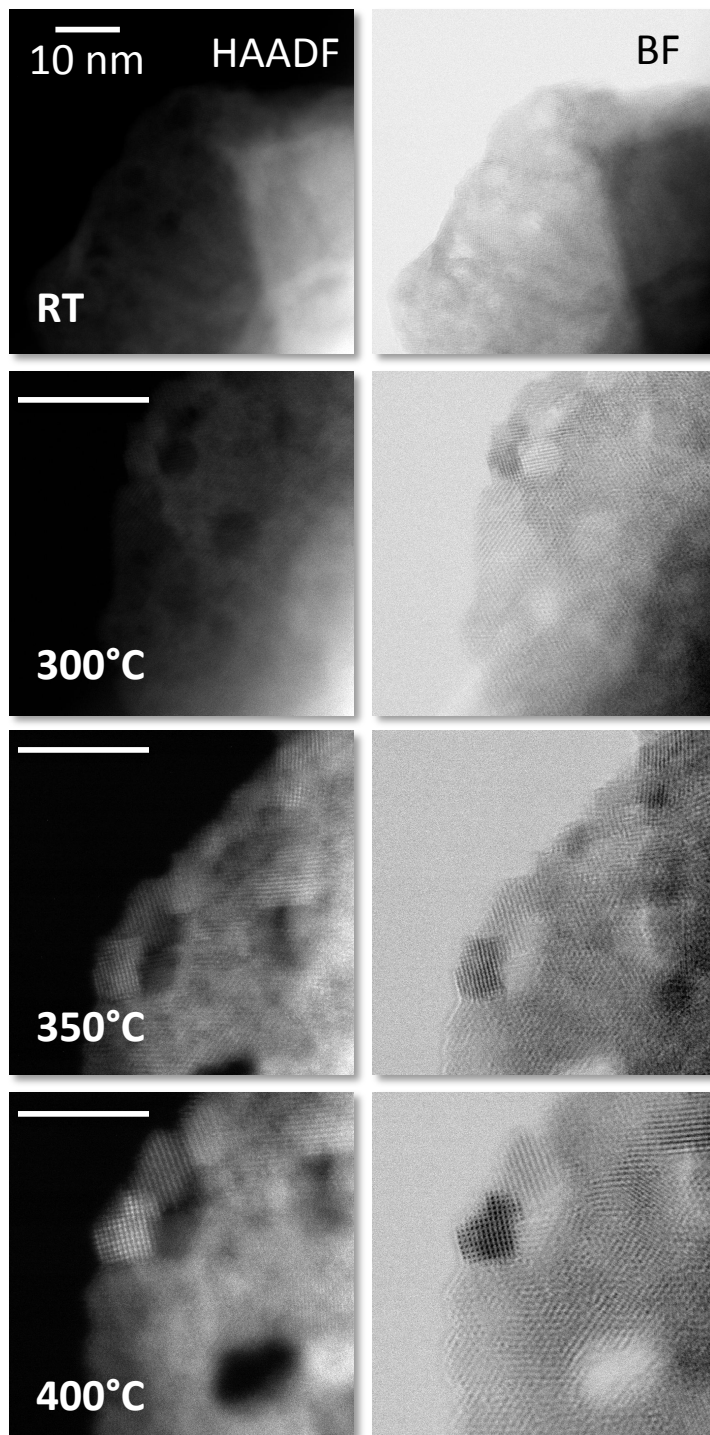


Figure 3. Simultaneously acquired high-angle annular dark field (HAADF, left column) and annular bright field (ABF, right column) images at high magnification, showing the evolution of the material at different temperatures: From top to bottom, room temperature, 300, 350 and 400 °C, respectively. The scale bars represent 10 nm.

Next, the sample was submitted to a gradual increase in temperature while, at the same time, acquiring ABF and HAADF images *in situ*. Figure 3, exhibits the gradual morphological and structural transformation of the material as a function of temperature. After heating the sample to 300 °C, noticeable structural changes take place, such as the beginning of the formation of small particles (e.g. see the top-left of the flake) as well as the appearance of some degree of crystallization within the thinnest areas at the edges.

When the temperature is raised to 350 °C, differentiation between the nanometric clusters starts to be more obvious and the degree of crystallinity of the surrounding matrix is further enhanced. Moreover, holding the sample temperature at 350 °C for few minutes drives the formation of perfect nanocrystals with clearly defined shapes and sizes in the few nm range (See. A further increasing in the temperature has no drastic effect beside an improvement of the crystallinity of both the FeNi₃ nanoparticles and the carbon matrix, as can be also seen in the high magnification images shown in Figure 4, in concordance with the XRD measurements.

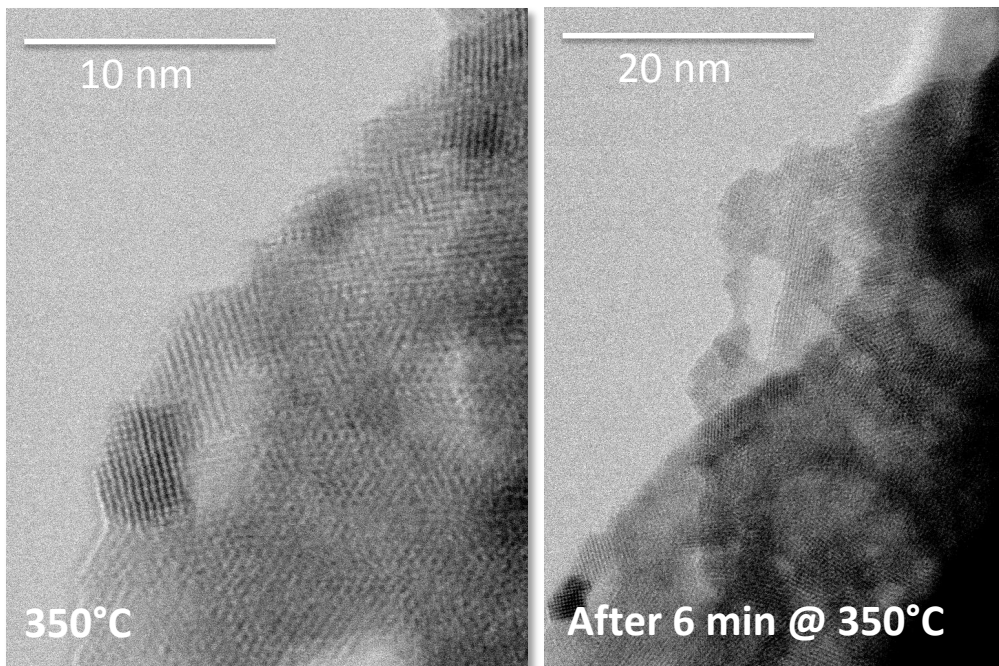


Figure 4. Atomic resolution ABF images showing the evolution of the dynamic behavior of the material after holding the temperature at 350 °C for 6 minutes.

Correspondingly, EELS compositional maps obtained from the analysis of the C K , O K , Fe $L_{2,3}$ or Ni $L_{2,3}$ edges shown in Figure 5 and Figure 6 clearly demonstrate how the metal distribution within the material went from being homogeneously distributed in the initial LDH structure into becoming a perfectly segregated nanoparticles of several tens of nanometers.

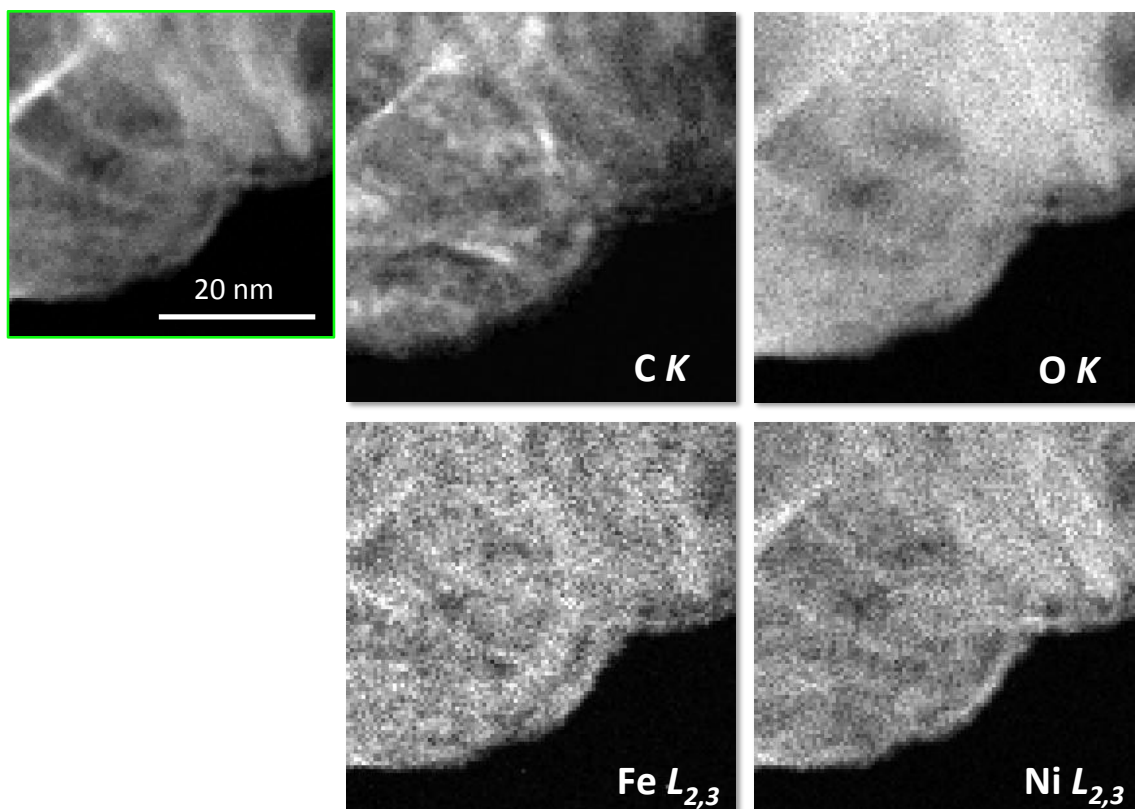


Figure 5. Electron energy-loss compositional maps of the pristine NiFe-LDH-Seb at RT.

Furthermore, EELS maps acquired at 400 °C, display a complete segregation of Ni and Fe oxides into nanometric clusters. A similar effect has been previously observed in this type of material and can be attributed to the effect of the lens magnetic field inside the microscope⁹. When the sample is brought back to room temperature, the structure is segregated and a distribution of Ni and Fe oxide NPs with a cotton are there to stay, without rest of LDH like structures Figure SI 6). Therefore, we can say that at room temperature we can observe the platelet-like crystals of LDH flakes seen sideways, with a relatively even distribution of O, Fe and Ni species within the nanocrystals. At 300 °C we can discern some structural changes, with initial small crystalline NPs,

but it is between 350 and 400 °C where most changes occurs, in perfect agreement with previous techniques. Finally, after 400 °C there are only bigger NPs, without rests of LDH like structures.

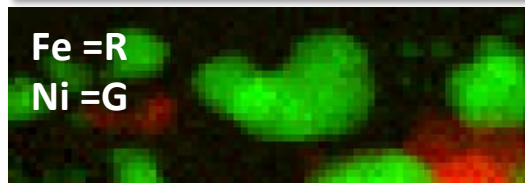
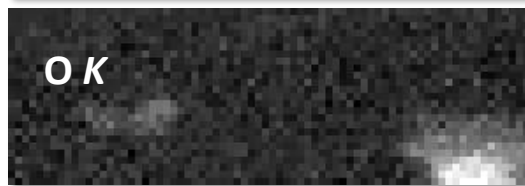
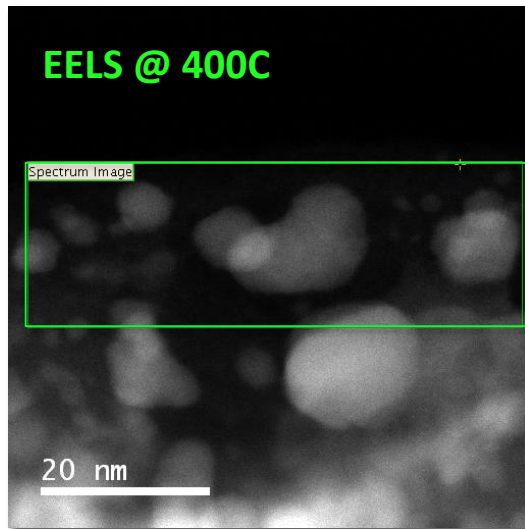


Figure 6. Electron energy-loss compositional maps at 400 °C at low magnifications showing the distribution of C, O, Fe and Ni. The left panels show the HAADF images of the areas where the EEL spectrum images were measured (marked with green rectangles), while the panels on the right exhibit the actual C *K*, O *K*, Fe *L*_{2,3} and Ni *L*_{2,3} images. The bottom panel in (b) depicts an overlay of the Fe (red) and Ni (green) images, showing the complete segregation of both species.

Figure 7 depicts a scheme summarizing the main steps involved in the LDH's transformation into a nanocomposite, showing that after the initial low-temperature desorption of water (<150°C), the formation of FeNi₃ clusters takes place until 350°C. Afterwards, between 350° and 400°C, the concerned collapse of the LDH structure with the graphitization of the sebacate molecules occurs. Concomitantly, the FeNi₃ nanoparticles growth until 400°C. Further increasing in the temperature results into a progressive graphitization and nanoparticles sintering.

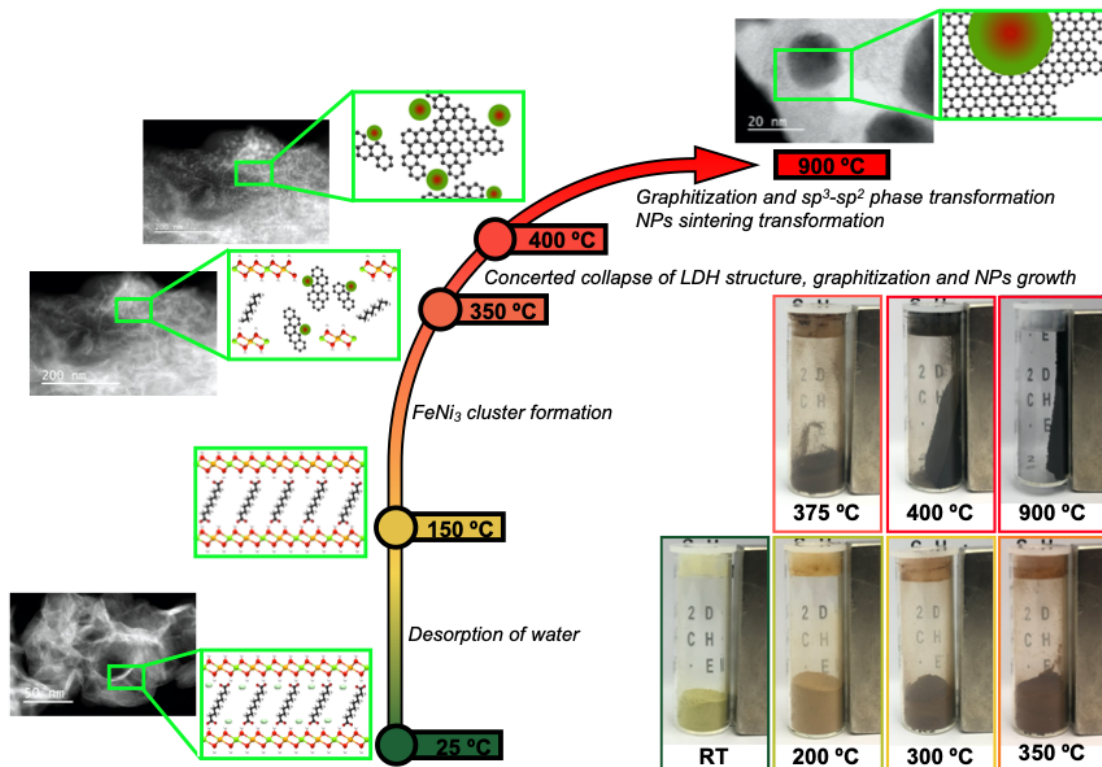


Figure 7. Schematic representation of the NC's formation showing the principal steps. As soon the temperature increases the loss of the interlayer water molecules take place at 150 °C. Around 350 °C, the LDH structure collapses with concerted dehydroxylation by the sebacate molecules decomposition. At the same time, the reduction of Ni^{II}-Fe^{III} takes place driving the formation of small NiFe NPs and a graphitization of the organic molecules. For higher temperatures, a progressive graphitization of the carbon matrix and sp³-sp² phase transformation occurs, simultaneously with a sintering process that increases the metallic NP's size. Hence, the magnetic behavior of the NP is observable.

3. CONCLUSIONS

In summary, with an unprecedented sum of complementary *in situ* techniques we have been able to observe the subtleties regarding the thermal transformation of NiFe layered double hydroxide intercalated with sebacate molecules (NiFe-LDH-Seb) into NiFe-carbon nanocomposites (NCs). All the different techniques are in good agreement, showing how the formation of small catalytically active FeNi₃ clusters precedes the collapse of the starting NiFe-LDH-Seb laminar structure. This process takes place in the range between 350 and 400 °C, driving the growth of FeNi₃ metal NPs by calcination. Remarkably, this process takes place at much lower temperatures than the conventional synthetic approaches used to form this alloy. These results provide a better understanding about the intriguing formation of carbon-based NCs employing layered hydroxides as precursors, providing tools for tuning their properties for different applications of interest. In this sense, *in situ* temperature-dependent experiments in the presence of the intrinsic magnetic field of the scanning transmission electron microscope, allow to observe the complete metal segregation of Ni and Fe even at 400 °C. This result is very important as it allows to envision a straightforward formation of highly electrochemically active NiFe-carbon nanocomposites.⁹

ASSOCIATED CONTENT

Supporting Information

AUTHOR INFORMATION

Corresponding Authors

*E-mail: mvarela@ucm.es. (M.V.)

*E-mail: gonzalo.abellan@uv.es. (G.A.)

*E-mail: eugenio.coronado@uv.es. (E.C.)

Notes

The authors declare no competing financial interest.

ACKNOWLEDGMENT

Financial support from the European Union (ERC Advanced Grant Mol-2D 788222, ERC Starting Grant 2D-PnictoChem 804110, ERC Proof of Concept Grant Hy-MAC 713704, and COST-Action on Molecular Spintronics (MOLSPIN CA15128)), the Spanish MINECO (Projects MAT2017-89943-R, MAT2015-66888-C3-3-R, RTI2018-097895-B-C43 co-financed by FEDER, and the Unit of Excellence “Maria de Maeztu” MDM-2015-0538), and the Generalitat Valenciana (Prometeo Program) is gratefully acknowledged. G.A. thanks for the support by the Deutsche Forschungsgemeinschaft DFG (FLAG-ERA AB694/2-1) and the Generalitat Valenciana (CIDEAGENT/2018/001 grant). G.A. received financial support through the Postdoctoral Junior Leader Fellowship Programme from “la Caixa” Banking Foundation. J.R. thanks the Spanish MINECO for his predoctoral grants. Electron microscopy observations were carried out at the ICTS ELECMI node at Centro Nacional de Microscopía Electrónica at the Universidad Complutense de Madrid. The authors thanks to Dr. María Dolores Jordán Martín for her kind assistance with the XPS measurements.

REFERENCES

- (1) Lewis, N. S.; Nocera, D. G. Powering the Planet: Chemical Challenges in Solar Energy Utilization. *Proc. Natl. Acad. Sci.* **2006**, *103* (43), 15729–15735. <https://doi.org/10.1073/pnas.0603395103>.
- (2) Gray, H. B. Powering the Planet with Solar Fuel. *Nat. Chem.* **2009**, *1* (1), 7–7. <https://doi.org/10.1038/nchem.141>.
- (3) Bonaccorso, F.; Colombo, L.; Yu, G.; Stoller, M.; Tozzini, V.; Ferrari, A. C.; Ruoff, R. S.; Pellegrini, V. Graphene, Related Two-Dimensional Crystals, and Hybrid Systems for Energy Conversion and Storage. *Science* **2015**, *347* (6217), 1246501. <https://doi.org/10.1126/science.1246501>.
- (4) Coronado, E.; Ribera, A.; Abellán, G. Graphitized Matrix Nanocomposites and Metal Nanoparticles with Supercapacitance and Magnetoresistance Properties. WO2013124503A1, August 29, 2013.
- (5) Abellán, G.; Coronado, E.; Martí-Gastaldo, C.; Ribera, A.; Otero, T. F. Magnetic Nanocomposites Formed by FeNi₃ Nanoparticles Embedded in Graphene. Application as Supercapacitors. *Part. Part. Syst. Charact.* **2013**, *30* (10), 853–863. <https://doi.org/10.1002/ppsc.201300186>.
- (6) Abellán, G.; Coronado, E.; Martí-Gastaldo, C.; Ribera, A.; F. Sánchez-Royo, J. Layered Double Hydroxide (LDH)–Organic Hybrids as Precursors for Low-Temperature Chemical Synthesis of Carbon Nanoforms. *Chem. Sci.* **2012**, *3* (5), 1481–1485. <https://doi.org/10.1039/C2SC01064J>.
- (7) Abellán, G.; Martínez, J. G.; Otero, T. F.; Ribera, A.; Coronado, E. A Chemical and Electrochemical Multivalent Memory Made from FeNi₃-Graphene Nanocomposites. *Electrochem. Commun.* **2014**, *39*, 15–18. <https://doi.org/10.1016/j.elecom.2013.11.026>.
- (8) Abellán, G.; Martí-Gastaldo, C.; Ribera, A.; Coronado, E. Hybrid Materials Based on Magnetic Layered Double Hydroxides: A Molecular Perspective. *Acc. Chem. Res.* **2015**, *48* (6), 1601–1611. <https://doi.org/10.1021/acs.accounts.5b00033>.
- (9) Romero, J.; Prima-Garcia, H.; Varela, M.; Miralles, S. G.; Oestreicher, V.; Abellán, G.; Coronado, E. Giant Enhancement in the Supercapacitance of NiFe–Graphene Nanocomposites Induced by a Magnetic Field. *Adv. Mater.* **2019**, *31* (28), 1900189. <https://doi.org/10.1002/adma.201900189>.
- (10) Abellán, G.; Coronado, E.; Martí-Gastaldo, C.; Pinilla-Cienfuegos, E.; Ribera, A. Hexagonal Nanosheets from the Exfoliation of Ni²⁺ - Fe³⁺ LDHs: A Route towards Layered Multifunctional Materials. *J. Mater. Chem.* **2010**, *20* (35), 7451–7455. <https://doi.org/10.1039/C0JM01447H>.
- (11) Abellán, G.; Carrasco, J. A.; Coronado, E.; Prieto-Ruiz, J. P.; Prima-García, H. In-Situ Growth of Ultrathin Films of NiFe-LDHs: Towards a Hierarchical Synthesis of Bamboo-Like

Carbon Nanotubes. *Adv. Mater. Interfaces* **2014**, *1* (6), 1400184. <https://doi.org/10.1002/admi.201400184>.

(12) Coronado, E.; Galán-Mascarós, J. R.; Martí-Gastaldo, C.; Ribera, A.; Palacios, E.; Castro, M.; Burriel, R. Spontaneous Magnetization in Ni–Al and Ni–Fe Layered Double Hydroxides. *Inorg. Chem.* **2008**, *47* (19), 9103–9110. <https://doi.org/10.1021/ic801123v>.

(13) Abellán, G.; Luis Jordá, J.; Atienzar, P.; Varela, M.; Jaafar, M.; Gómez-Herrero, J.; Zamora, F.; Ribera, A.; García, H.; Coronado, E. Stimuli-Responsive Hybrid Materials: Breathing in Magnetic Layered Double Hydroxides Induced by a Thermoresponsive Molecule. *Chem. Sci.* **2015**, *6* (3), 1949–1958. <https://doi.org/10.1039/C4SC03460K>.

(14) Lu, X.; Liang, G.; Zhang, Y. Synthesis and Characterization of Magnetic FeNi₃ Particles Obtained by Hydrazine Reduction in Aqueous Solution. *Mater. Sci. Eng. B* **2007**, *139* (2), 124–127. <https://doi.org/10.1016/j.mseb.2007.01.055>.

(15) Liu, X. G.; Li, B.; Geng, D. Y.; Cui, W. B.; Yang, F.; Xie, Z. G.; Kang, D. J.; Zhang, Z. D. (Fe, Ni)/C Nanocapsules for Electromagnetic-Wave-Absorber in the Whole Ku-Band. *Carbon* **2009**, *47* (2), 470–474. <https://doi.org/10.1016/j.carbon.2008.10.028>.

(16) Carrasco, J. A.; Romero, J.; Varela, M.; Hauke, F.; Abellán, G.; Hirsch, A.; Coronado, E. Alkoxide-Intercalated NiFe-Layered Double Hydroxides Magnetic Nanosheets as Efficient Water Oxidation Electrocatalysts. *Inorg. Chem. Front.* **2016**, *3* (4), 478–487. <https://doi.org/10.1039/C6QI00009F>.

(17) Conterosito, E.; Palin, L.; Antonioli, D.; Viterbo, D.; Mugnaioli, E.; Kolb, U.; Perioli, L.; Milanesio, M.; Gianotti, V. Structural Characterisation of Complex Layered Double Hydroxides and TGA-GC-MS Study on Thermal Response and Carbonate Contamination in Nitrate- and Organic-Exchanged Hydrotalcites. *Chem. – Eur. J.* **2015**, *21* (42), 14975–14986. <https://doi.org/10.1002/chem.201500450>.

(18) Anton, R. In Situ TEM Investigations of Reactions of Ni, Fe and Fe–Ni Alloy Particles and Their Oxides with Amorphous Carbon. *Carbon* **2009**, *47* (3), 856–865. <https://doi.org/10.1016/j.carbon.2008.11.038>.

(19) Abellán, G.; Schirowski, M.; Edlhalhammer, K. F.; Fickert, M.; Werbach, K.; Peterlik, H.; Hauke, F.; Hirsch, A. Unifying Principles of the Reductive Covalent Graphene Functionalization. *J. Am. Chem. Soc.* **2017**, *139* (14), 5175–5182. <https://doi.org/10.1021/jacs.7b00704>.

(20) Islam, M. R.; Guo, Z.; Rutman, D.; Benson, T. J. Immobilization of Triazabicyclodecene in Surfactant Modified Mg/Al Layered Double Hydroxides. *RSC Adv.* **2013**, *3* (46), 24247–24255. <https://doi.org/10.1039/C3RA43051K>.

(21) Hoekstra, J.; Beale, A. M.; Soulimani, F.; Versluijs-Helder, M.; Geus, J. W.; Jenneskens, L. W. Base Metal Catalyzed Graphitization of Cellulose: A Combined Raman Spectroscopy, Temperature-Dependent X-Ray Diffraction and High-Resolution Transmission Electron Microscopy Study. *J. Phys. Chem. C* **2015**, *119* (19), 10653–10661. <https://doi.org/10.1021/acs.jpcc.5b00477>.

Supporting Information

Insights into the formation of metal carbon nanocomposites using hybrid NiFe layered double hydroxides as precursors

*Jorge Romero*¹, *María Varela*^{2*}, *Mhamed Assebban*^{1,3}, *Victor Oestreicher*¹, *Jose L. Jordá*⁴, *Gonzalo Abellán*^{1,3*}, *Eugenio Coronado*^{1*}

¹ Instituto de Ciencia Molecular (ICMol), Universidad de Valencia, Catedrático José Beltrán 2, 46980, Paterna, Valencia, Spain.

² Universidad Complutense de Madrid, Instituto Pluridisciplinar & Departamento de Física de Materiales, Madrid 28040, Spain.

³ Department of Chemistry and Pharmacy and Joint Institute of Advanced Materials and Processes (ZMP), University Erlangen-Nürnberg, Henkestr. 42, 91054 Erlangen and Dr.-Mack Str. 81, 90762 Fürth, Germany.

⁴ Instituto de Tecnología Química (UPV-CSIC), Universitat Politècnica de València, Consejo Superior de Investigaciones Científicas, Avenida de los Naranjos s/n, 46022, Valencia, Spain.

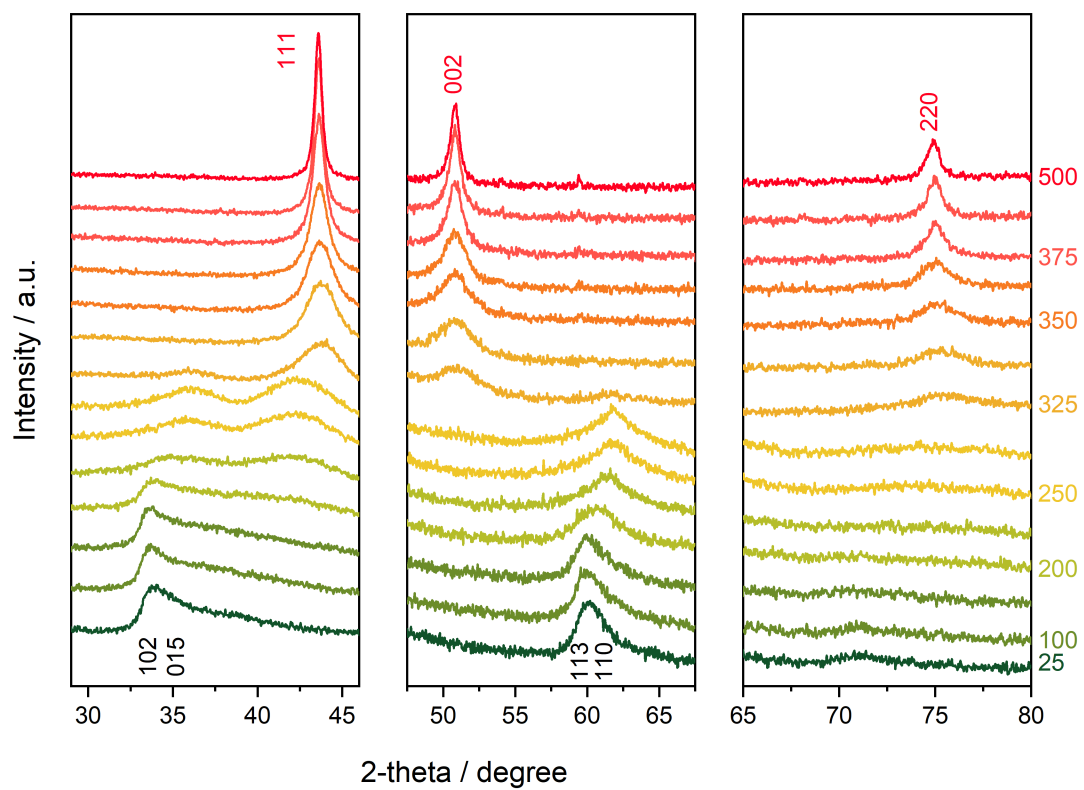


Figure SI 1. *In-situ X-Ray powder diffraction measurements in an inert heating chamber, showing the different peaks evolutions zones at different temperatures.*

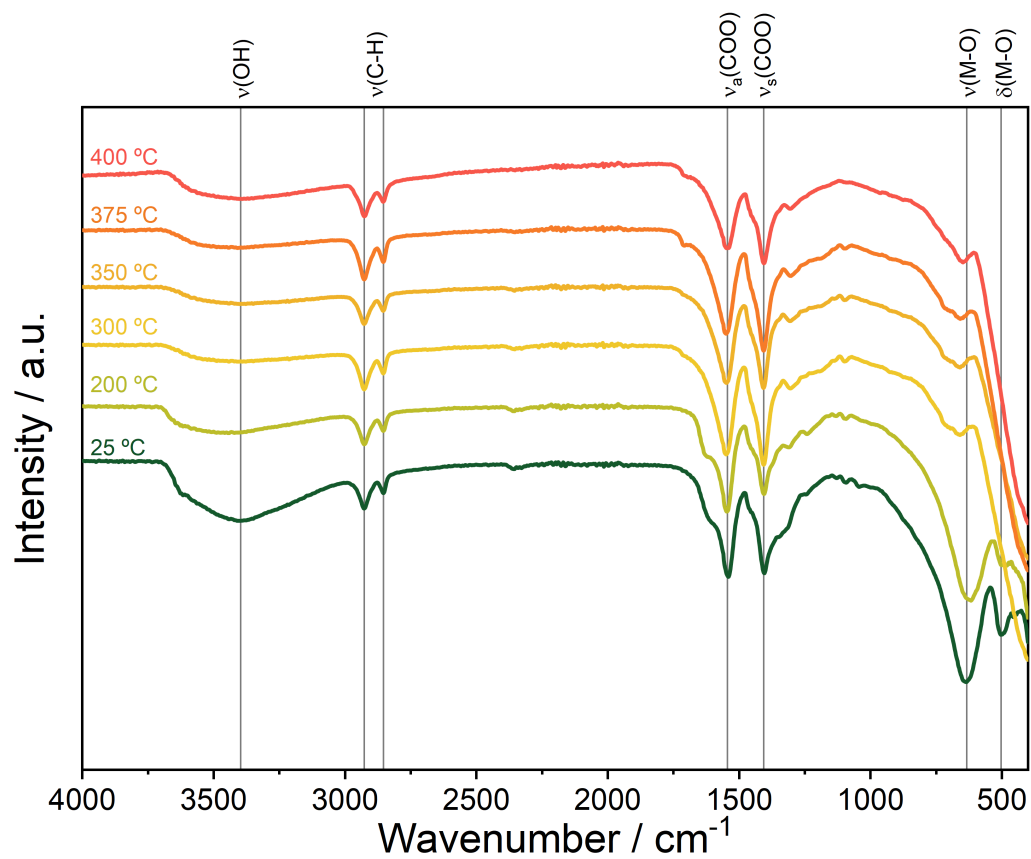


Figure SI 2. Infra-Red spectra of the pristine material and the *ex situ* calcinations at different temperatures.

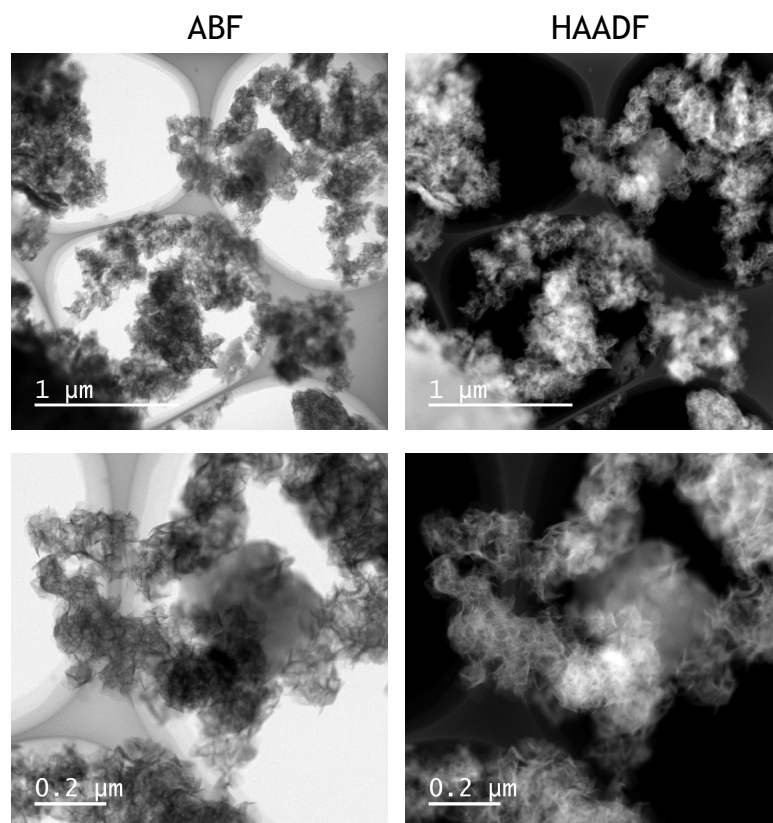


Figure SI 3. Low magnification, simultaneously acquired annular bright field (ABF) and high angle annular dark field (HAADF) images of the pristine NiFe-LDH-Sebacate at low magnifications.

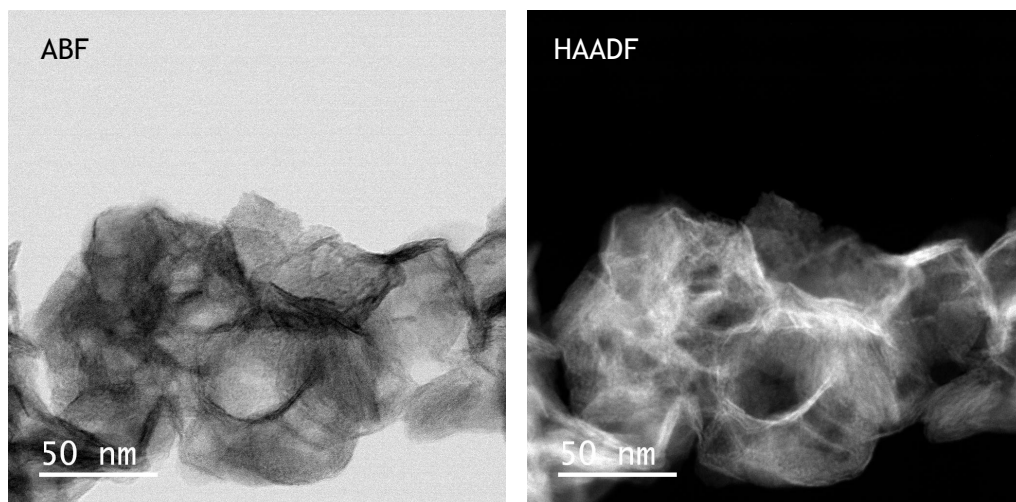


Figure SI 4. ABF and HAADF images of the pristine NiFe-LDH-Sebacate at intermediate magnifications.

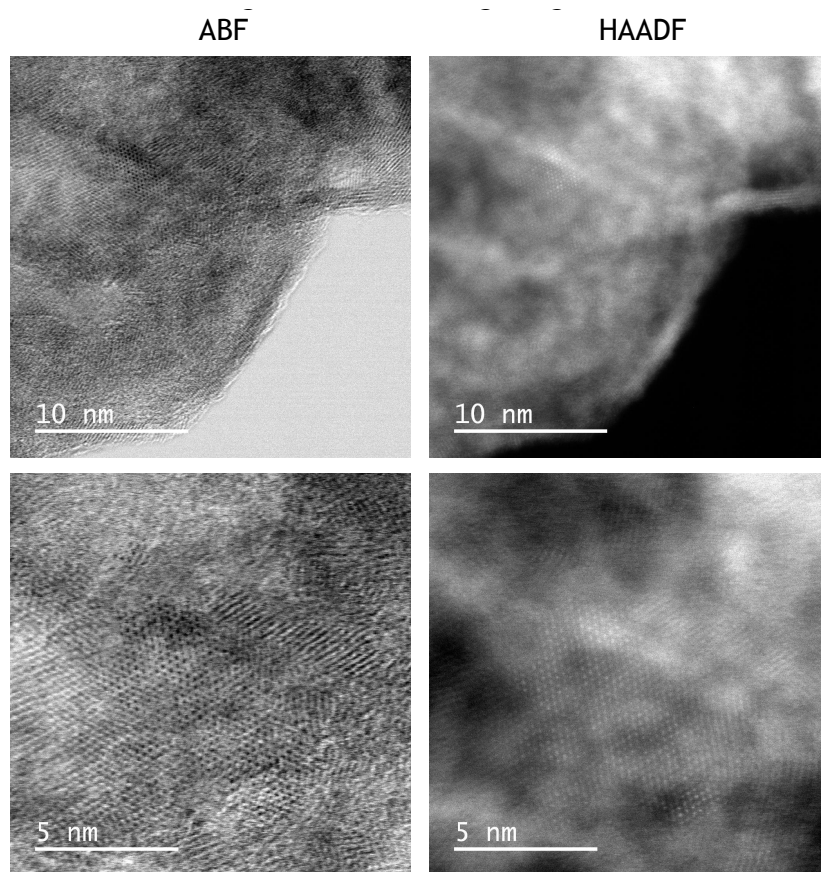


Figure SI 5. Atomic resolution ABF and HAADF images of the pristine NiFe-LDH-Sebacate.

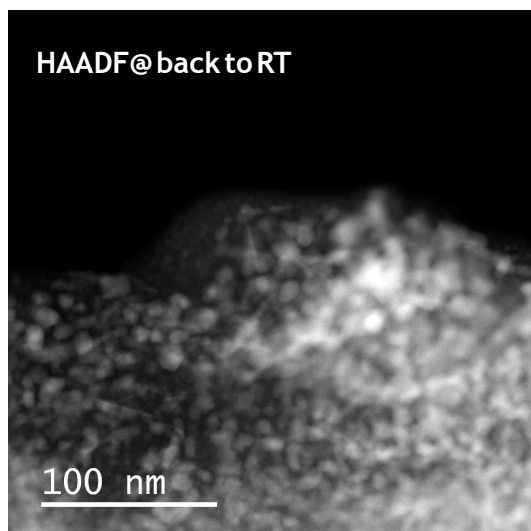


Figure SI 6. HAADF image obtained at room temperature after heat treatment.

Article 2

*Giant Enhancement in the Supercapacitance of NiFe–
Graphene Nanocomposites Induced by a Magnetic Field*

Advanced Materials. 2019, 31, 1900189

Vol. 31 • No. 28 • July 12 • 2019

www.advmat.de

ADVANCED MATERIALS



WILEY-VCH

Giant Enhancement in the Supercapacitance of NiFe–Graphene Nanocomposites Induced by a Magnetic Field

Jorge Romero, Helena Prima-Garcia, Maria Varela, Sara G. Miralles, Víctor Oestreich, Gonzalo Abellán,* and Eugenio Coronado*

The rapid rise in energy demand in the past years has prompted a search for low-cost alternatives for energy storage, supercapacitors being one of the most important devices. It is shown that a dramatic enhancement ($\approx 1100\%$, from 155 to 1850 F g⁻¹) of the specific capacitance of a hybrid stimuli-responsive FeNi₃–graphene electrode material can be achieved when the charge/discharge cycling is performed in the presence of an applied magnetic field of 4000 G. This result is related to an unprecedented magnetic-field-induced metal segregation of the FeNi₃ nanoparticles during the cycling, which results in the appearance of small Ni clusters (<5 nm) and, consequently, in an increase in pseudocapacitive sites. The results open the door to a systematic improvement of the capacitance values of hybrid supercapacitors, while moving the research in this area towards the development of magnetically addressable energy-storage devices.

Due to the pressing increase of global warming effects and the finite nature of fossil fuels, the search for alternative energy sources has dramatically boosted during the last few years.^[1,2] Hybrid systems consisting of layered materials have taken the lead in the design of advanced nanomaterials based on their superior electrochemical performance reliant on their unique physical properties, control over their organization, and efficient electronic communication due to hybridization between components.^[3,4] Energy-related applications that could benefit the most from these hybrid systems include flexible electronics, lithium


and sodium ion batteries with efficient anodes and cathodes, solar cells, or supercapacitors (SCs) with high energy and power densities, useful for industrial stationary applications, automotive transportation, and portable electronic applications.^[5] Such supercapacitors are key elements among energy storage devices due to their potential to deliver high power densities in short periods of time with high cyclability and durability.^[6] In supercapacitive devices, recent efforts trying to improve the energy and power densities have been devoted to optimize the internal configuration of the capacitor. This includes new synthetic approaches for electrode materials, novel capacitor configurations, or tailored porous hierarchies. Even though the fast development of electrode materials for SCs has dramatically increased the performance of these devices, there is still room for further improvement.^[7] In this context, a loosely investigated approach consists in the application of an external stimulus, such as a magnetic field.^[8–10] In principle, magnetic fields may affect the capacitive internal resistances since they can induce complex magnetohydrodynamic (MHD) phenomena in the electrolytes, offering a new tool for tuning the performance of SCs. Despite some remarkable efforts, this effect remains very small.^[11,12]

Here, we present an approach to overcome this limitation, consisting of incorporating magnetic nanoparticles in the electrochemically active material, which can be easily magnetized by an external field. We have recently reported the development of a low-temperature route to the synthesis of hierarchically structured magnetic graphene–FeNi₃ nanocomposites (MNC) using hybrid layered double hydroxides nanoreactors as precursors.^[13,14] These materials exhibit excellent performances as supercapacitors, and at the same time they behave as soft magnets at room temperature.^[14,15] Herein, we demonstrate that the application of a relatively weak magnetic field of 4000 G during galvanostatic charge–discharge cycles results in a dramatic enhancement of the specific capacitance near 1100% with respect to pristine MNC. A thorough characterization by means of electron microscopies, magnetic properties, transport measurements, X-ray photoelectron spectroscopy (XPS), Raman spectroscopy, and electrochemical measurements (cyclic voltammetry, galvanostatic charge/discharge, and potentiostatic electrochemical impedance spectroscopy (PEIS)) revealed that the origin of this effect is a full metal segregation of the magnetic nanoparticles induced by the magnetic field.

J. Romero, Dr. H. Prima-Garcia, Dr. S. G. Miralles, Dr. V. Oestreich, Dr. G. Abellán, Prof. E. Coronado
Instituto de Ciencia Molecular (ICMol)
Universidad de Valencia
Catedrático José Beltrán 2, 46890 Paterna, Spain
E-mail: gonzalo.abellan@uv.es; eugenio.coronado@uv.es

Prof. M. Varela
Universidad Complutense de Madrid
Instituto Pluridisciplinar
Instituto de Magnetismo Aplicado & Departamento de Física de Materiales
Madrid 28040, Spain

Dr. G. Abellán
Department of Chemistry and Pharmacy and Joint Institute of Advanced Materials and Processes (ZMP)
Friedrich-Alexander-Universität Erlangen-Nürnberg (FAU)
Nikolaus Fiebiger-Strasse 10, 91058 Erlangen and Dr.-Mack Strasse 81
90762 Fürth, Germany

 The ORCID identification number(s) for the author(s) of this article can be found under <https://doi.org/10.1002/adma.201900189>.

DOI: 10.1002/adma.201900189

To evaluate the performance of the pristine MNC under an external applied magnetic field, we used a homemade 3-electrode electrochemical cell fixed between the two magnetic poles of a controllable electromagnet and KOH 6 M as electrolyte (Figure 1; Figure S1, Supporting Information). The cyclic voltammograms under a magnetic field present an enlarged current and enclosed area of the curve, in which the anodic and cathodic peaks showed a shift toward more positive and negative potentials, respectively, indicative of a higher electrochemical reaction activity (Figures S2 and S3, Supporting Information). In the studied potential window, the main contribution to the electrochemical properties arises from the formation of a NiO shell. Concretely, a reversible process of insertion and extraction of OH⁻ ions should be expected, following the reaction: Ni^{II}O + OH⁻ ↔ Ni^{III}OOH + e⁻.^[4] Galvanostatic charge–discharge cycles without applying a magnetic field have been studied (MNC-C) showing an increase of the capacitance with the number of cycles of ≈140% after 300 cycles (from 155 F g⁻¹ with a current density of 1 A g⁻¹ to 400 F g⁻¹) (Figure S4, Supporting Information). In this sort of materials, the capacitance retention increases as a consequence of the activation of the MNC, usually generating metal oxides.^[11,12,16] Control experiments show that the performances are lower for the separate components of the nanocomposite (FeNi₃ NPs and graphene), indicative of a synergistic effect of the two components in the MNC (Figure S4, Supporting Information). In turn, the application of a magnetic field during the galvanostatic charge–discharge cycles (MNC-MC) manifests a more drastic increase of the capacitance retention and the pseudocapacitance/Faradaic contribution, whether the field is applied constantly or gradually (Figures S5 and S6, Supporting Information). The ideal performance was obtained for a constant applied field of 4000 G (where the MNC is fully magnetized, as we can see in Figure S7 in the Supporting Information), obtaining an increase of ≈600% in the specific capacitance after 300 cycles (from 155 to 1100 F g⁻¹). However, we observed a minimum increase in the performance if we further increase the applied field (we tested up to 6000 G in a continuous way, see Figure S5 in the Supporting Information). In any case, from the practical point of view, 4000 G represent an accessible magnetic field even for commercial permanent magnets. This specific capacitance increases even more and tends to a leveling after 1000 cycles,

reaching a capacity of ≈1850 ± 180 F g⁻¹ (Figure 1b). This represents an increase in the supercapacitance of ≈1100% with respect to the initial value, in contrast to the 250% (550 ± 60 F g⁻¹) of the MNC sample. We can then conclude that the performance in the capacitance is significantly higher when the material undergoes charge/discharge cycles in presence of a magnetic field. Also, we performed a comparative study of different densities of active material in the electrode, showing a better capacitance increase with 0.3 mg cm⁻² (see Figure S8 in the Supporting Information). The MNC-MC material exhibits good charge–discharge efficiency (Figure S10, Supporting Information) and excellent values of energy and power density (71.31 W h kg⁻¹ and 9450 W kg⁻¹) measured in 3-electrode cell configuration (Ragone plot can be found in Figure S11 in the Supporting Information). Taking into account that our active material undergoes a battery-type faradaic behavior, we have also calculated the capacity in mA h g⁻¹, obtaining excellent values of 155 to 360 mA h g⁻¹ at a discharge current density of 30 and 1 A g⁻¹, respectively (see Figure S12 in the Supporting Information). Furthermore, the MNC-MC material shows a good stability with capacitance retention greater than 90% after 10 000 cycles (Figure S13, Supporting Information). This is, to the best of our knowledge, the highest improvement ever obtained in the specific capacitance by means of magnetic fields. We should notice that the only precedent in this context has been reported by Guo and co-workers in a system formed by microtubular cotton fabrics decorated with metal nanoparticles.^[12] In this work the magnetic field effect has produced an increase in the capacitance of a 70% with values of 60 F g⁻¹ and a poor cyclability of less than 800 cycles.

For better understanding the fundamental behavior of the magnetocapacitive FeNi₃–carbon nanocomposites, PEIS measurements were performed in the MNC pristine sample with and without an externally applied magnetic field (see “Materials and Methods” and Figure S14 in the Supporting Information for a detailed description). Thus, three internal resistances are affected by the magnetic field: the solution resistance in bulk electrolyte (R_s), the electrode/electrolyte interfacial charge transfer resistance (R_{CT}) directly related to the electrode’s resistance, and the low frequency leakage resistance (R_{leak}) flowing across the double layer zone at the electrode–electrolyte interface. The most pronounced effect was observed for the R_{leak} .

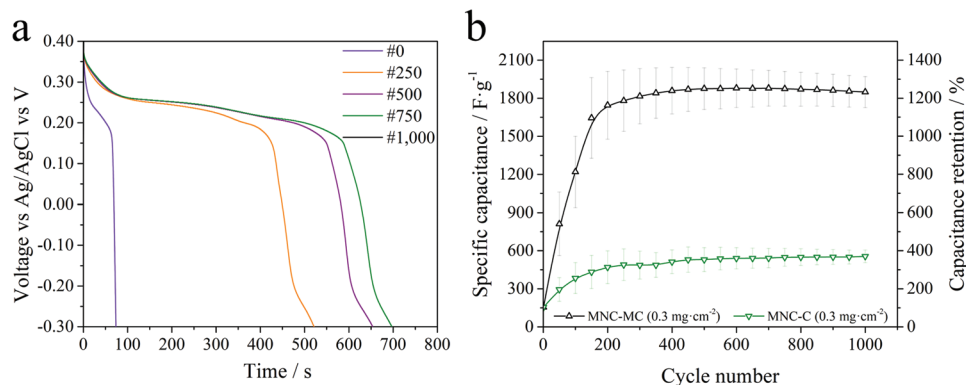


Figure 1. Electrochemical measurements under applied magnetic field. a) Galvanostatic discharges of the material in the presence of an external magnetic field showing the increase of the discharge time with the increase in the cycle number. b) Comparative capacitance retention of the material over 1000 cycles with (MNC-MC) and without (MNC-C) an external applied magnetic field and their corresponding specific capacitance values.

increasing from 764 to 920 Ω with the applied magnetic field, indicating that R_{leak} is responsible for the improvement in the energy storage performance of our device, and suggesting that in the presence of a magnetic field, the electrolytes can foster the development of the oxide surface, increasing notably the resistance of the double layer.^[11]

Statistical Raman spectroscopy (SRS) has been used to characterize the degree of graphitization and homogeneity of the materials.^[17] The mean spectra of MNC (average of an area of $20 \times 20 \mu\text{m}^2$), measured in backscattering geometry and using a 532 nm excitation wavelength, revealed the characteristic bands of graphene (i.e., D, G, and 2D) showing an average I_D/I_G ratio of 1.2 and 1.1 before and after the application of the magnetic field, respectively (Figure 2a). This suggests a slight decrease in the functionalization of the graphene matrix and indicates that it is resilient to the cycling process. The presence of the encapsulated metal oxides was detected after increasing one order of magnitude the laser power to 1.8 mW, with characteristic signals of M–O species in the 400–800 cm^{-1} region, most likely NiO and/or FeO_x (see inset in Figure 2a). The MNC-MC exhibited a more pronounced fluorescence background than that of the pristine counterpart. In stark contrast, the sample submitted to cycles without any magnetic field (MNC-C) exhibited a much more laser-sensitive carbon matrix, with an increased fluorescence background, indicative of the presence of metallic species and/or amorphous carbon. Indeed, a 633 nm excitation

wavelength was required to record the average spectra (see Figure S15 in the Supporting Information).

In order to shed light into the surface oxidation of the materials, X-ray photoelectron spectroscopy was performed. Each of the two spin–orbit components of the Ni 2p spectra shows three resolved features; those located at 853.2 and 856.4 eV can be attributed to metallic and divalent Ni (mainly NiO and $\text{Ni}(\text{OH})_2$), respectively, whereas the one located at 862.5 eV can be attributed to the so-called 6 eV Ni satellite.^[15] Compared to pristine MNC, both MNC-C and MNC-MC show the appearance of the Ni metal signal at 853.2 eV, indicative of surface oxidation. Remarkably, a more pronounced Ni–O peak is present in the MNC-MC. Similarly, the Fe 2p survey revealed weak photoelectron peaks at around 711 and 725 eV in the pristine material and the cycled samples (Fe 2p_{3/2}), confirming the iron oxidation (see Figure 2c,d and Figures S16–S22 in the Supporting Information). The application of the magnetic field induces a decrease in the C–O contribution of the C1s high resolution spectra, which explains the reduced I_D/I_G ratio previously observed in Raman spectroscopy.

Further insights on the chemical structural evolution were obtained from magnetic measurements at 300 K. MNC behave as soft magnet showing small coercive fields, and being fully magnetized at low fields at room temperature.^[14] The magnetic field exerts a big influence on the chemical reactions occurring in the MNC upon cycling. Thus, the hysteresis loops of the

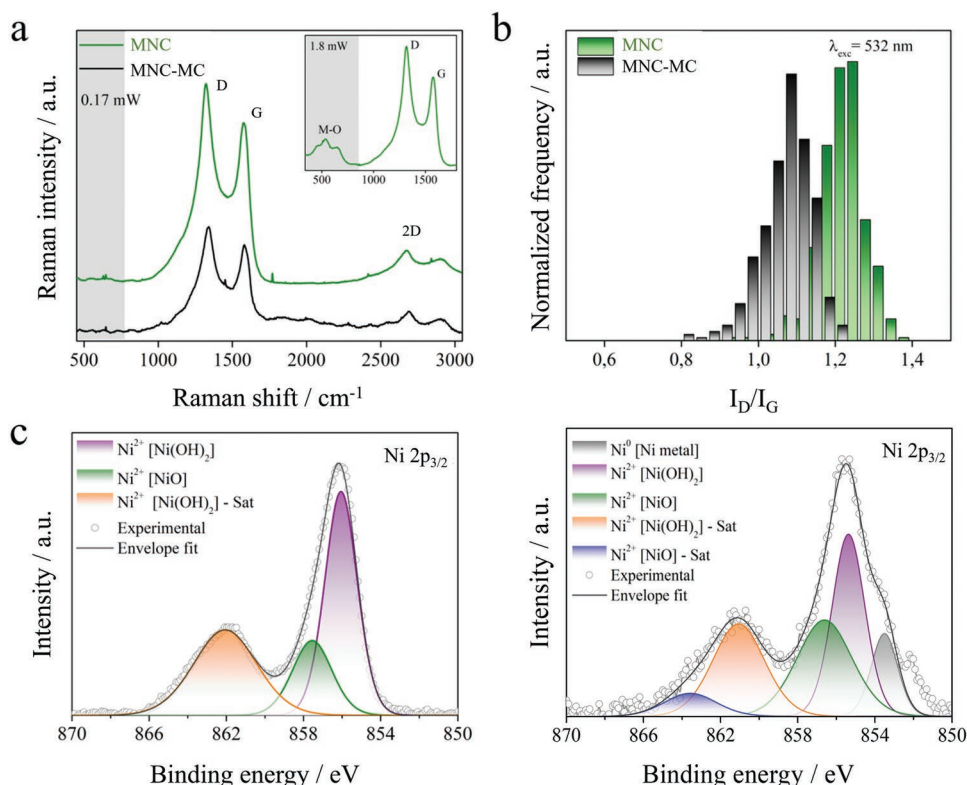


Figure 2. Raman, XPS, and magnetic characterization of MNC and MNC-MC. a) Statistical Raman spectroscopy of MNC (green) and MNC-MC (black) showing the average spectra collected at 0.17 mW ($\lambda_{\text{exc}} = 532 \text{ nm}$). The inset highlights the influence of laser power unveiling characteristic peaks associated to M–O vibrations, corresponding to the encapsulated FeNi_3 nanoparticles. b) Raman histograms (I_D/I_G ratio distribution) of the MNC and MNC-MC, showing the decrease in the I_D/I_G after the application of the magnetic field. c) High resolution XPS Ni_{2p} spectra of MNC and d) MNC-MC confirm that nickel oxidation is favored in presence of the magnetic field.

different materials showed a decrease of $\approx 58\%$ in the saturation magnetization (M_s), from ≈ 88 to 51 emu g^{-1} in the MNC-MC. Moreover, no significant differences in both remnant magnetization (M_r), and coercivity (H_c) values were measured (Figure S7, Supporting Information). Furthermore, conductivity measurements show an increase in the resistance of one order of magnitude upon magnetic cycling (from 200 ohm cm^{-1} in MNC to 6540 ohm cm^{-1} in MNC-MC), shifting from a metal conductor behavior to a semiconductor (Figures S23–S25, Supporting Information). Overall, PEIS, XPS, the magnetic measurements, and the increase in the resistance confirm that the oxidation processes at the surface of the metal nanoparticles are enhanced by the magnetic field.

However, although all these techniques point toward a preferential growth of electroactive oxide layers and a better structural resilience of the graphene matrix when the charge/discharge cycles take place in presence of a magnetic field, a direct microscopic evidence of this effect is strongly required. To tackle this challenge, we analyzed MNC, MNC-C, and MNC-MC samples by real-space techniques sensitive to both chemistry and structure, such as atomic-resolution aberration-corrected scanning transmission electron microscopy and electron energy-loss spectroscopy (STEM-EELS) at both 80 and 200 kV. Low magnification images of the pristine MNC material measured at 200 kV show a distribution of particles with uneven shapes and sizes in the 5–200 nm range, as depicted in the low magnification annular bright field (ABF) image in Figure 3a. The particles are coated with a C layer, as observed in the atomic resolution ABF images. The nanoparticles are crystalline but extended defects such as stacking faults and twin boundaries are often observed (even in the smaller particles, in the few nanometers size range). Observations at 80 kV allow minimizing electron beam irradiation damage. EEL spectrum imaging was used to obtain chemical maps of the samples. The particle composition was quite even, $\approx (74 \pm 2)\% \text{ Ni} / (26 \pm 2)\% \text{ Fe}$ in excellent accordance with the expected theoretical composition of FeNi_3 . Some surface oxidation was detected, mostly associated with an enhancement of the surface Fe signal, which comes along with a slight increase of the Fe $L_{2,3}$ intensity ratio. These findings point to a significant surface Fe oxidation (see Figure 3b), in line with previous reports on preferential formation of Fe-oxide on the surface of NiFe-permalloys, associated with the depletion of Fe from the bulk to the surface.^[18,19] Indeed, the fine structure of the O K edge suggests a strong Fe–O like signal (paramagnetic).^[20] No major segregation of metals or heavier species on the C matrix was observed. It is worth mentioning that the C coating was very stable, even for observations carried out at 200 kV.

On the other hand, the sample submitted to charge/discharge cycles in absence of a magnetic field (MNC-C) exhibited a quite unstable carbon matrix under the electron beam degrading fast at 200 kV, in excellent accordance to Raman spectroscopic studies. Low magnification images exhibit a

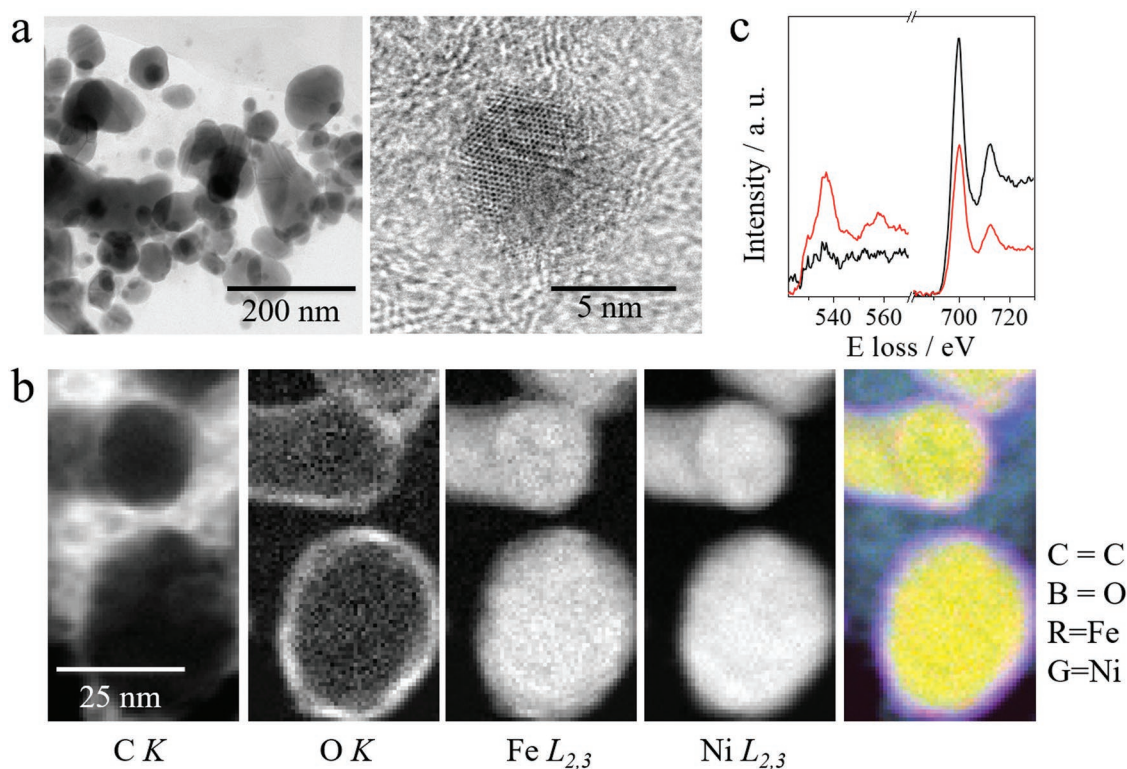


Figure 3. STEM and EELS analysis of MNC. a) Low (left) and high (right) resolution ABF images of the pristine MNC sample, obtained at 200 kV. b) Compositional maps, obtained via multiple linear least squares fitting of raw EELS data, corresponding to the C K , O K , Fe $L_{2,3}$, and Ni $L_{2,3}$ edges. The right panel shows a false overlay of the former, corresponding cyan (C), blue (B), red (R), and green (G) for C, O, Fe, and Ni, respectively. c) Averaged EEL spectra obtained from the surface (red) and the center of a pristine MNC nanoparticle (black). EELS data acquired at 80 kV.

higher density of small particles, with large amounts of smaller clusters in the few nanometers size range. Intermediate magnification images acquired at 80 kV to minimize the damage confirmed that a relatively high amount of material segregates on the C support in the form of small clusters <5 nm (see Figure S26, Supporting Information). This finding indicates that the initial FeNi₃ nanoparticles were electrochemically active and broke into small ones during the charge–discharge cycles. EELS maps show again a strong surface Fe oxidation. However, in this case small Ni-rich clusters have segregated outside the particles. The presence of the small clusters suggests activated electrochemical behavior, in agreement with the observed improved capacitance.

Finally, for the sample submitted to charge/discharge cycles in presence of a magnetic field (MNC-MC), simultaneously acquired ABF and high angle annular dark field (HAADF) images, revealed the wide formation of small precipitates, along with needle-shaped particles all over the sample (Figure 4a). The smaller particles tend to exhibit a core–shell like structure, single- or monodomain inside, with high crystallinity even after cycling, and appeared coated by uneven C layers (see Figure S27 in the Supporting Information for additional characterization). Moreover crystalline needle-shaped clusters and other crystalline small (<5 nm) particles can be observed on the C matrix. EELS analysis demonstrated that all clusters and needles consist of Ni, Fe, and O. A detailed analysis shows again a strong oxidation of the surface of the particles, which is mostly Fe oxide. Indeed, EELS fine structure, measured on the particles

surface revealed that the intensity of the O K onset prepeak increases, pointing to a more oxidized compound. However, an important finding was discovered when imaging the small clusters: they exhibit a strong Ni–Fe segregation. Figure 4b shows a total Ni–Fe separation with the small Fe-rich clusters heavily oxidized, while the Ni-rich clusters remain metallic and are only oxidized in the surface.

In order to clarify whether the magnetic-field metal segregation requires an electrochemical process or not, we have performed forefront in situ STEM-EELS analysis under the magnetic field of the microscope objective lens (of the order of 2T) and temperatures between room temperature (RT) and 400 °C. High resolution images of the pristine MNC sample exhibit cluster free surfaces (Figure 5a,b, left and top, respectively). However, after 15 h of exposure to the magnetic field at room temperature (Figure 5a, middle), some surface segregation has occurred in the form of a noticeable density of nanometric surface clusters. O K, Fe L_{2,3}, and Ni L_{2,3} EELS maps (Figure 5b, middle) confirm an inhomogeneous composition (along with oxidation) of the surface and such clusters. This segregation can be significantly sped up via heating. The right panel of Figure 5a, exhibits an image of the same particle, after being annealed in situ at 400 °C for ≈30 min and then quenched back to RT. The surface clusters have increased in size, almost duplicating their volume. The corresponding compositional maps in Figure 5b (bottom row) denote an enhanced segregation of Fe and Ni, along with an inhomogeneous oxidation reminiscent of the core–shell

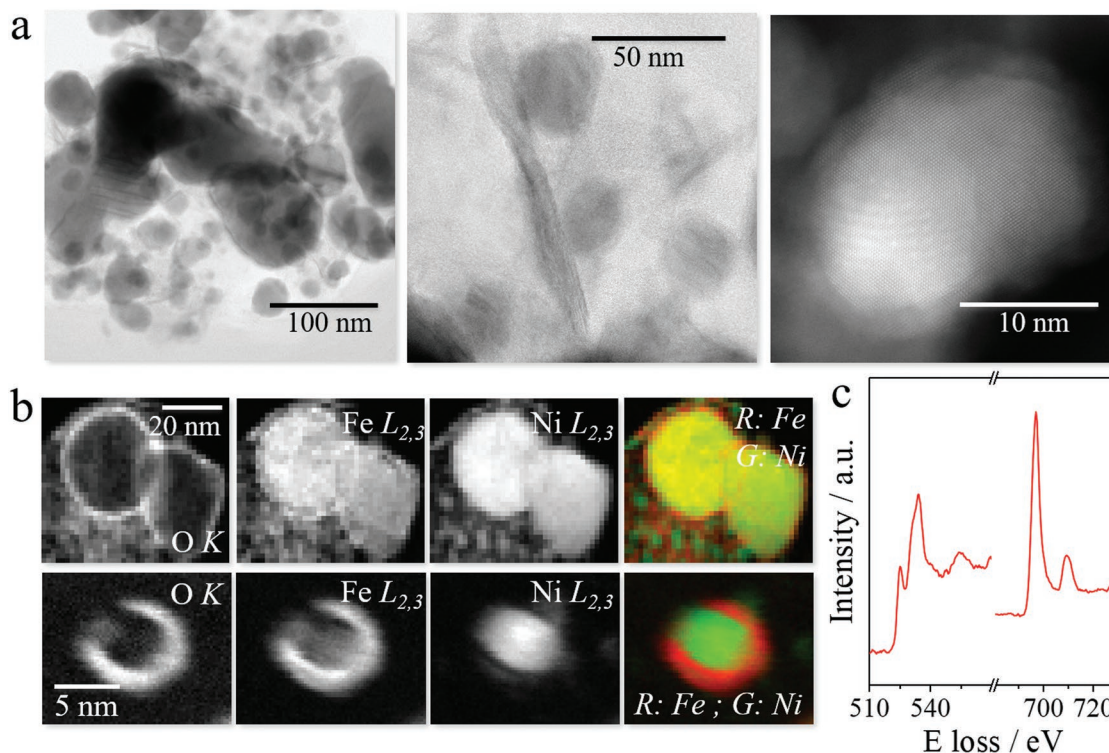


Figure 4. STEM and EELS analysis of MNC-MC. a) Low and intermediate magnification ABF images, along with a high resolution HAADF image of the MNC-MC specimen, acquired at 200 kV. b) Intermediate and high magnification EELS maps, including the O K, Fe L_{2,3}, and Ni L_{2,3} maps. Color maps show an overlay of the respective Fe (red) and Ni (green) maps. c) EEL spectrum from the Fe oxide surface of a cluster. EELS data recorded at 80 kV.

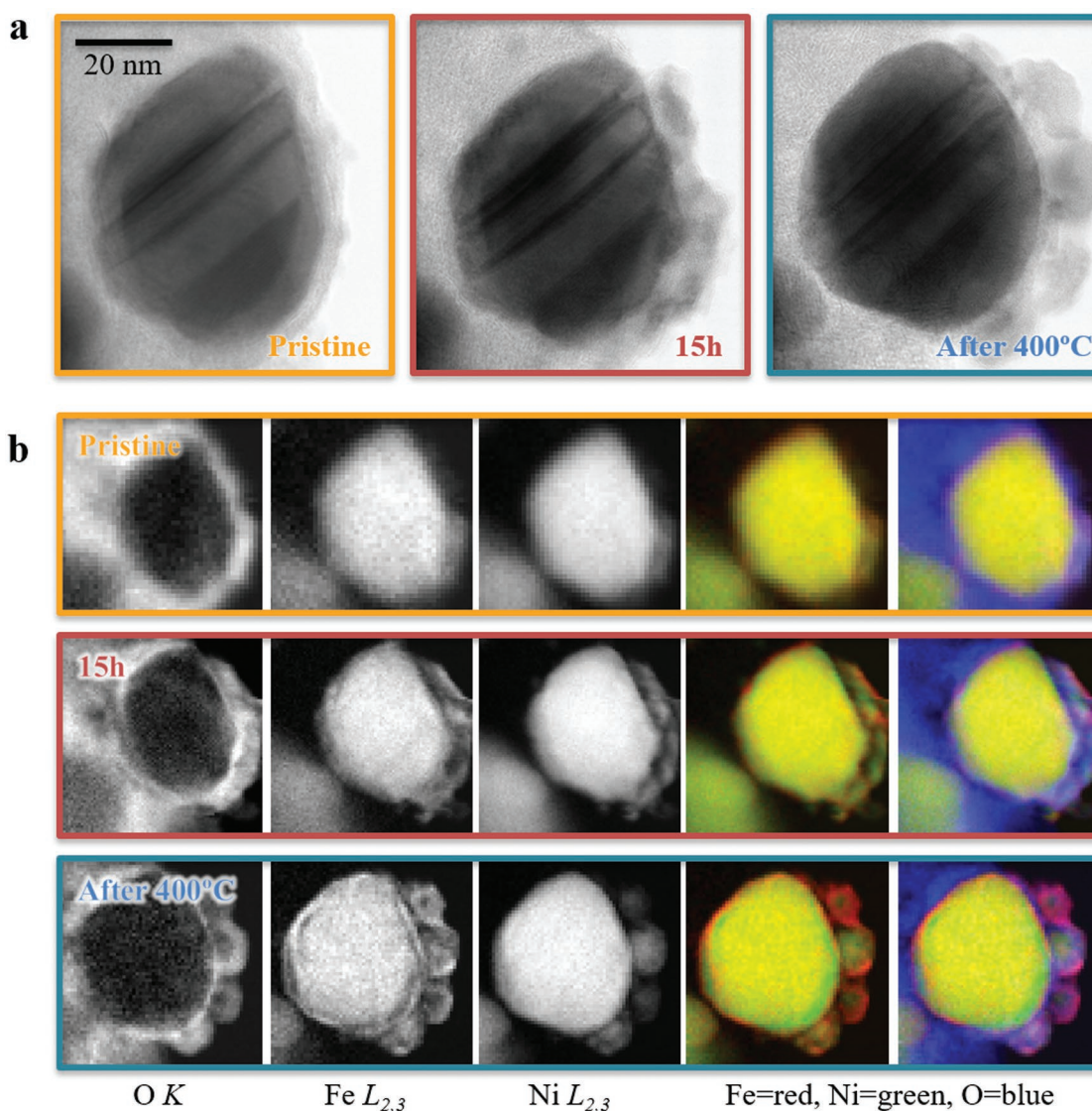


Figure 5. STEM-EELS analysis after in situ treatments. a) Sequential atomic resolution ABF images of an MNC particle. From left to right: pristine sample, after 15 h in the objective lens magnetic field ($>2T$) and after a 30 min annealing at 400 °C and fast quench back to RT, always under applied magnetic field. The scale bar represents 10 nm. b) EELS maps of the same particle. From left to right: O K, Fe $L_{2,3}$, Ni $L_{2,3}$, along with color overlays where red represents the Fe map, green is Ni, and blue is O. From top to bottom: pristine sample, after 15 h in the objective lens magnetic field ($>2T$) and after a 30 min annealing at 400 °C and fast quench back to RT, always under applied magnetic field. Some spatial drift during EELS mapping is present. All data acquired at room temperature at 80 kV.

morphology of the MNC-MC samples depicted in Figure 4b. These results point toward a significant temperature and field activated Fe/Ni surface segregation mechanism, which can be readily observed in videos acquired during subsequent in situ annealings at 400 °C, always under magnetic field (see Movies S1 and S2 in the Supporting Information, depicting the particle evolution at high temperatures). Moreover, these show that temperature seems to play a determining key role fostering the Fe migration to the surface and growing of crystalline segregated particles, which grow by coalescence. These results confirm the magnetic field-induced segregation process highlighting the importance of providing energy to the system either in the form of thermal agitation or electrochemical potential.

In view of the previous results, we can give an explanation of the magnetic field effects in the redox processes. According to White and co-workers,^[21] when a magnetic field is externally imposed in the electrochemical cell, the mass transport of electrolyte at the electrolyte/electrode interface is altered, which changes the electrical double layer at the electrode surface.^[22] These changes are mainly attributed to the MHD phenomenon, which accelerates the ion transportation rate within the electrolyte solution and the electron exchange at the electrolyte/electrode interface.^[9,23] Moreover, the magnetic field may generate magnetophoretic forces (i.e., Kelvin force and Maxwell stress) acting on generated paramagnetic ions, always present because any redox process where a single electron is transferred necessarily involves paramagnetic species.^[10] In fact, depending

on the magnetic field uniformity, the Maxwell stress may deform the shape of ion clouds near the electrode surface influencing the capacitance of the electrical double layer. In general, the magnetic field effects remain small for these redox processes. However, in the present case, these effects are strongly enhanced by the presence of ferromagnetic FeNi₃ nanoparticles. These nanoparticles are fully magnetized even in the presence of an applied field as small as 4000 G, thanks to their soft ferromagnetic nature. This leads to an increase in the total magnetic field at the very surface of the nanoparticle due to the generation of stray fields.^[24] The fact that minimum improvements in the capacitance retention are observed upon applying higher magnetic fields may support this hypothesis. As a consequence, an intense local gradient force will be generated in these boundary regions. The magnetic force will govern the dynamics of diamagnetic and paramagnetic molecules moving away from and toward regions of higher magnetic field strength, respectively. Moreover, the presence of magnetic fields could decrease the surface energy of the nanoparticles promoting the formation of new crystalline structures, as previously observed for NiO, Co₃O₄, NdFeB, and NiCo₂O₄ nanoparticles.^[25,26] In this sense, due to the MHD and magnetophoretic forces, we assume that the application of the magnetic field induces a more efficient penetration of the electrolyte, leading to the formation of oxide species and favoring the migration of Fe atoms from the inner part of the alloy particles to the surface, leaving behind fragments of almost unoxidized Ni clusters. Along this front, and corroborated by both *ex situ* and *in situ* STEM-EELS results, the magnetic field induces strong metal phase segregation, provoking the formation of crystalline nanometric (≤ 5 nm) cluster-like nanoparticles of Ni in close contact, together with an enhanced oxidation of the nanoparticles surface. These processes explain the reduced saturation magnetization observed in the MNC-MC. Additionally, the phase segregation indicates a loss of nanoparticle bonding and coupling with the conducting graphene matrix, explaining the observed decrease of the I_D/I_G ratio in the statistical Raman spectroscopy.^[16] The formation of these small clusters provides a dramatic increase of active sites for the development of Faradaic processes at the surface, in excellent accordance to the PEIS and XPS results, which suggest the presence of superficial oxide layers. Within the applied potential window, the very small Ni particle size and their NiO shell, which is a major source of pseudocapacitance,^[27] creates efficient diffusion paths for the OH⁻ ions, which significantly enhances the intercalation of the electrolyte ions and, therefore, the utilization of the electrode material, leading to an increase in the specific capacitance. Moreover, the resilient graphene matrix provides a conductive network between the metal clusters and acts as an optimal support avoiding sintering. This is the first time that the effect induced by a magnetic field results in a permanent improvement of the supercapacitive properties. This enhancement accounts for an impressive $\approx 1100\%$, leading to specific capacitance values of more than ≈ 1800 F g⁻¹. This performance is very competitive taking into account the values of worldwide extended carbon-based commercial supercapacitors (25–30 F g⁻¹), as well as some of the most recent related publications (<1010 F g⁻¹ for NiO–carbon based supercapacitors in 6 M KOH)^[28] and other carbon-based hybrid supercapacitors, e.g., 950 F g⁻¹ for MnO₂–CNT hybrids supercapacitors.^[29]

Last but not least, we have checked the scope of this approach synthesizing an unprecedented NiCo–MNC analogue showing a similar behavior with an increase of the specific capacitance of the device from 90 to 500 F g⁻¹; i.e., an enhancement of $\approx 450\%$ (Figures S28–S33, Supporting Information). These preliminary results point toward the possibility of extending the magnetic-field-enhanced effect to other transition metal/carbon-based nanocomposites and, in particular, to those magnetic nanoparticles containing Ni in their composition.

In summary, the application of external magnetic fields to FeNi₃–graphene nanocomposites during the galvanostatic charge–discharge cycles is twofold: On the one hand, it enhances the oxidation of the metal nanoparticles. On the other hand, it leads to an unprecedented metal phase segregation forming nanometric metal clusters of Ni in particular with an outstanding electrochemical activity. These newly formed metal clusters lead to a large increase of the Ni/NiO interfaces, and accounts for the dramatic increase of the specific capacitance of the device (average values from 155 to 1840 F g⁻¹; i.e., an enhancement of $\approx 1100\%$). These results open the door to an external magnetic field improvement of the specific capacitance in hybrid magnetic supercapacitors—a general feature taking into account that most of the conventionally employed Faradaic materials consist of magnetic transition metals like Ni, Co, or Fe—and brings us closer to the development of promising new magnetically switchable energy storage devices. Moreover, the intent of this work transcends energy storage because it underlines the influence of a magnetic field during an electrochemical reaction in carbon-based nanocomposites.

Supporting Information

Supporting Information is available from the Wiley Online Library or from the author.

Acknowledgements

Financial support from the European Union (ERC Advanced Grant Mol-2D 788222, ERC Starting Grant 2D-PnictoChem 804110, ERC Proof of Concept Grant Hy-MAC 713704, ERC Proof of Concept Grant MAGTOOLS, and COST-Action on Molecular Spintronics (MOLSPIN CA15128)), the Spanish MINECO (Projects MAT2017-89943-R, RTI2018-097895-B-C43 co-financed by FEDER, and the Unit of Excellence “Maria de Maeztu” MDM-2015-0538), and the Generalitat Valenciana (Prometeo Program) is gratefully acknowledged. G.A. thanks for the support by the DFG (FLAG-ERA AB694/2-1) and the Generalitat Valenciana (CIDEAGENT/2018/001 grant). G.A. received financial support through the Postdoctoral Junior Leader Fellowship Programme from “la Caixa” Banking Foundation. S.G.M. and J.R. thank the Spanish MINECO for their predoctoral grants. The authors thank Dr. Antonio Alberola-Catalan for his experimental support. Electron microscopy observations were carried out at the ICTS ELECOMI node at Centro Nacional de Microscopía Electrónica at the Universidad Complutense de Madrid.

Conflict of Interest

These materials and methods have been patented by E.C., G.A., H.P.-G., and J.R. with publication number WO2018011445A1. The rest of the authors declare no competing interests.

Keywords

magnetic materials, metal segregation, nanocomposites, supercapacitors

Received: January 9, 2019

Revised: April 1, 2019

Published online: May 13, 2019

-
- [1] N. S. Lewis, D. G. Nocera, *Proc. Natl. Acad. Sci. USA* **2006**, *103*, 15729.
- [2] H. B. Gray, *Nat. Chem.* **2009**, *1*, 7.
- [3] V. Nicolosi, M. Chhowalla, M. G. Kanatzidis, M. S. Strano, J. N. Coleman, *Science* **2013**, *340*, 1226419.
- [4] H. Wang, H. Dai, *Chem. Soc. Rev.* **2013**, *42*, 3088.
- [5] F. Bonaccorso, L. Colombo, G. Yu, M. Stoller, V. Tozzini, A. C. Ferrari, R. S. Ruoff, V. Pellegrini, *Science* **2015**, *347*, 1246501.
- [6] F. Beguin, E. Frackowiak, *Supercapacitors: Materials, Systems and Applications*, John Wiley & Sons, Weinheim, Germany **2013**.
- [7] G. Wang, L. Zhang, J. Zhang, *Chem. Soc. Rev.* **2012**, *41*, 797.
- [8] R. N. O'Brien, *ECS Trans.* **2007**, *3*, 23.
- [9] L. M. A. Monzon, J. M. D. Coey, *Electrochem. Commun.* **2014**, *42*, 38.
- [10] L. M. A. Monzon, J. M. D. Coey, *Electrochem. Commun.* **2014**, *42*, 42.
- [11] J. Zhu, M. Chen, H. Qu, Z. Luo, S. Wu, H. A. Colorado, S. Wei, Z. Guo, *Energy Environ. Sci.* **2012**, *6*, 194.
- [12] J. Zhu, M. Chen, H. Wei, N. Yerra, N. Haldolaarachchige, Z. Luo, D. P. Young, T. C. Ho, S. Wei, Z. Guo, *Nano Energy* **2014**, *6*, 180.
- [13] G. Abellán, E. Coronado, C. Martí-Gastaldo, A. Ribera, J. F. Sánchez-Royo, *Chem. Sci.* **2012**, *3*, 1481.
- [14] G. Abellán, E. Coronado, C. Martí-Gastaldo, A. Ribera, T. F. Otero, *Part. Part. Syst. Charact.* **2013**, *30*, 853.
- [15] G. Abellán, H. Prima-García, E. Coronado, *J. Mater. Chem. C* **2016**, *4*, 2252.
- [16] H. Wang, Y. Liang, M. Gong, Y. Li, W. Chang, T. Mefford, J. Zhou, J. Wang, T. Regier, F. Wei, H. Dai, *Nat. Commun.* **2012**, *3*, 917.
- [17] G. Abellán, M. Schirowski, K. F. Edelthammer, M. Fickert, K. Werbach, H. Peterlik, F. Hauke, A. Hirsch, *J. Am. Chem. Soc.* **2017**, *139*, 5175.
- [18] C. H. Bajorek, M. Nicolet, C. H. Wilts, *Appl. Phys. Lett.* **1971**, *19*, 82.
- [19] K. Asami, K. Hashimoto, *Corros. Sci.* **1984**, *24*, 83.
- [20] C. Colliex, T. Manoubi, C. Ortiz, *Phys. Rev. B* **1991**, *44*, 11402.
- [21] S. R. Ragsdale, K. M. Grant, H. S. White, *J. Am. Chem. Soc.* **1998**, *120*, 13461.
- [22] T. Z. Fahidy, *J. Appl. Electrochem.* **1983**, *13*, 553.
- [23] R. J. Moreau, *Magnetohydrodynamics*, Kluwer Academic Publishers, Norwell, MA **1990**.
- [24] L. Pietrobon, L. Fallarino, A. Bergen, A. Chuvillín, F. Casanova, L. E. Hueso, *Small* **2015**, *11*, 6295.
- [25] Y. Lu, T. Zhu, G. Zhang, Z. He, C. Lin, Y. Chen, H. Guo, *RSC Adv.* **2015**, *5*, 99745.
- [26] M. Wang, Q. Chen, *Chem. - Eur. J.* **2010**, *16*, 12088.
- [27] Q. Lu, M. W. Lattanzi, Y. Chen, X. Kou, W. Li, X. Fan, K. M. Unruh, J. G. Chen, J. Q. Xiao, *Angew. Chem., Int. Ed.* **2011**, *50*, 6847.
- [28] J. Cheng, B. Zhao, W. Zhang, F. Shi, G. Zheng, D. Zhang, J. Yang, *Adv. Funct. Mater.* **2015**, *25*, 7381.
- [29] J. Yan, Z. Fan, T. Wei, J. Cheng, B. Shao, K. Wang, L. Song, M. Zhang, *J. Power Sources* **2009**, *194*, 1202.

ADVANCED MATERIALS

Supporting Information

for *Adv. Mater.*, DOI: 10.1002/adma.201900189

Giant Enhancement in the Supercapacitance of NiFe–
Graphene Nanocomposites Induced by a Magnetic Field

Jorge Romero, Helena Prima-Garcia, Maria Varela, Sara G. Miralles, Víctor Oestreicher, Gonzalo Abellán, and Eugenio Coronado**

Supporting Information

Giant enhancement in the supercapacitance of NiFe-graphene nanocomposites induced by a magnetic field

By Jorge Romero, Helena Prima-Garcia, Maria Varela, Sara G. Miralles, Víctor Oestreicher, Gonzalo Abellán and Eugenio Coronado*.*

J. Romero, Dr. H. Prima-Garcia, Dr. S. G. Miralles, Dr. V. Oestreicher, Dr. G. Abellán, Prof. E. Coronado

Instituto de Ciencia Molecular (ICMol), Universidad de Valencia. Catedrático José Beltrán 2, 46890 Paterna, Spain.

Prof. M. Varela

Universidad Complutense de Madrid, Instituto Pluridisciplinar, Instituto de Magnetismo Aplicado & Departamento de Física de Materiales, Madrid 28040, Spain.

Dr. G. Abellán

Department of Chemistry and Pharmacy and Joint Institute of Advanced Materials and Processes (ZMP)

Friedrich-Alexander-Universität Erlangen-Nürnberg (FAU), Nikolaus Fiebiger-Strasse 10, 91058 Erlangen and Dr.-Mack Strasse 81, 90762 Fürth, (Germany).

E-mail: gonzalo.abellan@uv.es (G.A.) eugenio.coronado@uv.es (E.C.)

Materials and Methods

Chemicals

All chemicals reagents $\text{Ni}(\text{NO}_3)_2 \cdot 6\text{H}_2\text{O}$, $\text{Fe}(\text{NO}_3)_3 \cdot 9\text{H}_2\text{O}$, $\text{HO}_2\text{C}(\text{CH}_2)_8\text{CO}_2\text{H}$ (sebacic acid), $\text{FeSO}_4 \cdot 7\text{H}_2\text{O}$, $\text{NiCl}_2 \cdot 6\text{H}_2\text{O}$, NaOH , KOH (99,99%), HCl , Hydrazine, acetylene black, poly(vinylidene fluoride) (PVDF), benzyl alcohol, and ethanol (Aldrich, Fluka, Alfa-Aesar) were used as received without further purification. Ultrapure water was obtained from a Millipore Milli-Q equipment.

Synthesis of MNC

The magnetic nanocomposite (MNC) consist of FeNi_3 nanoparticles embedded in graphene matrix. The MNC has been obtained by calcination of hybrid NiFe-LDHs intercalated with sebacate anions under nitrogen atmosphere during 4 h at $900\text{ }^\circ\text{C}$, in a programmable oven with a $2\text{ }^\circ\text{C} \cdot \text{min}^{-1}$ scan rate and nitrogen flow of $40\text{ mL} \cdot \text{min}^{-1}$.^[1,2] The graphene matrix can be isolated from the nanocomposites by acid leaching (2M hydrochloric acid) during 12 hours with magnetic stirring.^[3]

Synthesis of the NP

The FeNi_3 nanoparticles were obtained in a typical procedure, 7.5 mmol of $\text{FeSO}_4 \cdot 7\text{H}_2\text{O}$ and 22.5 mmol of $\text{NiCl}_2 \cdot 6\text{H}_2\text{O}$ were dissolved in 50 mL of benzyl alcohol. After that, the mixture was heated up to $80\text{ }^\circ\text{C}$ in a thermostatic bath. Afterwards, a NaOH 5 M solution was drop-wise added to the mixture until it reached a pH of ca. 11.^[4] Then, 13mL of hydrazine hydrate was added, followed by gas evolution, as well as the precipitation of small black particles. This reduction procedure was set for 30 min. Finally, the particles were collected by a magnet and washed with Milli-Q water and EtOH for several times, and then dried in an oven at $60\text{ }^\circ\text{C}$ for 5h.^[5]

Synthesis of the MNC-MC

The magnetic nanocomposite with magnetic field (MNC-MC) was prepared using an electrode loaded with the MNC and submitted to galvanostatic cycles (from 0.4 to -0.3 vs. Ag/AgCl) in the presence of external magnetic field of 4000 G. Concretely, to perform the galvanostatic cycles, Ni-Foam was used as support, depositing the precursor with a suspension in pure ethanol, and then evaporating at $80\text{ }^\circ\text{C}$ for 2 hours. The galvanostatic cycles were performed at a current density of $10\text{ A} \cdot \text{g}^{-1}$ and $1\text{ A} \cdot \text{g}^{-1}$ for the charge and discharge processes, respectively. After 1000 cycles, the new material was extracted from the Ni Foam by sonication for 1 hour in pure ethanol. The sample MNC-C was obtained by applying the same procedure in the absence of magnetic field.

Physical Characterization

Metallic atomic composition of bulk samples was determined by means of electron probe microanalysis performed in a Philips SEM-XL30 equipped with an EDAX microprobe. Carbon, nitrogen, and hydrogen contents were determined by microanalytical procedures by using a LECO CHNS-932.

STEM-EELS observations were carried out in a JEOL ARM200cF equipped with a spherical aberration corrector, a cold field emission gun and a Gatan Quantum EEL spectrometer, operated at 80 and 200 kV. The intensity of the magnetic field within the objective lens pole piece gap is slightly over 2 T. In-situ heating experiments were carried out using a DENSsolutions Lighting D9 double tilt holder. EELS compositional maps were obtained by fitting EEL spectrum images to reference spectra via multiple linear least square (MLLS) fits.

Magnetic susceptibility measurements were performed on polycrystalline samples with a Quantum Design PPMS-9 model instrument. The susceptibility data were corrected by removing the diamagnetic contributions as deduced by using Pascal's constant tables. The dc data were collected in the range 2–300 K upon decreasing temperatures with an applied field of 1000 G, and hysteresis loops were collected between -5 and $+5\text{ T}$ at 300 K.

Raman spectroscopic characterization was carried out on a Horiba LabRAM Aramis confocal Raman microscope ($\lambda_{\text{exc}}=532$ and 633 nm) with a laser spot size of ca. $1\text{ }\mu\text{m}$ (Olympus LMPlanFl 100, NA 0.80). The incident laser power was kept as low as possible to avoid structural sample damage: 0.17–1.8 mW. Spectra were obtained with a CCD array at $-70\text{ }^\circ\text{C}$ —grating: 600 grooves per mm. Spectra were obtained from a $20 \times 20\text{ }\mu\text{m}$ area with $1\text{ }\mu\text{m}$ step size. Sample movement was carried out by an automated XY-scanning table.

The temperature dependent conductivity (σ) and magnetoresistance (MR) have been measured using a standard four-probe method with Pt wire as leads in the same PPMS-9 equipment, in the temperature range between 2 K to 300 K using Keithley devices, a current source (model 2400) and an electrometer (model 6154). Electrical contacts were made with highly conducting silver paints. Samples sizes were approximately of 3 mm^2 . The powders of nanocomposites were pressed into pellets for resistivity and MR measurements.

X-ray Photoelectron Spectroscopy (XPS) was performed ex situ at the X-ray Spectroscopy Service at the Universidad de Alicante using a K-Alpha X-ray photoelectron spectrometer system (Thermo Scientific). All spectra were collected using Al K_α radiation (1486.6 eV), monochromatized by a twin crystal monochromator, yielding a focused X-ray spot (elliptical in shape with a major axis length of $400\text{ }\mu\text{m}$) at $3\text{ mA} \cdot \text{C}$ and 12 kV. The alpha hemispherical analyzer was operated in the constant energy mode with survey scan pass energies of 200 eV to measure the whole energy band and 50 eV in a narrow scan to selectively measure the particular elements. XPS data were analyzed with Avantage software.

Electrochemical measurements

The materials were mixed with acetylene black and PVDF in a mass ratio of 80:10:10 in ethanol and deposited in a nickel foam electrode. The as-prepared nickel foam electrodes were dried overnight at 80 °C and pressed. Each working electrode contained about 0.3 or 1 mg of electroactive material and had a geometric surface area of about 1cm². A typical three-electrode experimental cell equipped with a steel sheet as the counter electrode and a double-membrane Metrohm Ag/AgCl (3M KCl) as the reference electrode was used for the electrochemical characterization of the nanocomposite materials trapped by the working electrodes. All the electrochemical measurements were carried out in 6M KOH (99,99%) aqueous solutions as the electrolyte. Ultrapure water was obtained from Milli-Q equipment. All the electrochemical experiments were performed at room temperature using a Potentiostat/Galvanostat Autolab 128N controlled by Nova 2.1 electrochemical software and a Gamry Interface 1000E potentiostat-galvanostat-ZRA controlled by Gamry's Global Software. The capacitance values were obtained by galvanostatic discharges with a minimum of three measures. The specific capacitance (C) was calculated from the galvanostatic cyclic chronopotentiometric curves according to Equation 1:

$$C_s = \frac{2 \cdot I \cdot \int V dt}{m \cdot \Delta V^2} \quad \text{Equation (1)}$$

where I is the charge/discharge current, Δt is the time for a full charge or discharge, m the weight in grams of the active material in the electrode layer, and ΔV is the voltage change after a full charge or discharge. To test the electrochemical property of the FeNi₃-G nanocomposite under different applied magnetic fields, a home-made electrochemical cell (see Fig. S1) was fixed between the two magnetic poles of an electromagnet (GMW 231HC and Bruker ELEXYS E580 for magnetic fields beyond 4,000 G). The magnetic field in the electrochemical measurements has been applied by an electromagnet controlled by home-made software. Preliminary tests under different permanent magnets have been controlled by a digital Gauss/Tesla meter Group3 DTM-133.

Ragone plots: the energy density should be calculated from a two-electrode cell as an operating device, with the formula:

$$E = \frac{C_s \cdot V^2}{2}$$

However, there is an approach, where the results received from 3-electrode cell are used to give an energy/power characterization, making a theoretical 2-electrode symmetric configuration (Energy Environ. Sci., 2010, 3, 1294–1301). Therefore, electrochemical results are given for a half-cell, so the calculations yield the formula:

$$E = \frac{C_s \cdot V^2}{8}$$

Using this formula and the typical formula for power density ($P = E/\Delta t$), we obtain the corresponding Ragone plot.

PEIS measurements were carried out at by applying AC amplitude of 10 mV in the frequency range of 0.01- 10 KHz at open circuit potential with the help of an impedance spectrum analyzer (GAMRY interface 1000E potentiostat). During the measurements, the electrochemical cells were placed in a Faraday cage. For the measurements under an applied magnetic field, the magnet was placed perpendicular to the surface of the electrode.

Supplementary Text

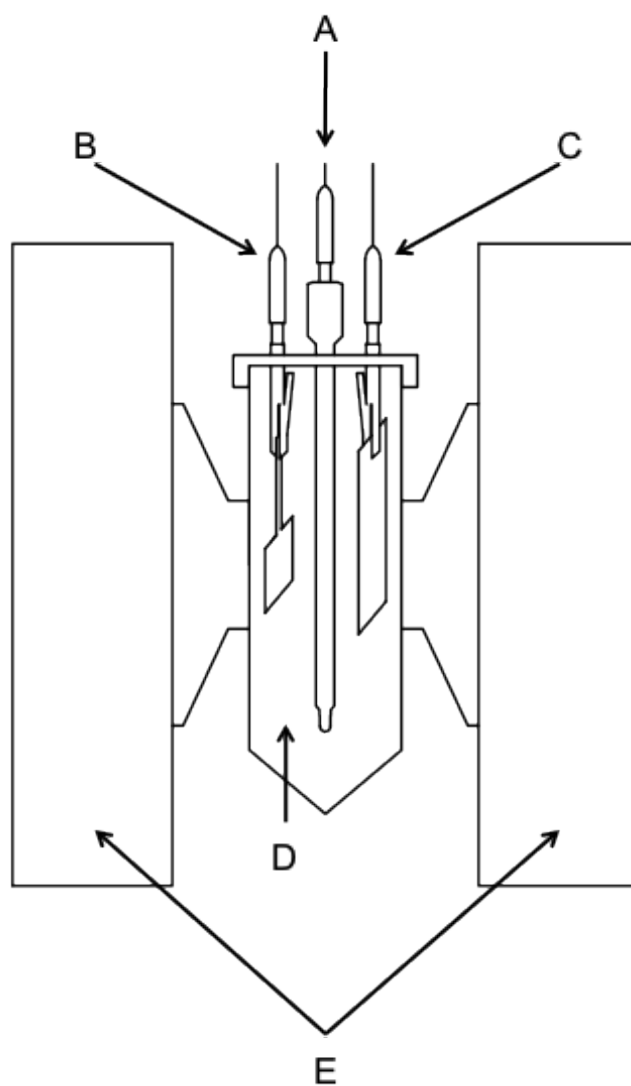


Figure SI 1.

Sketch of the home-made electrochemical cell created for synthesized the MNCO. The component (A) reference electrode, (B) working electrode, (C) counter electrode, (D) electrolyte and (E) magnet coils.

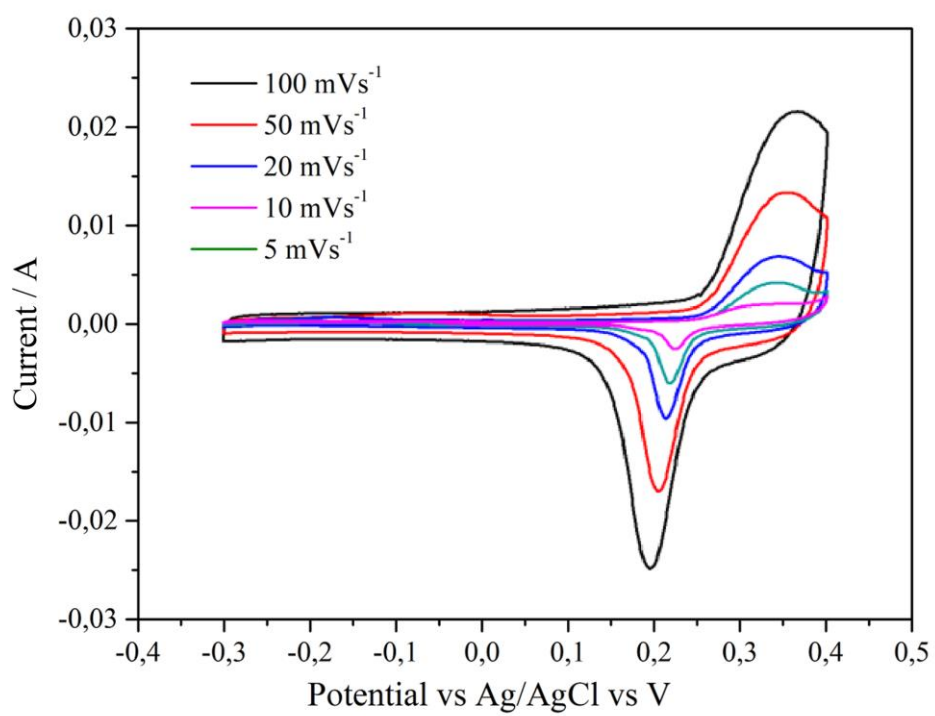


Figure SI 2.

Cyclic Voltamperometry of MNC in a three-electrode cell configuration using 6M KOH aqueous solution.

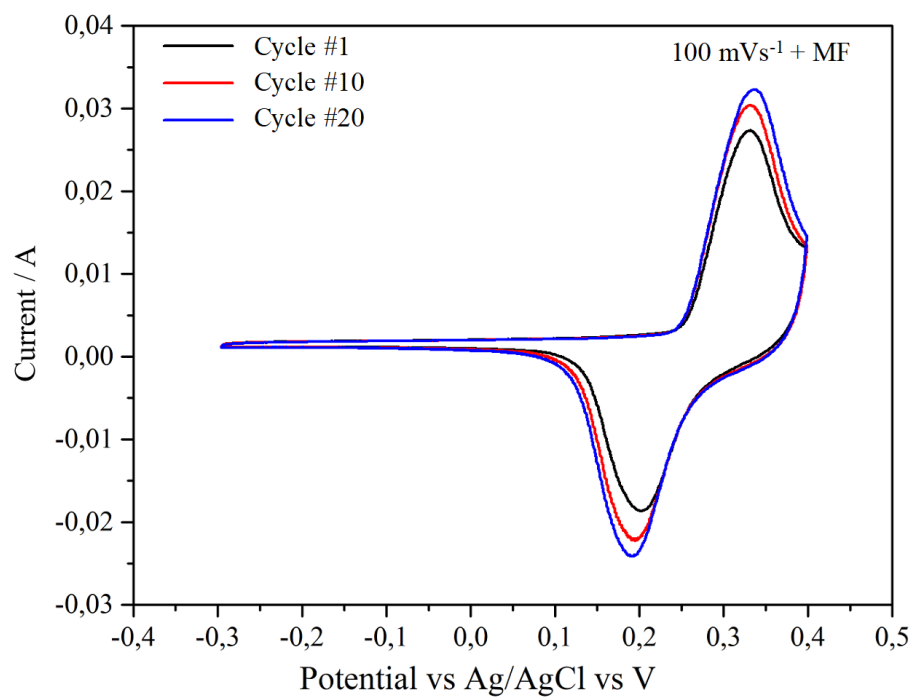


Figure SI 3.

Cyclic Voltamperometry of MNC in a three-electrode cell configuration using 6M KOH aqueous solution with an external magnetic field.

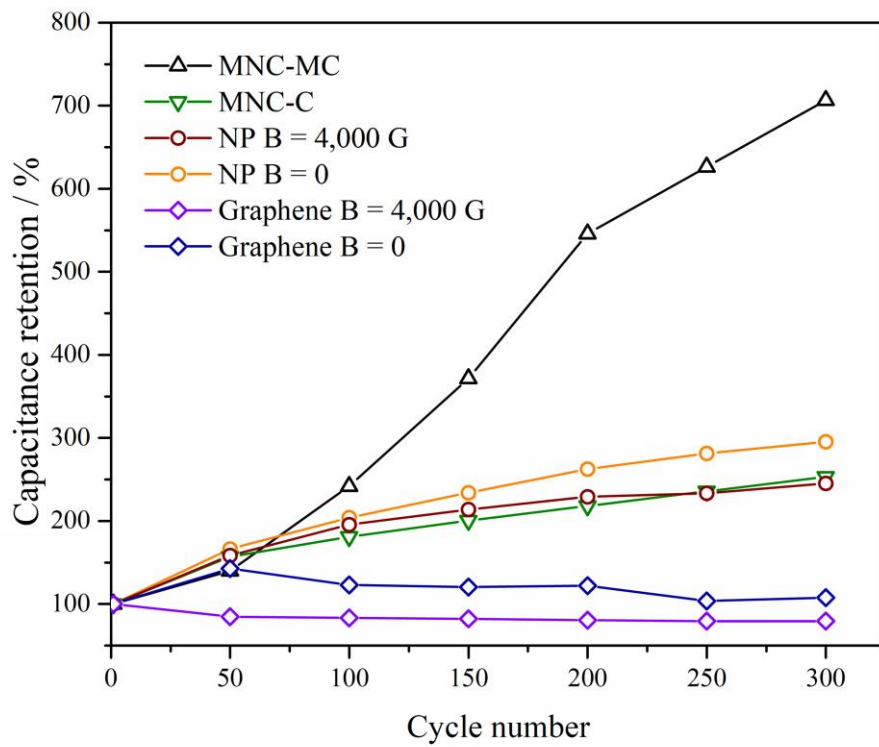


Figure SI 4.

Capacitance retention of the MNC and their components separately with and without a 4,000 G MF.

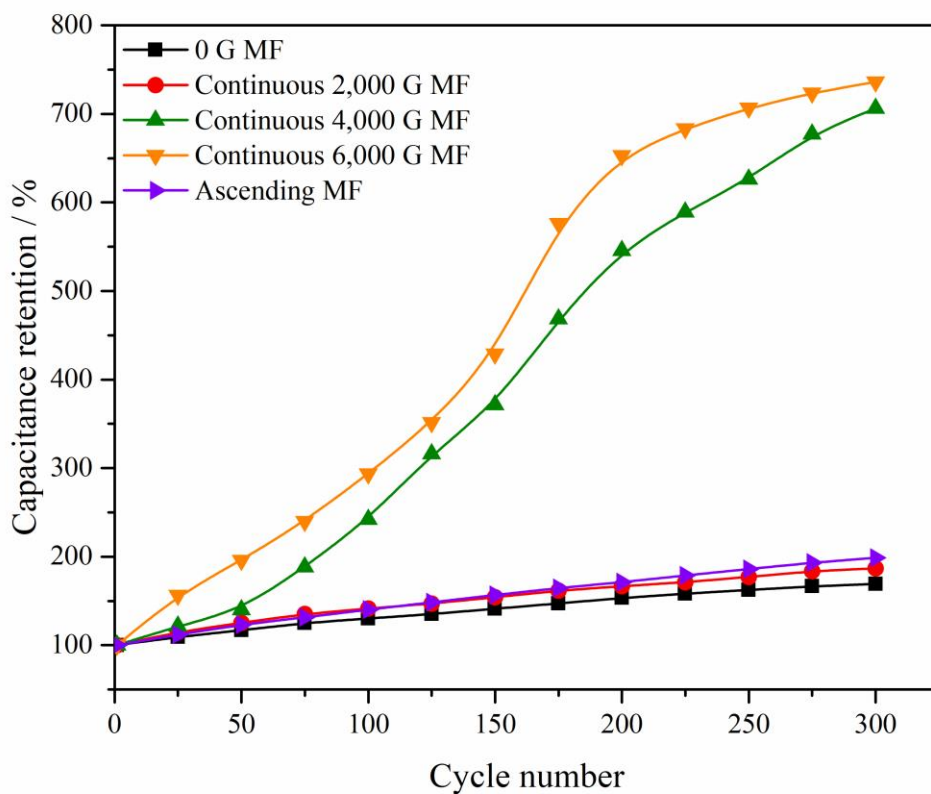


Figure SI 5.

Capacitance retention of the MNC applying different MFs. The different magnetic fields are a continuous MF of 2,000 G, 4,000 G and 6,000 G and an ascending MF from 50 to 8,000 G. The meaning of ascending field is that we programmed the electromagnet in order to automatically increase the magnetic field in 50 G every second, starting in 50 G and finishing with 8000 G, in a continuous way (that means back and forth).

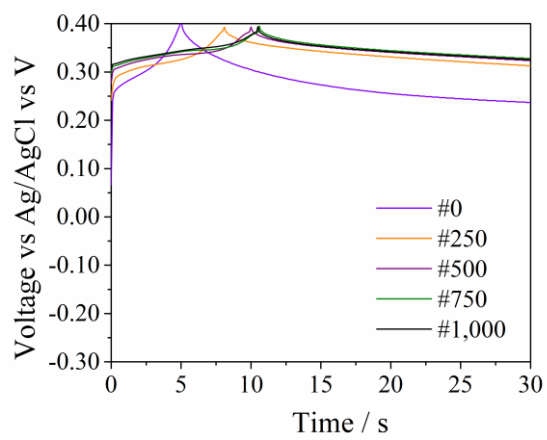
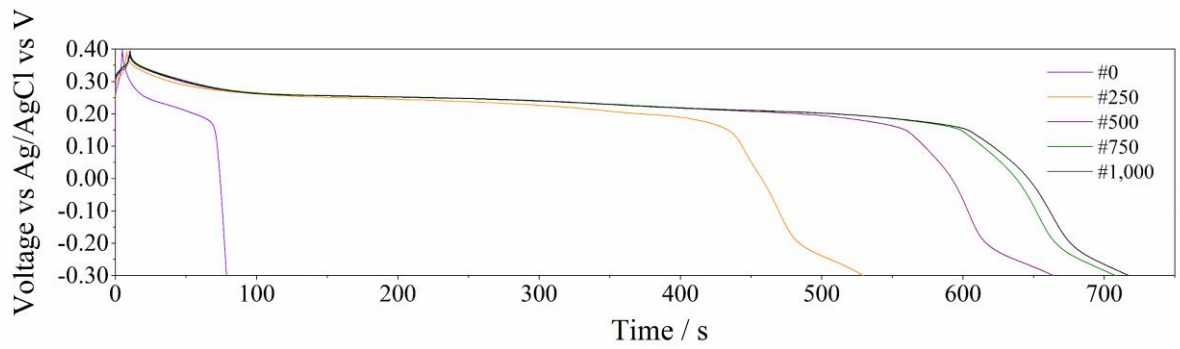


Figure SI 6.

Galvanostatic charge at $10 \text{ A}\cdot\text{g}^{-1}$ and discharges at $1 \text{ A}\cdot\text{g}^{-1}$ of the MNC in the presence of an external magnetic field.

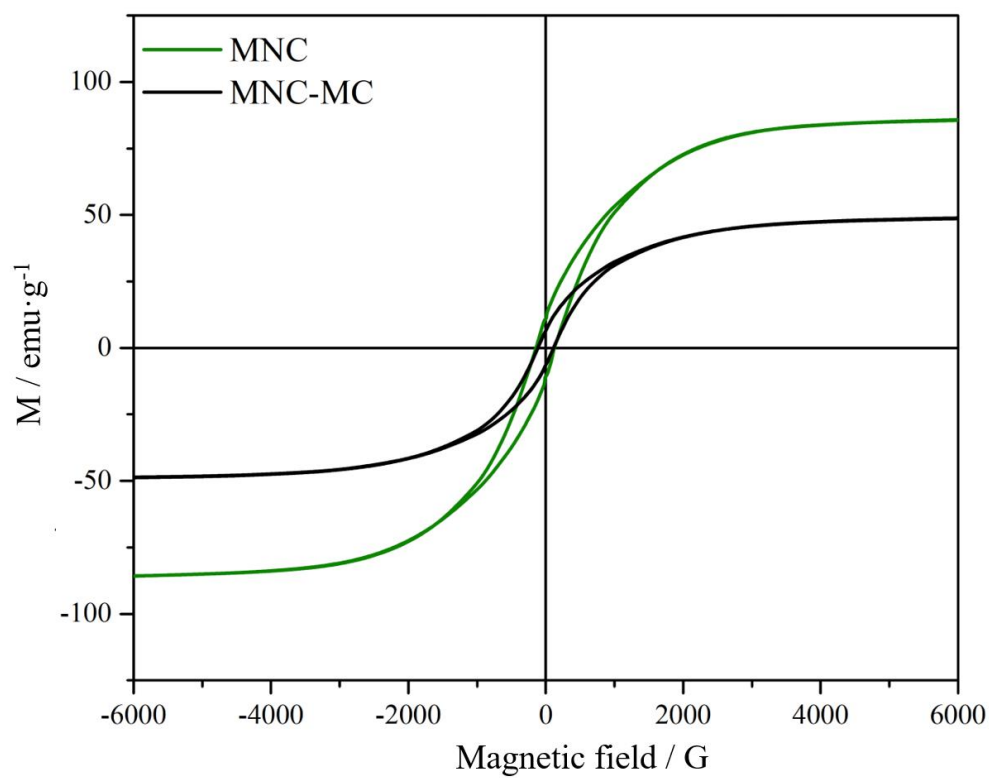


Figure SI 7.

Complete hysteresis loops measured at 300 K of the MNC and MNC-MC.

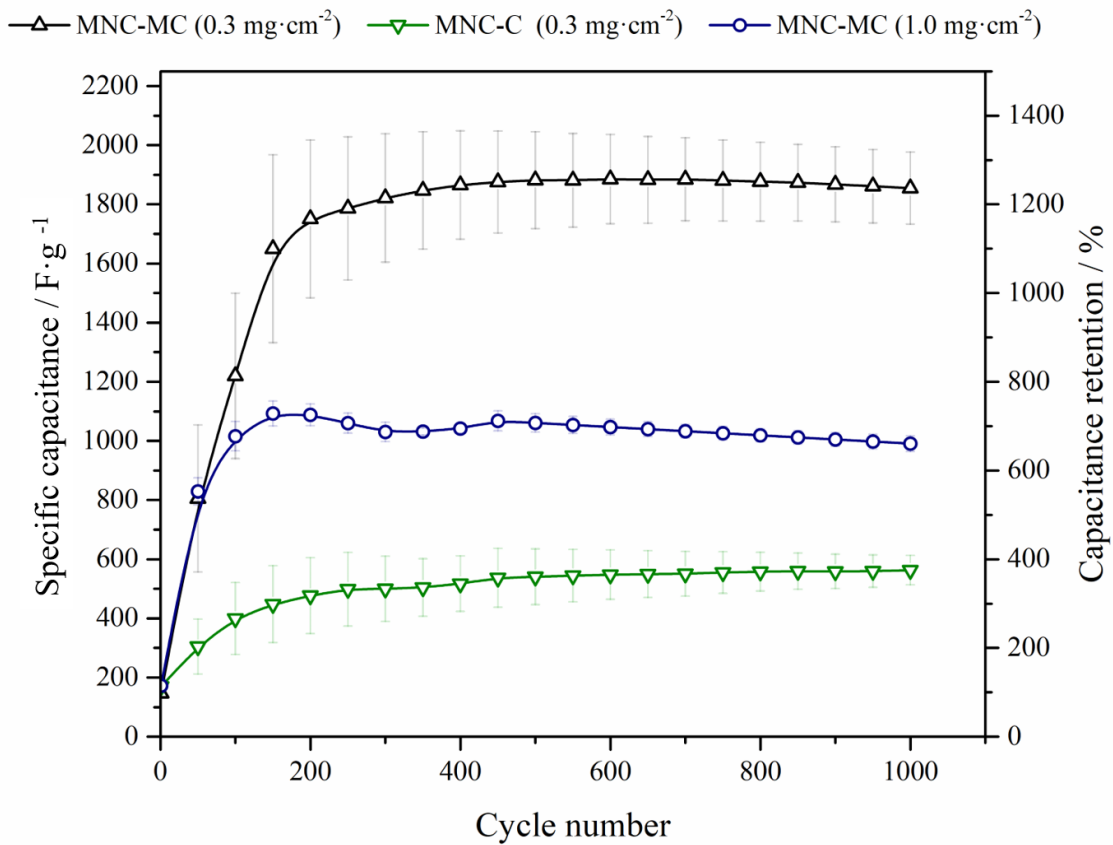


Figure SI 8.

Comparative capacitance retention of the material over 1,000 cycles with (MNC-MC) and without (MNC-C) an external applied magnetic field and different densities of material in the electrode and their corresponding specific capacitance values.

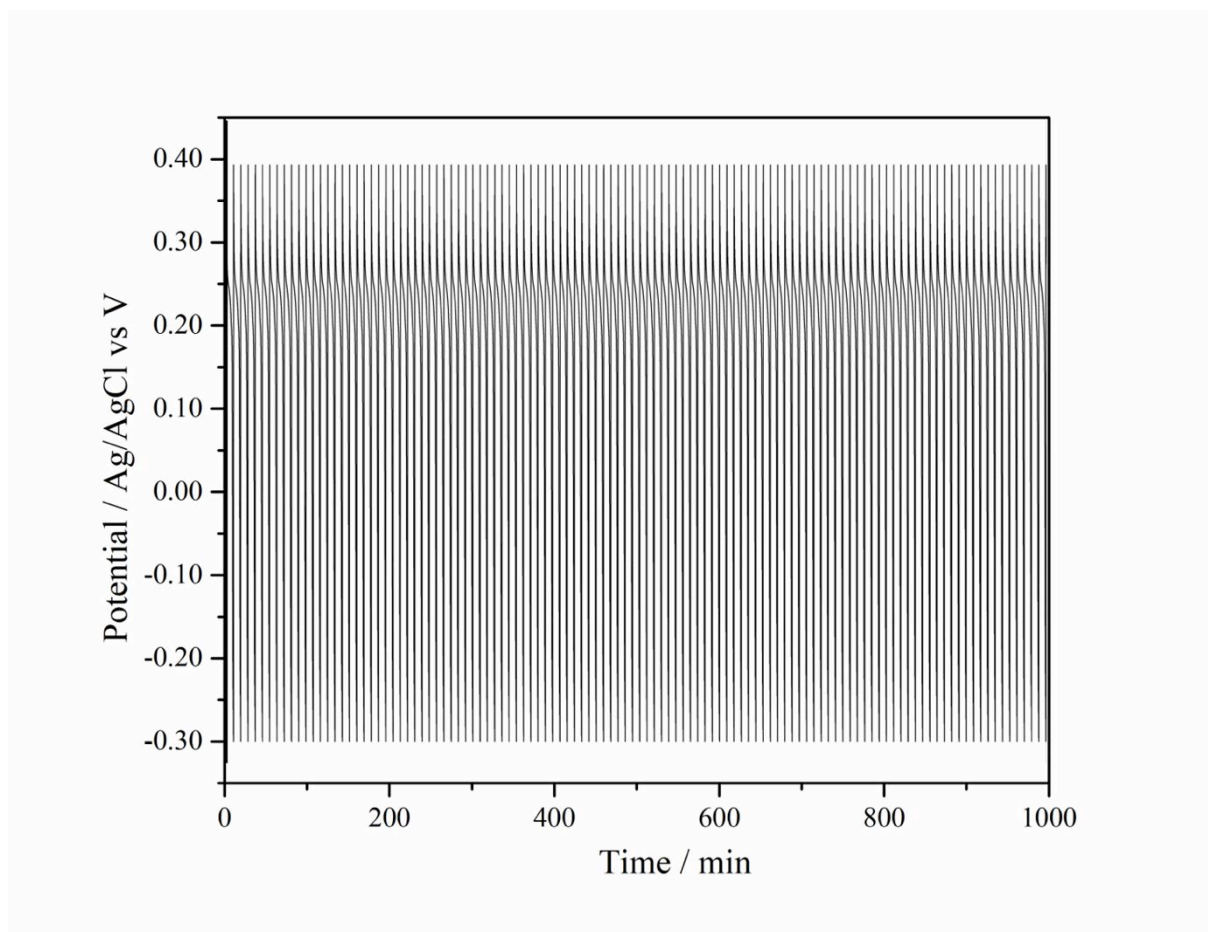


Figure SI 9.

First 1000 minutes of galvanostatic charge at $10 \text{ A}\cdot\text{g}^{-1}$ and discharges at $1 \text{ A}\cdot\text{g}^{-1}$ of the MNC in the presence of an external magnetic field.

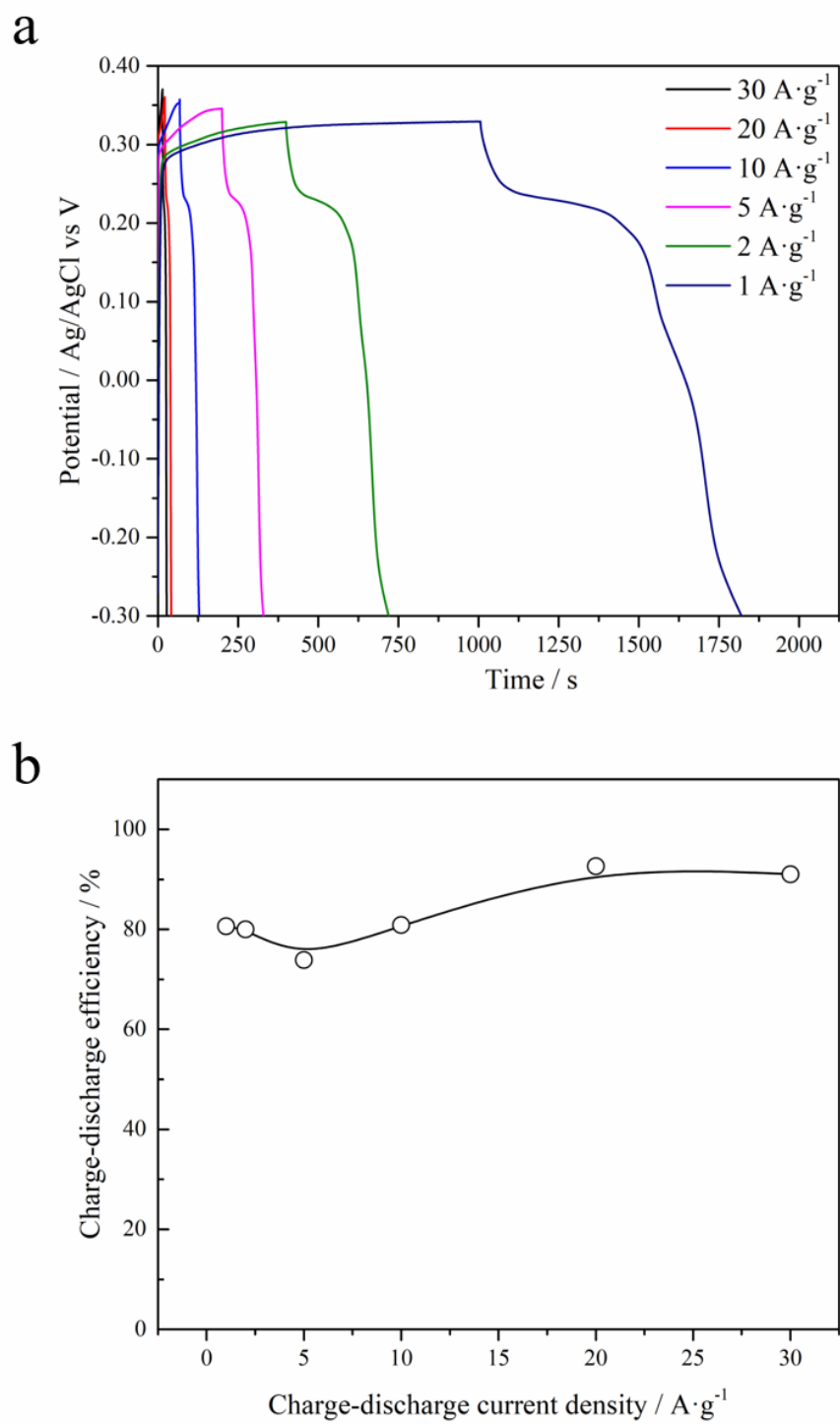


Figure SI 10.

a) Galvanostatic charge-discharge curves at different current densities of MNC-MC and b) their charge-discharge efficiency.

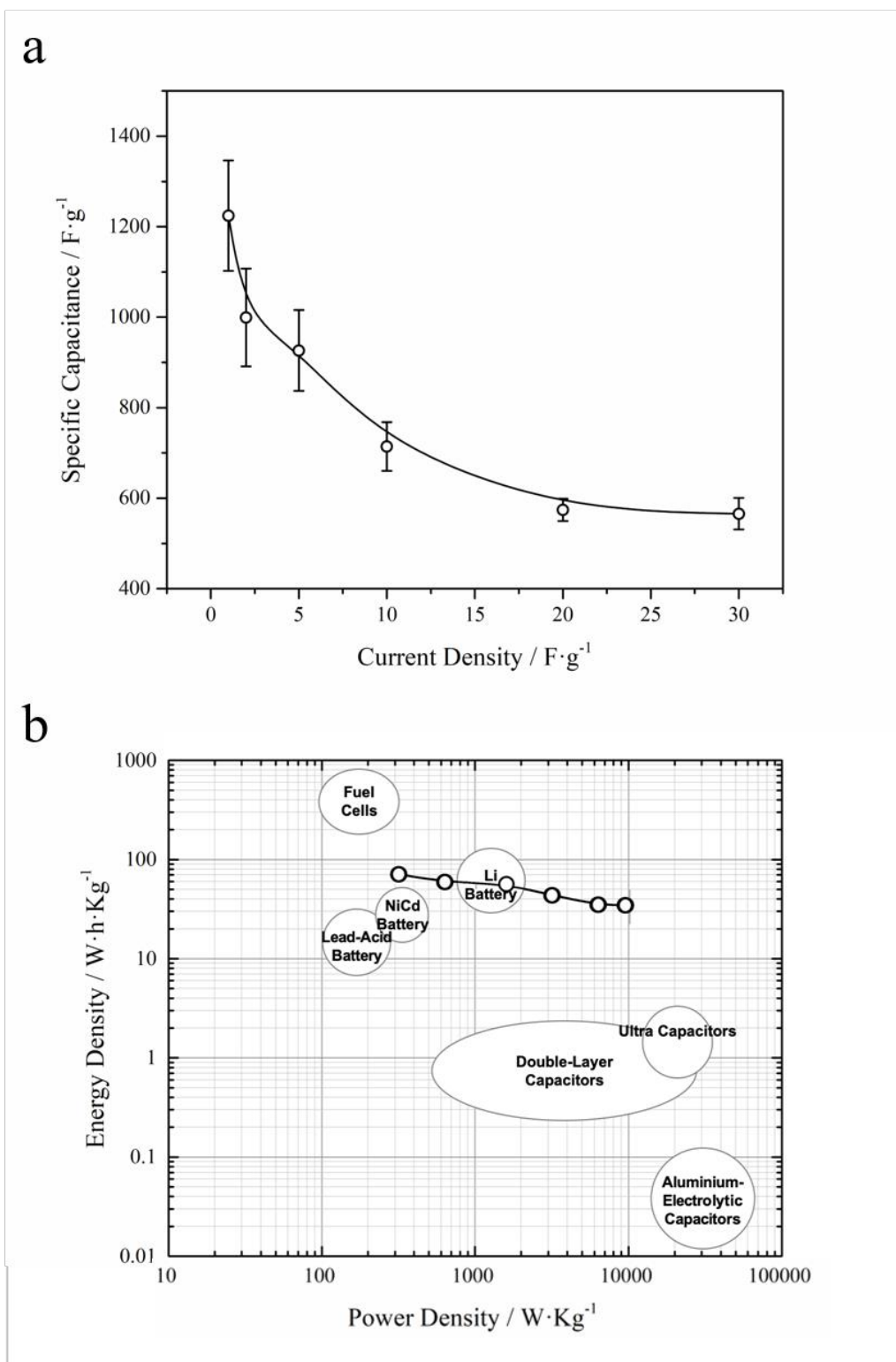


Figure SI 11.

a) Specific capacitance at different discharge current densities of MNC-MC. b) The corresponding Ragone plots calculated for a 3-electrode configuration.

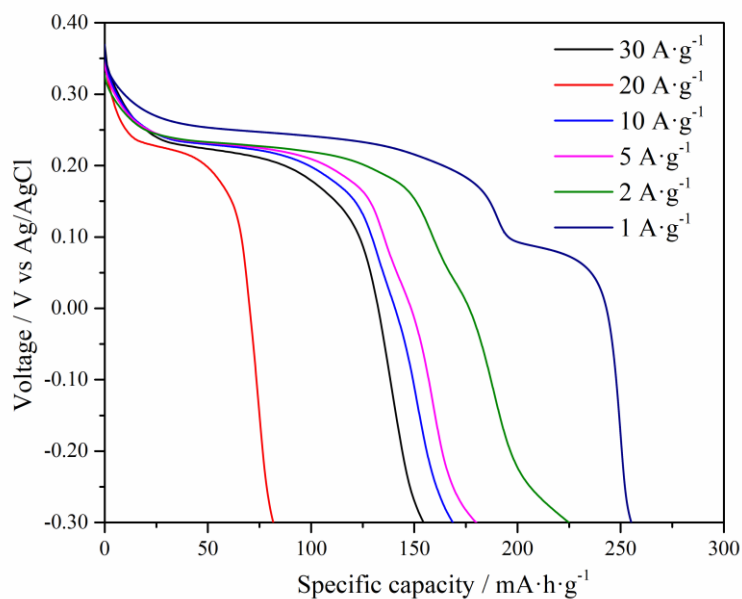
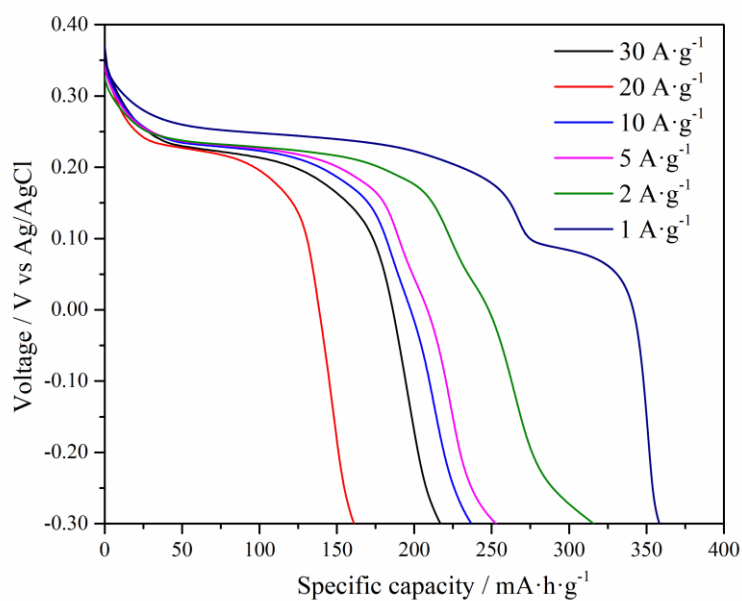


Figure SI 12.

Top. Specific capacity in mA·h·g⁻¹ of the MNC-MC at different discharge current densities calculated for a 3-electrode configuration and referred to the active material (*i.e.* Nickel). **Bottom.** Specific capacity in mA·h·g⁻¹ of the MNC-MC at different discharge current densities calculated for a 3-electrode configuration and referred to the total mass of the electrode.

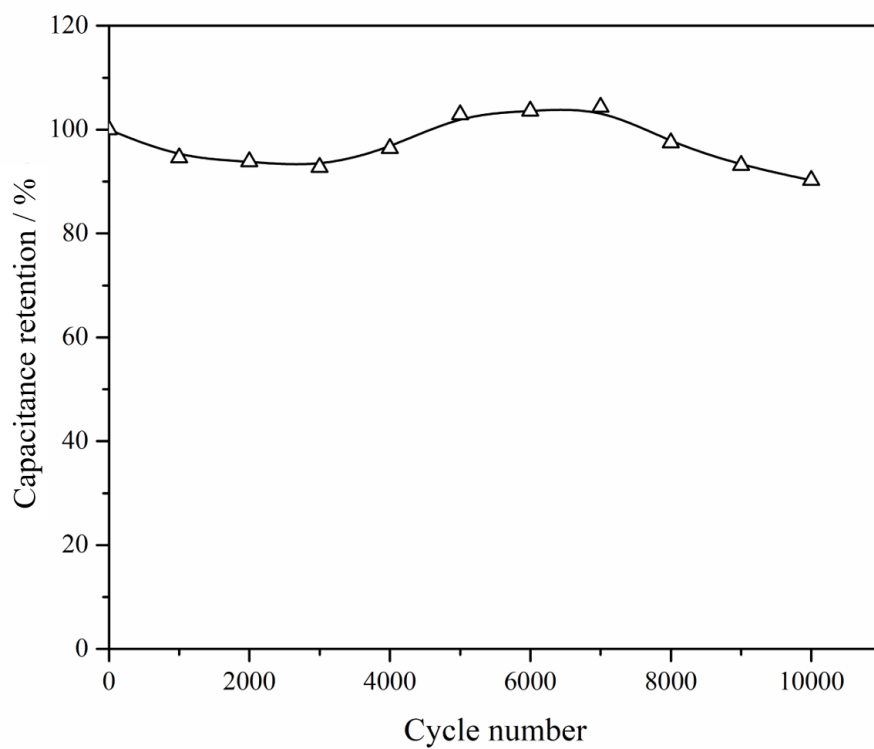


Figure SI 13.

Capacity retention of MNC-MC (prepared after submitting MNC to 1000 cycles in presence of an external magnetic field of 4000 G) during 10,000 charge–discharge cycles in the absence of an external magnetic field.

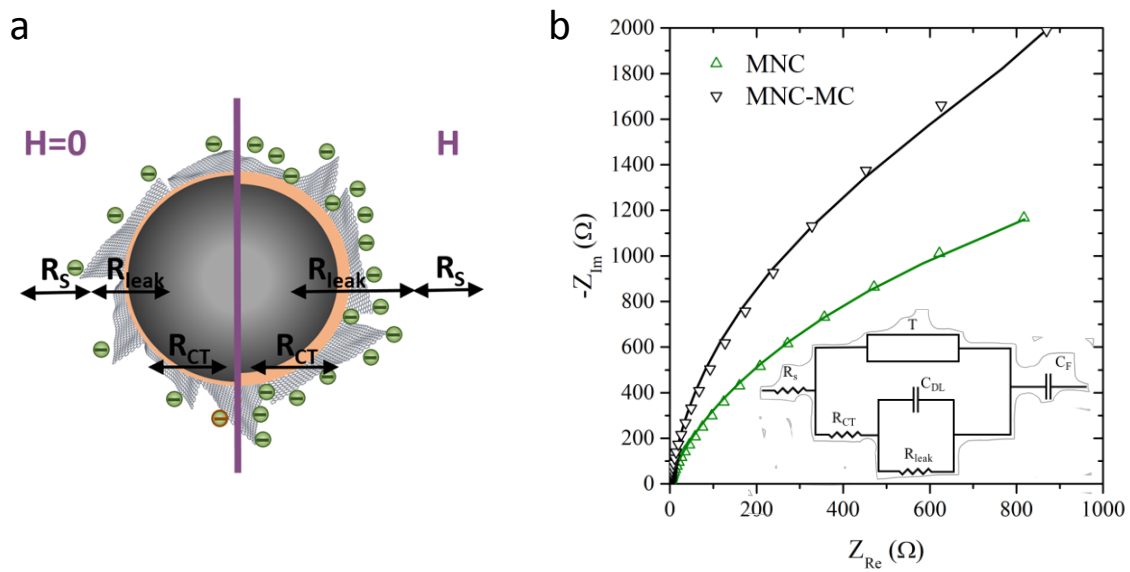


Figure SI 14.

a) Illustration of the effect of the magnetic field in the system. The MNC are sketched on the left hand side whereas the magnetic graphene- FeNi_3 nanocomposites in an external magnetic field (MNC-MC) are on the right. The oxidized layer increases due to the deeper penetration of the ions in the electrolyte when a magnetic field is applied. b) Impedance spectra for the nanocomposite with and without externally applied magnetic field. Solid lines are fittings to the equivalent circuit shown in the inset.

Potentiostatic electrochemical impedance spectroscopy (PEIS) measurements

The electrochemical pattern of the magnetocapacitive NiFe-graphene nanocomposites has been evaluated by means of PEIS.^[6-9] The measurements performed in the MNC have been compared with and without an externally applied magnetic field, in both cases protecting the electrochemical cell by means of a Faraday cage. Thus, the three internal resistances of the system can be affected by the application of a magnetic field: the solution resistance in bulk electrolyte (R_S), the electrode/electrolyte interfacial charge transfer resistance (R_{CT}) directly related to the electrode's resistance and the low frequency leakage resistance (R_{Leak}) in the double layer zone.^[10] In turn, the best optimization of the device in a magnetic field would occur when R_S and R_{CT} diminish and the R_{Leak} increases. In the presence of a magnetic field, the magnetohydrodynamic force^[11] affects the trajectory of the ions in the electrolyte (*i.e.* ions are able to penetrate further, due to the Lorentz force^[12]). Besides, the magnetic field also alters the resistance of the electrode itself (magnetoresistance).

To evaluate the variations of the resistances in the magnetocapacitor, we fitted the impedance curves to an equivalent circuit,^[10] sketched in the inset of Figure SI I 7b. The R_S in our system is really small compared to the R_{CT} and R_{Leak} , and remains nearly constant with and without field ($R_{S,H=0} = 1.6 \Omega$, $R_{S,H} = 1.5 \Omega$), showing that the transport is very good in the electrolyte both with and without an applied field. R_{CT} increases from $R_{CT,H=0} = 78 \Omega$ to $R_{CT,H} = 97 \Omega$ given its close relationship with the positive MR of the device. Lastly, R_{Leak} increases markedly from $R_{Leak,H=0} = 764 \Omega$ to $R_{Leak,H} = 920 \Omega$. PEIS indicates that the latter is responsible of the improvement in the energy storage performance of our device; ions in the magnetic field are able to enlarge the oxidized zone, increasing notably the resistance of the double layer.

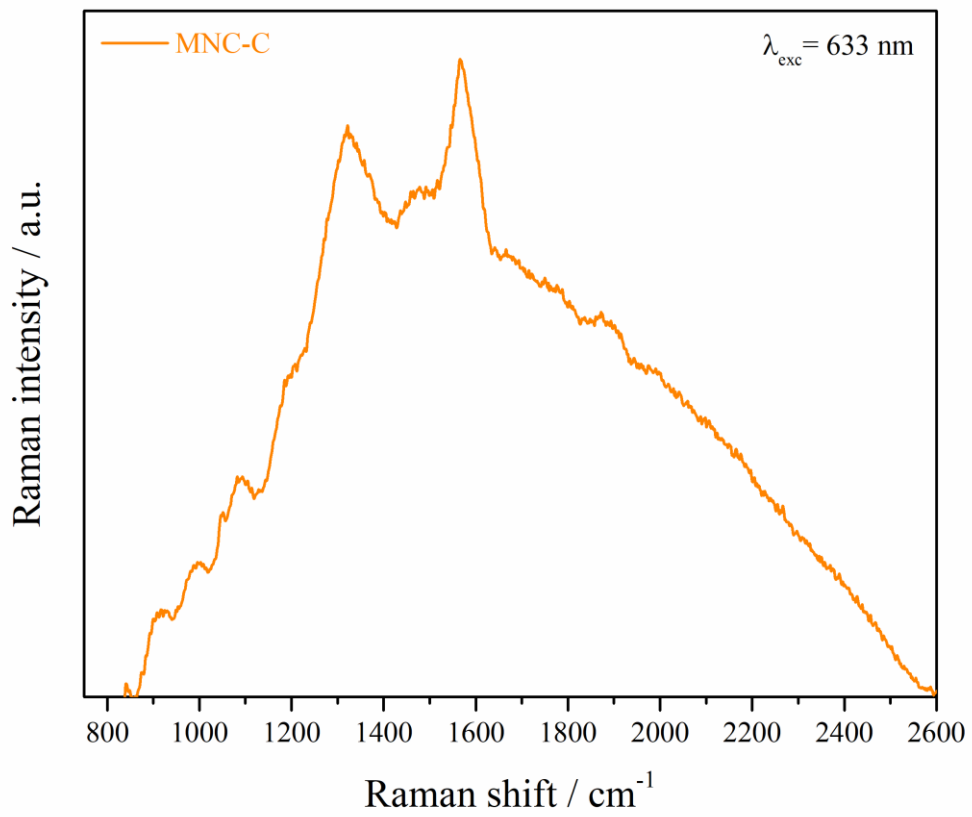


Figure SI 15.
Raman measurement of the MNC-C sample.

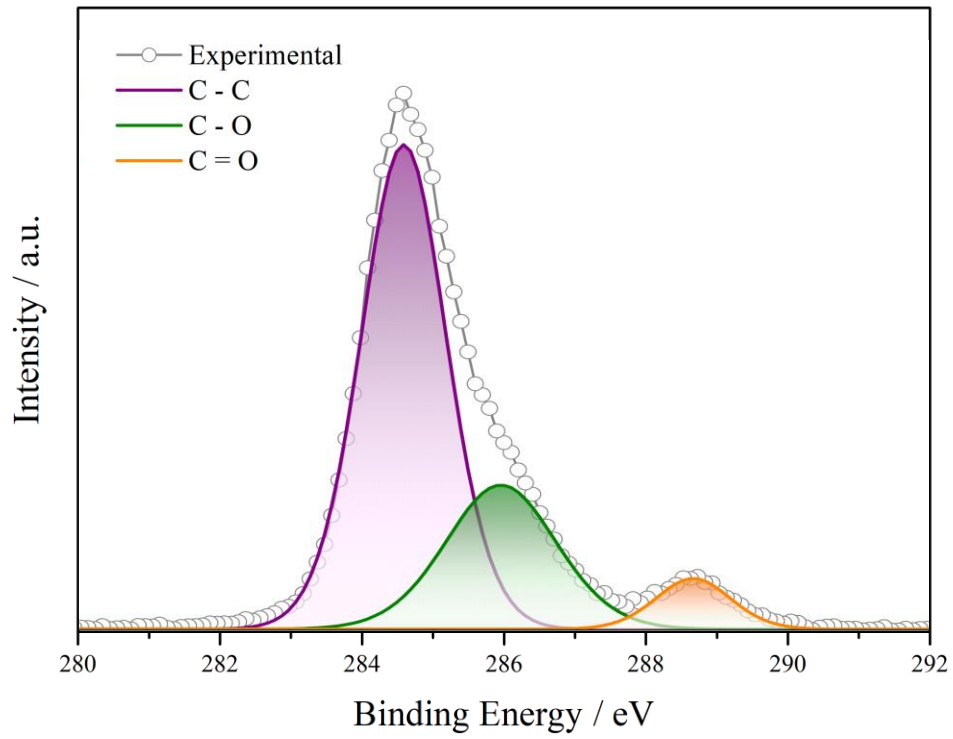


Figure SI 16.

XPS high-resolution C1s spectrum of MNC.

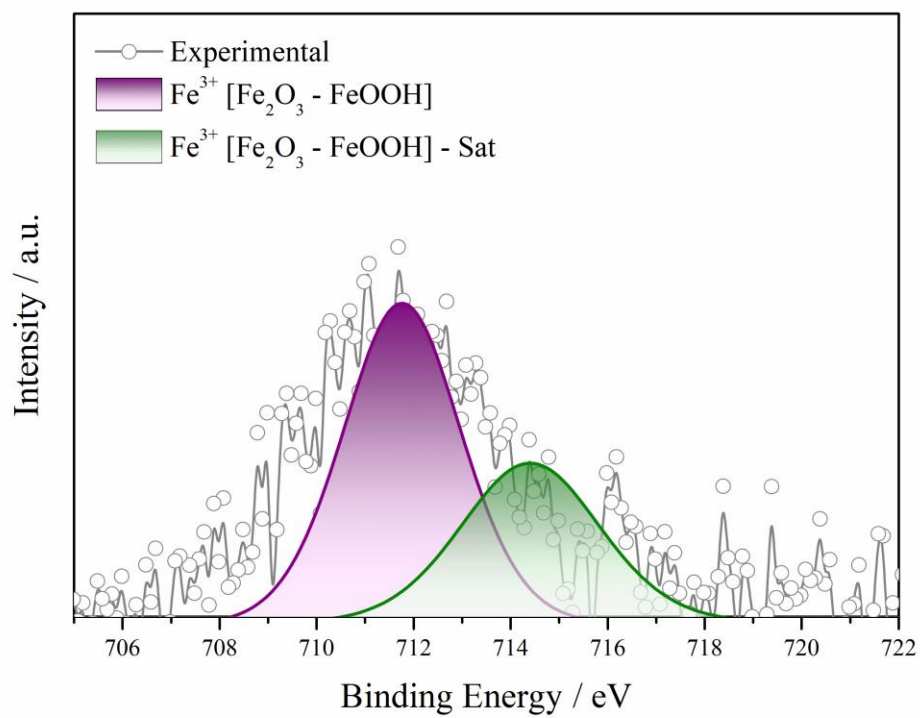


Figure SI 17.

XPS high-resolution $\text{Fe}2p_{3/2}$ spectrum of MNC.

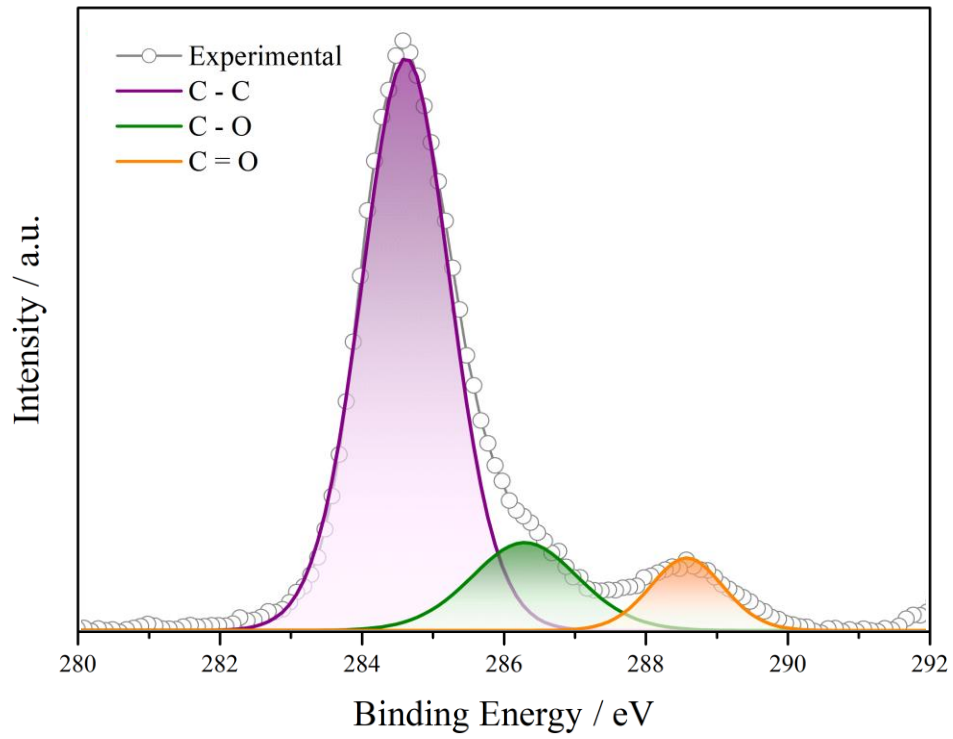


Figure SI 18.

XPS high-resolution C1s spectrum of MNC-C.

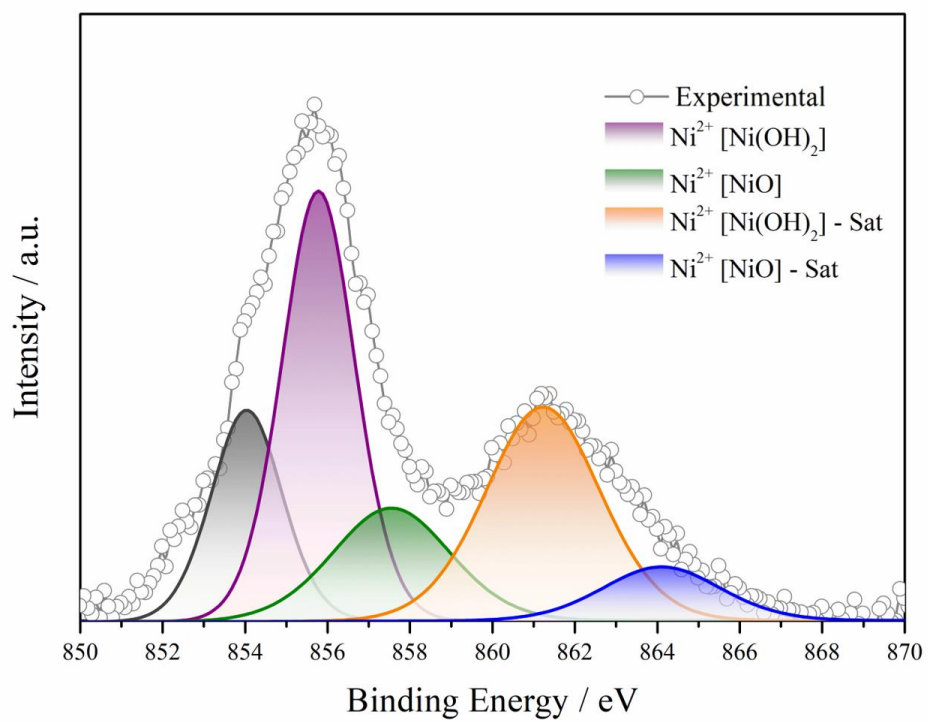


Figure SI 19.
XPS high-resolution Ni_{2p_{3/2}} spectrum of MNC-C.

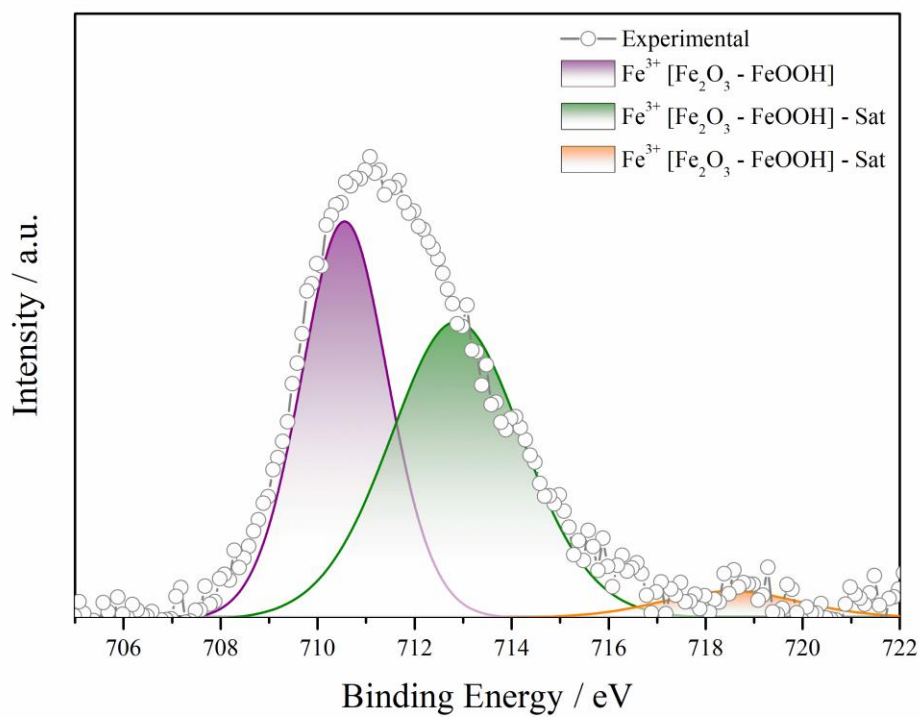


Figure SI 20.

XPS high-resolution $\text{Fe}2p_{3/2}$ spectrum of MNC-C.

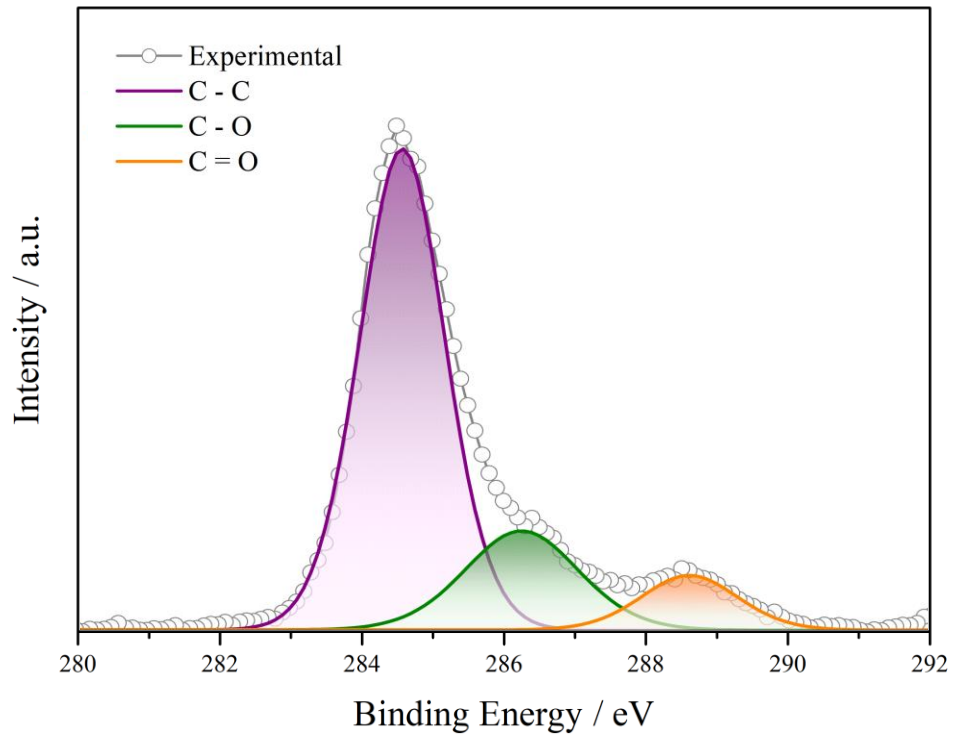


Figure SI 21.

XPS high-resolution C1s spectrum of MNC-MC.

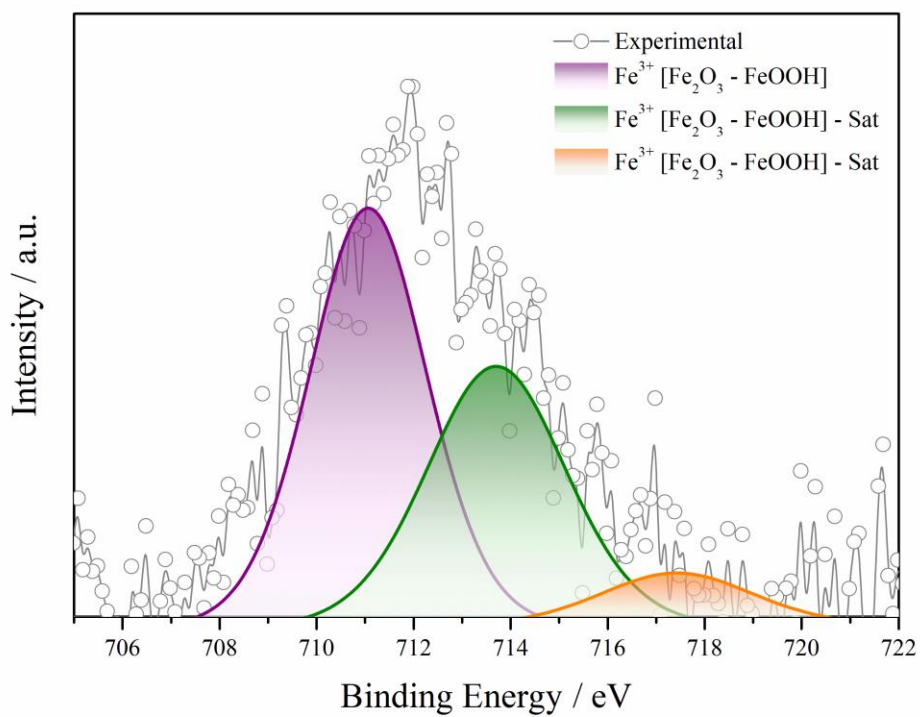


Figure SI 22.

XPS high-resolution Fe_{2p_{3/2}} spectrum of MNC-MC.

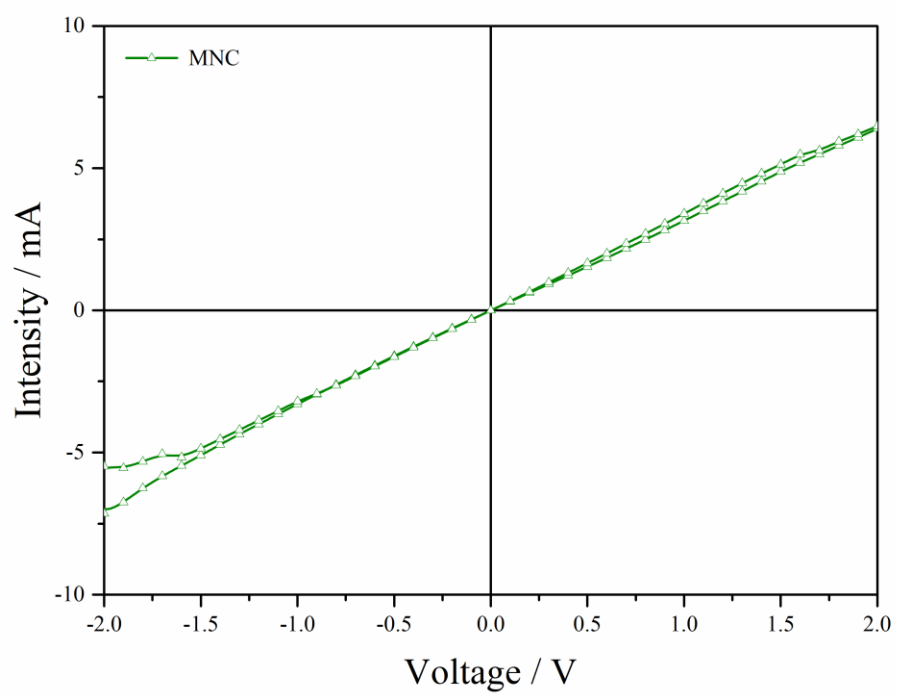


Figure SI 23.
Conductivity curve from MNC.

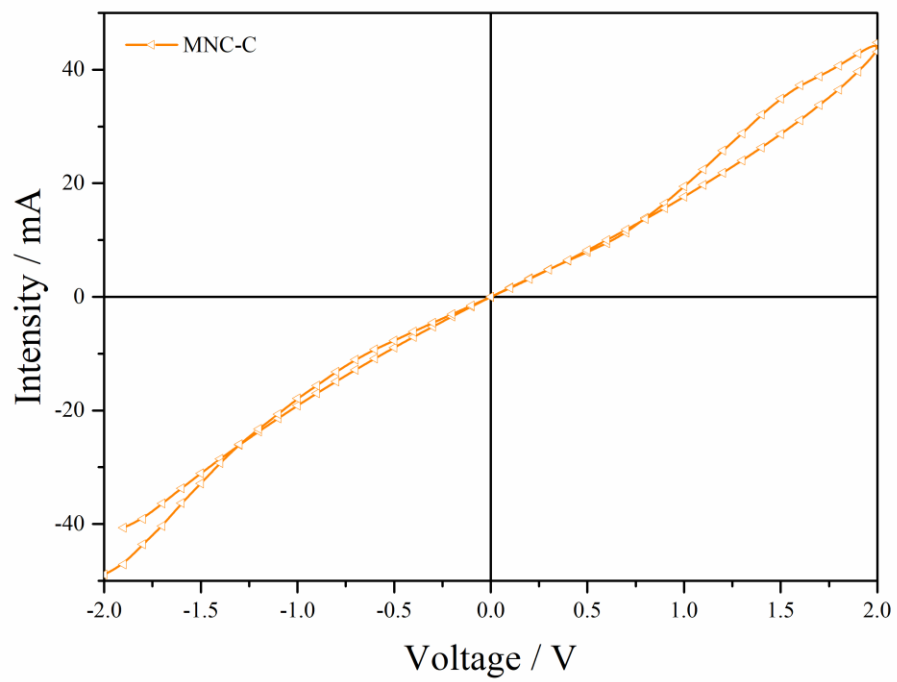


Figure SI 24.
Conductivity curve from MNC-C.

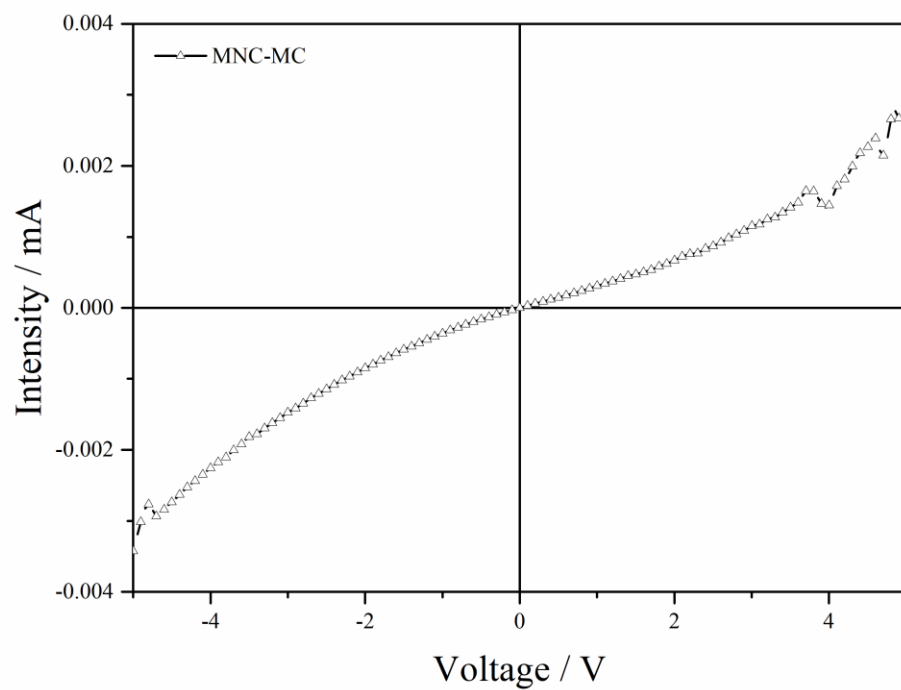


Figure SI 25.
Conductivity curve from MNC-MC.

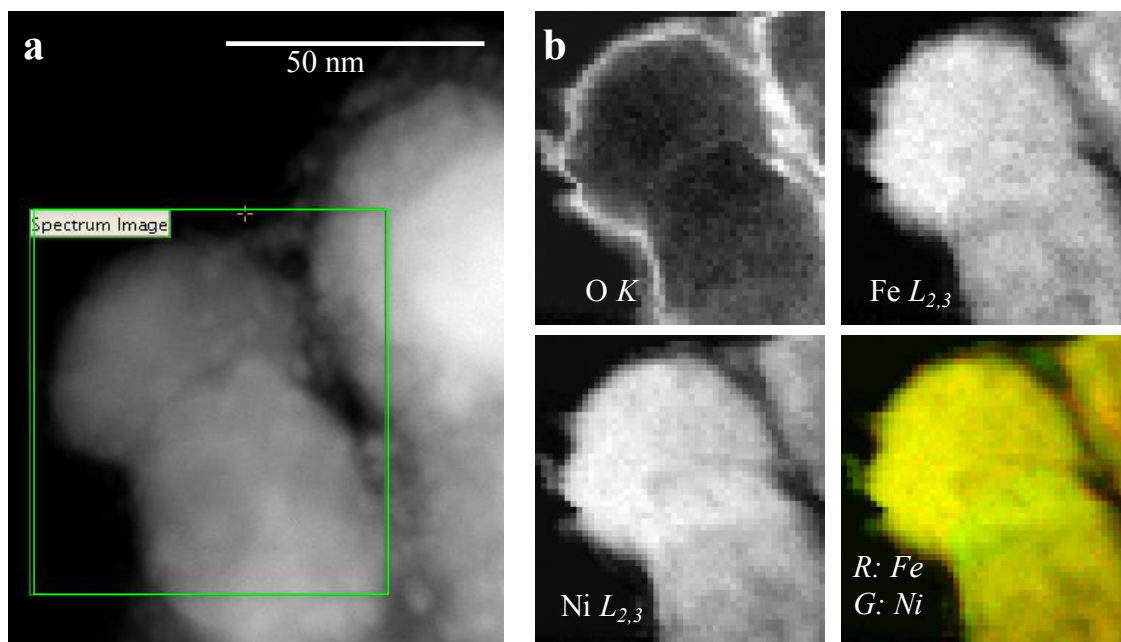


Figure SI 26.

a) Low magnification high angle annular dark field (HAADF) image of the MNC-C sample, obtained at 80 kV. Several nanometric clusters are observed around the larger particles. b) EELS maps for the particles inside the green rectangle highlighted on (a). The maps correspond to the O K, Fe L_{2,3} and Ni L_{2,3} edges, and have been obtained using a MLLS fit of the raw data. The bottom, right panel exhibits an overlay of the Fe (red) and Ni (green) maps. Data obtained at 80 kV.

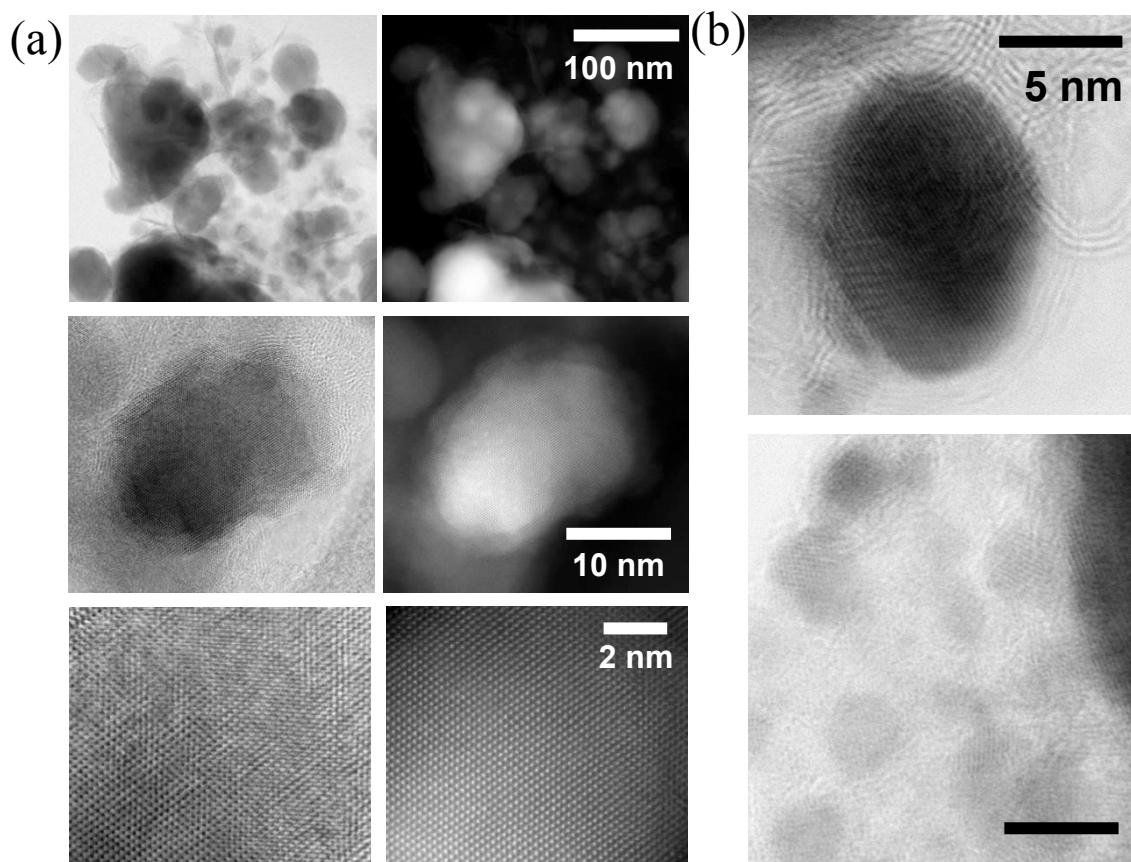
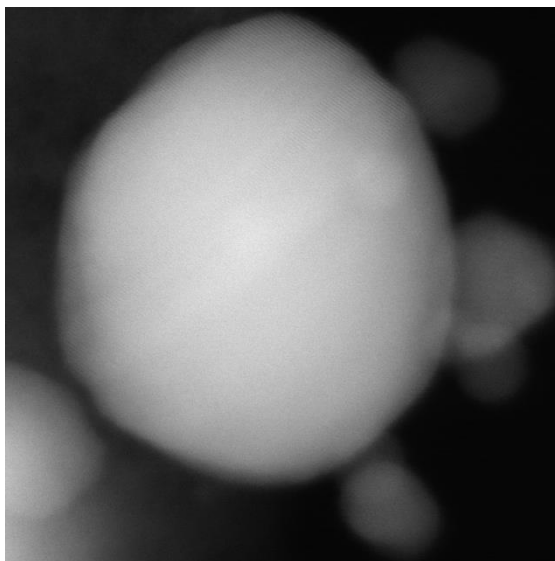


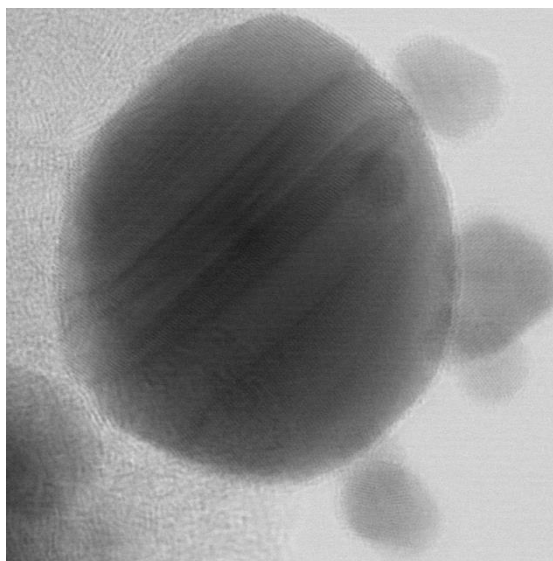
Figure SI 27.

(a) Simultaneously acquired annular bright field (ABF, left) and annular dark field (ADF, right) images. The top row panels exhibit intermediate magnification images. Larger particles, with sizes in the 10–100 nm range are observed. Also, smaller particles (in the 1–10 nm range) along with needle-shaped nanostructures are observed. The panels in the middle and lower rows display atomic resolution images of a nanoparticle, which exhibits a highly crystalline core surrounded by a shell and C layers. Data acquired at 200 kV. (b) ABF images showing high-resolution views of the particles. Nanometric clusters are visible around the larger particles, which are coated with C layers. The scale bars represent 5 nm. Data acquired at 80 kV in order to prevent damage to C structures.



Movie SI 1.

Simultaneously acquired HAADF movie showing the evolution of the MNC pristine nanoparticle while being held at a temperature of 400°C, under the applied magnetic field of the objective lens. The total time span of the experiment was close to 6 minutes (approximate speed 26x). Frames are approximately 35 nm x 35 nm in size. Data acquired at 80 kV.



Movie SI 2.

Simultaneously acquired ABF movie showing the evolution of the MNC pristine nanoparticle while being held at a temperature of 400°C, under the applied magnetic field of the objective lens. The total time span of the experiment was close to 6 minutes (approximate speed 26x). Frames are approximately 35 nm x 35 nm in size. Data acquired at 80 kV (see file attached).

In order to study the universality of the magnetic-field-enhance effect, we have developed the synthesis of Co(II)-Ni(II) layered hydroxides (1:1) with simonkolleite-like structure (also called alpha-hydroxides) containing sebacate at room temperature. The synthesis was adapted from recent reports obtaining analogous Co(II)-Ni(II) hydroxide structure containing chloride^[13], and also for the synthesis of Ni(II) hydroxide containing dicarboxylic acids.^[14]

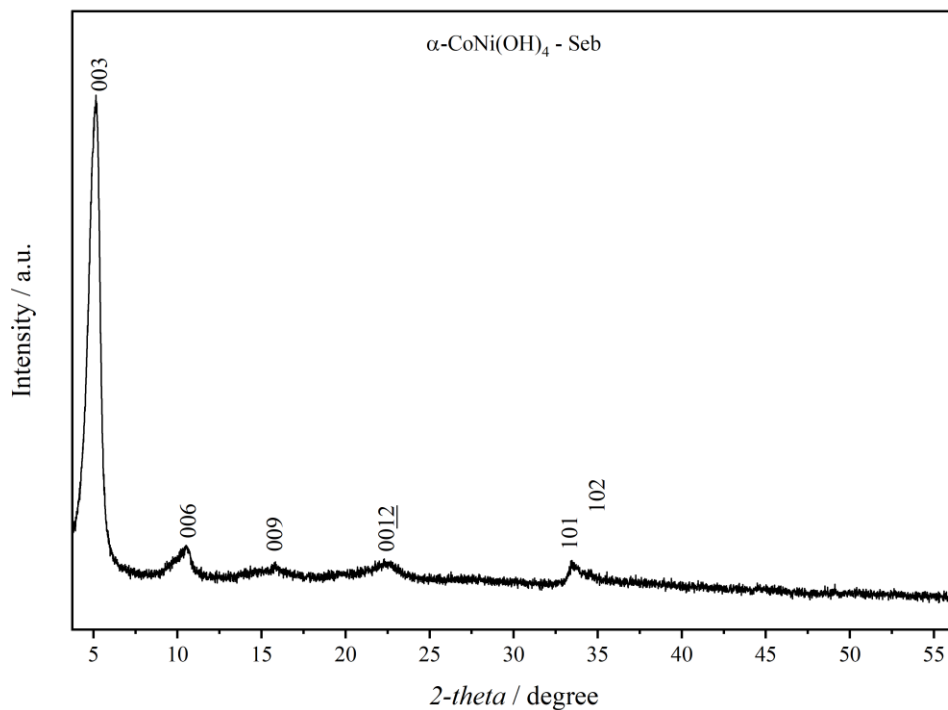


Figure SI 28.

XRPD of α -CoNi(OH)₄-Seb (CoNi 1:1).

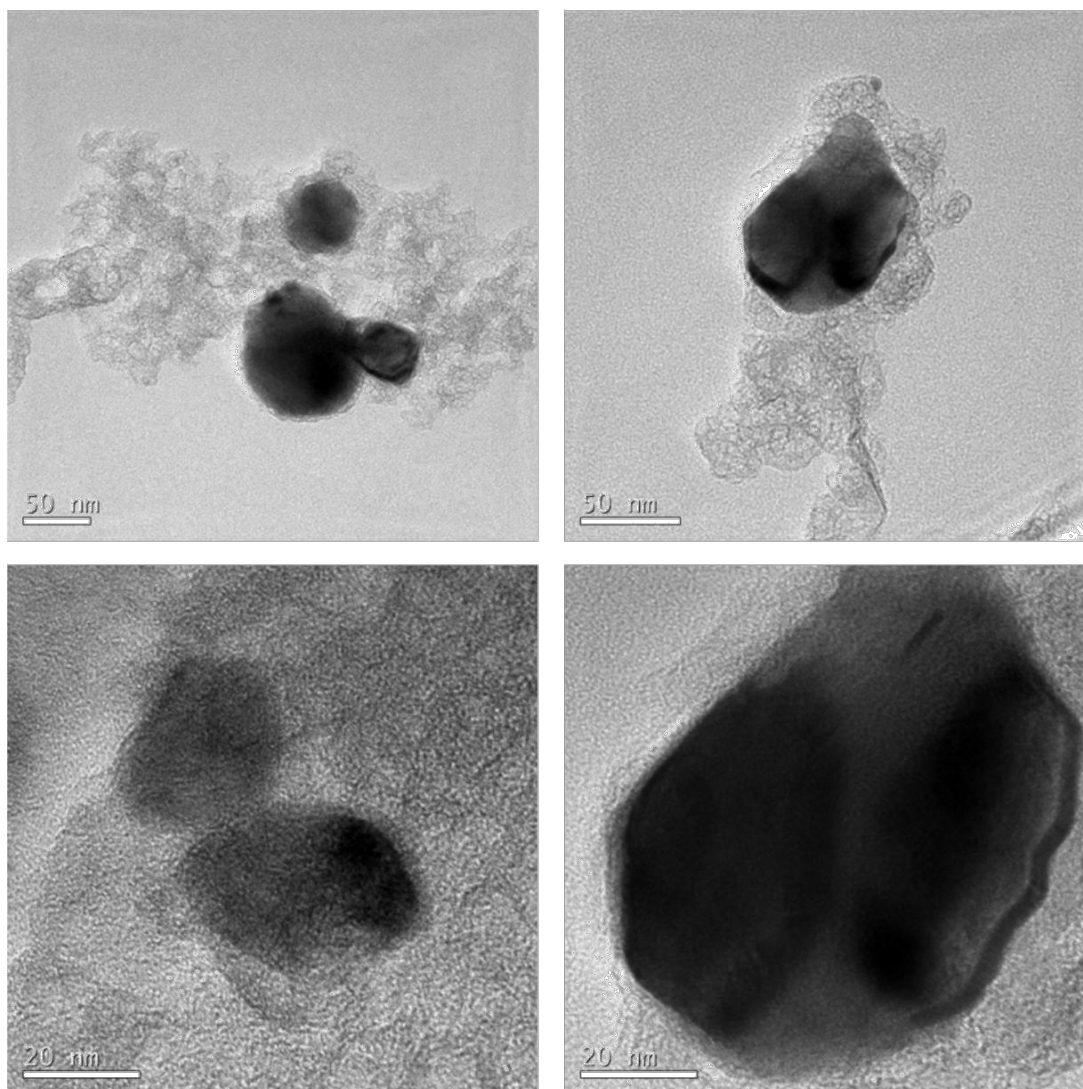


Figure SI 29.

HR-TEM images (measured at 200 kV) of the CoNi-Nanocomposite analog obtained after calcination under nitrogen atmosphere of α -CoNi-(OH)₄-Seb precursor.

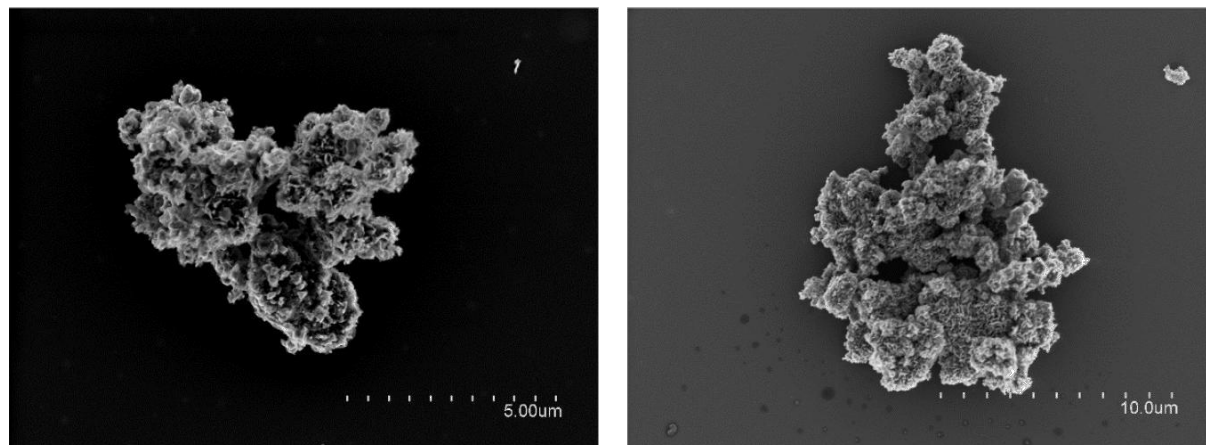


Figure SI 30.

FE-SEM images of the CoNi-Nanocomposite.

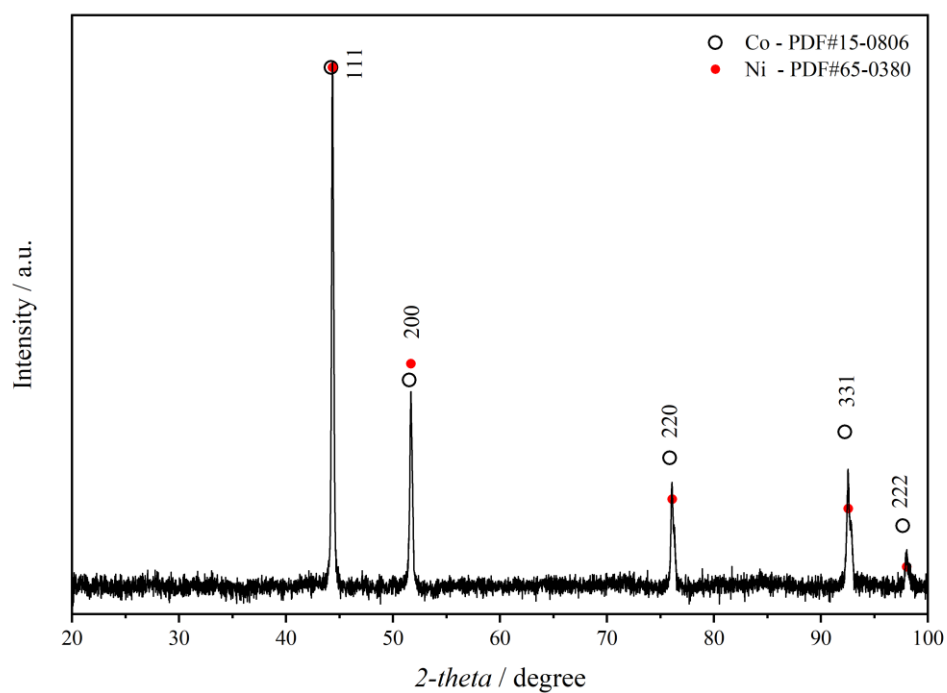


Figure SI 31.

XRPD of the CoNi-Nanocomposite showing the formation of a metallic CoNi alloy.

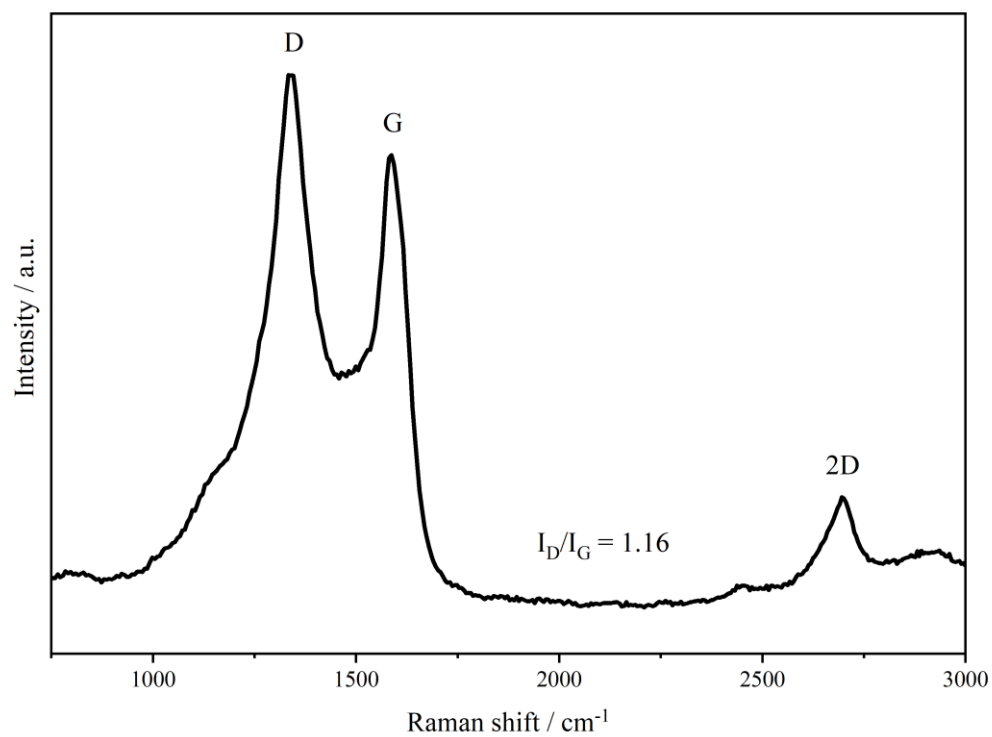


Figure SI 32.

Mean Raman spectrum of the CoNi-Nanocomposite.

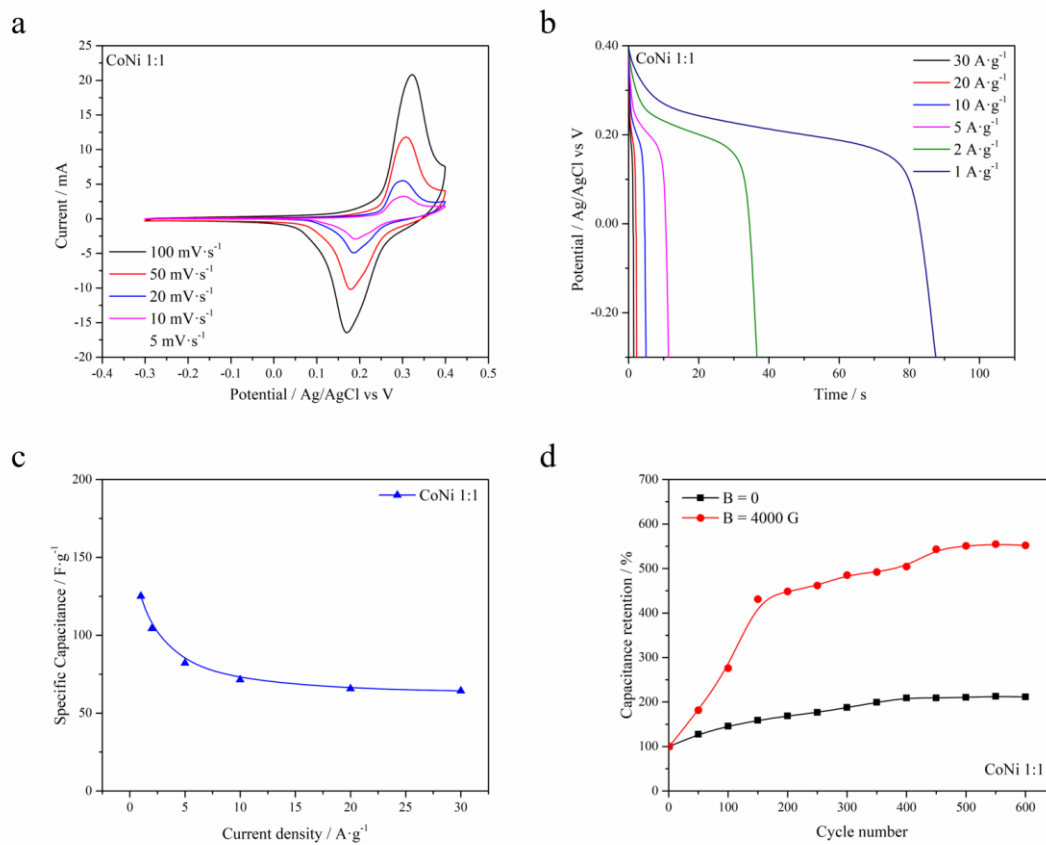


Figure SI 33.

Electrochemical measurements of the CoNi-Nanocomposite in 6 M KOH. a) Cyclic Voltammetry and b) galvanostatic discharges at different current densities of the CoNi-Nanocomposite. c) Specific capacitance at different current densities. d) Comparative capacitance retention of the NiCo-Nanocomposite over 600 cycles with and without an external applied magnetic field and their corresponding specific capacitance values.

References:

- [1] N. S. Lewis, D. G. Nocera, *Proc Natl Acad Sci* **2006**, *103*, 15729.
- [2] G. Abellán, M. Schirowski, K. F. Edelhalthammer, M. Fickert, K. Werbach, H. Peterlik, F. Hauke, A. Hirsch, *J. Am. Chem. Soc.* **2017**, *139*, 5175.
- [3] V. Nicolosi, M. Chhowalla, M. G. Kanatzidis, M. S. Strano, J. N. Coleman, *Science* **2013**, *340*, 1226419.
- [4] G. Abellán, H. Prima-García, E. Coronado, *J. Mater. Chem. C* **2016**, *4*, 2252.
- [5] C. h. Bajorek, M. Nicolet, C. h. Wilts, *Appl. Phys. Lett.* **1971**, *19*, 82.
- [6] M. Biswal, A. Banerjee, M. Deo, S. Ogale, *Energy Environ. Sci.* **2013**, *6*, 1249.
- [7] F. Béguin, V. Presser, A. Balducci, E. Frackowiak, *Adv. Mater.* **2014**, *26*, 2219.
- [8] H. Gu, H. Wei, J. Guo, N. Haldolaarachige, D. P. Young, S. Wei, Z. Guo, *Polymer* **2013**, *54*, 5974.
- [9] J. Xu, S. Gai, F. He, N. Niu, P. Gao, Y. Chen, P. Yang, *J Mater Chem A* **2014**, *2*, 1022.
- [10] J. Zhu, M. Chen, H. Wei, N. Yerra, N. Haldolaarachchige, Z. Luo, D. P. Young, T. C. Ho, S. Wei, Z. Guo, *Nano Energy* **2014**, *6*, 180.
- [11] J. Zhu, M. Chen, H. Qu, Z. Luo, S. Wu, H. A. Colorado, S. Wei, Z. Guo, *Energy Environ. Sci.* **2012**, *6*, 194.
- [12] L. M. A. Monzon, J. M. D. Coey, *Electrochem. Commun.* **2014**, *42*, 38.
- [13] N. Arencibia, V. Oestreicher, F.A. Viva, M. Jobbágy, *RSC Adv.* **2017**, *7*, 5595.
- [14] N. Tarutani, Y. Tokudome, M. Jobbágy; F.A. Viva, G.J.A.A. Soler-Illia, M. Takahashi, *Chem. Mater.* **2016**, *28*, 5606.

Chapter 3

Supercapacitive N-doped graphene

3.1 Introduction

Carbon based materials are considered suitable materials for SCs, due to their high specific surface area, good electronic conductivity, excellent chemical stability, easy processing, low cost, and wide operating temperature range¹. These materials exhibit high capacitance as a consequence of a predominant EDLC behaviour (Figure 3.1). A major wide variety of carbon materials have been used as electrode materials in SCs, such as active carbons (AC)², carbon aerogels^{3,4}, CNTs⁵, carbon nanofibres⁶, *etc.* Conventional ACs, with a theoretical capacitance of 100~300Fg⁻¹ and moderate cost, exhibit an excellent stability in several electrolytes, but their efficiency is dramatically reduced with charge/discharge cycling. This decrease in efficiency, which is crucial to meet the current demands, is usually given to limitations in the ion transport through the pores, provoking insufficient electrochemical accessibility.

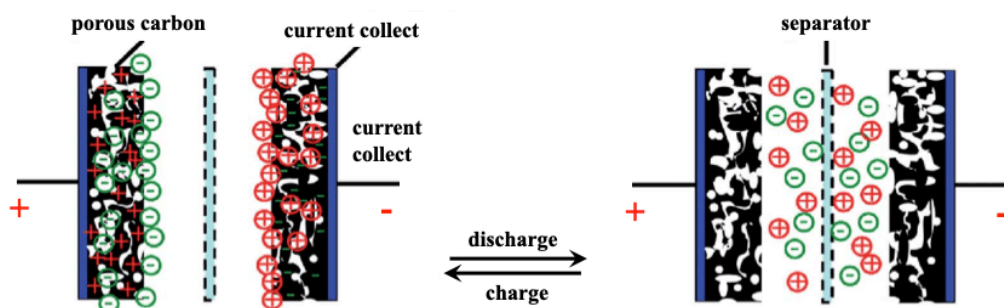


Figure 3.1. Schematic diagram of the charged and discharged electric double layer capacitor⁷.

Owing to this limitation, intense research effort is now focused on synthesizing resilient carbon nanomaterials with suitable pore size distributions and high values of specific surface area¹. Recently, graphene nanosheets, two-dimensional layers of sp²-bonded carbon, have been found to be an ideal carbon electrode material for SCs because of its unique properties, such as high surface area, excellent electrical and thermal conductivity and mechanical strength⁸. Traditionally graphene has been synthesized by mechanical exfoliation of graphite, liquid-phase exfoliation, epitaxial growth on substrates, and chemical vapour deposition using catalytic surfaces, obtaining a non-porous graphene that typically does not exceed 200 F·g⁻¹ at 1·A·g⁻¹ when used as an electrode material in SCs. To avoid this limitation, several synthetic routes have been

developed to obtain highly corrugated graphene with improved porosity. For example, by employing a MgO template procedure using methane in a tube furnace under an argon flow, the specific capacitance can be increased which exhibit to *ca.* $245 \text{ F}\cdot\text{g}^{-1}$ at $1\cdot\text{A}\cdot\text{g}^{-1}$, a better performance compared to the chemically reduced graphene due to a narrow distribution of mesopores and open structure with large surface area^{8,9}. Additionally, by a combined method of ion exchange and activation with NaOH using as the carbon precursor an acrylic resin ion exchanged with a metal, porous graphene with 3D structures has been synthesised, with a specific capacitance of *ca.* $305 \text{ F}\cdot\text{g}^{-1}$ at $0.5\cdot\text{A}\cdot\text{g}^{-1}$ ¹¹. However, the development of scalable and cost-effective synthetic methods of porous graphene still remains a challenge.

As we have seen in the previous chapter, in our group it hybrid organic-inorganic LDHs have been used as catalytic precursors of a graphitized porous carbon material exhibiting high values of specific capacitance even, at high current densities ($607 \text{ F}\cdot\text{g}^{-1}$ at $10\cdot\text{A}\cdot\text{g}^{-1}$)¹²⁻¹⁴. The success of this approach relies on the atomic in-plane distribution of the catalytic ions in the LDH layers, favouring the graphitisation process and subsequent formation of carbon nanoforms^{15,16}.

In this chapter we extend this concept to a different scenario in which the catalytic ions are incorporated into a laminar organic precursor instead of forming a laminar catalytic structure like in the LDH case. For this purpose, we looked for a precursor with an appropriate structure, because this type of calcination process is limited by the formation of partially amorphous carbon instead of graphene^{17,18}.

In this sense, layered covalent organic frameworks (COFs) represent an ideal candidate. These materials show ordered structures with high carbon content, and the presence of cavities with electron donor nitrogen atoms¹⁹. As COFs offer uniform nanopores (and predictive design criteria to organize functional building blocks), they have been also used to prepare electrodes for energy-based devices including electrochemical capacitors²⁰⁻²². Moreover, COFs could be an ideal graphene precursor for different reasons: I) its porous laminar structure and the possibility of coordinating catalytic metallic ions through their imine receptors^{23,24}. II) The structure of the COFs has nitrogen atoms, which allows the possibility to incorporate at the same time nitrogen as a dopant in the final graphene. Therefore, one can have a precursor with catalytic metals and the possibility of incorporating N hetero atoms in a single step reaction, leading to

N-doped porous graphene. This is remarkable, in light of the last reports regarding the improved performance of N-doped graphene in SCs^{9,25-27}.

3.2 Summary of the most important results

The main objective of the present chapter is to obtain corrugated porous N-doped graphene with supercapacitive behaviour, as well as the study of its properties. The conventional processes to obtain graphene are expensive and rather inefficient, therefore it is intended to obtain a straight forward and scalable synthetic method taking advantage of the high versatility of molecular layered materials. In order to overcome this challenge, a calcination synthetic method has been proposed, using a COF-1 (a COF with a structure similar to graphite with rigid 2D layers composed by benzene) functionalised with catalytic amount of metals ions (Fe^{III} , Co^{II} and Ni^{II}) into the cavities, as precursors.

The synthesis of the COF-1 was carried out at room temperature following a previous reported method²⁴. After the synthesis, the COF-1 was vigorously stirred in a methanol solution of $\text{M}(\text{acac})_n$ ($\text{M} = \text{Fe}^{\text{III}}$, Co^{II} and Ni^{II}) for 24 h at 25 °C. Spectroscopic analysis of COF-1-M by FT-IR, elemental analysis, and TXRF confirm the incorporation of the metal ions into the COF-1 structure. Once the different precursors were obtained, a thermal treatment in a tubular oven at 900 °C under a nitrogen atmosphere was performed. The final materials of all samples were a black residue, named as (N)G1 derived from COF-1 without metal and (N)G2, (N)G3 and (N)G4 for those functionalized with catalytic metals COF-1-M ($\text{M} = \text{Fe}(2)$, $\text{Co}(3)$, $\text{Ni}(4)$).

With high resolution TEM we confirmed the critical influence of the employed metal salts in the catalytic process, showing a partially amorphous structure for (N)G1, in contrast with the other (N)G-M samples, showing the formation of corrugated graphitic forms. (N)G4 exhibited less defined morphology, with a strongly disordered graphitic structure, whereas (N)G3 revealed the presence of disordered cage-like graphitic carbon nanoforms consisting of 5–15 layers of graphene. In contrast, the morphology of (N)G2 exhibited a well-defined hierarchical structure, showing high crystalline graphene nanocages of 3–7 graphene layers exhibiting a very open structure⁹. These results show the key role that iron plays in catalytic graphitization processes, in good agreement with recent reports in the literature^{28,29}.

To evaluate the graphitic character and quality of the as-obtained porous carbon matrices, we analysed the surfaces by XPS. To confirm that the iron derivative was the graphitic sample with the highest C-C sp^2 . Moreover, high-resolution N1s spectra showed

the presence of nitrogen as a dopant in all the samples, with values in the 0.8–1.9% range, similar to other reported N-doped graphene or microporous carbons^{25,26}. The deconvoluted peak revealed four different N types, *i.e.* pyridinic-N, pyrrolic-N, graphitic-N and pyridine-N-oxide groups, being specially interesting that (N)G2 exhibited the highest amount of pyridinic-N and pyrrolic-N, usually related to an increase in the capacitive contribution³⁰. Raman spectroscopy was also used to observe the characteristic G and D bands. The I_D/I_G ratios exhibit similar values (1.0–1.3) for all the samples, but the 2D band at *ca.* 2669 cm^{-1} was only present in the (N)G2 and (N)G3 samples, suggesting higher crystallinity, in excellent agreement with XPS measurements^{25,27}.

Finally, textural characterization, using N_2 at 77 K and CO_2 at 273 K adsorption–desorption isotherms, showed the highest surface area ($1147 \text{ m}^2 \cdot \text{g}^{-1}$), pore volume ($0.961 \text{ cm}^3 \cdot \text{g}^{-1}$) and narrow micropores ($<0.7 \text{ nm}$) volume ($0.471 \text{ cm}^3 \cdot \text{g}^{-1}$) for the (N)G2 sample. Interestingly, all the samples exhibited a larger micropore volume obtained from the CO_2 adsorption data than the total micropore volume deduced from the N_2 isotherm, a characteristic phenomenon of carbon molecular sieves with narrow constrictions (pore opening below 0.4 nm), demonstrating that this hierarchical porosity can play a relevant role in the supercapacitive behaviour³¹

To illustrate the application of these materials as SCs, their electrochemical properties were evaluated in a basic aqueous medium (6 M KOH) using a typical three-electrode cell by CV and galvanostatic CP from -1 to 0 V vs. Ag/AgCl. CV curves for the metal functionalised samples exhibit a typical EDLC rectangular-shape, with the highest CV area for the (N)G2 sample, indicative of an effective ion diffusion and good conductivity. The specific capacitance of the samples was analysed by means of galvanostatic charge/discharge measurements, using several electrodes prepared from different batches in order to test the reliability of this synthetic route. From these experiments it is clear that the best performance was achieved for the (N)G2 sample, with an overall maximum specific capacitance of *ca.* $460 \text{ F} \cdot \text{g}^{-1}$ at $10 \cdot \text{A} \cdot \text{g}^{-1}$, a value among the highest compared with those recently reported for related nitrogen-doped graphene-like materials or highly corrugated graphene^{27,32–34}.

Which respect to the kinetic behaviour of the different samples, we carried out potentiostatic EIS measurements, in which the analysis of the Nyquist plots, (N)G2 displays a near vertical line in the high frequency region compared to the other samples,

indicative of a better capacitive behaviour (vertical line for an ideal capacitor). In addition, the small semicircular shapes in the high frequency region suggest low charge-transfer resistances, mainly attributed to the N-doping. Moreover, to check the stability of the (N)G2, we evaluated the capacity retention after 10,000 charge/discharge cycles, observing capacity retention values higher than 90%, indicative of good stability and with similar capacity retention values than the others samples.

The excellent properties of the (N)G2 material were attributed, on the one hand, to the presence of nitrogen atoms, which enhances the surface wettability by electrolytes and also improves the charge transfer of the electrode materials^{18,35}. On the other hand, the laminar hierarchical porous structure allowed easy electrolyte penetration, efficiently exposing the active surface of graphene to the electrolyte^{29,36}. In fact, (N)G2 exhibited the highest specific surface area, micro- and mesopore volumes. It is worth mentioning that the contribution of pores smaller than the size of solvated electrolyte ions (narrow micropores) could play an important role favouring the increase of double-layer capacitance in carbons³⁷. Overall, all the studied techniques are in good agreement pointing towards (N)G2 as the best candidate of this family of materials for the development of supercapacitors.

In order to test (N)G2 more closely to the performance of commercially available packaged cells, we used a fixture two-electrode configuration cell^{38,39}. It is worth to remark the complication and effort to extract the full potential of these materials in this type of devices, with different variables like different cell configurations (symmetric or asymmetric), the electrolytes to improve the cell voltage (alkaline, acid organic, *etc.*), modification of the electrode contact, mass and thickness, *etc.* In this case, we developed a test of (N)G2 as symmetric two-electrode supercapacitors in the same medium with a potential range of 0–1 V. We used directly assembled electrodes with *ca.* 10 mg of active material in order to obtain reliable measurements^{39,40}. As for the three-electrodes configuration cell, we obtained typical rectangular-shaped CVs at different scan rates, and the corresponding galvanostatic discharge curves, showing an appropriate supercapacitive behaviour. With this configuration, the maximum specific capacitance was $175 \text{ F}\cdot\text{g}^{-1}$ at a current density of $0.2 \text{ A}\cdot\text{g}^{-1}$, *ca.* 38% of that obtained in the three-electrode cell configuration. In terms of energy values, the supercapacitive device could deliver a maximum energy density of $6.1 \text{ W}\cdot\text{h}\cdot\text{kg}^{-1}$, with a corresponding power density of $50 \text{ W}\cdot\text{kg}^{-1}$. In addition, when the current density increases to $20 \text{ A}\cdot\text{g}^{-1}$, the maximum

power density is $5000 \text{ W} \cdot \text{kg}^{-1}$. These values are comparable with other recently reported carbon-based symmetric supercapacitors working in alkaline solutions using the same electrochemical window^{40–43}.

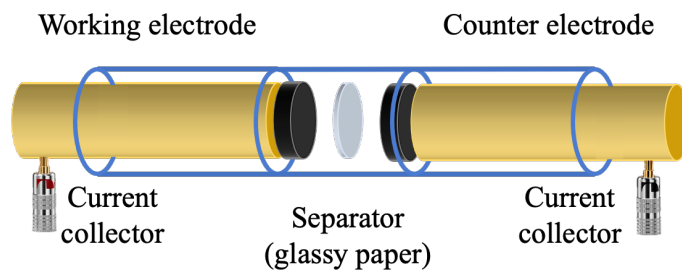


Figure 3.2. Schematic diagram of a two-electrode configuration cell.

Finally, to illustrate the performance of our system, we used two (N)G2/(N)G2 devices connected in series as the power supply for a commercial green light-emitting diode.

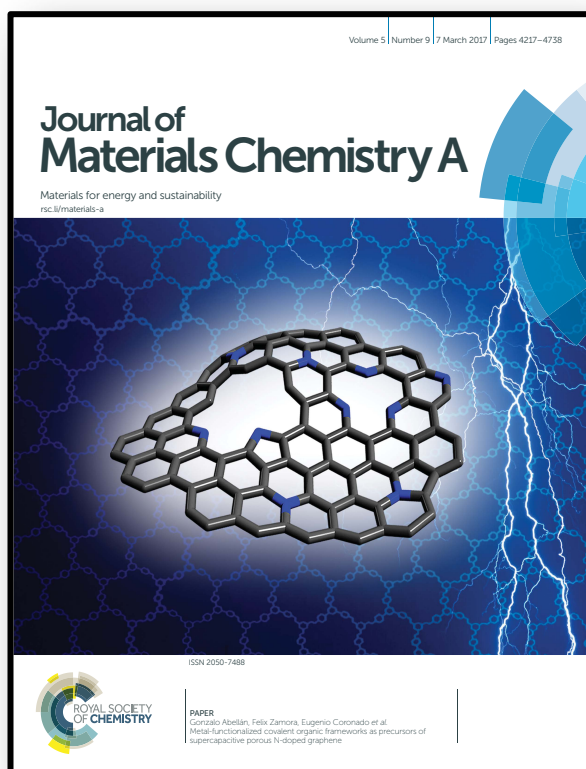
3.3 Contribution of the author

3.3.1 Article 3: “Metal-functionalized covalent organic frameworks as precursors of supercapacitive porous N-doped graphene”

The main contribution was to demonstrate that corrugated graphene can be obtained using a 2D covalent organic framework (COF-1) with metals ions (Fe^{III} , Co^{II} and Ni^{II}) into the cavities of the laminar structure. With a controlled calcination process are can obtain this corrugated graphene with a hierarchical N-doped porous structure, showing a supercapacitive behavior. We studied the difference in the structure of the corrugated graphene depending on the metal ion used, obtaining a better structure and supercapacitive behavior with iron. In addition, we were able to assemble the first real battery prototype in our institute, using a *Swaguelok*[®] cell as two electrode battery.

The author synthesized the material by a calcination process, characterized and discussed the results of all samples of NCs. The electrochemical measurements in the typical three electrode cells and the assembly of devices for two electrode measurements with their analysis were also carried out by the author. The author wrote the paper in collaboration with the other authors.

Note about the paper: Article 4 was selected to be the inside front cover of its respective issue:



3.4 References

1. Li, X. & Wei, B. Supercapacitors based on nanostructured carbon. *Nano Energy* **2**, 159–173 (2013).
2. Li, B. *et al.* Nitrogen-doped activated carbon for a high energy hybrid supercapacitor. *Energy Environ. Sci.* **9**, 102–106 (2016).
3. Saliger, R., Fischer, U., Herta, C. & Fricke, J. High surface area carbon aerogels for supercapacitors. *J. Non-Cryst. Solids* **225**, 81–85 (1998).
4. Wei, Y.-Z., Fang, B., Iwasa, S. & Kumagai, M. A novel electrode material for electric double-layer capacitors. *J. Power Sources* **141**, 386–391 (2005).
5. Senokos, E. *et al.* Large-Area, All-Solid, and Flexible Electric Double Layer Capacitors Based on CNT Fiber Electrodes and Polymer Electrolytes. *Adv. Mater. Technol.* **2**, 1600290 (2017).
6. Chen, L.-F., Lu, Y., Yu, L. & Wen (David) Lou, X. Designed formation of hollow particle-based nitrogen-doped carbon nanofibers for high-performance supercapacitors. *Energy Environ. Sci.* **10**, 1777–1783 (2017).
7. Wu, X.-L. & Xu, A.-W. Carbonaceous hydrogels and aerogels for supercapacitors. *J. Mater. Chem. A* **2**, 4852–4864 (2014).
8. C. Ferrari, A. *et al.* Science and technology roadmap for graphene, related two-dimensional crystals, and hybrid systems. *Nanoscale* **7**, 4598–4810 (2015).
9. Yan, J. *et al.* Advanced Asymmetric Supercapacitors Based on Ni(OH)₂/Graphene and Porous Graphene Electrodes with High Energy Density. *Adv. Funct. Mater.* **22**, 2632–2641 (2012).
10. Ning, G. *et al.* Gram-scale synthesis of nanomesh graphene with high surface area and its application in supercapacitor electrodes. *Chem. Commun.* **47**, 5976–5978 (2011).
11. Li, Y., Li, Z. & Shen, P. K. Simultaneous Formation of Ultrahigh Surface Area and Three-Dimensional Hierarchical Porous Graphene-Like Networks for Fast and Highly

Stable Supercapacitors. *Adv. Mater.* **25**, 2474–2480 (2013).

12. Abellán, G., Coronado, E., Martí-Gastaldo, C., Ribera, A. & Otero, T. F. Magnetic Nanocomposites Formed by FeNi₃ Nanoparticles Embedded in Graphene. Application as Supercapacitors. *Part. Part. Syst. Charact.* **30**, 853–863 (2013).

13. Abellán, G., Martínez, J. G., Otero, T. F., Ribera, A. & Coronado, E. A chemical and electrochemical multivalent memory made from FeNi₃-graphene nanocomposites. *Electrochem. Commun.* **39**, 15–18 (2014).

14. Abellán, G., Martí-Gastaldo, C., Ribera, A. & Coronado, E. Hybrid Materials Based on Magnetic Layered Double Hydroxides: A Molecular Perspective. *Acc. Chem. Res.* **48**, 1601–1611 (2015).

15. Abellán, G., Coronado, E., Martí-Gastaldo, C., Ribera, A. & F. Sánchez-Royo, J. Layered double hydroxide (LDH)–organic hybrids as precursors for low-temperature chemical synthesis of carbon nanoforms. *Chem. Sci.* **3**, 1481–1485 (2012).

16. Abellán, G., Carrasco, J. A., Coronado, E., Prieto-Ruiz, J. P. & Prima-García, H. In-Situ Growth of Ultrathin Films of NiFe-LDHs: Towards a Hierarchical Synthesis of Bamboo-Like Carbon Nanotubes. *Adv. Mater. Interfaces* **1**, 1400184 (2014).

17. Liu, R., Wu, D., Feng, X. & Müllen, K. Nitrogen-Doped Ordered Mesoporous Graphitic Arrays with High Electrocatalytic Activity for Oxygen Reduction. *Angew. Chem. Int. Ed.* **49**, 2565–2569 (2010).

18. Zhang, L. *et al.* Highly graphitized nitrogen-doped porous carbon nanopolyhedra derived from ZIF-8 nanocrystals as efficient electrocatalysts for oxygen reduction reactions. *Nanoscale* **6**, 6590–6602 (2014).

19. Côté, A. P. *et al.* Porous, Crystalline, Covalent Organic Frameworks. *Science* **310**, 1166–1170 (2005).

20. Kou, Y., Xu, Y., Guo, Z. & Jiang, D. Supercapacitive Energy Storage and Electric Power Supply Using an Aza-Fused π -Conjugated Microporous Framework. *Angew. Chem. Int. Ed.* **50**, 8753–8757 (2011).

21. DeBlase, C. R., Silberstein, K. E., Truong, T.-T., Abruña, H. D. & Dichtel, W. R. β -

Ketoenamine-Linked Covalent Organic Frameworks Capable of Pseudocapacitive Energy Storage. *J. Am. Chem. Soc.* **135**, 16821–16824 (2013).

22. DeBlase, C. R. *et al.* Rapid and Efficient Redox Processes within 2D Covalent Organic Framework Thin Films. *ACS Nano* **9**, 3178–3183 (2015).

23. Ding, S.-Y. & Wang, W. Covalent organic frameworks (COFs): from design to applications. *Chem. Soc. Rev.* **42**, 548–568 (2013).

24. de la Peña Ruigómez, A. *et al.* Direct On-Surface Patterning of a Crystalline Lamellar Covalent Organic Framework Synthesized at Room Temperature. *Chem. – Eur. J.* **21**, 10666–10670 (2015).

25. Wang, H., Maiyalagan, T. & Wang, X. Review on Recent Progress in Nitrogen-Doped Graphene: Synthesis, Characterization, and Its Potential Applications. *ACS Catal.* **2**, 781–794 (2012).

26. Jin, Z.-Y., Lu, A.-H., Xu, Y.-Y., Zhang, J.-T. & Li, W.-C. Ionic Liquid-Assisted Synthesis of Microporous Carbon Nanosheets for Use in High Rate and Long Cycle Life Supercapacitors. *Adv. Mater.* **26**, 3700–3705 (2014).

27. Peng, H. *et al.* A facile and rapid preparation of highly crumpled nitrogen-doped graphene-like nanosheets for high-performance supercapacitors. *J. Mater. Chem. A* **3**, 13210–13214 (2015).

28. Maldonado-Hódar, F. J., Moreno-Castilla, C., Rivera-Utrilla, J., Hanzawa, Y. & Yamada, Y. Catalytic Graphitization of Carbon Aerogels by Transition Metals. *Langmuir* **16**, 4367–4373 (2000).

29. Synthesis of Partially Graphitic Ordered Mesoporous Carbons with High Surface Areas - Gao - 2011 - Advanced Energy Materials - Wiley Online Library. <https://onlinelibrary.wiley.com/doi/10.1002/aenm.201000009>.

30. M. Hassan, F. *et al.* Pyrrolic-structure enriched nitrogen doped graphene for highly efficient next generation supercapacitors. *J. Mater. Chem. A* **1**, 2904–2912 (2013).

31. Carrasco, J. A. *et al.* Small-pore driven high capacitance in a hierarchical carbon via carbonization of Ni-MOF-74 at low temperatures. *Chem. Commun.* **52**, 9141–9144

(2016).

32. Yan, J., Liu, J., Fan, Z., Wei, T. & Zhang, L. High-performance supercapacitor electrodes based on highly corrugated graphene sheets. *Carbon* **50**, 2179–2188 (2012).

33. Jeong, H. M. *et al.* Nitrogen-Doped Graphene for High-Performance Ultracapacitors and the Importance of Nitrogen-Doped Sites at Basal Planes. *Nano Lett.* **11**, 2472–2477 (2011).

34. Lin, T. *et al.* Nitrogen-doped mesoporous carbon of extraordinary capacitance for electrochemical energy storage. *Science* **350**, 1508–1513 (2015).

35. Sun, L. *et al.* Nitrogen-doped graphene with high nitrogen level via a one-step hydrothermal reaction of graphene oxide with urea for superior capacitive energy storage. *RSC Adv.* **2**, 4498–4506 (2012).

36. Ding, S.-Y. *et al.* Construction of Covalent Organic Framework for Catalysis: Pd/COF-LZU1 in Suzuki–Miyaura Coupling Reaction. *J. Am. Chem. Soc.* **133**, 19816–19822 (2011).

37. Chmiola, J. *et al.* Anomalous Increase in Carbon Capacitance at Pore Sizes Less Than 1 Nanometer. *Science* **313**, 1760–1763 (2006).

38. Beguin, F. & Frackowiak, E. *Supercapacitors: Materials, Systems, and Applications*. (John Wiley & Sons, 2013).

39. Stoller, M. D. & Ruoff, R. S. Best practice methods for determining an electrode material's performance for ultracapacitors. *Energy Environ. Sci.* **3**, 1294–1301 (2010).

40. Patiño, J. *et al.* Phosphorus-doped carbon–carbon nanotube hierarchical monoliths as true three-dimensional electrodes in supercapacitor cells. *J. Mater. Chem. A* **4**, 1251–1263 (2016).

41. Lei, Z. *et al.* A high-energy-density supercapacitor with graphene –CMK-5 as the electrode and ionic liquid as the electrolyte. *J. Mater. Chem. A* **1**, 2313–2321 (2013).

42. Huang, X., Wang, Q., Chen, X. Y. & Zhang, Z. J. N-doped nanoporous carbons for the supercapacitor application by the template carbonization of glucose: The systematic

comparison of different nitridation agents. *J. Electroanal. Chem.* **748**, 23–33 (2015).

43. Li, Y. & Zhao, D. Preparation of reduced graphite oxide with high volumetric capacitance in supercapacitors. *Chem. Commun.* **51**, 5598–5601 (2015).

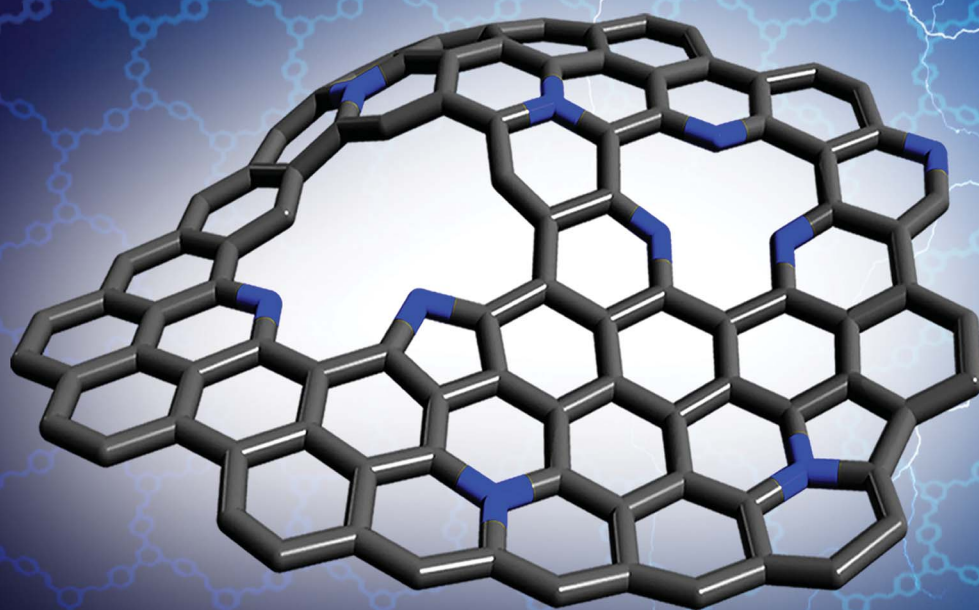
Article 3

*Metal-functionalized covalent organic frameworks as precursors
of supercapacitive porous N-doped graphene*

Journal of Materials Chemistry A. 2017 , 5, 4343-4351

Journal of Materials Chemistry A

Materials for energy and sustainability
rsc.li/materials-a



ISSN 2050-7488



PAPER

Gonzalo Abellán, Felix Zamora, Eugenio Coronado *et al.*
Metal-functionalized covalent organic frameworks as precursors of
supercapacitive porous N-doped graphene

Cite this: *J. Mater. Chem. A*, 2017, 5, 4343

Metal-functionalized covalent organic frameworks as precursors of supercapacitive porous N-doped graphene†

Jorge Romero,^{‡a} David Rodríguez-San-Miguel,^{‡bc} Antonio Ribera,^a Rubén Mas-Ballesté,^b Toribio F. Otero,^d Ilse Manet,^e Fabiola Licio,^f Gonzalo Abellán,^{*ag} Felix Zamora^{*bc} and Eugenio Coronado^{*a}Received 26th October 2016
Accepted 17th November 2016

DOI: 10.1039/c6ta09296a

www.rsc.org/MaterialsA

Covalent Organic Frameworks (COFs) based on polyimine with several metal ions (Fe^{III}, Co^{II} and Ni^{II}) adsorbed into their cavities have shown the ability to generate N-doped porous graphene from their pyrolysis under controlled conditions. These highly corrugated and porous graphene sheets exhibit high values of specific capacitance, which make them useful as electrode materials for supercapacitors.

Introduction

Supercapacitors (SCs) have attracted increased attention as energy storage devices in the scientific community because of their high reversibility, quick charge/discharge rates and excellent energy and power densities.¹ The suitable selection of the electrodes is crucial in this sort of devices, as the selected material must have high specific surface area, accurate pore size distributions, good thermal stability and stable electrochemical behaviour.² In this sense, carbonaceous materials such as activated carbon, mesoporous carbons or nanotubes occupy a privileged position.³ Traditionally, activated carbons have been used as materials for commercial SC electrodes due to their moderate cost and high capacity, but their performance is dramatically reduced with charge/discharge cycling, which is crucial to meet the current demands (electric vehicles, elevators,

etc.). This reduction in performance is generally related to limitations in the transport of ions through the pores, provoking insufficient electrochemical accessibility.

Nowadays, intense research effort is focused on synthesizing carbon nanomaterials with suitable pore size distributions and high values of specific surface area.³ In this context, graphene seems to be an outstanding candidate because of its unique properties, such as high surface area, excellent electrical and thermal conductivity and mechanical strength.⁴ Graphene has been synthesized traditionally by mechanical exfoliation of graphite, liquid-phase exfoliation, epitaxial growth on substrates, and chemical vapour deposition using catalytic surfaces. However, the non-porous graphene obtained by these routes does not exceed 200 F g⁻¹ at 1 A g⁻¹ when used as an electrode material in SCs. In order to synthesize highly corrugated graphene with improved porosity several synthesis routes have been developed, for example by employing a MgO template procedure using methane in a tube furnace under an argon flow.⁵⁻⁷ This porous graphene exhibits high specific capacity (*ca.* 245 F g⁻¹ at 1 A g⁻¹) and better performance compared to the chemically reduced graphene due to its narrow distribution of mesopores and open structure with large surface area. Additionally, highly corrugated graphene sheets have been obtained upon cooling graphene oxide in liquid nitrogen (*ca.* 349 F g⁻¹ at 2 mV s⁻¹).⁸ More recently, porous graphene with 3D structures has been prepared by a combined method of ion exchange and activation with NaOH using as the carbon precursor an acrylic resin ion exchanged with a metal (*ca.* 305 F g⁻¹ at 0.5 A g⁻¹).⁹ However, the development of scalable and cost-effective synthesis methods of porous graphene still remains a challenge. In this regard, any advance in synthesis would have a major impact in the field of energy storage and conversion and particularly in SCs.⁴

Recently, some of us reported the use of hybrid organic-inorganic layered double hydroxides (LDHs) as catalytic precursors of a graphitized porous carbon material exhibiting

^aInstituto de Ciencia Molecular (ICMol), Universidad de Valencia, 46980 Paterna, Spain. E-mail: eugenio.coronado@uv.es

^bDepartamento de Química Inorgánica y Condensed Matter Physics Center (IFIMAC), Universidad Autónoma de Madrid, Madrid, Spain. E-mail: felix.zamora@uam.es

^cInstituto Madrileño de Estudios Avanzados en Nanociencia (IMDEA Nanociencia), 28049 Madrid, Spain

^dCenter for Electrochemistry and Intelligent Materials (CEMI), Universidad Politécnica de Cartagena, Cartagena, Spain

^eConsiglio Nazionale delle Ricerche – Istituto per la Sintesi Organica e la Fotoreattività (CNR-ISOF), Via Gobetti 101, 40129 Bologna, Italy

^fCNR-IMM, Istituto per la Microelettronica e Microsistemi, via P. Gobetti 101, 40129 Bologna, Italy

^gDepartment of Chemistry and Pharmacy, Joint Institute of Advanced Materials and Processes (ZMP), University Erlangen-Nürnberg, Henkestr. 42, 91054 Erlangen and Dr.-Mack Str. 81, 90762 Fürth, Germany. E-mail: gonzalo.abellan@fau.de

† Electronic supplementary information (ESI) available: Experimental details and further characterization including confocal fluorescence, FT-IR, solid-state ¹³C-NMR, XRD, GIXRD, TG/DTA, FESEM, EDAX, XPS, porosity metrics, and additional electrochemical experiments. See DOI: 10.1039/c6ta09296a

‡ These authors contributed equally to this work.

high values of specific capacitance even at high current densities (607 F g^{-1} at 10 A g^{-1}).^{10–12} The success of this approach relies on the atomic in-plane distribution of the catalytic ions in the LDH layers, favouring the graphitisation process and subsequent formation of carbon nanoforms.^{13,14}

Along this front, we tried to extend this concept to a different scenario in which the catalytic ions are incorporated into a laminar carbonaceous precursor instead of forming a laminar catalytic structure like in the LDH case. To this end, a suitable selection of the precursor material with an appropriate structure is required, as the overall performance in this type of calcination processes is limited by the formation of partially amorphous carbon instead of graphene.^{15,16} Layered covalent organic frameworks (COFs) consist of ordered structures with high carbon content, and the presence of cavities with electron donor nitrogen atoms.¹⁷ From the electrochemical point of view, the unique ability of COFs to offer uniform nanopores (and predictive design criteria to organize functional building blocks) has been also used to prepare electrodes for energy-based devices including electrochemical capacitors.^{18,19} Moreover, COFs could be an ideal graphene precursor, as they exhibit a laminar porous morphology and the ability to coordinate metallic ions through their imine receptors (Fig. 1).^{20,21} Even more appealing is the possibility to incorporate at the same time nitrogen as a dopant in the final graphene, in light of the last reports regarding the improved performance of N-doped graphene in SCs.^{22–25} Moreover, in contrast to conventional physico-chemical N-doping techniques (e.g. CVD and arch discharge), the use of COFs could help to incorporate N heteroatoms in a single step reaction leading to N-doped porous graphene.^{26,27}

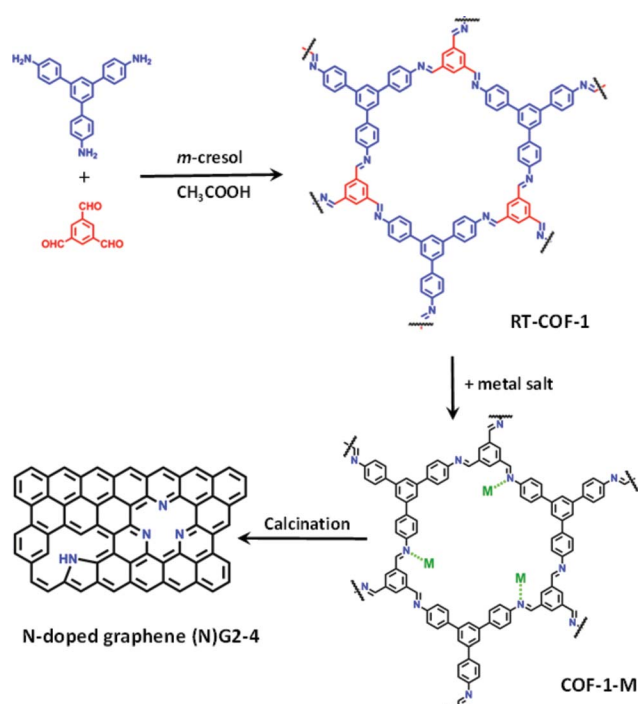


Fig. 1 General scheme of the work showing the RT-COF-a and COF-1-M structures, as well as the calcination process to produce N-doped graphenes.

Herein, we report a method consisting of calcination at moderate temperatures (below $1000 \text{ }^\circ\text{C}$) of a COF based on polyimine (Schiff base), which shows the ability to adsorb catalytic metal ions (Fe^{III} , Co^{II} and Ni^{II}) into its cavities. The resulting corrugated and porous N-doped graphene exhibits excellent behaviour as an electrode material for SCs under basic pH.

Results and discussion

The direct reaction between 1,3,5-tris(4-aminophenyl)benzene and 1,3,5-benzenetricarbaldehyde, 1 : 1 molar ratio, in *m*-cresol at room temperature leads to a characteristic yellow gel of COF-1 (see the ESI and SI 1†).²¹ The material was vigorously stirred in a methanol solution of $\text{M}(\text{acac})_n$ ($\text{M} = \text{Fe}^{\text{III}}$, Co^{II} , Ni^{II} ; acac = acetylacetonate) for 24 h at $25 \text{ }^\circ\text{C}$. Spectroscopic analysis of COF-1-M by FT-IR (SI 2†), as well as elemental analysis and TXRF confirm the incorporation of the metal ions into the RT-COF-1 structure. The FT-IR spectra of COF-1-M clearly show the presence of both imine $\text{C}=\text{N}$ and $\text{C}-\text{C}=\text{N}-\text{C}$ stretching bands at 1617 cm^{-1} and 1280 cm^{-1} , respectively (SI 2†). The metal ion content was evaluated by TXRF showing that $\text{Fe}(\text{III})$ is incorporated in a 1 : 280 Fe : N atomic ratio. For $\text{Co}(\text{II})$ the atomic ratio is similar (1 : 190 Co : N), while $\text{Ni}(\text{II})$ is incorporated in a smaller ratio (1 : 760 Ni : N). These values represent 0.19–0.05% of the starting material added to the reaction. Synchrotron radiation grazing incidence X-ray diffraction (GIXRD) data of COF-1-Fe confirm the presence of the two most characteristic diffraction peaks of RT-COF-1 (named as 1 and 2 in Fig. 2B and C) with a general broadening of the peaks indicating a partial amorphization of the initial structure (SI 3†).

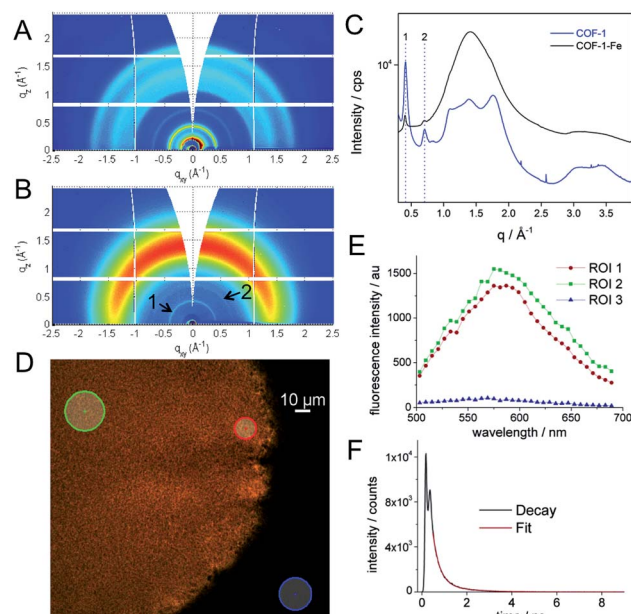


Fig. 2 (A, B) GIXRD of RT-COF-1 and COF-1-Fe. (C) radial integration of the 2D-GIXRD images, (D) confocal fluorescence image for excitation at 488 nm of RT-COF-1 and (E) its confocal fluorescence spectra in the selected ROI. (F) The graph shows the fluorescence decay of RT-COF-1 measured on the confocal system.

This change is associated with the decrease of the intensity of the Bragg rings and the appearance of an amorphous halo in Fig. 2B, which could be related to a layer-to-layer separation.²⁸ Similar observations have been reported for Pd(II) incorporation in a closely related COF.²⁹ The incorporation of Co(II) and Ni(II) causes a more pronounced effect with a complete loss of structural order. This is probably a consequence of the high structural distortion caused by the metal ion incorporation between the RT-COF-1 layers. Furthermore, the influence of metal-functionalization was followed by confocal fluorescence imaging measurements on SiO₂ substrates. After exciting RT-COF-1 at 488 nm, a green fluorescence signal peak at ca. 580 nm was observed. We also obtained a fluorescence lifetime image for excitation at 405 nm. A tail-fit of the fluorescence decay yielded two lifetimes of 0.3 and 1.1 ns with similar weight. While the observation of a short lifetime – close to the resolution limit – may be due to scattering, the second lifetime is likely due to the species giving the fluorescence spectrum peak at 580 nm (Fig. 2D–F). In turn, dramatic quenching of the fluorescence was observed after metal incorporation, probably due to the Fe(III) heavy-metal effect or metal-to-ligand charge transfer (MLCT), as previously observed for other Fe³⁺-imine systems (SI 4†).

This physical change strongly suggests Fe(III) incorporation into the RT-COF-1 structure rather than physisorption. The controlled thermal treatment of the COF-1-M carried out in a tubular oven at 900 °C under a nitrogen atmosphere produces a black residue for all materials, named as (N)G1 from RT-COF-1 and (N)G2, (N)G3 and (N)G4 from COF-1-M (M = Fe (2), Co (3), Ni (4)). The pyrolysis procedure results in carbon yields in the range of 55–67% as obtained by thermogravimetric analysis (see SI 5†). The TEM analysis of (N)G1 clearly shows the formation of a partially amorphous structure. In contrast, in the other (N)G-M samples, TEM and EDAX analyses clearly show the formation of corrugated graphitic forms. The morphology of (N)G2 consists of a well-defined hierarchical structure, rather similar to that previously named as graphene nanocages (Fig. 3A–C).⁷ It consists of a lamellar porous material based on cages of 3–7 graphene layers exhibiting a very open structure. The iron compound is a well-known and efficient catalyst for graphitization of organic aerogels or mesoporous carbons, favouring the graphitization process.^{34,35} In addition, the pyrolysis and gasification processes that occur during the heat treatment of the different compounds could also play an important role in the final morphology of the materials, as gases like CO or CO₂ formed during the heat-treatment could act as very efficient porogens.^{9,36} On the other hand, (N)G3 revealed the presence of several cage-like graphitic carbon nanoforms consisting of 5–15 layers of graphene, whereas (N)G4 exhibited less defined morphology, with a strongly disordered graphitic structure (SI 6†). The observed poorest morphologies could be related to the complete loss of the structural order exhibited by the COF-1-Co and COF-1-Ni precursors after metal functionalization, in comparison to that of COF-1-Fe. These results suggest a critical influence of the employed metal salts in the catalytic process, despite the small metal incorporation.⁹ In fact, a control experiment using metal sulfates instead of acetylacetonates

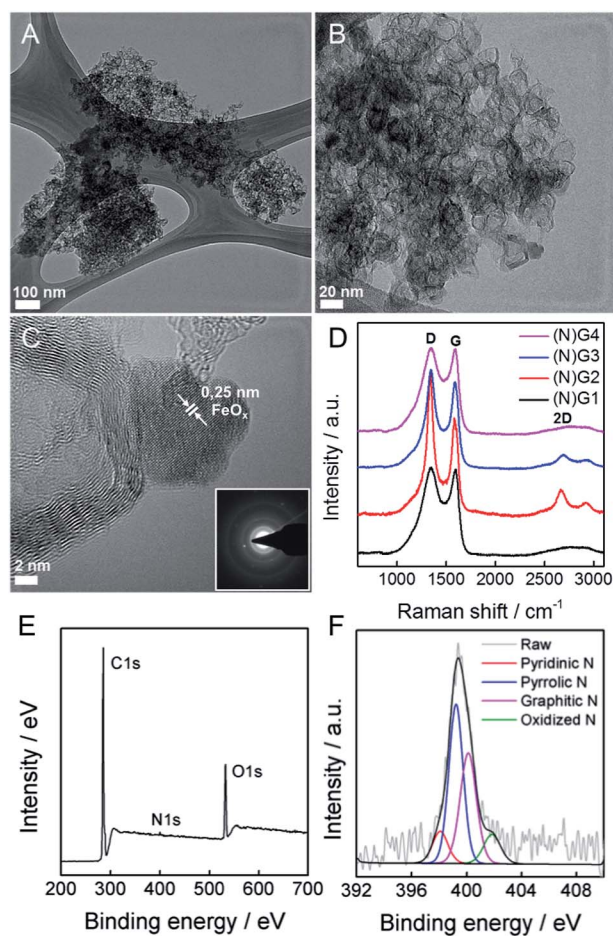


Fig. 3 (A–C) HRTEM of (N)G2, general overview and higher magnifications. The inset in (C) corresponds to the electron diffraction pattern. (D) Comparative Raman spectra. (E) XPS survey spectrum for (N)G2. (F) High-resolution N1s spectrum of (N)G2.

shows a rather different behaviour with poor graphitization and the formation of micrometric metal particles after the calcination process. In any case, further studies are required to deeply understand the metal functionalization of COFs and their effect on the catalytic graphitization.

To evaluate the presence of metal residues in the final (N)G-M samples, we have performed inductively coupled plasma-optical emission spectroscopy (ICP-OES) analysis, showing that the metal content is below 0.1% for all the samples (see SI 7†). This point was also corroborated by TG analysis in air, showing the absence of any residue after calcination at 1000 °C (SI 8†). As a matter of fact, after a careful inspection of (N)G2, it was possible to find some residual metal nanoparticles, as depicted in Fig. 3C. Based on the general lattice spacing between two adjacent planes observed in the HRTEM images, the small nanoparticle seems to correspond to crystalline FeO_x (Fig. 3C).¹⁴ Indeed, electron diffraction confirms the presence of the characteristic FeO_x patterns.

Surface analysis by XPS confirmed the predominant sp² character of all the graphitic samples (N)G2 being the sample with the highest C–C sp² proportion in agreement with XRD and Raman spectroscopy, *vide infra*, with binding energies of

284.6 ± 0.1 eV. Moreover, no metal signal was detected in any sample, in excellent accordance with the ICP-OES, EDX and TG experiments, highlighting that the presence of the catalytic metals is residual (see SI 9†). Nitrogen could be incorporated as “lattice N” within the carbon network or “chemical N” in the form of functional groups at the periphery of the graphene plane. The high-resolution N1s spectra peaking at *ca.* 400 eV shows the presence of nitrogen as a dopant in all the samples, with values in the 0.8–1.9% range, similar to other recently reported N-doped graphene or microporous carbon nanosheets (Fig. 3E and SI 9†).^{22,37} The deconvoluted peak reveals four different N types, *i.e.* pyridinic-N, pyrrolic-N, graphitic-N and pyridine-N-oxide groups, the pyridinic- and graphitic-type nitrogen being predominant for all the samples (Fig. 3F). Interestingly, (N)G2 exhibited the highest amount of pyridinic-N and pyrrolic-N compared to the rest of the samples, usually related to an increase in the capacitive contribution.³⁸ Moreover, FESEM-EDAX mappings were measured to further confirm the homogeneous distribution of nitrogen (SI 10†).

Raman spectroscopy was also used to evaluate the graphitic character of the samples. Characteristic G and D bands were observed at around 1585 and 1348 cm⁻¹, respectively, in good accordance with that expected for N-doped graphene. The *I*_D/*I*_G ratios exhibited similar values (1.0–1.3) for all the samples. Moreover, there is a splitting in the G band at *ca.* 1613 cm⁻¹ (D' band) in the spectrum of (N)G2 related to the increased disorder in the sp² content. Interestingly, the 2D band at *ca.* 2669 cm⁻¹ was only present in the (N)G2 and (N)G3 samples suggesting higher crystallinity, in excellent agreement with XPS measurements (Fig. 3D).^{22,25} This point was further confirmed by X-ray powder diffraction (SI 11†).

Textural characterization of the samples was performed using N₂ and CO₂ adsorption–desorption isotherms at 77 K and 273 K, respectively (see Fig. 4, Table 1 and SI 12–13† for complete porosity metrics).

The N₂ isotherms of (N)G1–(N)G4 exhibit combined characteristics of type II and type IV isotherms. The specific surface area was measured by the Brunauer–Emmett–Teller (BET) method showing values between *ca.* 844 and 1147 m² g⁻¹, remarkably higher than those of the pristine RT-COF-1 (329 m² g⁻¹) and the COF-1-M (620 m² g⁻¹).²¹ Interestingly, the sample (N)G2 exhibited the highest surface area (1147 m² g⁻¹) and pore volume (0.961 cm³ g⁻¹) in the series. The pore size distribution

(PSD) was analysed by quenched solid density functional theory (QSDFT; SI 13†), showing a narrow distribution of micropores of *ca.* 1 nm, as well as mesopores in the 4–30 nm range, probably related to the nanocavities originated by the corrugation of graphene, in agreement with the HRTEM observations. We also measured CO₂ adsorption at 273 K in order to evaluate the presence of narrow micropores (<0.7 nm). Also in this case (N)G2 exhibited the highest value (0.471 cm³ g⁻¹), with a narrow micropore contribution of *ca.* 50% of the total pore volume of the material. Interestingly, all the samples exhibited a larger micropore volume (*V*_{μ(<0.7 nm)}), obtained from the CO₂ adsorption data, than the total micropore volume (*V*_{μDR}) deduced from the N₂ isotherm. This phenomenon is typical of carbon molecular sieves, and clearly indicates the presence of narrow constrictions (pore opening below 0.4 nm), these kinetic restrictions being more detrimental for N₂ adsorption (77 K) compared to CO₂ (273 K).^{39,40} This hierarchical porosity can play a relevant role in the supercapacitive behaviour (*vide infra*).⁴¹

To illustrate the application of these materials in the field of supercapacitors, their electrochemical properties were evaluated in 6 M aqueous KOH using a three-electrode system. Fig. 5 shows typical cyclic voltammetry (CV) curves for the four graphitic materials from -1 to 0 V vs. Ag/AgCl at a scan rate of 50 mV s⁻¹. The CVs of the metal-functionalized samples ((N)G2–4) exhibit a rectangular-shape, even at 500 mV s⁻¹, indicative of a remarkable rate capability. This is more pronounced for the sample (N)G2, exhibiting the highest CV area. In turn, (N)G1 shows a triangular-like morphology indicative of a less-effective ion diffusion and the poorest conductivity (see SI 14†). According to Pumera and co-workers, the residual metal centers could play an important role, indeed the presence of transition metal traces on graphene could dramatically affect its electrochemical behavior.^{42,43} Along this front, we have also tested the samples under positive potential windows in order to determine whether the presence of metal residues (always below 0.1% as demonstrated by ICP-OES) has an influence or not (see SI 15†). Indeed, it is possible to observe the redox peaks arising from the cobalt and nickel traces, superimposed on that of the Ni-foam collector. This indicates that the presence of metal residues could contribute to the pseudocapacitance of the materials, despite the predominant character of the electrical double layer capacitance (EDLC) from the N-doped carbon matrix. The specific capacitance of the samples was analysed by means of galvanostatic charge/discharge measurements using several electrodes prepared from different batches in order to test the reliability of this synthesis route. From these experiments it is clear that the best performance was achieved for the (N)G2 sample under negative potentials, with an overall maximum specific capacitance of *ca.* 460 F g⁻¹ at 1 A g⁻¹, a value among the highest compared with those recently reported for related nitrogen-doped graphene-like materials or highly corrugated graphene flakes (Fig. 5C and D, SI 14†).^{8,25,44,45} It is worth to remark here the long tail exhibited at low discharge currents by (N)G2 and (N)G3, probably related to a pseudocapacitive effect as previously described for other N-doped carbons.⁴⁶ In any case, slight carbon degradation cannot be completely excluded. The (N)G3 and (N)G4 samples showed 160 and 125 F g⁻¹ at 1 A

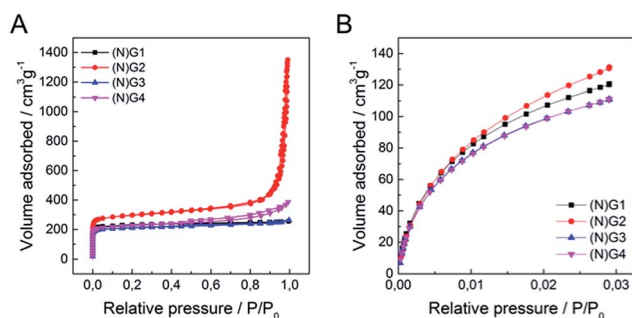


Fig. 4 (A) N₂ adsorption/desorption isotherms at 77 K of (N)G1–(N)G4, (B) CO₂ adsorption/desorption isotherms at 273 K of (N)G1–(N)G4.

Table 1 Textural parameters obtained from N₂ (77 K) and CO₂ (273 K) adsorption data

Sample	S_{BET}^a (m ² g ⁻¹)	V_t^b (cm ³ g ⁻¹)	$V_{\mu(<0.7 \text{ nm})}^c$ (cm ³ g ⁻¹)	$V_{\mu\text{DR}}^d$ (cm ³ g ⁻¹)	V_{meso}^e (cm ³ g ⁻¹)
(N)G1	927	0.959	0.413	0.354	0.605
(N)G2	1147	0.961	0.471	0.446	0.515
(N)G3	844	0.960	0.399	0.325	0.635
(N)G4	893	0.959	0.383	0.343	0.616

^a Data obtained from N₂-adsorption. Specific surface area calculated by the BET method. ^b Total pore volume at $P/P_0 = 0.96$. ^c Data obtained from CO₂-adsorption. Volume of narrow micropores (<0.7 nm) calculated according to the DR method. ^d Micropore volume calculated from N₂-adsorption using the DR method. ^e Mesopore volume was calculated as the difference of total (V_t) at $P/P_0 = 0.96$ and N₂ micropore volume ($V_{\mu\text{DR}}$).

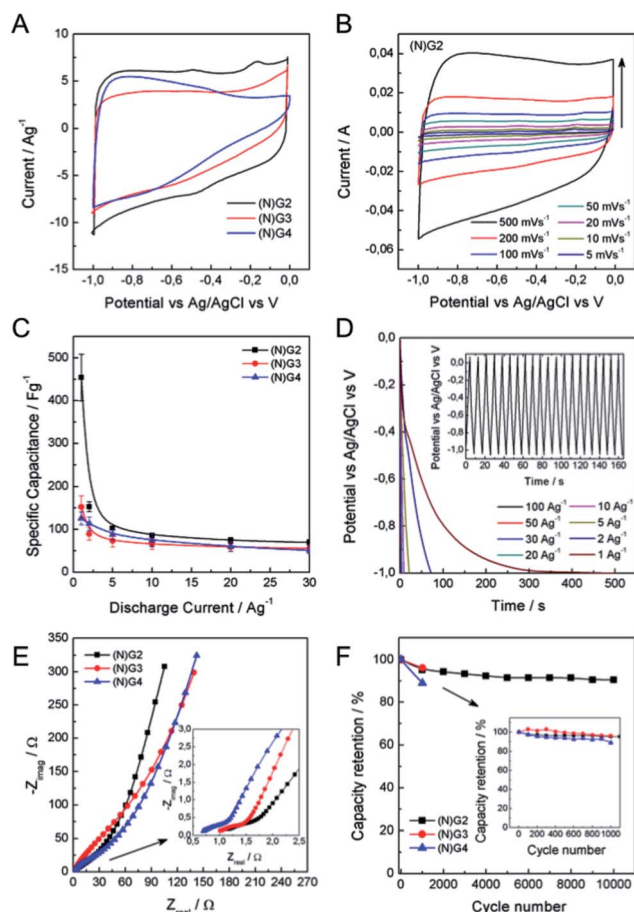


Fig. 5 Electrochemical measurements in a three-electrode cell configuration using 6M KOH aqueous solution. (A) Comparative CV of all the samples. (B) CV of (N)G2 at different scan rates. (C) Comparative specific capacitance of all the samples at different discharge current densities. (D) Galvanostatic discharge curves at different discharge current densities of (N)G2. The inset shows the stationary galvanostatic charge/discharge curves at a current density of 10 A g⁻¹. (E) Nyquist plots of (N)G2-4. The inset shows the expanded high frequency region. (F) Capacity retention of (N)G2 in 10 000 charge-discharge cycles. The inset shows the capacity retention of all samples after 1000 cycles.

g⁻¹, respectively (Fig. 5C). For positive potential windows we observed a maximum value of ca. 121 and 218 F g⁻¹ for (N)G3 and (N)G4, respectively (SI 15.7†). Interestingly, (N)G4 exhibited ca. 200 F g⁻¹ even at 30 A g⁻¹, highlighting the versatility of this route to create highly active materials.

In order to shed light on the excellent electrochemical behavior of these materials we have performed blank experiments showing the negligible contribution by the Ni-foam collector to the pseudocapacitance (see SI 16†). Moreover, we have studied the sample (N)G2 using a carbon felt collector showing a similar behavior, and exhibiting a maximum capacity of ca. 545 F g⁻¹ (see SI 17† for additional experimental information).

To further gain insights into the kinetic behavior of the different samples, we carried out electrochemical impedance spectroscopic (EIS) measurements (Fig. 5E). From the analysis of the Nyquist plots, (N)G2 displays a near vertical line compared to the other samples within the low-frequency region, indicative of a better capacitive behavior (vertical line for an ideal capacitor). The small semicircular shapes in the EIS plots in the high frequency region are related to the charge transfer resistance at the electrode/electrolyte interface (inset in Fig. 5E). All the samples exhibited similar small diameters suggesting low charge-transfer resistances, mainly attributed to the N-doping. Moreover, we have also evaluated the capacity retention of (N)G2 after 10,000 charge/discharge cycles, observing capacity retention values higher than 90%, indicative of good stability. Similar capacity retention values were observed for (N)G3-4 (Fig. 5F). It is worth noting that large measuring periods lead to partial loss of the active material from the Ni-foam.⁴⁷

The excellent properties of the (N)G2 material are attributed, on the one hand, to the presence of nitrogen atoms, which enhances the surface wettability by electrolytes and also improves the charge transfer of the electrode materials.^{16,48} On the other hand, the laminar hierarchical porous structure allows easy electrolyte penetration, efficiently exposing the active surface of graphene to the electrolyte.^{9,24} In fact, (N)G2 exhibited the highest specific surface area, micro- and mesopore volumes. It is worth mentioning that the contribution of pores smaller than the size of solvated electrolyte ions (narrow micropores) could play an important role favouring the increase of double-layer capacitance in carbons.⁴¹ Overall, all the studied techniques are in good agreement pointing towards (N)G2 as the best candidate of this family of materials for the development of supercapacitors.

It is well-known that a test fixture configuration, like a two-electrode cell, is more closely related to the performance of commercially available packaged cells.^{1,49} In this sense, we have developed a preliminary test of (N)G2 in symmetric two-electrode supercapacitors. We used directly assembled electrodes, KOH 6 M

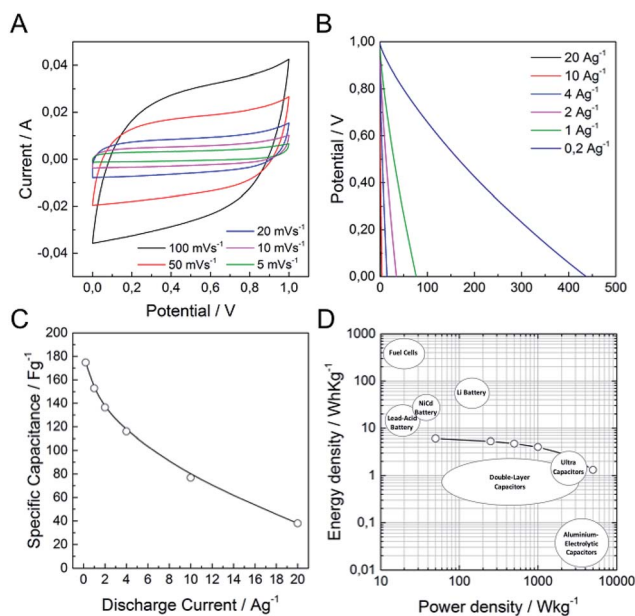


Fig. 6 Electrochemical measurements of (N)G2 in a symmetric two-electrode cell configuration using 6 M KOH aqueous solution. (A) CV at different scan rates. (B) Galvanostatic discharge curves at different current densities. (C) Specific capacitance at different discharge current densities. (D) Ragone plot of the supercapacitive device among various commercial energy-storage devices (source data from US Defense Logistics Agency).

as the aqueous electrolyte, and *ca.* 10 mg of active material in order to obtain reliable measurements.^{49,50} Fig. 6a shows the typical rectangular-shaped cyclic voltammograms at different scan rates ranging from 5 to 100 mV s^{-1} , and the corresponding galvanostatic discharge curves, showing an appropriate supercapacitive behavior. The maximum specific capacitance was 175 F g^{-1} at a current density of 0.2 A g^{-1} , *ca.* 38% of that obtained in the three-electrode cell configuration (Fig. 6c). Fig. 6d shows the Ragone plot of the (N)G2/(N)G2 symmetric supercapacitors in the potential range of 0–1 V. The supercapacitive device could deliver a maximum energy density of 6.1 W h kg^{-1} , with a corresponding power density of 50 W kg^{-1} . In addition, when the current density increases to 20 A g^{-1} , the maximum power density is 5000 W kg^{-1} . These values compare favorably with other recently reported carbon-based symmetric supercapacitors working in alkaline solutions using the same electrochemical window.^{50–54} It is worth to remark here that additional device optimization efforts to extract the full potential of these materials are currently on going in our labs. This includes: different cell configurations, the use of other electrolytes to improve the cell voltage, or modification of the electrode contact, mass and thickness. Finally, to illustrate the performance of our system, we used two (N)G2/(N)G2 devices connected in series as the power supply for a commercial green light-emitting diode (see SI 18[†]).

Conclusions

The fact that the COF-1-M materials incorporate metal ions (Fe^{III} , Co^{II} and Ni^{II}) into the cavities of their laminar structures

favours corrugated graphene formation upon controlled thermal treatment. In this sense, the structure, morphology and disposition of the COF precursor lead to the formation of a hierarchical N-doped porous structure. This strategy avoids the need for the use of any additional template, allowing the formation of corrugated graphene in a one-pot reaction from the COF-1-M precursors. These materials exhibited a promising behaviour as electrode materials in supercapacitors. Concretely, the Fe derivative ((N)G2) shows an overall specific capacity of *ca.* 460 F g^{-1} at a current density of 1 A g^{-1} . This work paves the way for the development of highly corrugated N-doped porous graphene of great interest not only in supercapacitors, but also as Oxygen Reduction Reaction (ORR) electrocatalysts or in Li-ion batteries.

Experimental information

Materials

1,3,5-Benzenetricarboxaldehyde was obtained from Manchester Organics. 1,3,5-Tris-(4'-aminophenyl)benzene was prepared according to literature procedures.²¹ Other chemicals and solvents were obtained from Aldrich Chemical Co. and used without further purification unless specified.

Synthesis

Synthesis of COF-1. 100 mg (0.285 mmol) of 1,3,5-tris-(4'-aminophenyl)benzene was dissolved in 5 mL of *m*-cresol. 46.1 mg (0.285 mmol) of 1,3,5-benzenetricarboxaldehyde was dissolved in another 5 mL of *m*-cresol and 1 mL of acetic acid. Both solutions were mixed at room temperature and a yellow gel was formed, it was allowed to react for additional 30 min. The gel was repeatedly washed with methanol and THF and dried in vacuum at $100 \text{ }^\circ\text{C}$ for 24 h to yield 126 mg (96%) of COF-1 as a yellow solid. Elemental analysis calculated for $\text{C}_{33}\text{H}_{26}\text{N}_3\text{O}_{2.5}$: C: 78.47%, H: 5.29%, N: 8.32%. Found: C: 78.59%, H: 4.91%, N: 8.57%.

Synthesis of COF-1-M. 100 mg (0.285 mmol) of 1,3,5-tris-(4'-aminophenyl)benzene was dissolved in 5 mL of *m*-cresol. 46.1 mg (0.285 mmol) of 1,3,5-benzenetricarboxaldehyde was dissolved in another 5 mL of *m*-cresol and 1 mL of acetic acid. Both solutions were mixed at room temperature and a yellow gel (COF-1) was formed, it was allowed to react for additional 30 min. Then the material was vigorously stirred in 52 mL of a 0.011 mol L^{-1} methanol solution of the corresponding $\text{M}(\text{acac})_n$ ($\text{M} = \text{Fe}, \text{Co}, \text{Ni}$, acac = acetylacetonate, $n = 3$ for Fe and 2 for Co, Ni). After 24 h it was filtered, washed with methanol and THF and dried in vacuum at $100 \text{ }^\circ\text{C}$ for 24 h. The yields obtained were: COF-1-Fe: 129 mg (97%); COF-1-Co: 131 mg (99%); COF-1-Ni: 115 mg (88%). Elemental analysis calculated for $\text{C}_{33}\text{H}_{26}\text{N}_3\text{O}_{2.5}$: C: 78.47%, H: 5.29%, N: 8.32%. Found for COF-1-Fe: C: 80.58%, H: 4.87%, N: 8.20%. Found for COF-1-Co: C: 80.52%, H: 5.21%, N: 7.83%. Found for COF-1-Ni: C: 81.09%, H: 5.25%, N: 8.72%.

Synthesis of N-doped graphene. (N)G1 from COF-1 and (N)G2-4 from COF-1-M ($\text{M} = \text{Fe}$ (2), Co (3), Ni (4)). COF-1 and COF-1-M were pyrolyzed in a N_2 atmosphere at $900 \text{ }^\circ\text{C}$ for 4 h in

a programmable oven with a heating ramp of $2\text{ }^{\circ}\text{C min}^{-1}$ and a N_2 flux of 100 mL min^{-1} . N-doped graphene is obtained as a black powder with yields in the range of 56–68%.

Physical characterization

Carbon, nitrogen and hydrogen contents were determined by microanalytical procedures by using a LECO CHNS-932.

The atomic composition of bulk samples was determined by means of electron probe microanalysis performed in a Philips SEM-XL30 equipped with an EDAX microprobe.

HRTEM studies of the hybrid material were carried out on a JEM-2010 microscope (JEOL, Japan) operating at 200 kV. Samples were prepared by dropping a sonicated suspension of the material in ethanol on a carbon-coated copper grid. The digital analysis of the HRTEM images was done using a Digital Micrograph 1.80.70 for GMS 1.8.0 by Gatan.

FESEM studies were performed on a Hitachi S-4800 microscope operating at an accelerating voltage of 20 kV and without metallization of the samples.

ATR-FT-IR spectra were recorded on a Perkin Elmer Spectrum 100 with a universal ATR accessory with a spectral range of $4000\text{--}650\text{ cm}^{-1}$.

Total reflection X-ray fluorescence was performed on a Bruker TXRF S2 PICOFOX spectrometer at 50 kV and 600 mA, with an acquisition time of 500 s and 10 ppm of vanadium as the internal standard.

High resolution solid-state nuclear magnetic resonance (NMR) spectra were recorded at ambient pressure on a Bruker AV 400 WB spectrometer using a triple channel (BL4 X/Y/1H) and Bruker magic angle-spinning (MAS) probe with 4 mm (outside diameter) zirconia rotors. The magic angle was adjusted by maximizing the number and amplitudes of the signals of the rotational echoes observed in the ^{79}Br MAS FID signal from KBr. Cross-polarization with MAS (CP-MAS) was used to acquire ^{13}C data at 100.61 MHz. The ^1H ninety degree pulse widths were both $3.1\text{ }\mu\text{s}$. The CP contact time varied from 3.5 ms. High power two-pulse phase modulation (TPPM) ^1H decoupling was applied during data acquisition. The decoupling frequency corresponded to 80 kHz. The MAS sample spinning rate was 10 kHz. Recycle delays between scans were 4 s, depending upon the compound as determined by observing no apparent loss in the ^{13}C signal from one scan to the next. The ^{13}C chemical shifts are given relative to tetramethylsilane as zero ppm, calibrated using the methylene carbon signal of adamantane assigned to 29.5 ppm as the secondary reference.

Grazing incidence X-ray diffraction (GIXRD) measurements were carried out using COF-1 and COF-1-Fe deposited on SiO_2/Si wafer at an XRD1-ELETTRA beamline at Trieste's synchrotron facility (Italy) using a monochromatic beam with a wavelength of $1\text{ }\text{\AA}$ and size of $\text{HxV} = (200 \times 200)\text{ }\mu\text{m}^2$. 2D-GIXRD images were collected using a 2D camera (Pilatus detector) placed normal to the incident beam at a distance of 200 mm. Several images were collected by translating the sample 0.5 mm in a direction perpendicular to the beam to probe the sample homogeneity.

Thermogravimetric analysis (TGA) of the composite was carried out with a Mettler Toledo TGA/SDTA 851 apparatus in

the $25\text{--}900\text{ }^{\circ}\text{C}$ temperature range at a $2\text{ }^{\circ}\text{C min}^{-1}$ scan rate and under a nitrogen flow of 100 mL min^{-1} .

XRPD patterns of COF-1-Co and COF-1-Ni were collected with a Bruker D8 Advance X-ray diffractometer ($\text{Cu-K}\alpha$ radiation; $\lambda = 1.5418\text{ }\text{\AA}$) equipped with a Lynxeye detector. Samples were mounted on a flat sample plate. Patterns were collected in the $3.5^{\circ} < 2\theta < 35^{\circ}$ range with a step size of 0.016° and exposure time of 0.8 s per step.

XRPD patterns of (N)G1-4 were collected with a Siemens d-500 X-ray diffractometer ($\text{Cu-K}\alpha$ radiation; $\lambda = 1.5418\text{ }\text{\AA}$) equipped with a rotating anode D-max Rigaku operating at 80 mA and 45 kV. Samples were mounted on a flat sample plate. Profiles were collected in the $2.5^{\circ} < 2\theta < 70^{\circ}$ range with a step size of 0.05° .

Confocal fluorescence imaging was performed on an inverted Nikon A1 laser scanning confocal microscope equipped with a CW argon ion laser for excitation at 457, 488 and 514 nm (Melles Griot, 40 mW), and a diode laser for excitation at 405 nm (LDH-D-C-405 of Picoquant GmbH Berlin, Germany) operating both in continuous mode (50 mW) and pulsed at 40 MHz (1.0 mW average power for pulse FWHM of 70 ps). Confocal fluorescence imaging was carried out on the samples at room temperature. The images were collected using a Nikon PLAN APO VC $20\times$ NA 0.75 objective or a Nikon PLAN APO VC $60\times$ NA 1.40 oil immersion objective. Images of 512×512 have been acquired applying a scan speed of 1 frame in 1–4 s and the pixel dimension of the xy plane falls in the range $0.21\text{--}0.4\text{ }\mu\text{m}$. Hexagonal pinhole dimension was set to 1.0 au corresponding to $38\text{ }\mu\text{m}$ and optical thickness of 440 nm. A dichroic mirror reflecting 405, 488, 541 and 640 nm was used. Bandpass filters in front of the PMT selected fluorescence in the ranges of 500–550 and 560–615 nm. Spectral imaging was done with a Nikon 32-PMT array detector with resolution varying from 6 to 10 nm per channel. For fluorescence lifetime imaging a time-correlated single photon counting (TCSPC) system of Picoquant GmbH Berlin was used exciting at 405 nm. Photons were detected in TTTR mode with two Single Photon Avalanche Diodes manufactured by Micro Photon Devices (MPD), Bolzano, Italy. Fluorescence was filtered with the opportune fluorescence SEMROCK bandpass filter 520/40 nm. A PicoHarp 300 photon processor completes the TCSPC system. SymPhoTime v. 5.1 analysis software was used for image processing and lifetime fitting. A tail fit with multi-exponential functions was performed to analyze fluorescence decays of selected ROI. The system allowed measurement of fluorescence lifetimes from 300 ps up to several nanoseconds. Elemental analysis was performed in the Universidad Complutense de Madrid (CAI de Técnicas Geológicas) by inductively coupled-plasma optical emission spectroscopy (ICP-OES) on solutions prepared by treating the samples in a nitric acid/hydrochloric acid mixture in a Teflon reactor.

The Raman measurements (Jobin-Yvon LabRam HR 800 Raman Microscope) were carried out at room temperature with the 532 nm line of an Ar ion laser as an excitation source.

The porous texture of all the materials prepared was characterized by N_2 adsorption at 77 K and CO_2 at 273 K using an AUTOSORB-6 apparatus. Samples were degassed for 8 hours at

523 K and 5×10^{-5} bar prior to analysis. Surface areas were estimated according to the BET model, and pore size dimensions were calculated by the solid density functional theory (QSDFT) for the adsorption branch assuming a cylindrical pore model. The micropore volumes were determined by applying t -plot and DR methods to the N_2 and CO_2 adsorption data.

Electrochemical characterization

For the electrochemical measurements a mixture of acetylene black and PVDF in ethanol in a mass ratio of 80 : 10 : 10 was prepared and deposited on a nickel foam electrode. The as-prepared nickel foam electrodes were dried overnight at 80 °C and pressed. Each working electrode contained about 1 mg of electroactive material and had a geometric surface area of about 1 cm². A typical three-electrode experimental cell equipped with a steel sheet as the counter electrode and a Metrohm Ag/AgCl (3 M KCl) as the reference electrode was used for the electrochemical characterization of the nanocomposite materials trapped by the working electrodes. All the electrochemical measurements were carried out in 6 M KOH (99.99%) aqueous solutions as the electrolyte. Ultrapure water was obtained from Milli-Q equipment. All the electrochemical experiments were performed at room temperature using an AUTOLAB PGSTAT 128N potentiostat–galvanostat controlled by Nova 2.0 electrochemical. The specific capacitance (C) was calculated from the cyclic chronopotentiometric curves according to eqn (1):

$$C = I\Delta t/m\Delta V \quad (1)$$

where I is the charge/discharge current, Δt is the time for a full charge or discharge, m the weight in grams of the active material in the electrode layer, and ΔV is the voltage change after a full charge or discharge.

A two-electrode symmetric supercapacitor was assembled using a Swagelok cell, with a pellet consisting of a mixture of (N) G2 and Teflon (9 : 1 proportion) as positive and negative electrodes. The average mass of each electrode was about 5 mg of active material. The employed electrolyte was aqueous 6 M KOH, and a cellulose membrane was used for separating the electrodes. The test voltage range was optimized to 0–1 V. All the electrochemical tests were carried out at room temperature using a GAMRY 5000E potentiostat–galvanostat controlled by Gamry Software. The specific capacitance was calculated according to the following equation:

$$C_s = \frac{2 \times I \times \Delta t}{m \times \Delta V} \quad (2)$$

where C_s (F g⁻¹) is the specific capacitance, I (A) the discharge current, Δt (s) the discharge time, and ΔV (V) the voltage window. The energy density, E (W h kg⁻¹), and the power density, P (W kg⁻¹), were estimated by using the following expressions, normalizing to the mass of two carbon electrodes:

$$E = \frac{C_s \times \Delta V^2}{8 \times 3.6} \quad (3)$$

$$P = \frac{E}{\Delta t} \quad (4)$$

where ΔV (V) is the voltage used for the measurement and Δt (h) is the corresponding discharge time.

Acknowledgements

We are grateful to the EU (FET-OPEN 2D-INK, grant agreement 648786), the Spanish MINECO (Projects MAT2016-77608-C3-1-P, MAT-2014-56143-R, CTQ-2014-59209-P, FEDER-MAT2012-38318-C03 and Excellence Unit Maria de Maeztu, MDM-2015-0538), and the Generalitat Valenciana (Prometeo Program and ISIC-Nano). Support from the INNOCIDE program through Vicerectorat d'Investigació i Política Científica of the University of Valencia is also acknowledged. J. R. and D. R. thank the Spanish MECED for FPI and FPU grants, respectively. G. A. thanks the EU for a Marie Curie Fellowship (FP7/2013-IEF-627386). Dedicated to Prof. Nazario Martín on the occasion of his 60th birthday.

Notes and references

- 1 F. Beguin and E. Frackowiak, *Supercapacitors: Materials, Systems and Applications*, John Wiley & Sons, 2013.
- 2 G. Wang, L. Zhang and J. Zhang, *Chem. Soc. Rev.*, 2012, **41**, 797–828.
- 3 X. Li and B. Wei, *Nano Energy*, 2013, **2**, 159–173.
- 4 A. C. Ferrari, F. Bonaccorso, V. Fal'ko, K. S. Novoselov, S. Roche, P. Bøggild, S. Borini, F. H. L. Koppens, V. Palermo, N. Pugno, J. A. Garrido, R. Sordan, A. Bianco, L. Ballerini, M. Prato, E. Lidorikis, J. Kivioja, C. Marinelli, T. Ryhänen, A. Morpurgo, J. N. Coleman, V. Nicolosi, L. Colombo, A. Fert, M. Garcia-Hernandez, A. Bachtold, G. F. Schneider, F. Guinea, C. Dekker, M. Barbone, Z. Sun, C. Galiotis, A. N. Grigorenko, G. Konstantatos, A. Kis, M. Katsnelson, L. Vandersypen, A. Loiseau, V. Morandi, D. Neumaier, E. Treossi, V. Pellegrini, M. Polini, A. Tredicucci, G. M. Williams, B. H. Hong, J.-H. Ahn, J. M. Kim, H. Zirath, B. J. van Wees, H. van der Zant, L. Occhipinti, A. D. Matteo, I. A. Kinloch, T. Seyller, E. Quesnel, X. Feng, K. Teo, N. Rupesinghe, P. Hakonen, S. R. T. Neil, Q. Tannock, T. Löfwander and J. Kinaret, *Nanoscale*, 2015, **7**, 4598–4810.
- 5 J. Yan, Z. Fan, W. Sun, G. Ning, T. Wei, Q. Zhang, R. Zhang, L. Zhi and F. Wei, *Adv. Funct. Mater.*, 2012, **22**, 2632–2641.
- 6 G. Ning, Z. Fan, G. Wang, J. Gao, W. Qian and F. Wei, *Chem. Commun.*, 2011, **47**, 5976–5978.
- 7 K. Xie, X. Qin, X. Wang, Y. Wang, H. Tao, Q. Wu, L. Yang and Z. Hu, *Adv. Mater.*, 2012, **24**, 347–352.
- 8 J. Yan, J. Liu, Z. Fan, T. Wei and L. Zhang, *Carbon*, 2012, **50**, 2179–2188.
- 9 Y. Li, Z. Li and P. K. Shen, *Adv. Mater.*, 2013, **25**, 2474–2480.
- 10 G. Abellán, E. Coronado, C. Martí-Gastaldo, A. Ribera and T. F. Otero, *Part. Part. Syst. Charact.*, 2013, **30**, 853–863.
- 11 G. Abellán, J. G. Martínez, T. F. Otero, A. Ribera and E. Coronado, *Electrochem. Commun.*, 2014, **39**, 15–18.

- 12 G. Abellán, C. Martí-Gastaldo, A. Ribera and E. Coronado, *Acc. Chem. Res.*, 2015, **48**, 1601–1611.
- 13 G. Abellán, E. Coronado, C. Martí-Gastaldo, A. Ribera and J. F. Sánchez-Royo, *Chem. Sci.*, 2012, **3**, 1481–1485.
- 14 G. Abellan, J. A. Carrasco, E. Coronado, J. P. Prieto-Ruiz and H. Prima-García, *Adv. Mater. Interfaces*, 2014, **1**, 1400184.
- 15 R. Liu, D. Wu, X. Feng and K. Müllen, *Angew. Chem., Int. Ed.*, 2010, **49**, 2565–2569.
- 16 L. Zhang, Z. Su, F. Jiang, L. Yang, J. Qian, Y. Zhou, W. Li and M. Hong, *Nanoscale*, 2014, **6**, 6590–6602.
- 17 A. P. Côté, A. I. Benin, N. W. Ockwig, M. O'Keeffe, A. J. Matzger and O. M. Yaghi, *Science*, 2005, **310**, 1166–1170.
- 18 C. R. DeBlase, K. E. Silberstein, T.-T. Truong, H. D. Abruña and W. R. Dichtel, *J. Am. Chem. Soc.*, 2013, **135**, 16821–16824.
- 19 C. R. DeBlase, K. Hernández-Burgos, K. E. Silberstein, G. G. Rodríguez-Calero, R. P. Bisbey, H. D. Abruña and W. R. Dichtel, *ACS Nano*, 2015, **9**, 3178–3183.
- 20 S.-Y. Ding and W. Wang, *Chem. Soc. Rev.*, 2013, **42**, 548–568.
- 21 A. de la Peña Ruigómez, D. Rodríguez-San-Miguel, K. C. Stylianou, M. Cavallini, D. Gentili, F. Liscio, S. Milita, O. M. Roscioni, M. L. Ruiz-González, C. Carbonell, D. Maspoeh, R. Mas-Ballesté, J. L. Segura and F. Zamora, *Chem.–Eur. J.*, 2015, **21**, 10666–10670.
- 22 H. Wang, T. Maiyalagan and X. Wang, *ACS Catal.*, 2012, **2**, 781–794.
- 23 Z. Wen, X. Wang, S. Mao, Z. Bo, H. Kim, S. Cui, G. Lu, X. Feng and J. Chen, *Adv. Mater.*, 2012, **24**, 5610–5616.
- 24 X. Zhuang, F. Zhang, D. Wu and X. Feng, *Adv. Mater.*, 2014, **26**, 3081–3086.
- 25 H. Peng, G. Ma, K. Sun, Z. Zhang, Q. Yang, F. Ran and Z. Lei, *J. Mater. Chem. A*, 2015, **3**, 13210–13214.
- 26 Z. Xiang, D. Cao, L. Huang, J. Shui, M. Wang and L. Dai, *Adv. Mater.*, 2014, **26**, 3315–3320.
- 27 M. Barrejón, A. Primo, M. J. Gómez-Escalonilla, J. L. G. Fierro, H. García and F. Langa, *Chem. Commun.*, 2015, **51**, 16916–16919.
- 28 S.-Y. Ding, J. Gao, Q. Wang, Y. Zhang, W.-G. Song, C.-Y. Su and W. Wang, *J. Am. Chem. Soc.*, 2011, **133**, 19816–19822.
- 29 S. B. Kalidindi, H. Oh, M. Hirscher, D. Esken, C. Wiktor, S. Turner, G. Van Tendeloo and R. A. Fischer, *Chem.–Eur. J.*, 2012, **18**, 10848–10856.
- 30 J.-Q. Wang, L. Huang, M. Xue, Y. Wang, L. Gao, J. H. Zhu and Z. Zou, *J. Phys. Chem. C*, 2008, **112**, 5014–5022.
- 31 E. Hao, T. Meng, M. Zhang, W. Pang, Y. Zhou and L. Jiao, *J. Phys. Chem. A*, 2011, **115**, 8234–8241.
- 32 S. Shobana, P. Subramaniam, L. Mitu, J. Dharmaraja and S. Arvind Narayan, *Spectrochim. Acta, Part A*, 2015, **134**, 333–344.
- 33 J. Nandre, S. Patil, P. Patil, S. Sahoo, C. Redshaw, P. Mahulikar and U. Patil, *J. Fluoresc.*, 2014, **24**, 1563–1570.
- 34 F. J. Maldonado-Hódar, C. Moreno-Castilla, J. Rivera-Utrilla, Y. Hanzawa and Y. Yamada, *Langmuir*, 2000, **16**, 4367–4373.
- 35 W. Gao, Y. Wan, Y. Dou and D. Zhao, *Adv. Energy Mater.*, 2011, **1**, 115–123.
- 36 M. Sevilla and A. B. Fuertes, *ACS Nano*, 2014, **8**, 5069–5078.
- 37 Z.-Y. Jin, A.-H. Lu, Y.-Y. Xu, J.-T. Zhang and W.-C. Li, *Adv. Mater.*, 2014, **26**, 3700–3705.
- 38 F. M. Hassan, V. Chabot, J. Li, B. K. Kim, L. Ricardez-Sandoval and A. Yu, *J. Mater. Chem. A*, 2013, **1**, 2904–2912.
- 39 R. V. R. A. Rios, J. Silvestre-Albero, A. Sepúlveda-Escribano, M. Molina-Sabio and F. Rodríguez-Reinoso, *J. Phys. Chem. C*, 2007, **111**, 3803–3805.
- 40 A. Wahby, J. M. Ramos-Fernández, M. Martínez-Escandell, A. Sepúlveda-Escribano, J. Silvestre-Albero and F. Rodríguez-Reinoso, *ChemSusChem*, 2010, **3**, 974–981.
- 41 J. Chmiola, G. Yushin, Y. Gogotsi, C. Portet, P. Simon and P. L. Taberna, *Science*, 2006, **313**, 1760–1763.
- 42 A. Ambrosi, C. K. Chua, B. Khezri, Z. Sofer, R. D. Webster and M. Pumera, *Proc. Natl. Acad. Sci. U. S. A.*, 2012, **109**, 12899–12904.
- 43 L. Wang, A. Ambrosi and M. Pumera, *Angew. Chem., Int. Ed.*, 2013, **52**, 13818–13821.
- 44 H. M. Jeong, J. W. Lee, W. H. Shin, Y. J. Choi, H. J. Shin, J. K. Kang and J. W. Choi, *Nano Lett.*, 2011, **11**, 2472–2477.
- 45 T. Lin, I.-W. Chen, F. Liu, C. Yang, H. Bi, F. Xu and F. Huang, *Science*, 2015, **350**, 1508–1513.
- 46 T. Akhter, M. M. Islam, S. N. Faisal, E. Haque, A. I. Minett, H. K. Liu, K. Konstantinov and S. X. Dou, *ACS Appl. Mater. Interfaces*, 2016, **8**, 2078–2087.
- 47 G. Abellán, J. A. Carrasco, E. Coronado, J. Romero and M. Varela, *J. Mater. Chem. C*, 2014, **2**, 3723–3731.
- 48 L. Sun, L. Wang, C. Tian, T. Tan, Y. Xie, K. Shi, M. Li and H. Fu, *RSC Adv.*, 2012, **2**, 4498.
- 49 M. D. Stoller and R. S. Ruoff, *Energy Environ. Sci.*, 2010, **3**, 1294.
- 50 J. Patiño, N. López-Salas, M. C. Gutiérrez, D. Carriazo, M. L. Ferrer and F. del Monte, *J. Mater. Chem. A*, 2016, **4**, 1251–1263.
- 51 D.-W. Wang, F. Li, M. Liu, G. Q. Lu and H.-M. Cheng, *Angew. Chem. Int. Ed.*, 2008, **120**, 379–382.
- 52 Z. Lei, Z. Liu, H. Wang, X. Sun, L. Lu and X. S. Zhao, *J. Mater. Chem. A*, 2013, **1**, 2313–2321.
- 53 X. Huang, Q. Wang, X. Y. Chen and Z. J. Zhang, *J. Electroanal. Chem.*, 2015, **748**, 23–33.
- 54 Y. Li and D. Zhao, *Chem. Commun.*, 2015, **51**, 5598–5601.

Supplementary Information

Layered Metal-functionalized Covalent Organic Frameworks as Precursors of Supercapacitive Porous N-doped Graphene

Jorge Romero,^{a,‡} David Rodriguez-San-Miguel,^{b,c,‡} Antonio Ribera,^a Rubén Mas-
Ballesté,^b Toribio F. Otero,^d Ilse Manet,^e Fabiola Licio,^f Gonzalo Abellán,^{*a,g} Felix
Zamora,^{*b,c} and Eugenio Coronado^{*a}

- a. Instituto de Ciencia Molecular (ICMol), Universidad de Valencia, 46980 Paterna, Spain. E-mail: eugenio.coronado@uv.es.
- b. Departamento de Química Inorgánica y Condensed Matter Physics Center (IFIMAC), Universidad Autónoma de Madrid, Madrid, Spain. E-mail: felix.zamora@uam.es.
- c. Instituto Madrileño de Estudios Avanzados en Nanociencia (IMDEA Nanociencia) 28049 Madrid (Spain).
- d. Center for Electrochemistry and Intelligent Materials (CEMI), Universidad Politécnica de Cartagena, Cartagena, Spain.
- e. Consiglio Nazionale delle Ricerche - Istituto per la Sintesi Organica e la Fotoreattività (CNR-ISOF), Via Gobetti 101, 40129 Bologna (Italy).
- f. CNR-IMM, Istituto per la Microelettronica e Microsistemi, via P. Gobetti 101, I-40129 Bologna (Italy).
- g. Department of Chemistry and Pharmacy and Joint Institute of Advanced Materials and Processes (ZMP), University Erlangen-Nürnberg, Henkestr. 42, 91054 Erlangen and Dr.-Mack Str. 81, 90762 Fürth, Germany.

Contents

SI 1. Solid state ^{13}C NMR of **COF-1**

SI 2. FT-IR of **COF-1** and **COF-1-M**

SI 3. XRD of **COF-1-Co** and **COF-1-Ni**

SI 4. Confocal fluorescence microscopy

SI 5. Thermogravimetric analysis of **COF-1** and **COF-1-M** under N_2 atmosphere

SI 6. HRTEM microscopy of **(N)G1-4**

SI 7. ICP-OES analysis of **(N)G2-4**

SI 8. Thermogravimetric analysis of **(N)G1-4** in air

SI 9. XPS of **(N)G1-4**

SI 10. FESEM microscopy of **(N)G2**

SI 10.1 EDAX microanalysis

SI 10.2 Mapping of carbon and nitrogen

SI 11. XRPD of **(N)G1-4**

SI 12. Nitrogen adsorption data of **COF-1**

SI 13. Textural parameters of **(N)G1-4**

SI 14. Electrochemical properties of **(N)G1-4** at negative potentials.

SI 15. Electrochemical properties of **(N)G2-4** at positive potentials.

SI 16. Electrochemical study of pristine Ni-foam and carbon felt collectors.

SI 17. Electrochemical study of **(N)G2-4** using carbon felt collectors.

SI 18. Symmetric two-electrode supercapacitor as power supply of green LED.

SI 1. Solid state ^{13}C -NMR of COF-1.

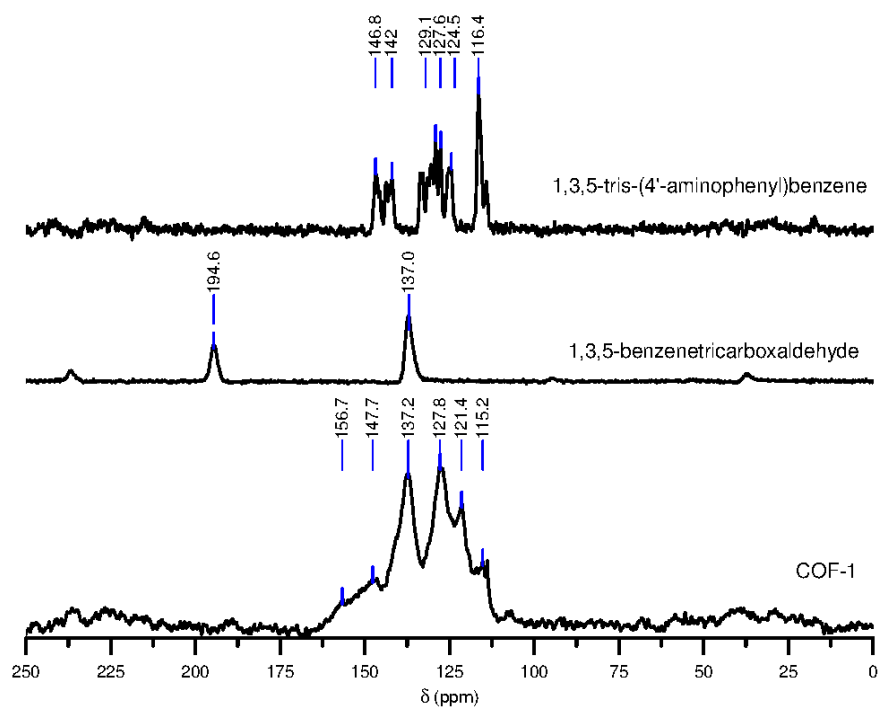


Figure SI 1.1. Stack plot of the ^{13}C NMR spectra of COF-1 and its monomers.

SI 2. FT-IR of COF-1 and COF-1-M

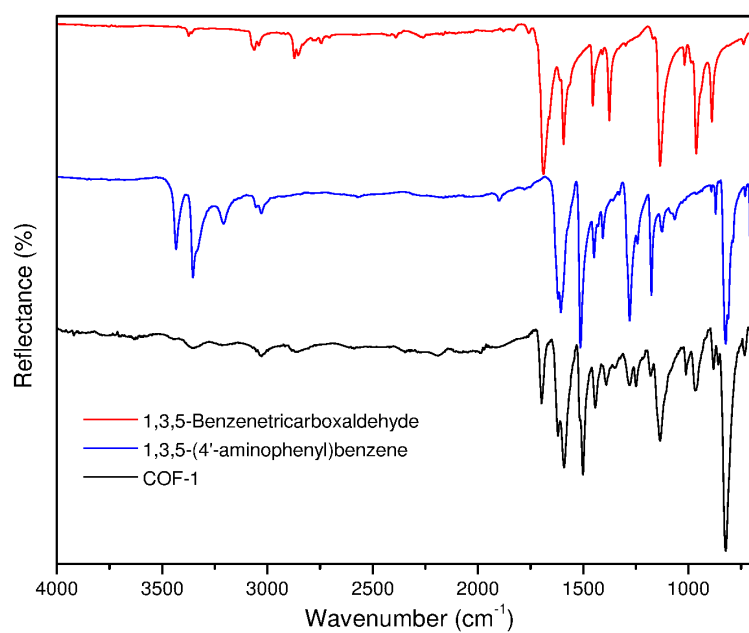


Figure SI 2.1. Stack plot of the ATR-FT-IR spectra of **COF-1** and its monomers.

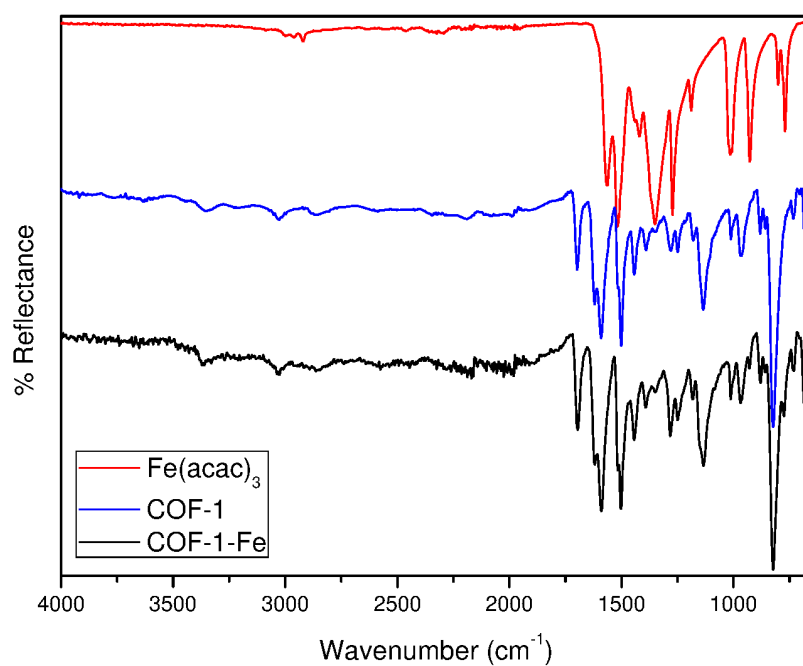


Figure SI 2.2. Stack plot of the ATR-FT-IR spectra of **COF-1**, Fe(acac)₃ and **COF-1-Fe**.

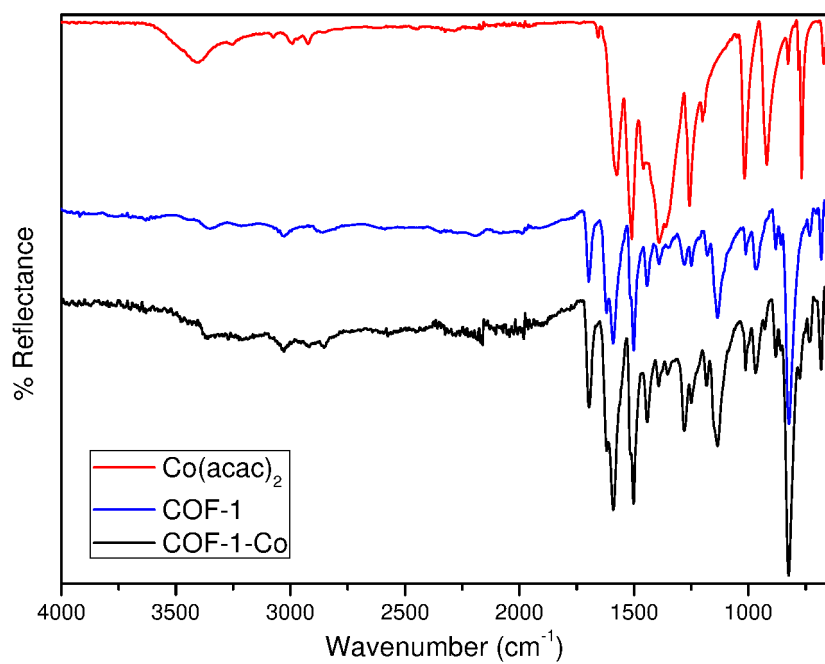


Figure SI 2.3. Stack plot of the ATR-FT-IR spectra of **COF-1**, **Co(acac)₂** and **COF-1-Co**.

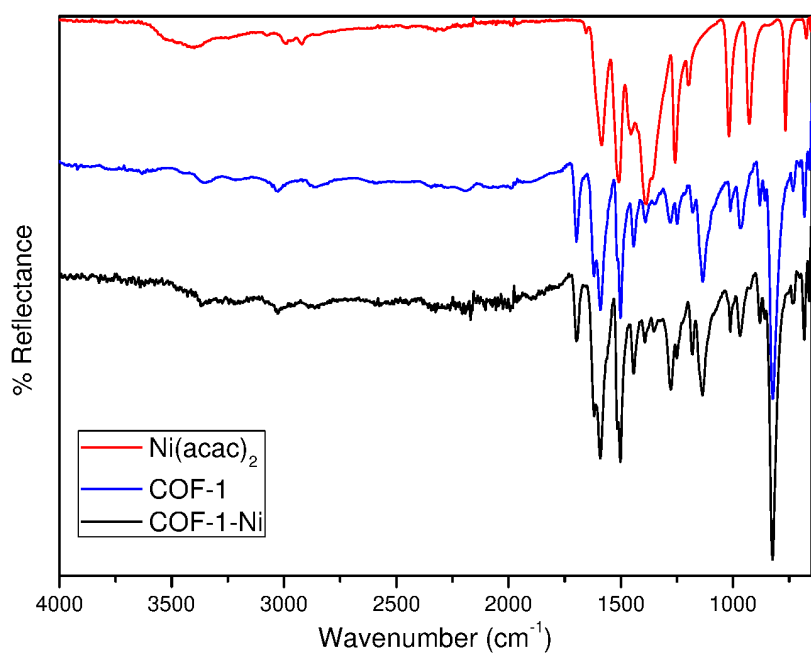


Figure SI 2.4. Stack plot of the ATR-FT-IR spectra of **COF-1**, **Ni(acac)₂** and **COF-1-Ni**.

SI 3. XRD of COF-1-Co and COF-1-Ni.

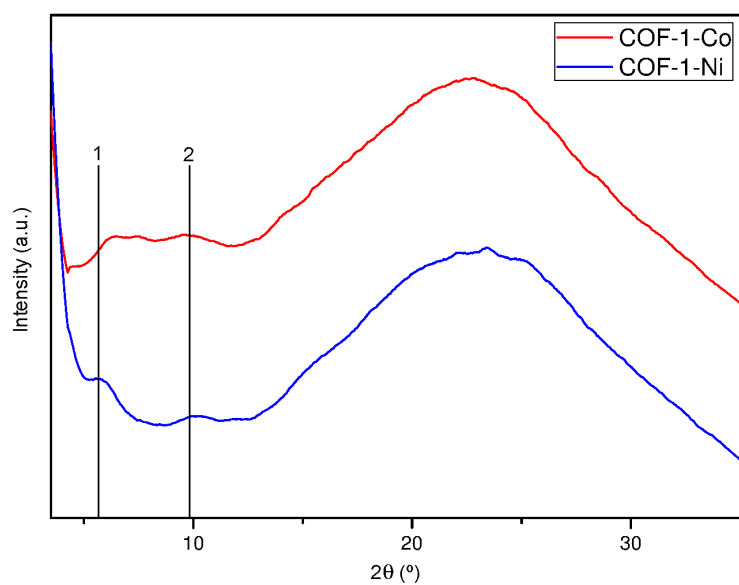


Figure SI 3.1. Stack plot of the XRD patterns of **COF-1-Co** and **COF-1-Ni**. Lines 1 and 2 mark the position of the two most characteristic diffraction peaks of **COF-1**, as shown in **Figure 2c**.

SI 4. Confocal fluorescence microscopy

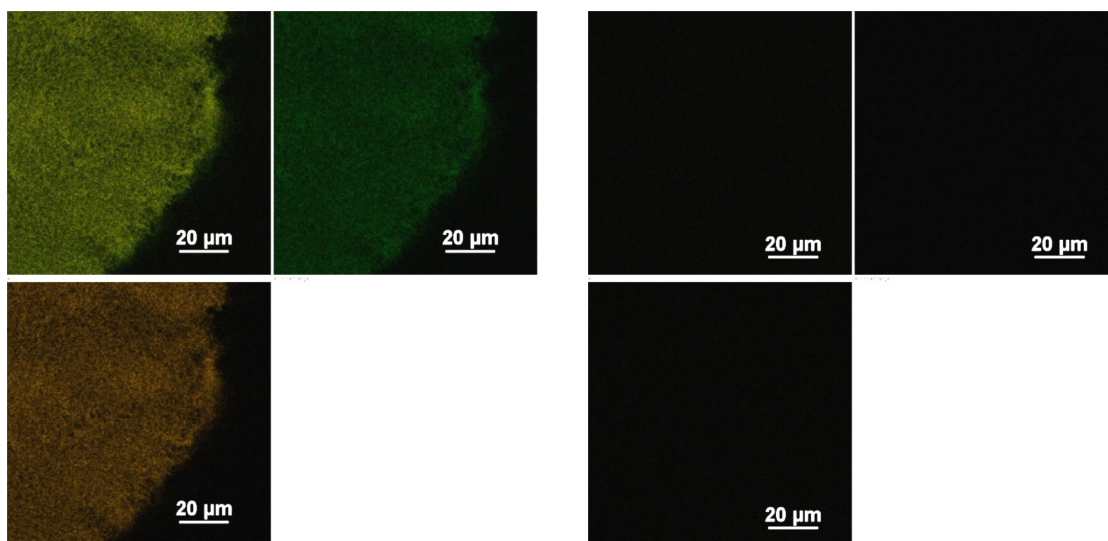


Figure SI 4.1. Confocal images of **COF-1** before (left) and after (right) treatment with Fe(III) that have been obtained in identical experimental conditions. The fluorescence of the **COF-1** material is completely quenched after the treatment. Excitation was performed at 488 nm; fluorescence was collected in the ranges 500-550 and 560-615 nm using a 60X objective.

SI 5. Thermogravimetric analysis of **COF-1** and **COF-1-M** under N₂ atmosphere

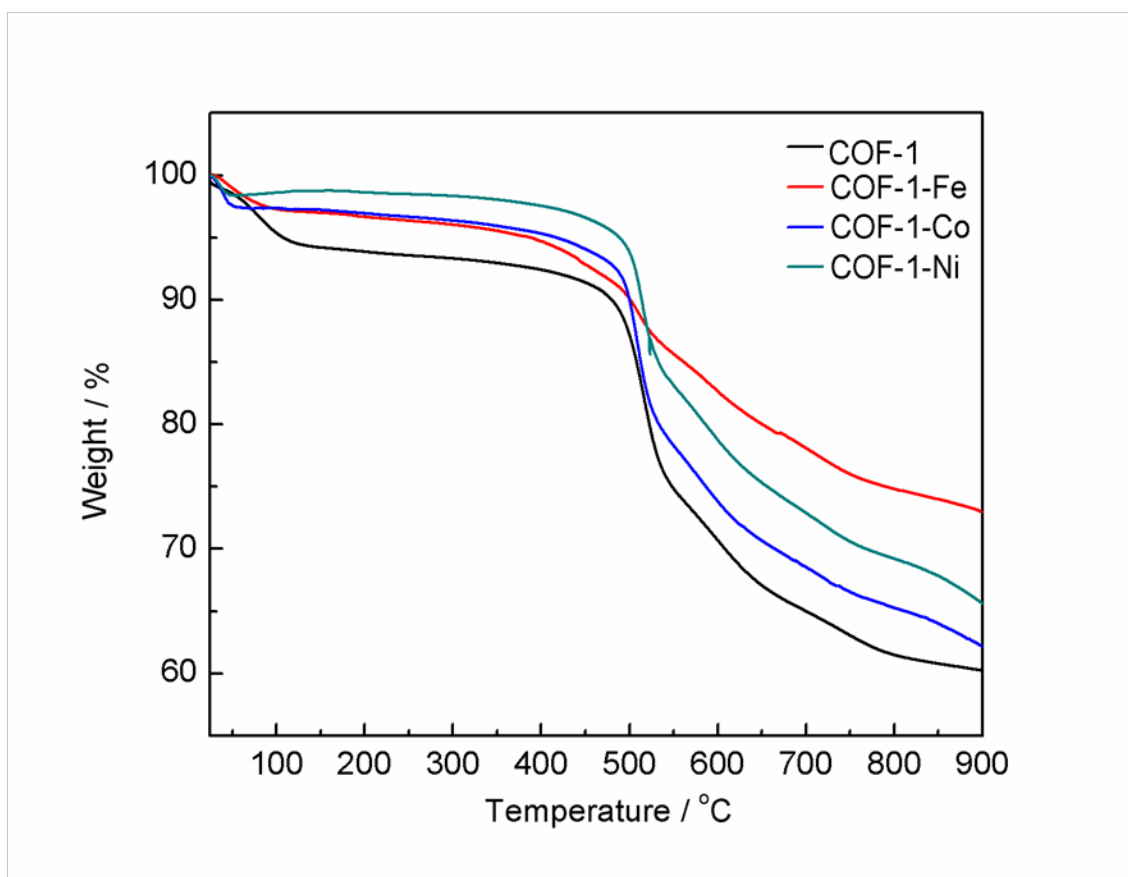


Figure SI 5.1. TGA traces of COF-1 and COF-1-M.

SI 6. HRTEM microscopy of (N)G1-4

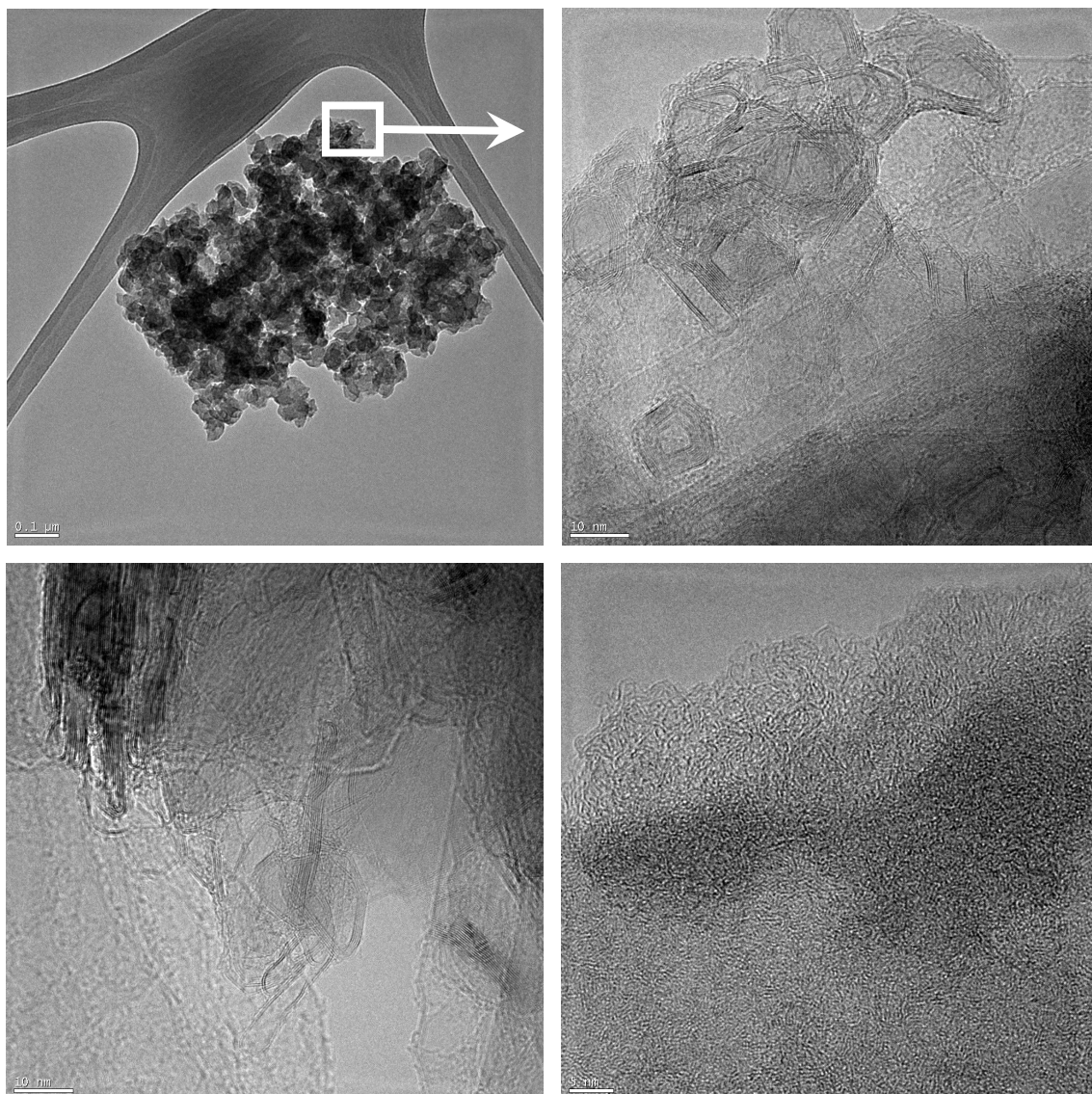


Figure SI 6.1. HRTEM images of (N)G1. Although it is possible to find some graphitic nanostructures (shown in zoom), the sample mainly consists on amorphous micro/mesoporous carbon.

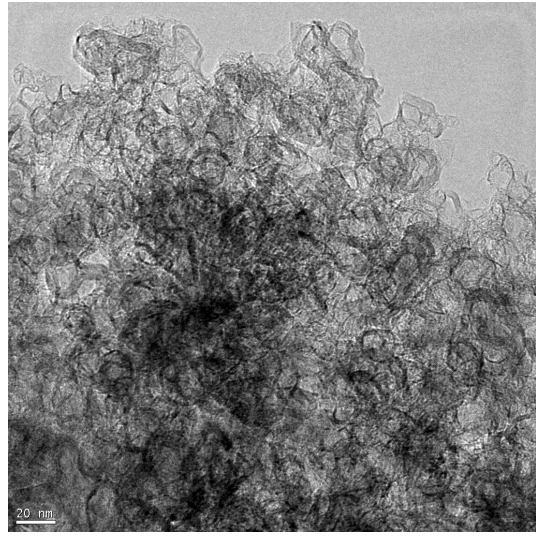
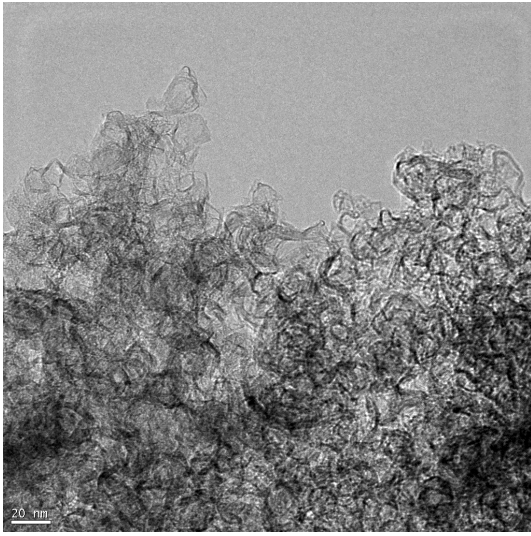


Figure SI 6.2. Additional HRTEM images of (N)G2 showing the formation of well-defined cage-like carbon nanostructures.

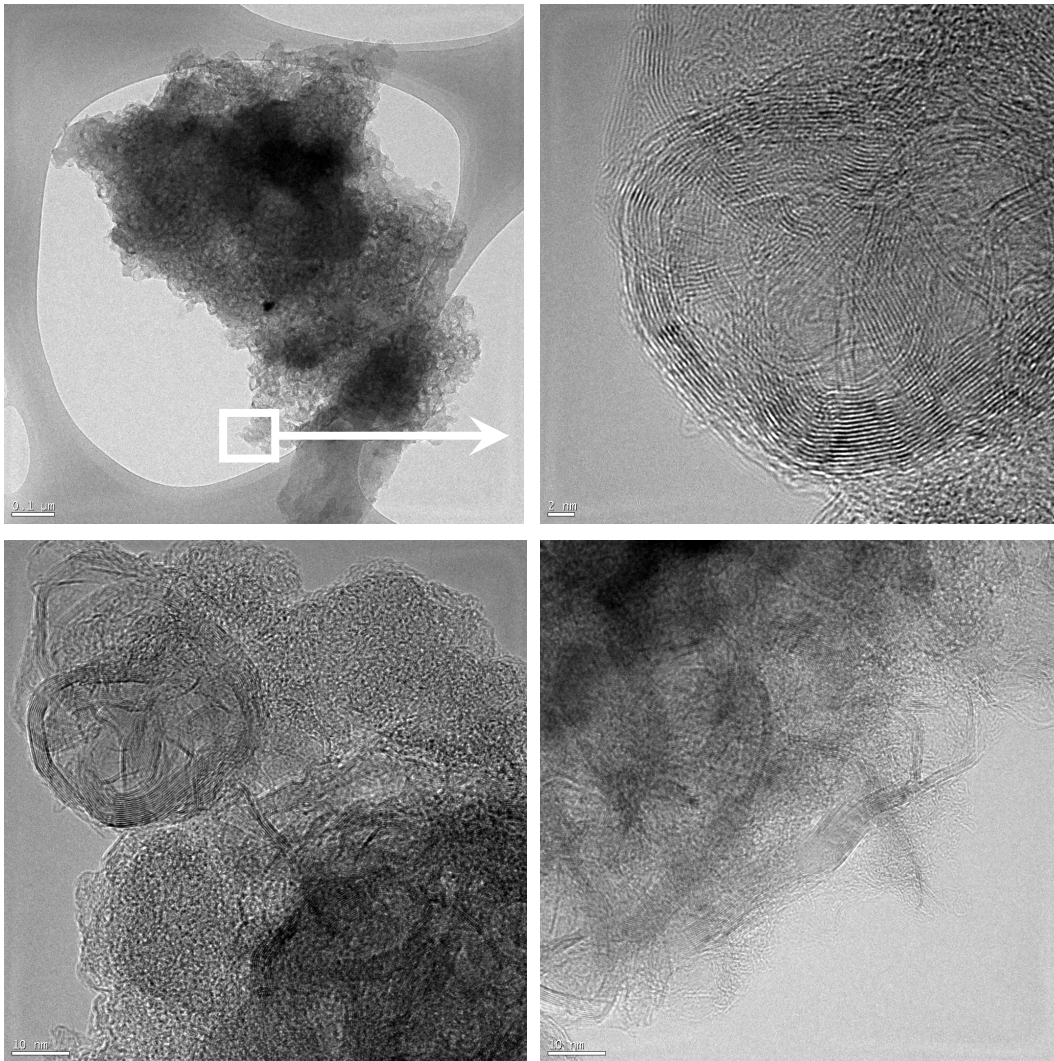


Figure SI 6.3. HRTEM images of **(N)G3** well-defined onion-like carbon nanostructures.

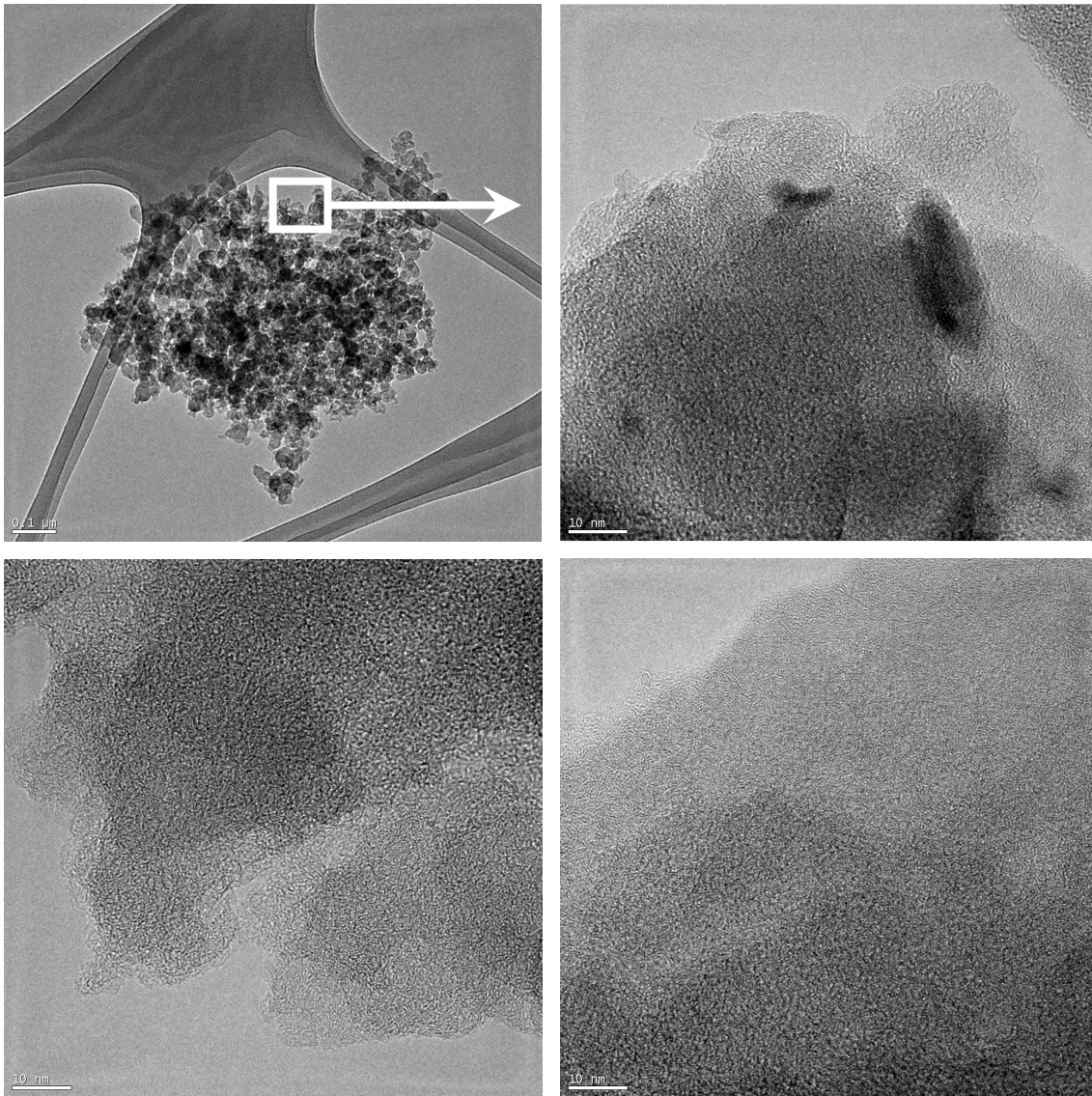
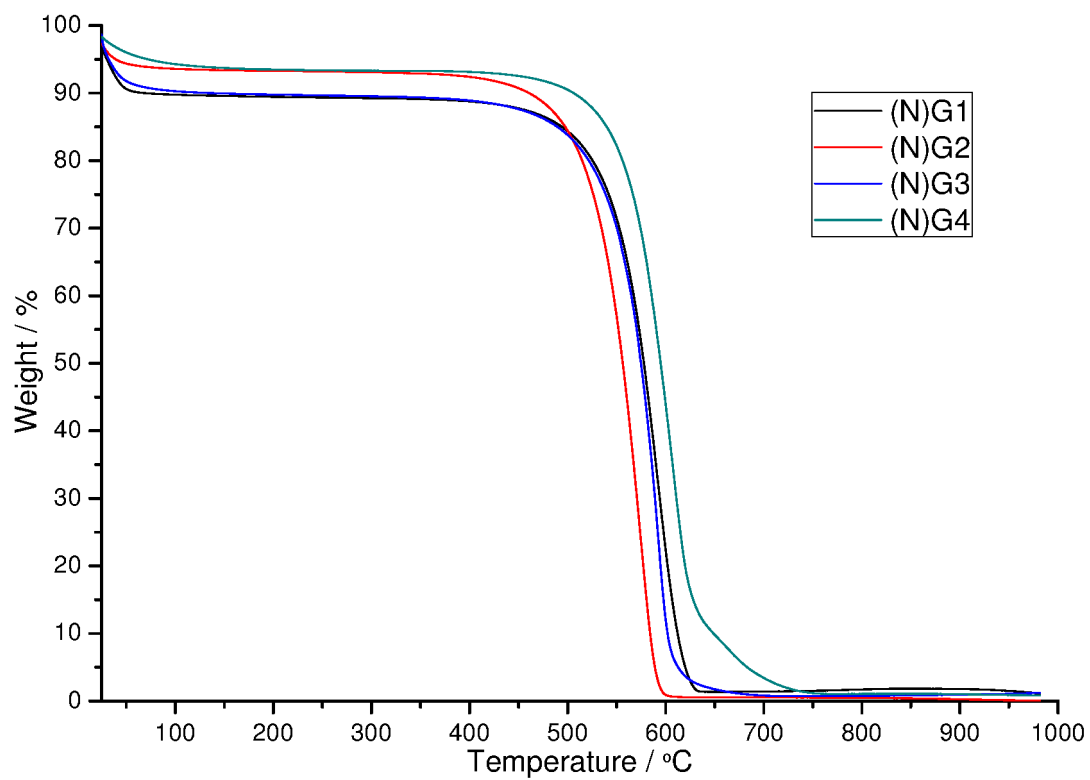


Figure SI 6.4. HRTEM images of (N)G4. The sample consists of amorphous meso/microporous carbon.

SI 7. ICP-OES analysis of (N)G2-4

<i>Sample</i>	<i>Fe / %</i>	<i>Co / %</i>	<i>Ni / %</i>
<i>(N)G2</i>	$0,070 \pm 0,002$	-	-
<i>(N)G3</i>	-	$0,028 \pm 0,001$	-
<i>(N)G4</i>	$0,023 \pm 0,001$	-	$0,041 \pm 0,002$

SI 8. Thermogravimetric analysis of (N)G1-4 in air



SI 9. XPS of (N)G1-4

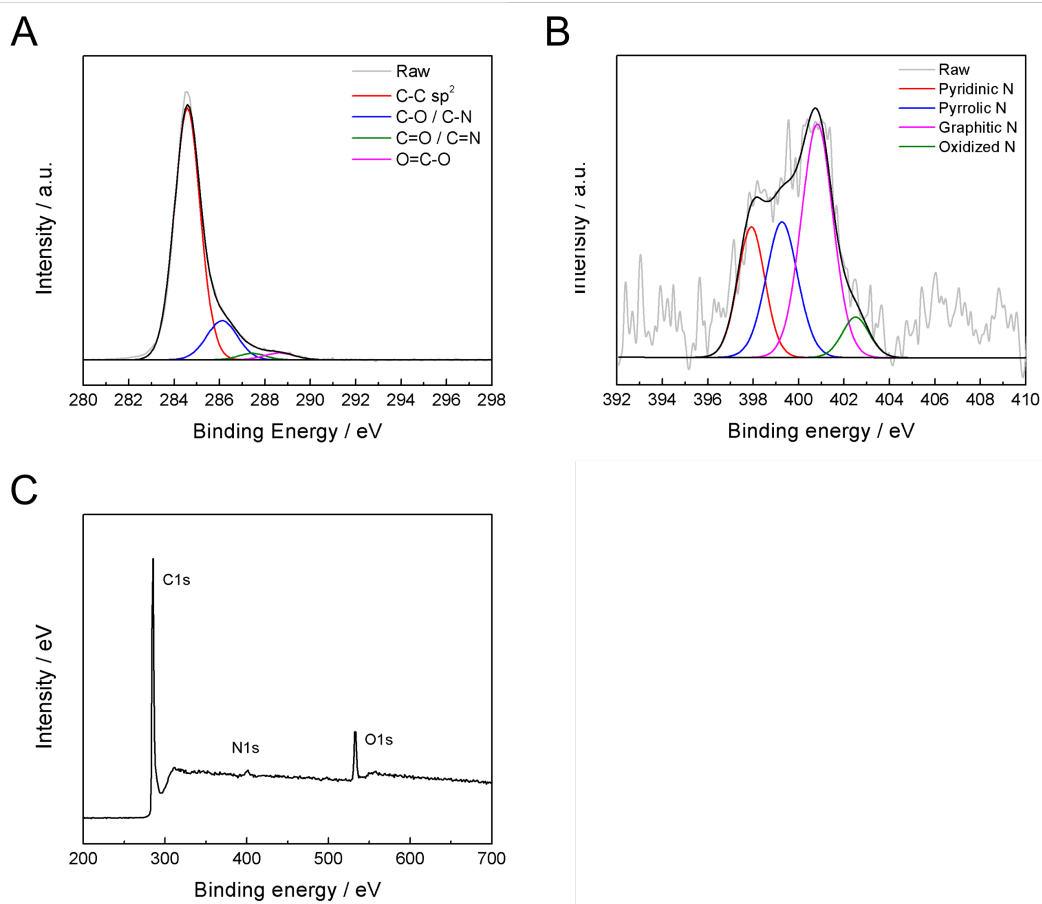


Figure SI 9.1. (A) High-resolution C1s spectrum and (B) N1s of (N)G1. (C) XPS survey spectrum for (N)G1.

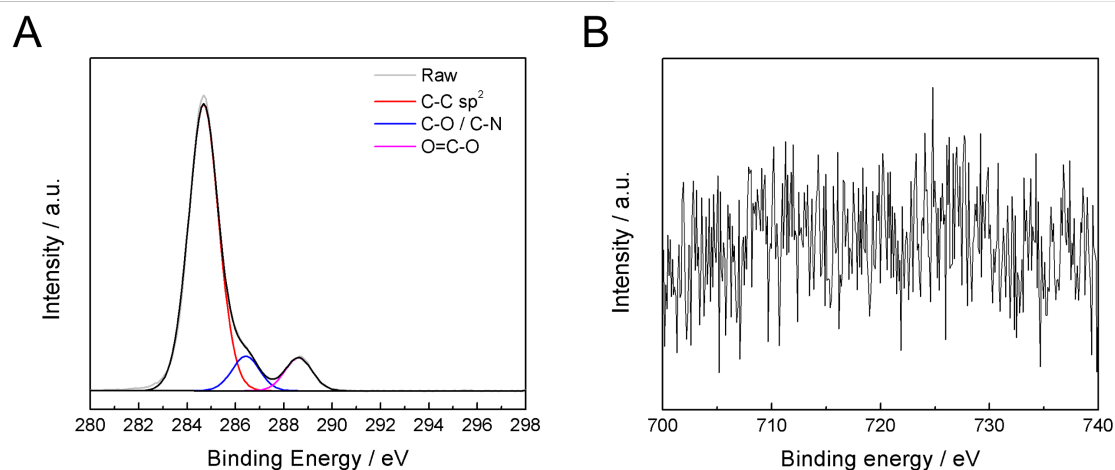


Figure SI 9.2. (A) High-resolution C1s spectrum and (B) Fe2p of (N)G2.

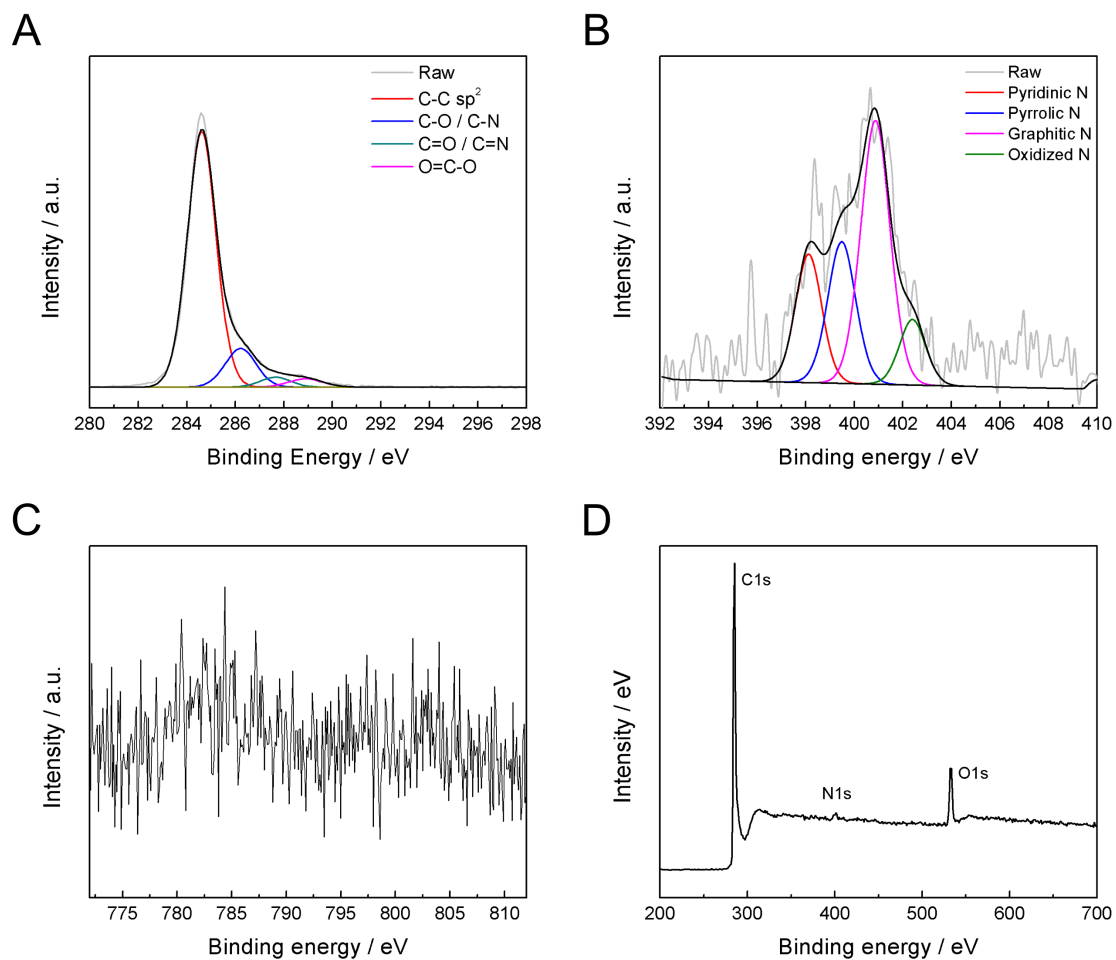


Figure SI 9.3. (A) High-resolution C1s spectrum, (B) N1s and (C) Co2p of (N)G3. (D) XPS survey spectrum for (N)G3.

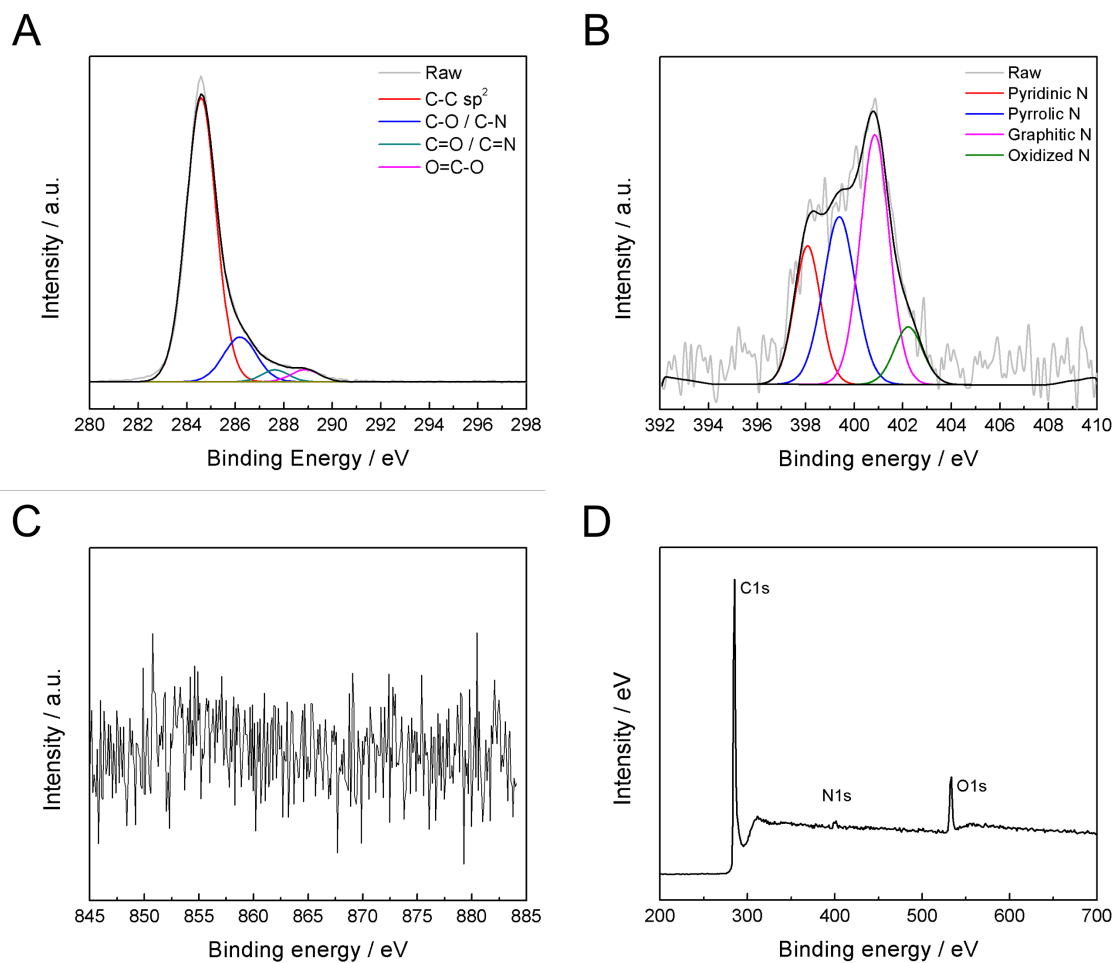


Figure SI 9.4. (A) High-resolution C1s spectrum, (B) N1s and (C) Ni2p of (N)G4. (D) XPS survey spectrum for (N)G4.

Table SI 9.1 Atomic composition (expressed as atomic percentage) of (N)G1-4 as determined by XPS analysis.

<i>Sample</i>	<i>C (at. %)</i>	<i>N (at. %)</i>	<i>O (at. %)</i>
<i>(N)G1</i>	87.26 ± 1.98	1.88 ± 0.12	11.09 ± 2.21
<i>(N)G2</i>	84.23 ± 0.08	0.84 ± 0.01	14.93 ± 0.11
<i>(N)G3</i>	89.31 ± 0.18	1.67 ± 0.01	9.03 ± 0.18
<i>(N)G4</i>	89.30 ± 0.18	1.78 ± 0.25	8.92 ± 0.42

Table SI 9.2 Relative content of different N species to total N of (N)G1-4.

<i>Sample</i>	<i>N1 Pyridinic N</i>	<i>N2 Pyrrolic N</i>	<i>N3 Graphitic N</i>	<i>N4 Pyridine N-Oxide</i>	<i>(N1+N2)</i>
<i>(N)G1</i>	0.21	0.27	0.45	0.07	0.48
<i>(N)G2</i>	0.10	0.45	0.36	0.10	0.54
<i>(N)G3</i>	0.20	0.24	0.46	0.11	0.44
<i>(N)G4</i>	0.20	0.30	0.40	0.09	0.50

Table SI 9.3 Relative content of different C species to total C of (N)G1-4.

<i>Sample</i>	<i>C-M</i>	<i>C-C</i>	<i>C-O / C-N</i>	<i>C=O / C=N</i>	<i>O=C-O</i>
<i>(N)G1</i>	-	80.12	14.86	2.31	2.70
<i>(N)G2</i>	-	82.23	9.14	-	8.63
<i>(N)G3</i>	-	80.15	13.17	3.43	3.26
<i>(N)G4</i>	-	79.69	13.88	3.10	3.33

SI 10. FESEM microscopy of (N)G2

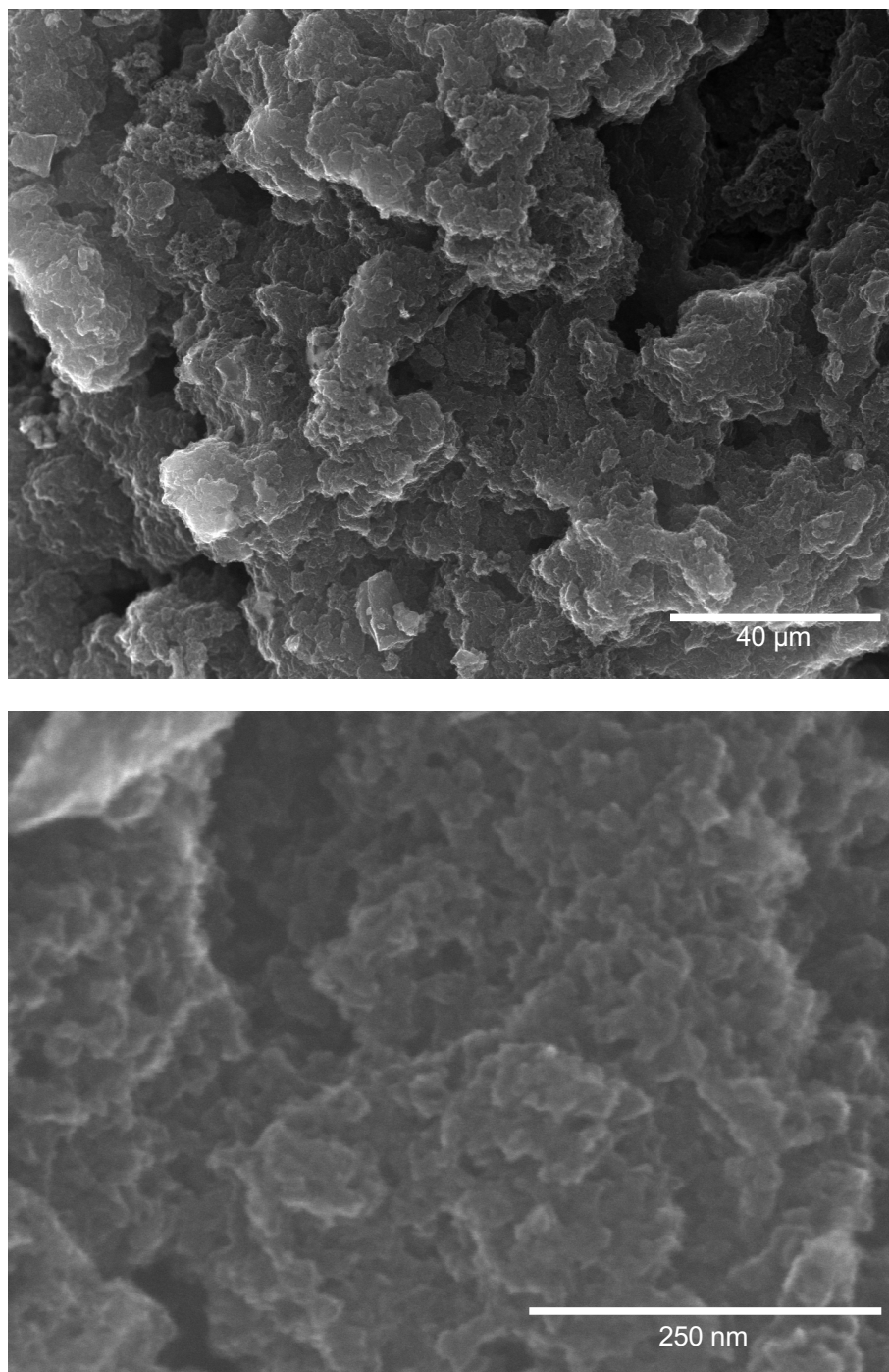


Figure SI 10.1. FESEM images of (N)G2.

SI 10.1 EDAX microanalysis of **(N)G2**

Table SI 10. EDAX analysis of **(N)G2**.

	wt %	at %
C	76.87	80.58
N	11.66	10.48
O	11.32	8.91
Fe	0.16	0.04

SI 10.2 Mapping of carbon and nitrogen of (N)G2

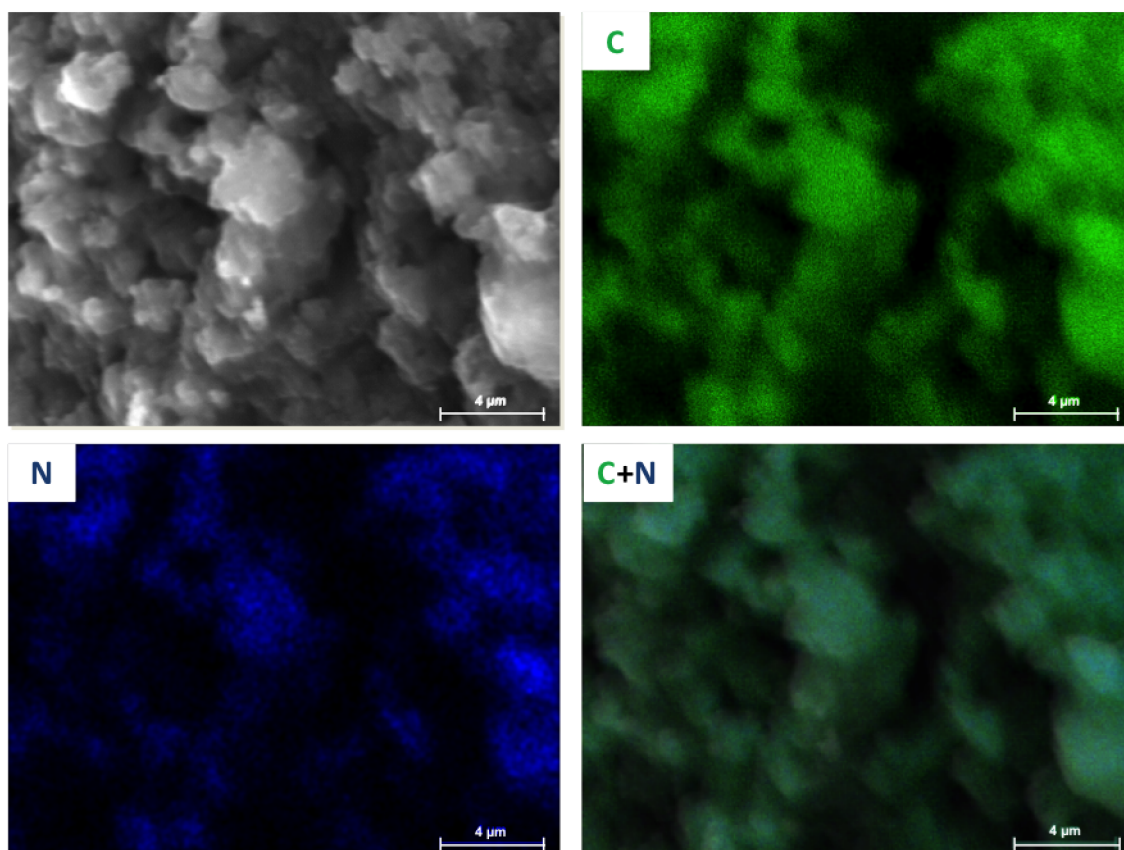


Figure SI 10.2. Field-emission scanning electron microscopy with elemental mapping (FESEM-EDS) images of (N)G2 showing the homogeneous distribution of C (green) and N (blue) in the sample.

SI 11. XRPD of (N)G1-4

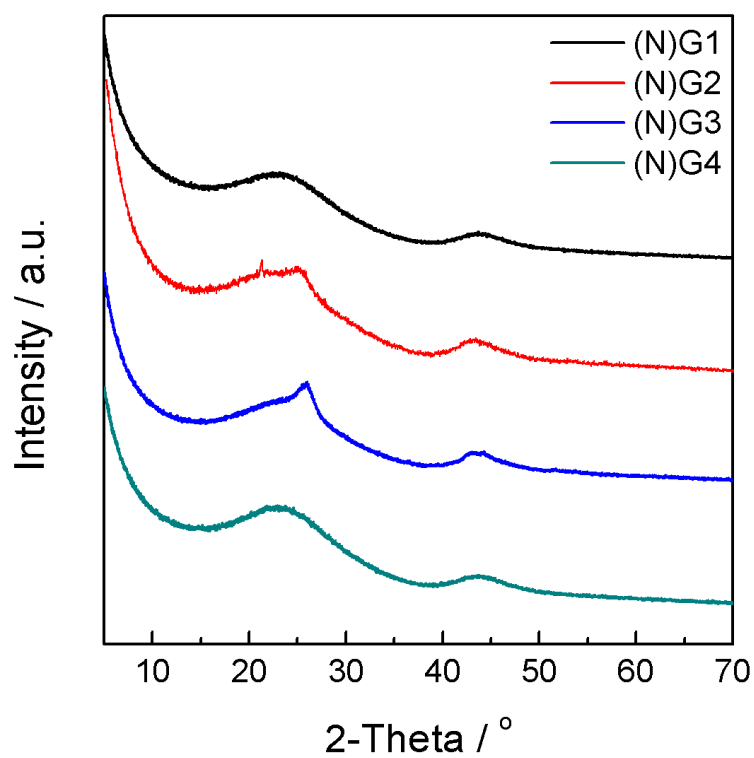


Figure SI 11.1. X-ray powder diffraction patterns of (N)G1, (N)G2, (N)G3 and (N)G4 showing typical graphitic diffraction peaks.

SI 12. Nitrogen adsorption data of COF-1

Thermal treatment of COF-1 at 150 °C and 10^{-3} bar overnight produced the activation of the material. Nitrogen isotherms were performed to confirm the permanent porosity of the activated COF-1 at 77 K. From the N₂ isotherm, the BET surface area was found to be 329 m²/g in the range of $p/p^0 = 0.05-0.3$, which is close to other values recently reported for similar imine-linked COFs. The fitting of the N₂ adsorption data to the Dubinin-Radushkevich equation provides a pore volume of 0.224 cm³/g.¹

SI 13. Textural parameters of (N)G1-4

Table SI 13. Surface area and pore volume values of (N)G1-4 obtained from N₂ and CO₂ adsorption/desorption isotherms at 77 and 273K.

Sample	S _{BET} ^a (m ² g ⁻¹)	t-plot		V _t ^b (cm ³ g ⁻¹)	V _{μ(<0.7 nm)} ^c (cm ³ g ⁻¹)	V _{μDR} ^d (cm ³ g ⁻¹)	V _{meso} ^e (cm ³ g ⁻¹)	V _{meso (P/P₀=0.7)} ^f (cm ³ g ⁻¹)	PSD _{QSDFT} (mm) ^g	
		S _μ ^a (m ² g ⁻¹)	S _r ^a (m ² g ⁻¹)						micro	meso
(N)G1	927	862	65	0.959	0.413	0.354	0.605	0.381	1.1	4.6, >5.0
(N)G2	1147	925	222	0.961	0.471	0.446	0.515	0.557	1.2	4.4, >5.0
(N)G3	844	776	68	0.960	0.399	0.325	0.635	0.367	1.2	4.8, >5.0
(N)G4	893	753	140	0.959	0.383	0.343	0.616	0.432	1.1	5.7, >5.0

^a Data obtained from N₂-adsorption. Specific surface area calculated by BET method. Microporous surface contribution S_μ and external surface S_r calculated using t-plot. ^b Total pore volume at P/P₀=0.96. ^c Data obtained from CO₂-adsorption. Volume of narrow micropores (<0.7 nm) calculated according to the DR method. ^d Micropore volume calculated from N₂-adsorption using DR method. ^e Mesopore volume was calculated according to: V_{meso} = V_{Total} - V_{μDR}. ^f Mesopore volume (V_{meso (P/P₀=0.7)}) was calculated as the difference of total (V_t) at P/P₀ = 0.7 and micropore volume (V_{μDR}). ^g Pore size distribution was analysed by using the solid density functional theory (QSDFT) for the adsorption branch assuming a cylindrical pore model.

SI 14. Electrochemical properties of **(N)G1-4** at negative potentials

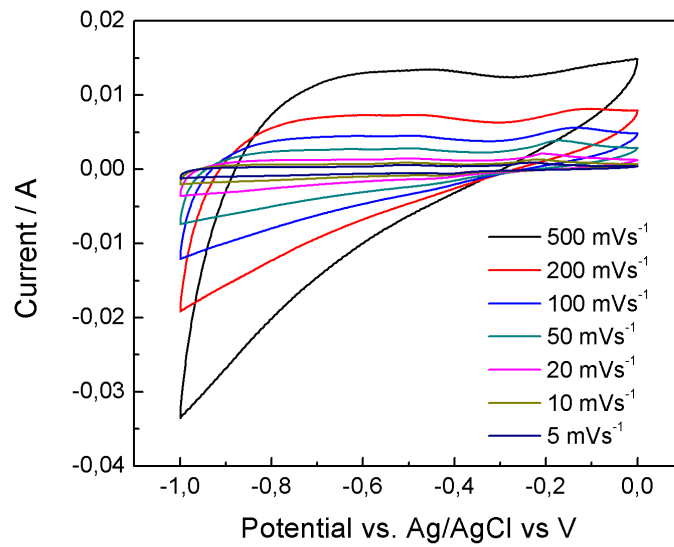


Figure SI 14.1. CV of **(N)G1** at different scan rates.

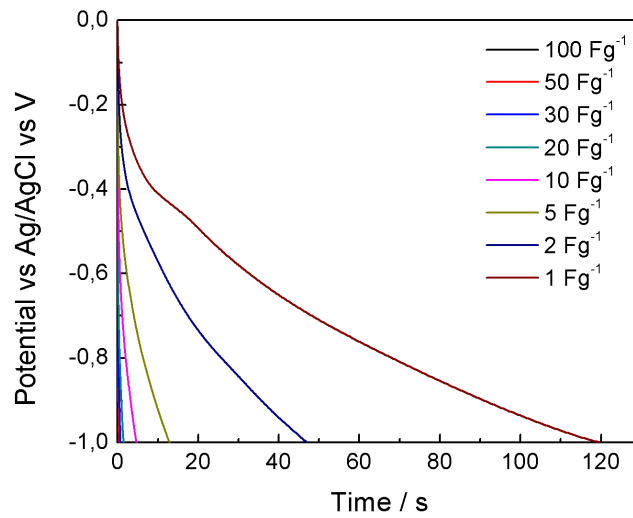


Figure SI 14.2. Discharge curve of **(N)G1**.

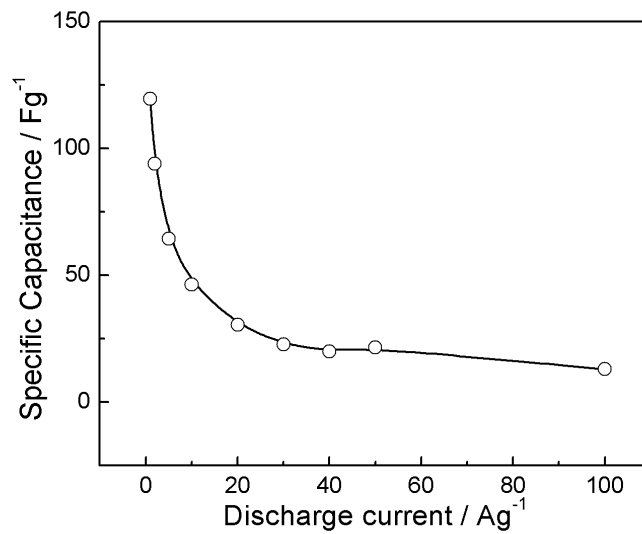


Figure SI 14.3. Specific capacitance of **(N)G1** at different current densities.

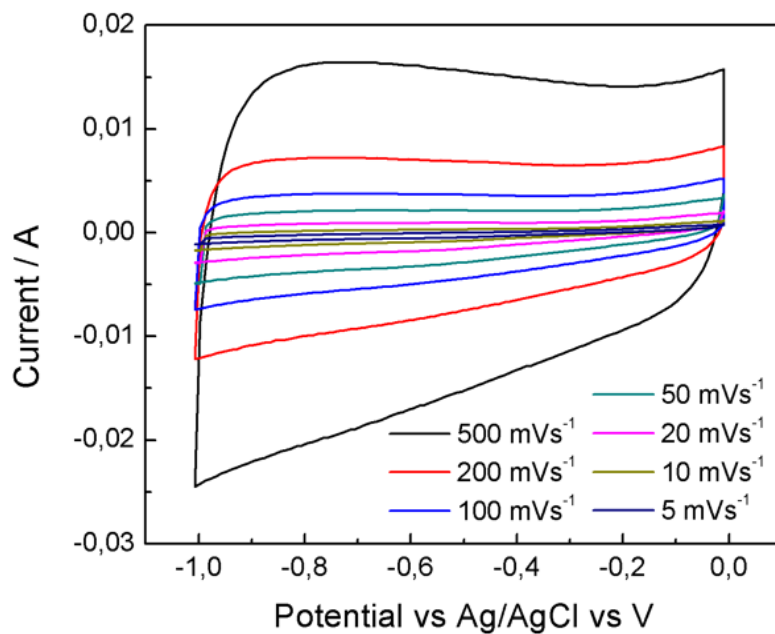


Figure SI 14.4. CV of (N)G3 at different scan rates.

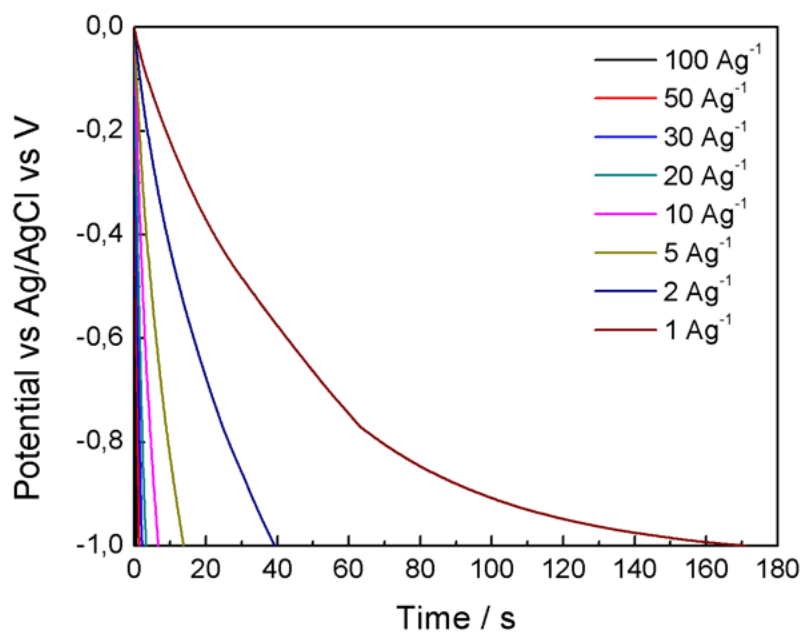


Figure SI 14.5. Discharge curve of (N)G3.

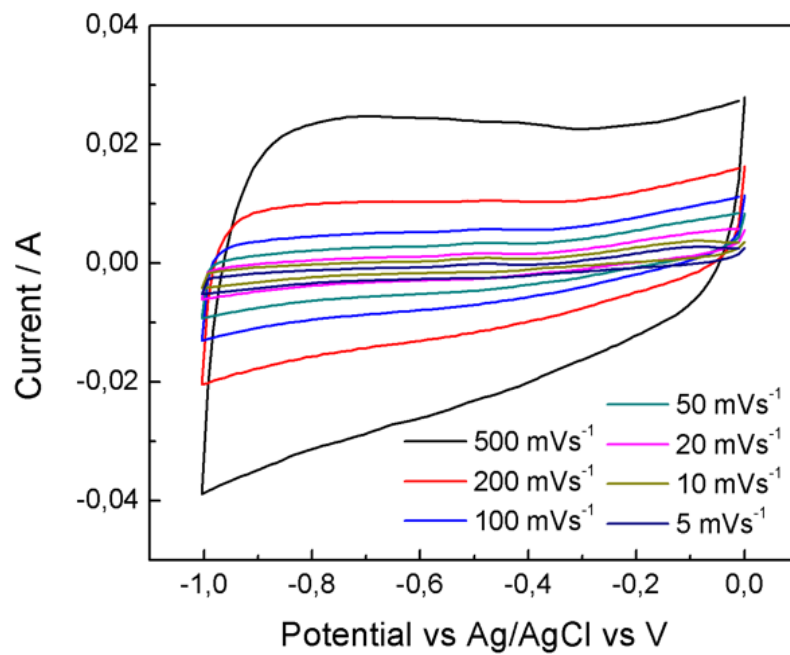


Figure SI 14.6. CV of (N)G4 at different scan rates

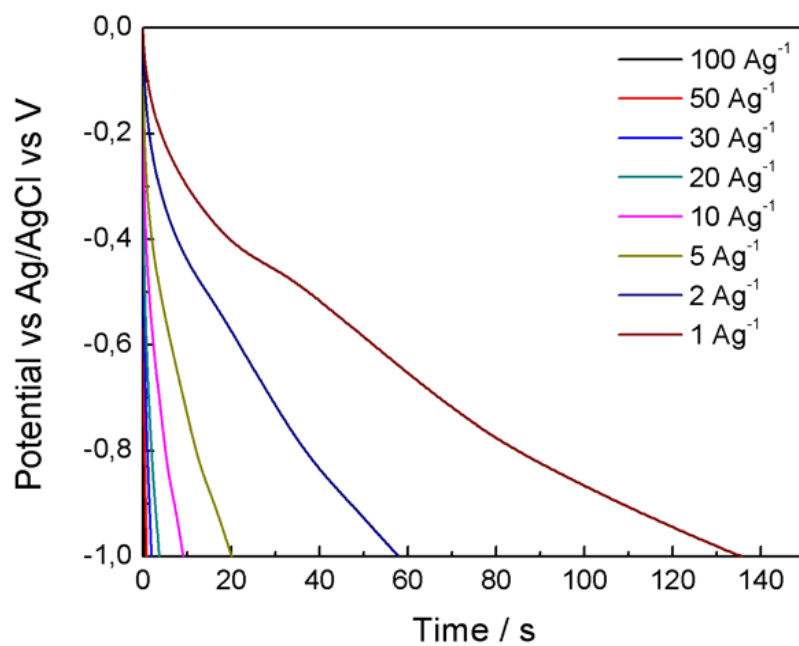


Figure SI 14.7. Discharge curve of (N)G4.

SI 15. Electrochemical properties of (N)G2-4 at positive potentials

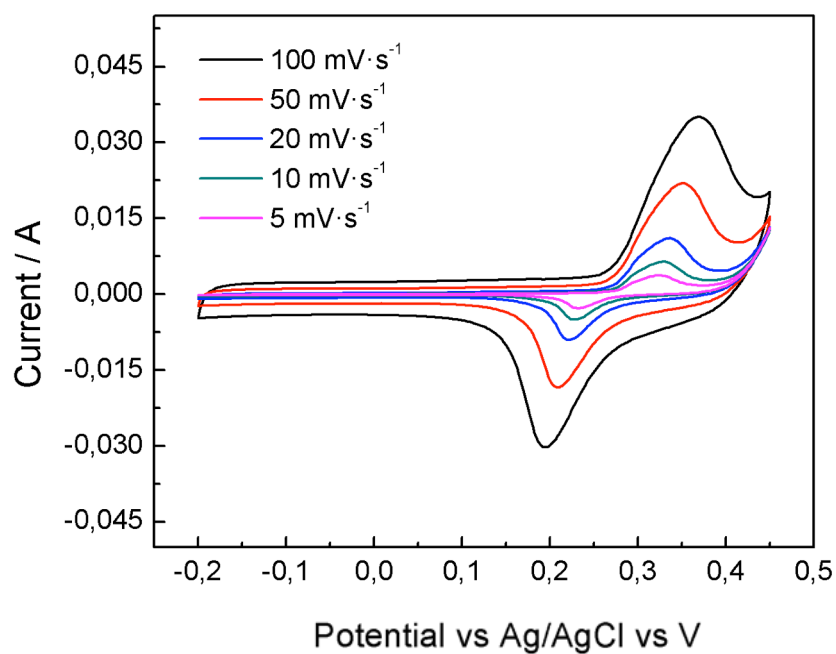


Figure SI 15.1. CV of (N)G2 at different scan rates

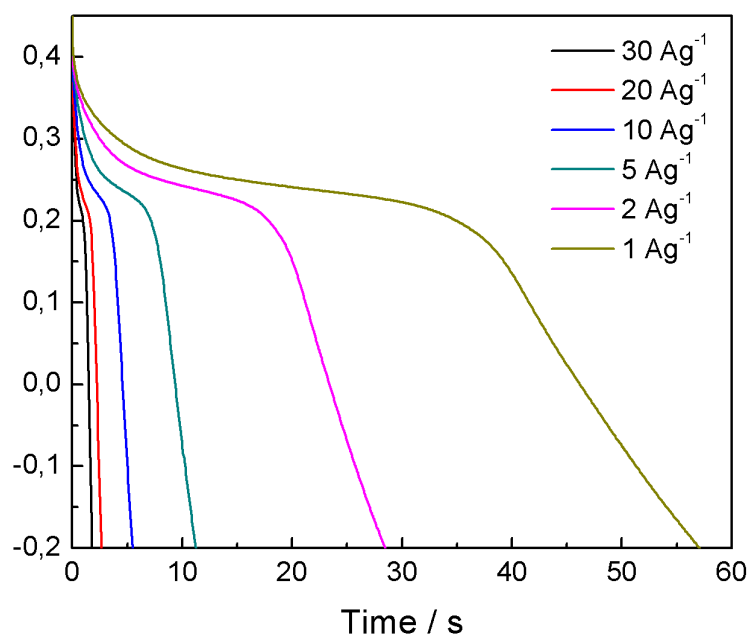


Figure SI 15.2. Discharge curve of (N)G2

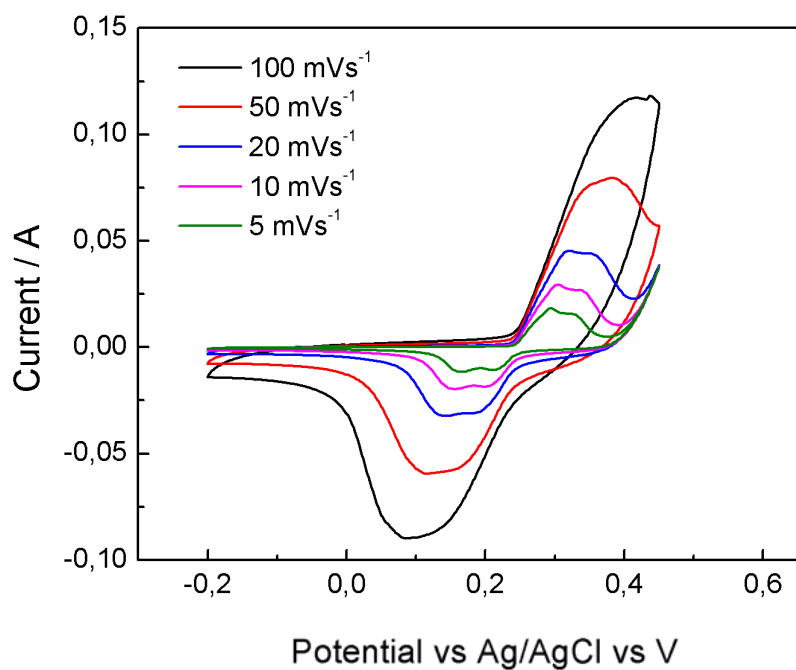


Figure SI 15.3. CV of (N)G3 at different scan rates

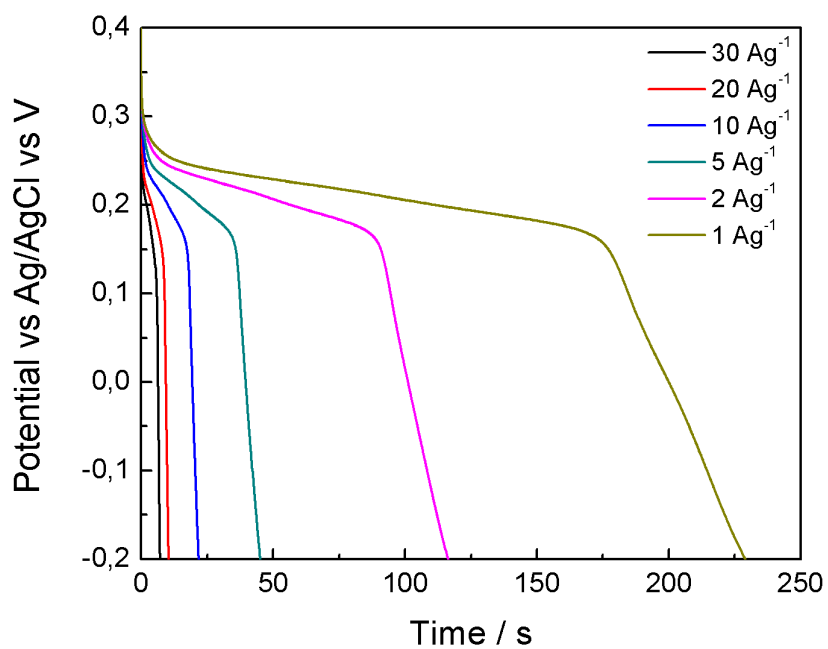


Figure SI 15.4. Discharge curve of (N)G3.

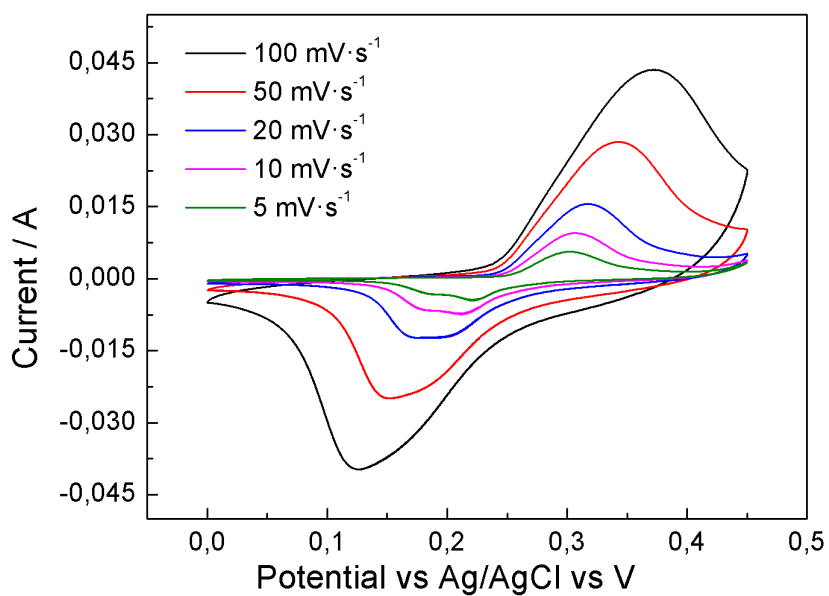


Figure SI 15.5. CV of (N)G4 at different scan rates

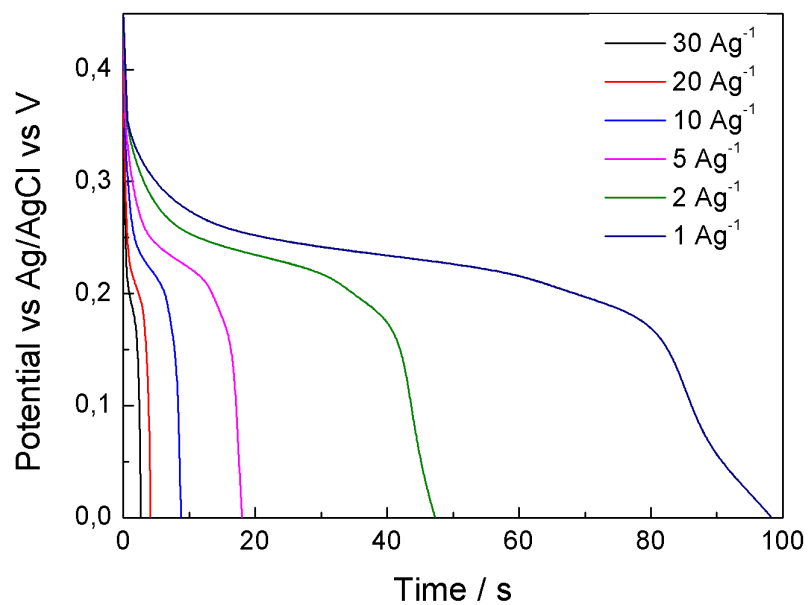


Figure SI 15.6. Discharge curve of (N)G4.

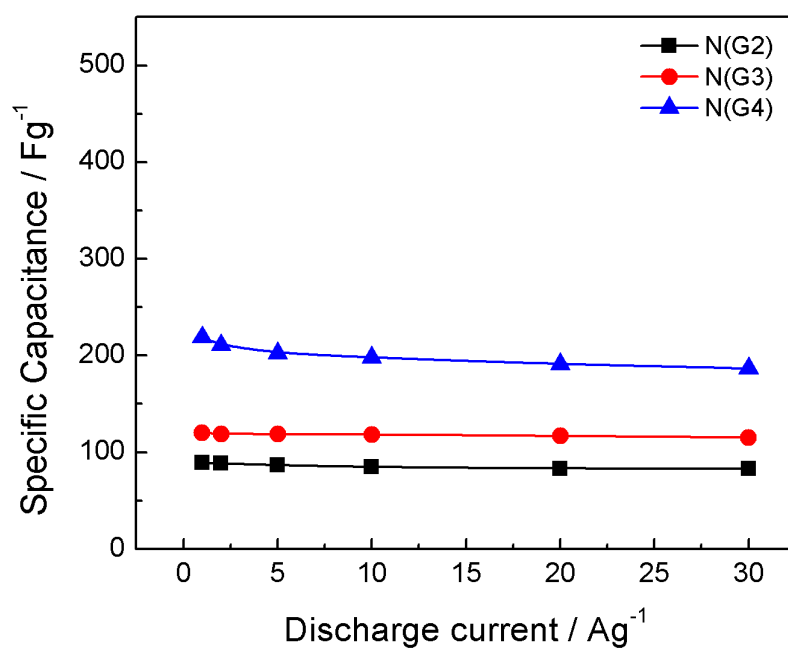


Figure SI 15.7. Specific capacitance of (N)G2-4 at different current densities measured in positive potential windows.

SI 16. Electrochemical study of pristine Ni-foam and carbon felt collectors

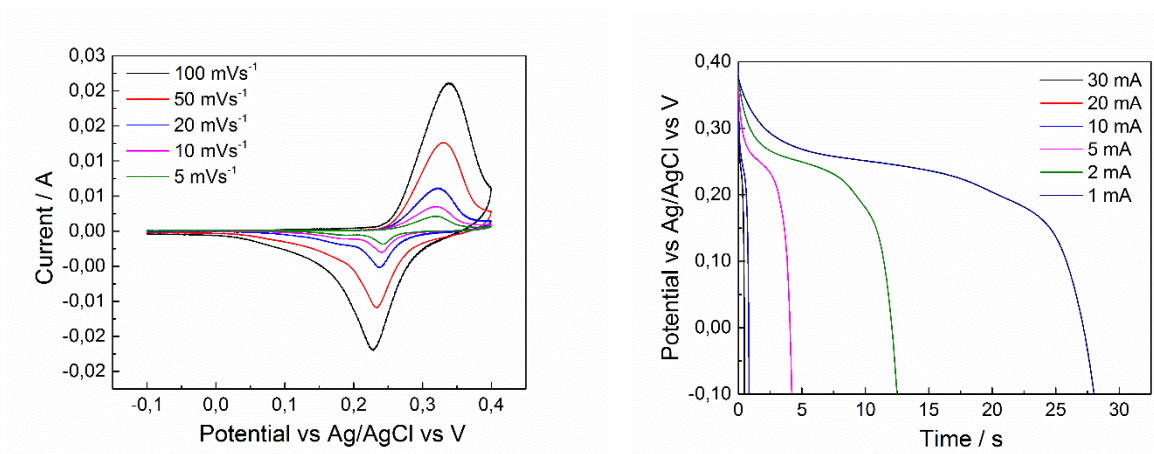
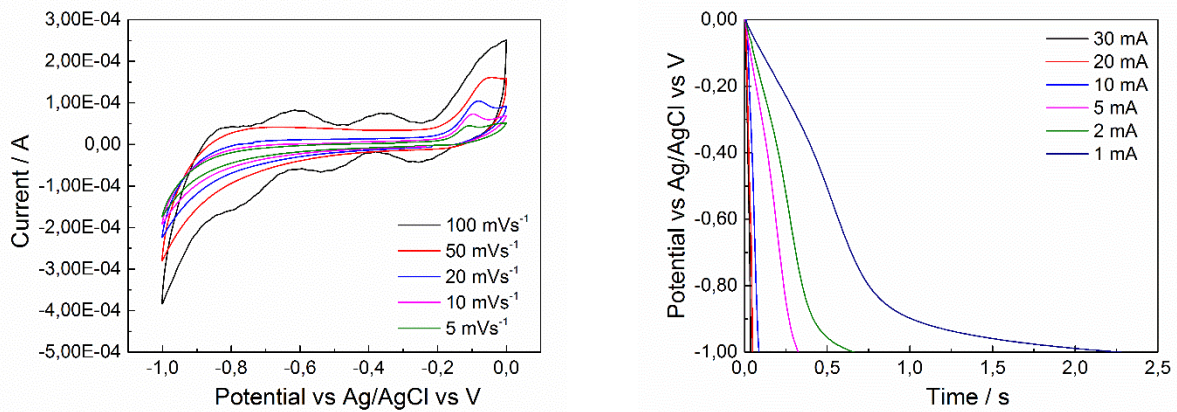


Figure SI 16.1. (A) CV of Ni-foam electrode (1 cm²) at different scan rates using the -0.1–0.4 V potential window. (B) Galvanostatic discharge curves at different discharge



currents.

Figure SI 16.2. (A) CV of Ni-foam electrode (1 cm²) at different scan rates using the -1–0 V potential window. (B) Galvanostatic discharge curves at different discharge

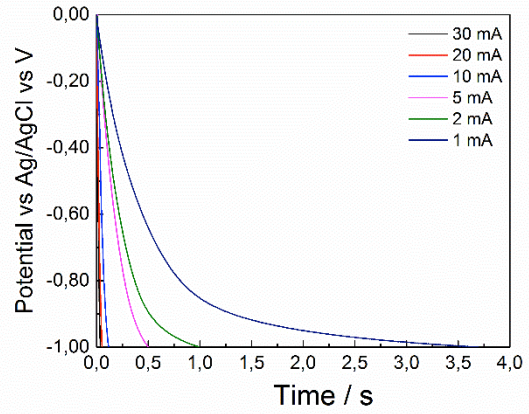
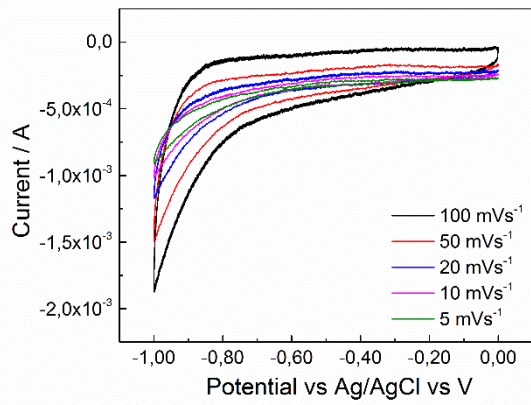


Figure SI 16.3. (A) CV of Carbon-felt electrode (1 cm²) at different scan rates. (B) Galvanostatic discharge curves at different discharge currents.

SI 17. Electrochemical study of **(N)G2** using carbon felt collectors

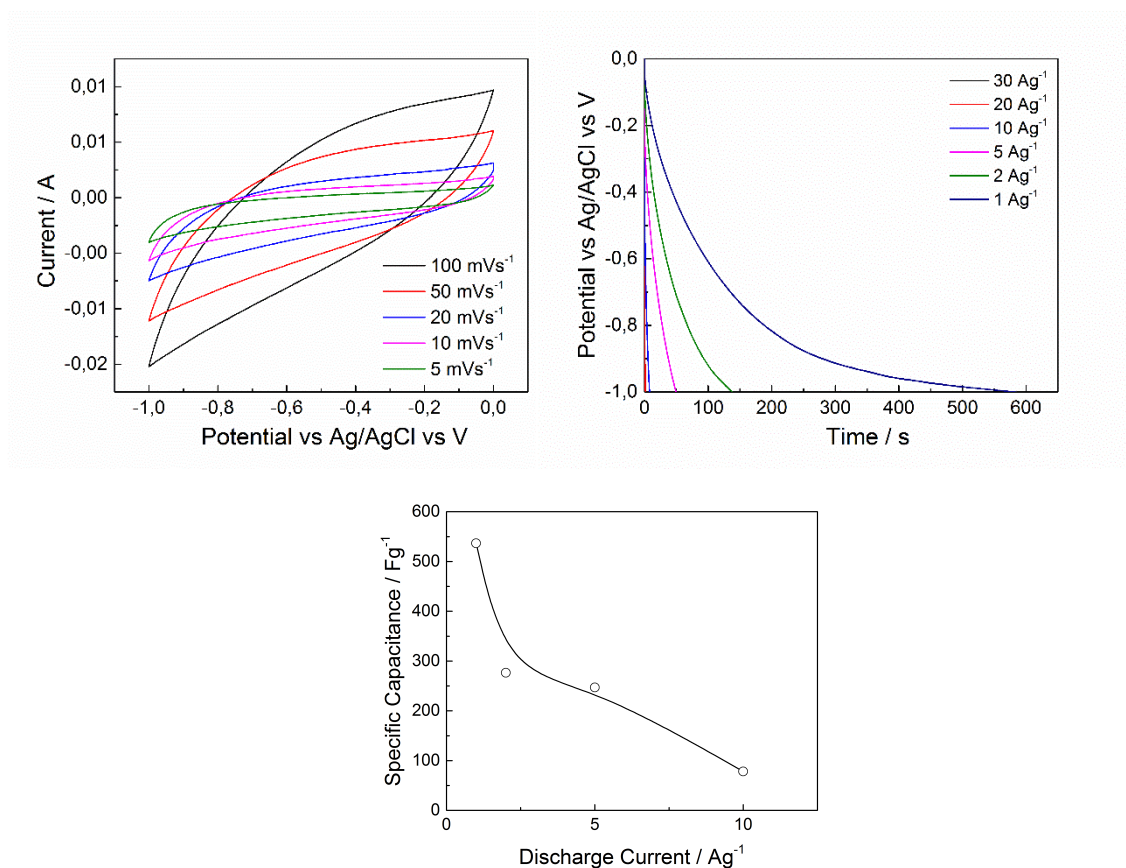
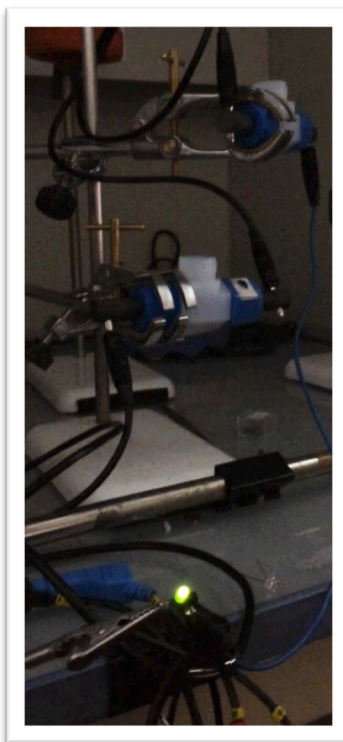


Figure SI 17.1. (A) CV of **(N)G2** at different scan rates. (B) Galvanostatic discharge curves at different discharge current densities of **(N)G2**. (C) Specific capacitance of **(N)G2** at different discharge current densities in 6 M KOH aqueous solution.

SI 18. Symmetric two-electrode supercapacitor as power supply of a green LED



Chapter 4

Nanocomposite OER catalysis

5.1 Introduction

The global demand for energy has been increasing rapidly¹⁻⁷, and it is anticipated that within the next 15 years the energy demand will be increased to the double. Until now, most of the total energy come from finite reserves fossil fuels; therefore, it is necessary to reduce our dependence on carbon-based fuels and look for alternative source energy. Hydrogen (H₂), with its high mass-specific energy density has been considered to be a promising energy source and a substitute for fossil fuels⁸⁻¹⁰. One of the most efficient ways of producing H₂ at low cost and high purity is water oxidation reaction or OER, a half-reaction involved in water splitting, which has been intensely investigated for decades because of its prime role in water splitting, rechargeable metal-air batteries and fuel cells.¹¹⁻¹⁵.

So far, noble metal based catalysts are the most stable in all pH values showing a fair activity towards OER; however, their high price and shortage are the main disadvantages in practical applications. Currently, a large number of alternative materials with better OER activity have been developed, including noble-metals hybrids with carbon-based materials (*e.g.* graphene and graphene oxide, CNT, nitrogen-doped carbon, *etc.*), alloys, oxides and oxy- hydroxides of earth abundant metals (*e.g.* Mn, Co, Ni, and Fe) and their composite with carbon as well as complex ternary structures of spinel and perovskite systems¹⁶⁻²⁷.

Nowadays, carbon-based NC with non-noble metals represent a promising family of materials with excellent performance as electrode materials for OER²⁸⁻³⁰. There are many methods that can be employed to prepare these materials, including laser ablation, chemical vapor decomposition (CVD), nanocasting, chemical or physical activation methods, *etc.*³¹⁻³⁷ Recently, the thermal stability, internal voids and unique structural/chemical flexibility of metal-organic frameworks (MOFs) have been used to produce carbon-based porous NC by direct calcination. This strategy is similar to the nanocasting method³⁸, traditionally used for producing hierarchical porous carbons by pyrolysis of mesoporous hosts filled with carbon precursors, and followed by removal of the inorganic template. In comparison, MOFs offer higher synthetic flexibility than the nanocasting approach, where their hybrid organic/inorganic nature allows for producing nanoporous carbons by direct decomposition of the organic linkers in their structure with

no need for auxiliary carbon sources^{39,40}. Despite their typical low conductivity and poor stability, which limits their use in energy storage or conversion devices, MOFs have been demonstrated as suitable precursors for fabricating heteroatom-doped nanocarbons materials through calcination processes that exhibit excellent electrocatalytic activities and can therefore be used in energy-related applications^{41–55}. Specially, MOFs are assembled by metal centers and organic linkers with permanent porosity. Upon pyrolysis, MOFs act as both a precursor and a self-sacrificing template: the metal components provide an intrinsic metal source to derive nanostructures of metals or metal oxides, depending on the processing conditions such as atmosphere and temperature; the organic components, on the other hand, can be directly used as a carbon source to prepare nanoporous carbons⁵⁶.

Recently, zeolitic imidazolate frameworks (ZIFs), a subfamily of MOFs consisting of tetrahedral metal centres connected by imidazolate-based organic linkers with a crystalline structure analogue to those of zeolites⁵⁷, have been successfully used as a template and precursor to create N-doped nanocarbons³⁹. This is due to their highly ordered nanoporous structure and the use of nitrogen-rich organic ligands, resulting in an abundance of nitrogen incorporation which significantly enhances the electrocatalytic performance towards oxygen reaction (ORR) and OER^{58,59}. Nevertheless, numerous efforts have been made in order to increase the catalytic activity of the nanocomposites resultant from the pyrolysis of a given ZIF. In this sense, it has been recently demonstrated that the inclusion of extrinsic iron sources before carbonization, either by insertion of iron-based molecular complexes within the pores of a ZIF^{60–64}, or by direct mixing the ZIF with an iron-based material^{65–67}, significantly improves the electrocatalytic efficiency of the resultant nanocomposite.

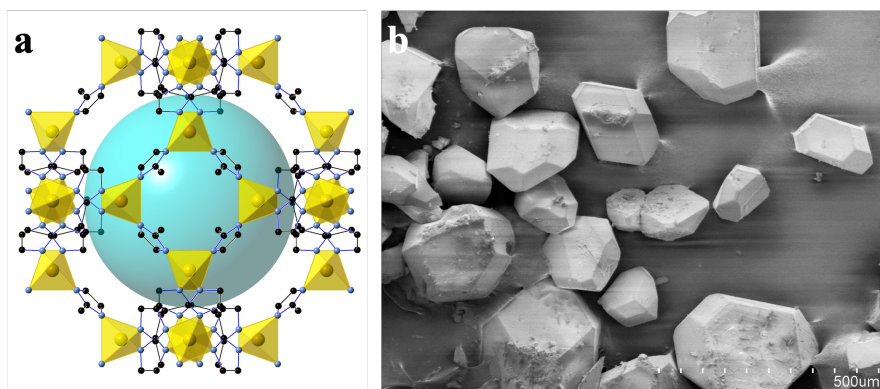


Figure 5.1. (a) Crystal structure of the iron ZIF-8 analogue, the MUV-3. Key: Fe, yellow; C, black; N, blue. The blue sphere (diameter of 11 Å) is placed in the structure to represent the empty space of the structure. Hydrogen atoms have been omitted for clarity. (b) SEM image of MUV-3 crystals.

The most prominent member of the ZIF family is $\text{Zn}(\text{Meim})_2$ (MeimH = 2-methylimidazole), also known as ZIF-8, which has been widely studied due to its high porosity and straight forward preparation, including its conversion into a highly graphitic nitrogen-doped carbon structure with good performance in ORR, OER and hydrogen evolution reaction (HER)^{54,68,69}. The isostructural cobalt analogue of ZIF-8, $\text{Co}(\text{Meim})_2$, also known as ZIF-67⁷⁰, has also been used as the precursor of N-doped carbon nanotubes with outstanding electrochemical ORR and OER performance⁷¹⁻⁷⁴. However, the highly interesting iron member of this family formed exclusively by iron(II) centres, *i.e.* $\text{Fe}(\text{Meim})_2$, has surprisingly remained elusive despite the vast number of potential applications associated with this Fe-based solid, especially as a single precursor for the formation of N-doped carbon materials for OER. Indeed, Fe is an excellent catalyst for the formation of carbon nanoforms, as is reported in the literature⁷⁵⁻⁷⁷, and usually Fe-containing catalysts are more efficient than Co-containing ones⁷⁸⁻⁸⁰. Thus, $\text{Fe}(\text{Meim})_2$ is expected to be a superior single precursor for the formation of electrocatalytic NCs; however, all attempts to adapt the different synthetic solvent-based procedures of ZIF-8 or ZIF-67 result unfruitful when using Fe(II) instead.

In the present work, we report for the very first time a solvent-free synthesis compatible with Fe(II) to obtain MUV-3 (MUV: Materials of University of Valencia), the iron analogue of ZIF-8, and its use as a single source in the direct synthesis of a

nanocomposite with extraordinary OER performance, surpassing the properties of any other related carbon-based NC.

5.2 Summary of the most important results

The main objective of the present Chapter is to obtain a NC form by a N-doped graphitic matrix and iron NP with catalytic behaviour, as well as the study of its properties. The structural properties of the new MUV-3, being porous and containing nitrogen and iron in its structure, make it a very good candidate to be used as a precursor for a NC for oxigent evolution reaction.

The synthesis of the precursor was performed by a solvent-free synthesis, obtaining iron analogue of ZIF-8, adapting a previously described method for the preparation of nonporous iron azolates^{81–83}. The reaction of ferrocene and 2-methylimidazole at 150 °C for 48h under vacuum, in the presence of 4,4-bipyridine (acting as a template). The formation of the MUV-3 was revealed by magnetic and spectroscopic characterization. After that, a low-temperature processing of MUV-3 in a CVD oven at 700 °C for 3.5 h under nitrogen atmosphere yields a black powdered carbon material, which is subsequently treated with an acid leaching using sulfuric acid in order to remove residual metals, obtaining the final NC-MUV-3.

FE-SEM shows that the crystalline morphology of the MUV-3 is completely lost after the thermal treatment, giving a carbonaceous material. High-resolution TEM confirms the formation of the NC, with a corrugated carbon matrix of several graphene layers and residual Fe NPs (*ca.* 0.8% according to inductively coupled plasma-optical emission spectroscopy (ICP-OES) analysis) of *ca.* 10–30 nm in size embedded in the carbon matrix. The formation of these nanostructures is related to the *in-situ* formation in which iron is present in the structure of the precursor, as we have observed in literature for Co^{74,77,84}.

Further insights on the surface chemical composition though X-ray photoelectron spectroscopy (XPS) show the predominant sp² character of the graphitic carbon and a nitrogen doping. The high-resolution N1s spectra peaking shows the presence of nitrogen as a dopant (*ca.* 1.10 %), and its deconvolution reveals the four different N types (*i.e.* pyridinic-N, pyrrolic-N, graphitic-N and pyridine-N-oxide groups), being predominant the graphitic-type nitrogen (49.1%)⁸⁵. In addition, statistical Raman spectroscopy (>7000 single point spectra) shows the characteristic G and D bands, as well as a marked 2D

band, indicative of a high degree of graphitization, in accordance with XPS. An inspection of the I_D/I_G ratios of *ca.* 0.85 suggests a low density of disorder and carbon defects.

Textural characterization of NC-MUV-3 was performed using N_2 and CO_2 adsorption-desorption isotherms at 77 K and 273 K, respectively. The N_2 isotherm reveals a specific surface area of $463 \text{ m}^2 \cdot \text{g}^{-1}$, a total pore volume of $0.960 \text{ cm}^3 \cdot \text{g}^{-1}$ and a narrow distribution of mesopores of *ca.* 4 nm. The CO_2 isotherm confirms the presence of narrow micropores (<0.7 nm) revealing a value of $0.120 \text{ cm}^3 \cdot \text{g}^{-1}$, with a narrow micropores contribution of *ca.* 12 % of the total pore volume⁷⁷.

All these properties make the NC-MUV-3 a very good candidate for electrochemical catalysis in OER, therefore, we tested in two different basic mediums (1 and 0.1 M KOH) in a standard three-electrode cell by LSV, CP and CA. LSV measurements show an excellent electro-chemical performance, with low onset potentials of 1.588 and 1.541 V vs the reversible hydrogen electrode (RHE) for 1 and 0.1 M KOH, respectively. Also, different parameters were calculated to quantify the electrochemical performance: the overpotential (η) at different current densities, the current densities (j) at different overpotentials and the Tafel slopes. On the one hand, overpotentials of 316 mV (1.542 V vs RHE) and 335 mV (1.561 V vs RHE) are required at $j = 10 \text{ mA} \cdot \text{cm}^{-2}$ in 1 and 0.1 M KOH, respectively. These values are much lower than those of other of ZIF-derived electrocatalysts. On the other hand, a current density of $331 \text{ mA} \cdot \text{cm}^{-2}$ at 0.74 V (2.0 V vs RHE) is obtained in 0.1 M KOH. This value is much better than that for the Co analogue and commercial catalysts like IrO_2 and $NiFeOOH$ ^{72,74,86,87}. In addition, the excellent catalytic activity of NC-MUV-3 is also reflected in the Tafel slopes, showing values in the range of 37 and 48 mV per decade in 1 and 0.1 M KOH, respectively.

Finally, the stability and durability of the NC-MUV-3 powdered catalyst was tested by CP at constant current densities j of 10 and $15 \text{ mA} \cdot \text{cm}^{-2}$ and with CA at constant overpotentials, η , of 300 and 400 mV for 15 h, showing an excellent stability in all cases. Such remarkable activity, outperforming most current noble-metal-free electrocatalysts, is likely to be the result from the combination of ultrathin and conductive graphitized carbon shells rich in defects, a uniform N-doping, high porosity composed of micro- and mesopores facilitating the diffusion of the electrolyte, and the presence of encapsulated Fe NP of small dimensions. It is worth to remark that these results are among the best reported so far in the literature for any carbon-based NCs.

5.3 Contribution of the author

5.3.1 Article 4: *“Solvent-Free Synthesis of ZIFs: A Route toward the Elusive Fe(II) Analogue of ZIF-8”*

The main contribution in this work was to show that with a controlled calcination process at low-temperatures of the iron analogue of ZIF-8 we can obtain a NC of N-doped graphitic matrix and iron NP with catalytic behaviour. Due to its excellent performance as an OER catalyst, we patented these results in 2017 (WO2019053312A1: *“Marco imidazolato zeolítico de hierro, proceso para su obtención y nanocomposite derivado del mismo”*)

The author synthesized by different calcination process the nanocomposite material and characterized and discussed the results. All electrochemical measurements and their analysis were also carried out by the author. The author wrote the paper and the patent in collaboration with the other co-authors.

5.4 References

1. Dou, Y. *et al.* Graphene-like holey Co₃O₄ nanosheets as a highly efficient catalyst for oxygen evolution reaction. *Nano Energy* **30**, 267–275 (2016).
2. Wang, Z.-L., Xu, D., Xu, J.-J. & Zhang, X.-B. Oxygen electrocatalysts in metal–air batteries: from aqueous to nonaqueous electrolytes. *Chem. Soc. Rev.* **43**, 7746–7786 (2014).
3. Qu, K., Zheng, Y., Dai, S. & Qiao, S. Z. Graphene oxide-polydopamine derived N, S-codoped carbon nanosheets as superior bifunctional electrocatalysts for oxygen reduction and evolution. *Nano Energy* **19**, 373–381 (2016).
4. Wu, G. *et al.* Carbon nanocomposite catalysts for oxygen reduction and evolution reactions: From nitrogen doping to transition-metal addition. *Nano Energy* **29**, 83–110 (2016).
5. Tang, D. *et al.* Carbon Quantum Dot/NiFe Layered Double-Hydroxide Composite as a Highly Efficient Electrocatalyst for Water Oxidation. *ACS Appl. Mater. Interfaces* **6**, 7918–7925 (2014).
6. Tahir, M. *et al.* Tubular graphitic-C₃N₄: a prospective material for energy storage and green photocatalysis. *J. Mater. Chem. A* **1**, 13949–13955 (2013).
7. Tahir, M. *et al.* Large scale production of novel g-C₃N₄ micro strings with high surface area and versatile photodegradation ability. *CrystEngComm* **16**, 1825–1830 (2014).
8. Crabtree, G. W., Dresselhaus, M. S. & Buchanan, M. V. The Hydrogen Economy. *Phys. Today* **57**, 39–44 (2004).
9. Dresselhaus, M. S. & Thomas, I. L. Alternative energy technologies. *Nature* **414**, 332–337 (2001).
10. Choi, C. L. *et al.* WS₂ nanoflakes from nanotubes for electrocatalysis. *Nano Res.* **6**, 921–928 (2013).

11. Carmo, M., Fritz, D. L., Mergel, J. & Stolten, D. A comprehensive review on PEM water electrolysis. *Int. J. Hydrog. Energy* **38**, 4901–4934 (2013).
12. Jiao, F. & Frei, H. Nanostructured cobalt and manganese oxide clusters as efficient water oxidation catalysts. *Energy Environ. Sci.* **3**, 1018–1027 (2010).
13. Mills, A. Heterogeneous redox catalysts for oxygen and chlorine evolution. *Chem. Soc. Rev.* **18**, 285–316 (1989).
14. Yagi, M. & Kaneko, M. Molecular Catalysts for Water Oxidation. *Chem. Rev.* **101**, 21–36 (2001).
15. Dau, H. *et al.* The Mechanism of Water Oxidation: From Electrolysis via Homogeneous to Biological Catalysis. *ChemCatChem* **2**, 724–761 (2010).
16. Tahir, M. *et al.* Efficient water oxidation through strongly coupled graphitic C₃N₄ coated cobalt hydroxide nanowires. *J. Mater. Chem. A* **4**, 12940–12946 (2016).
17. Li, Y., Hasin, P. & Wu, Y. Ni_xCo_{3-x}O₄ Nanowire Arrays for Electrocatalytic Oxygen Evolution. *Adv. Mater.* **22**, 1926–1929 (2010).
18. Zhao, Y. *et al.* Ultrafine NiO Nanosheets Stabilized by TiO₂ from Monolayer NiTi-LDH Precursors: An Active Water Oxidation Electrocatalyst. *J. Am. Chem. Soc.* **138**, 6517–6524 (2016).
19. Chen, R., Wang, H.-Y., Miao, J., Yang, H. & Liu, B. A flexible high-performance oxygen evolution electrode with three-dimensional NiCo₂O₄ core-shell nanowires. *Nano Energy* **11**, 333–340 (2015).
20. Wang, Y. *et al.* Reduced Mesoporous Co₃O₄ Nanowires as Efficient Water Oxidation Electrocatalysts and Supercapacitor Electrodes. *Adv. Energy Mater.* **4**, 1400696 (2014).
21. Meng, Y. *et al.* Structure–Property Relationship of Bifunctional MnO₂ Nanostructures: Highly Efficient, Ultra-Stable Electrochemical Water Oxidation and Oxygen Reduction Reaction Catalysts Identified in Alkaline Media. *J. Am. Chem. Soc.* **136**, 11452–11464 (2014).

22. Fekete, M. *et al.* Highly active screen-printed electrocatalysts for water oxidation based on β -manganese oxide. *Energy Environ. Sci.* **6**, 2222–2232 (2013).
23. Bergmann, A., Zaharieva, I., Dau, H. & Strasser, P. Electrochemical water splitting by layered and 3D cross-linked manganese oxides: correlating structural motifs and catalytic activity. *Energy Environ. Sci.* **6**, 2745–2755 (2013).
24. Liu, R., Wu, D., Feng, X. & Müllen, K. Nitrogen-Doped Ordered Mesoporous Graphitic Arrays with High Electrocatalytic Activity for Oxygen Reduction. *Angew. Chem. Int. Ed.* **49**, 2565–2569 (2010).
25. Smith, R. D. L. *et al.* Photochemical Route for Accessing Amorphous Metal Oxide Materials for Water Oxidation Catalysis. *Science* **340**, 60–63 (2013).
26. Feng, J.-X., Ye, S.-H., Xu, H., Tong, Y.-X. & Li, G.-R. Design and Synthesis of FeOOH/CeO₂ Heterolayered Nanotube Electrocatalysts for the Oxygen Evolution Reaction. *Adv. Mater.* **28**, 4698–4703 (2016).
27. Zhu, Y., Zhou, W., Sunarso, J., Zhong, Y. & Shao, Z. Phosphorus-Doped Perovskite Oxide as Highly Efficient Water Oxidation Electrocatalyst in Alkaline Solution. *Adv. Funct. Mater.* **26**, 5862–5872 (2016).
28. Rodríguez-reinoso, F. The role of carbon materials in heterogeneous catalysis. *Carbon* **36**, 159–175 (1998).
29. Maruyama, J., Sumino, K., Kawaguchi, M. & Abe, I. Influence of activated carbon pore structure on oxygen reduction at catalyst layers supported on rotating disk electrodes. *Carbon* **42**, 3115–3121 (2004).
30. Flandrois, S. & Simon, B. Carbon materials for lithium-ion rechargeable batteries. *Carbon* **37**, 165–180 (1999).
31. Thess, A. *et al.* Crystalline Ropes of Metallic Carbon Nanotubes. *Science* **273**, 483–487 (1996).
32. Zheng, B. *et al.* Efficient CVD Growth of Single-Walled Carbon Nanotubes on Surfaces Using Carbon Monoxide Precursor. *Nano Lett.* **2**, 895–898 (2002).

-
33. Yang, Xu, Tomita, A. & Kyotani, T. The Template Synthesis of Double Coaxial Carbon Nanotubes with Nitrogen-Doped and Boron-Doped Multiwalls. *J. Am. Chem. Soc.* **127**, 8956–8957 (2005).
34. Yang, Q.-H. *et al.* Dual Raman Features of Double Coaxial Carbon Nanotubes with N-Doped and B-Doped Multiwalls. *Nano Lett.* **5**, 2465–2469 (2005).
35. Hou, P.-X. *et al.* Synthesis of Nitrogen-Containing Microporous Carbon with a Highly Ordered Structure and Effect of Nitrogen Doping on H₂O Adsorption. *Chem. Mater.* **17**, 5187–5193 (2005).
36. Kim, T.-W., Park, I.-S. & Ryoo, R. A Synthetic Route to Ordered Mesoporous Carbon Materials with Graphitic Pore Walls. *Angew. Chem. Int. Ed.* **42**, 4375–4379 (2003).
37. Ahmadpour, A. & Do, D. D. The preparation of active carbons from coal by chemical and physical activation. *Carbon* **34**, 471–479 (1996).
38. Lu, A.-H. & Schüth, F. Nanocasting: A Versatile Strategy for Creating Nanostructured Porous Materials. *Adv. Mater.* **18**, 1793–1805 (2006).
39. Chaikittisilp, W. *et al.* Nanoporous carbons through direct carbonization of a zeolitic imidazolate framework for supercapacitor electrodes. *Chem. Commun.* **48**, 7259–7261 (2012).
40. Shih, Y.-H. *et al.* Nanoporous Carbons Derived from Metal-Organic Frameworks as Novel Matrices for Surface-Assisted Laser Desorption/Ionization Mass Spectrometry. *Small* **12**, 2057–2066 (2016).
41. Liu, B., Shioyama, H., Akita, T. & Xu, Q. Metal-Organic Framework as a Template for Porous Carbon Synthesis. *J. Am. Chem. Soc.* **130**, 5390–5391 (2008).
42. Mai, H. D., Rafiq, K. & Yoo, H. Nano Metal-Organic Framework-Derived Inorganic Hybrid Nanomaterials: Synthetic Strategies and Applications. *Chem. – Eur. J.* **23**, 5631–5651 (2017).
43. Kaneti, Y. V. *et al.* Nanoarchitected Design of Porous Materials and Nanocomposites from Metal-Organic Frameworks. *Adv. Mater.* **29**, 1604898 (2017).

44. Xia, W., Mahmood, A., Zou, R. & Xu, Q. Metal–organic frameworks and their derived nanostructures for electrochemical energy storage and conversion. *Energy Environ. Sci.* **8**, 1837–1866 (2015).
45. Liu, J., Zhu, D., Guo, C., Vasileff, A. & Qiao, S.-Z. Design Strategies toward Advanced MOF-Derived Electrocatalysts for Energy-Conversion Reactions. *Adv. Energy Mater.* **7**, 1700518 (2017).
46. Shen, K., Chen, X., Chen, J. & Li, Y. Development of MOF-Derived Carbon-Based Nanomaterials for Efficient Catalysis. *ACS Catal.* **6**, 5887–5903 (2016).
47. Liang, Z., Qu, C., Guo, W., Zou, R. & Xu, Q. Pristine Metal–Organic Frameworks and their Composites for Energy Storage and Conversion. *Adv. Mater.* **30**, 1702891 (2018).
48. Sun, J.-K. & Xu, Q. Functional materials derived from open framework templates/precursors: synthesis and applications. *Energy Environ. Sci.* **7**, 2071–2100 (2014).
49. Dang, S., Zhu, Q.-L. & Xu, Q. Nanomaterials derived from metal–organic frameworks. *Nat. Rev. Mater.* **3**, 1–14 (2017).
50. Wu, H. B. & Lou, X. W. (David). Metal-organic frameworks and their derived materials for electrochemical energy storage and conversion: Promises and challenges. *Sci. Adv.* **3**, eaap9252 (2017).
51. Qian, Y., Khan, I. A. & Zhao, D. Electrocatalysts Derived from Metal–Organic Frameworks for Oxygen Reduction and Evolution Reactions in Aqueous Media. *Small* **13**, 1701143 (2017).
52. Cao, X., Tan, C., Sindoro, M. & Zhang, H. Hybrid micro-/nano-structures derived from metal–organic frameworks: preparation and applications in energy storage and conversion. *Chem. Soc. Rev.* **46**, 2660–2677 (2017).
53. Wang, W., Xu, X., Zhou, W. & Shao, Z. Recent Progress in Metal-Organic Frameworks for Applications in Electrocatalytic and Photocatalytic Water Splitting. *Adv. Sci.* **4**, 1600371 (2017).

54. Wang, H., Zhu, Q.-L., Zou, R. & Xu, Q. Metal-Organic Frameworks for Energy Applications. *Chem* **2**, 52–80 (2017).
55. M. Barkholtz, H. & Liu, D.-J. Advancements in rationally designed PGM-free fuel cell catalysts derived from metal–organic frameworks. *Mater. Horiz.* **4**, 20–37 (2017).
56. Chaikittisilp, W., Ariga, K. & Yamauchi, Y. A new family of carbon materials: synthesis of MOF-derived nanoporous carbons and their promising applications. *J. Mater. Chem. A* **1**, 14–19 (2013).
57. Park, K. S. *et al.* Exceptional chemical and thermal stability of zeolitic imidazolate frameworks. *Proc. Natl. Acad. Sci.* **103**, 10186–10191 (2006).
58. Ma, S., Goenaga, G. A., Call, A. V. & Liu, D.-J. Cobalt Imidazolate Framework as Precursor for Oxygen Reduction Reaction Electrocatalysts. *Chem. – Eur. J.* **17**, 2063–2067 (2011).
59. Tian, J. *et al.* Optimized Synthesis of Fe/N/C Cathode Catalysts for PEM Fuel Cells: A Matter of Iron–Ligand Coordination Strength. *Angew. Chem. Int. Ed.* **52**, 6867–6870 (2013).
60. Zhao, D. *et al.* Highly Efficient Non-Precious Metal Electrocatalysts Prepared from One-Pot Synthesized Zeolitic Imidazolate Frameworks. *Adv. Mater.* **26**, 1093–1097 (2014).
61. Proietti, E. *et al.* Iron-based cathode catalyst with enhanced power density in polymer electrolyte membrane fuel cells. *Nat. Commun.* **2**, 1–9 (2011).
62. Palaniselvam, T., Biswal, B. P., Banerjee, R. & Kurungot, S. Zeolitic Imidazolate Framework (ZIF)-Derived, Hollow-Core, Nitrogen-Doped Carbon Nanostructures for Oxygen-Reduction Reactions in PEFCs. *Chem. – Eur. J.* **19**, 9335–9342 (2013).
63. Chen, Y. *et al.* Isolated Single Iron Atoms Anchored on N-Doped Porous Carbon as an Efficient Electrocatalyst for the Oxygen Reduction Reaction. *Angew. Chem. Int. Ed.* **56**, 6937–6941 (2017).
64. Deng, Y. *et al.* Well-Defined ZIF-Derived Fe–N Codoped Carbon Nanoframes as Efficient Oxygen Reduction Catalysts. *ACS Appl. Mater. Interfaces* **9**, 9699–9709 (2017).

65. Zhao, D. *et al.* Iron imidazolate framework as precursor for electrocatalysts in polymer electrolyte membrane fuel cells. *Chem. Sci.* **3**, 3200–3205 (2012).
66. Zheng, R. *et al.* A hollow spherical doped carbon catalyst derived from zeolitic imidazolate framework nanocrystals impregnated/covered with iron phthalocyanines. *J. Mater. Chem. A* **4**, 7859–7868 (2016).
67. Guan, B. Y., Yu, L. & Lou, X. W. (David). A dual-metal–organic-framework derived electrocatalyst for oxygen reduction. *Energy Environ. Sci.* **9**, 3092–3096 (2016).
68. Zhang, W. *et al.* Hollow carbon nanobubbles: monocrystalline MOF nanobubbles and their pyrolysis. *Chem. Sci.* **8**, 3538–3546 (2017).
69. Jiang, H.-L. *et al.* From Metal–Organic Framework to Nanoporous Carbon: Toward a Very High Surface Area and Hydrogen Uptake. *J. Am. Chem. Soc.* **133**, 11854–11857 (2011).
70. Banerjee, R. *et al.* High-Throughput Synthesis of Zeolitic Imidazolate Frameworks and Application to CO₂ Capture. *Science* **319**, 939–943 (2008).
71. Tang, J. *et al.* Thermal Conversion of Core–Shell Metal–Organic Frameworks: A New Method for Selectively Functionalized Nanoporous Hybrid Carbon. *J. Am. Chem. Soc.* **137**, 1572–1580 (2015).
72. Dou, S., Li, X., Tao, L., Huo, J. & Wang, S. Cobalt nanoparticle-embedded carbon nanotube/porous carbon hybrid derived from MOF-encapsulated Co₃O₄ for oxygen electrocatalysis. *Chem. Commun.* **52**, 9727–9730 (2016).
73. Wang, X. *et al.* MOF derived catalysts for electrochemical oxygen reduction. *J. Mater. Chem. A* **2**, 14064–14070 (2014).
74. Xia, B. Y. *et al.* A metal–organic framework-derived bifunctional oxygen electrocatalyst. *Nat. Energy* **1**, 15006 (2016).
75. Maldonado-Hódar, F. J., Moreno-Castilla, C., Rivera-Utrilla, J., Hanzawa, Y. & Yamada, Y. Catalytic Graphitization of Carbon Aerogels by Transition Metals. *Langmuir* **16**, 4367–4373 (2000).

76. Gao, W., Wan, Y., Dou, Y. & Zhao, D. Synthesis of Partially Graphitic Ordered Mesoporous Carbons with High Surface Areas. *Adv. Energy Mater.* **1**, 115–123 (2011).
77. Romero, J. *et al.* Metal-functionalized covalent organic frameworks as precursors of supercapacitive porous N-doped graphene. *J. Mater. Chem. A* **5**, 4343–4351 (2017).
78. Bezerra, C. W. B. *et al.* A review of Fe–N/C and Co–N/C catalysts for the oxygen reduction reaction. *Electrochimica Acta* **53**, 4937–4951 (2008).
79. Abellán, G., Coronado, E., Martí-Gastaldo, C., Ribera, A. & F. Sánchez-Royo, J. Layered double hydroxide (LDH)–organic hybrids as precursors for low-temperature chemical synthesis of carbon nanoforms. *Chem. Sci.* **3**, 1481–1485 (2012).
80. Fan, K. *et al.* Hollow Iron–Vanadium Composite Spheres: A Highly Efficient Iron-Based Water Oxidation Electrocatalyst without the Need for Nickel or Cobalt. *Angew. Chem. Int. Ed.* **56**, 3289–3293 (2017).
81. Seel, F., Wende, P., Marcolin, H. E., Trautwein, A. T. & Maeda, Y. Eisen(II)-Verbindungen von Imidazolen. *Z. Für Anorg. Allg. Chem.* **426**, 198–204 (1976).
82. Spek, A. L., Duisenberg, A. J. M. & Feiters, M. C. The structure of the three-dimensional polymer poly[μ -hexakis(2-methylimidazolato-N,N')-triiron(II)], [Fe₃(C₄H₅N₂)₆]_n. *Acta Crystallogr. C* **39**, 1212–1214 (1983).
83. Rettig, S. J., Storr, A., Summers, D. A., Thompson, R. C. & Trotter, J. Transition Metal Azolates from Metallocenes. 2. Synthesis, X-ray Structure, and Magnetic Properties of a Three-Dimensional Polymetallic Iron(II) Imidazolate Complex, a Low-Temperature Weak Ferromagnet. *J. Am. Chem. Soc.* **119**, 8675–8680 (1997).
84. Lu, A.-H. *et al.* Highly stable carbon-protected cobalt nanoparticles and graphite shells. *Chem. Commun.* 98–100 (2005) doi:10.1039/B414146F.
85. Wang, H., Maiyalagan, T. & Wang, X. Review on Recent Progress in Nitrogen-Doped Graphene: Synthesis, Characterization, and Its Potential Applications. *ACS Catal.* **2**, 781–794 (2012).
86. Sánchez, V., Storr, A. & Thompson, R. C. Magnetic and structural studies on 1,3-diazolate complexes of cobalt(II) □ The characterization of three new cobalt(II)

molecule-based magnets. *Can. J. Chem.* **80**, 133–140 (2002).

87. Dionigi, F. & Strasser, P. NiFe-Based (Oxy)hydroxide Catalysts for Oxygen Evolution Reaction in Non-Acidic Electrolytes. *Adv. Energy Mater.* **6**, 1600621 (2016).

Article 4

*Solvent-Free Synthesis of ZIFs: A Route toward the
Elusive Fe(II) Analogue of ZIF-8*

Journal of the American Chemical Society. 2019, 141, 7173–7180

Solvent-Free Synthesis of ZIFs: A Route toward the Elusive Fe(II) Analogue of ZIF-8

Javier López-Cabrelles,^{†,⊥} Jorge Romero,^{†,⊥} Gonzalo Abellán,^{†,‡,§,ⓑ} Mónica Giménez-Marqués,^{†,ⓑ} Miguel Palomino,^{||} Susana Valencia,^{||} Fernando Rey,^{||,ⓑ} and Guillermo Mínguez Espallargas^{*,†,ⓑ}

[†]Instituto de Ciencia Molecular (ICMol), Universidad de Valencia, c/Catedrático José Beltrán, 2, 46980 Paterna, Spain

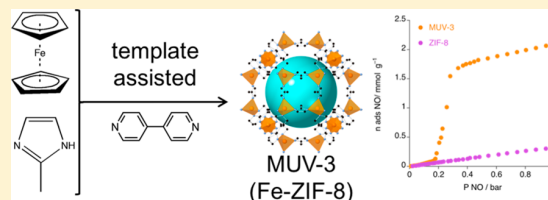
[‡]Department of Chemistry and Pharmacy, Friedrich-Alexander-Universität Erlangen-Nürnberg (FAU), Henkestraße 42, 91054 Erlangen, Germany

[§]Joint Institute of Advanced Materials and Processes (ZMP), Friedrich-Alexander-Universität Erlangen-Nürnberg (FAU), Dr.-Mack Straße 81, 90762 Fürth, Germany

^{||}Instituto de Tecnología Química (UPV-CSIC), Universitat Politècnica de València–Consejo Superior de Investigaciones Científicas, Av. de los Naranjos s/n, 46022 Valencia, Spain

Supporting Information

ABSTRACT: Herein we report the synthesis of an elusive metal–organic framework, the iron(II) analogue of ZIF-8 with the formula Fe(2-methylimidazolate)₂, here denoted as MUV-3. The preparation of this highly interesting porous material, inaccessible by common synthetic procedures, occurs in a solvent-free reaction upon addition of an easily detachable template molecule, yielding single crystals of MUV-3. This methodology can be extended to other metals and imidazolate derivatives, allowing the preparation of ZIF-8, ZIF-67, and the unprecedented iron(II) ZIFs Fe(2-ethylimidazolate)₂ and Fe(2-methylbenzimidazolate)₂. The different performance of MUV-3 toward NO sorption, in comparison to ZIF-8, results from the chemisorption of NO molecules, which also causes a gate-opening behavior. Finally, the controlled pyrolysis of MUV-3 results in a N-doped graphitic nanocomposite that exhibits extraordinary performance for the oxygen evolution reaction (OER), with low overpotential at different current densities (316 mV at 10 mA cm⁻²), low Tafel slope (37 mV per decade), high maximum current density (710 mA cm⁻² at 2.0 V vs RHE), and great durability (15 h).



INTRODUCTION

The development of metal–organic frameworks (MOFs) has grown very rapidly in the last few years, with numerous applications in a wide range of different fields resulting from the ample chemical versatility of this type of crystalline porous material.¹ An interesting feature of these solids is the possibility of modifying the metal content while retaining the same structure, thus offering a unique opportunity to tune their physical properties. This is exemplified by the extensive family M-MOF-74 with the formula M₂(dobdc) (dobdc⁴⁻ = 2,5-dioxidobenzene-1,4-dicarboxylate), which can be prepared for an ample range of metals, such as Mg, Mn, Fe, Co, Ni, Cu, and Zn or a combination of these.² Indeed, whereas Mg-MOF-74 is optimum for CO₂ capture,³ Fe-MOF-74 is suitable for alkane/alkene separation.⁴

Zeolitic imidazolate frameworks (ZIFs) are a subfamily of MOFs consisting of tetrahedral metal centers connected by imidazolate organic ligands.⁵ The most prominent member of this family is arguably Zn(Meim)₂ (MeimH = 2-methylimidazole),⁶ also known as ZIF-8, which has a sodalite (SOD) topology. This microporous crystalline solid has been widely studied in applications involving gas storage and separation because of its high porosity, high chemical stability, low

synthetic cost, easy preparation and is even commercially available. Four isostructural metal analogues to ZIF-8 have been reported to date: Co(Meim)₂ (also known as ZIF-67),⁷ Cd(Meim)₂ (also known as CdIF-1),⁸ Mg(Meim)₂,⁹ and more recently Mn(Meim)₂.¹⁰ However, the highly interesting iron analogue, i.e. Fe(Meim)₂, formed exclusively by iron(II) centers, has been elusive despite the vast number of potential applications of this solid, including catalysis, environmental and biomedical applications related to the low toxicity of endogenous iron(II).¹¹ In addition, Fe-based MOFs are good candidates for biomimetic studies with small molecules such as nitric oxide and its redox transformations.¹² Indeed, all attempts to adapt the different synthetic solvent-based procedures of ZIF-8 or ZIF-67 have been unfruitful when Fe(II) is used instead.¹³

Considering energy-related applications, MOFs have been demonstrated as suitable precursors for fabricating heteroatom-doped nanocarbons materials (NCs) that exhibit excellent activities for catalytic reactions.¹⁴ In particular, ZIF-derived nanocomposites have shown exceptional electrochemical

Received: March 11, 2019

Published: April 11, 2019

catalytic activity,¹⁵ which can be further improved with the inclusion of extrinsic iron sources before carbonization, either by insertion of iron-based molecular complexes within the pores of a ZIF or by directly mixing the ZIF with an iron-based material.¹⁶ Therefore, the highly porous Fe(Meim)₂, with a regular distribution of iron centers at the atomic level, is expected to be a superior single precursor for the formation of electrocatalytic NCs.

RESULTS AND DISCUSSION

Synthesis of MUV-3. In the present work, we report for the very first time a solvent-free synthesis compatible with Fe(II) to obtain MUV-3 (MUV: materials of University of Valencia), the iron analogue of ZIF-8, adapting a previously described method for the preparation of nonporous iron azolates.¹⁷ The reaction of ferrocene and 2-methylimidazole at 150 °C under vacuum, in the presence of 4,4'-bipyridine (acting as a template), results after 48 h in the formation of yellow single crystals of MUV-3 in a quantitative manner (Figure 1a). Structural, magnetic, and spectroscopic character-

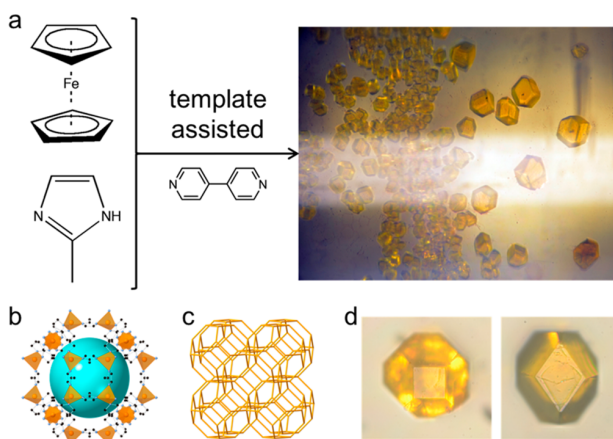


Figure 1. (a) Synthetic route to form MUV-3. (b) Crystal structure of MUV-3. Color key: Fe, orange tetrahedra; C, black balls; N, blue balls. The blue sphere (diameter of 11 Å) represents the empty space of the structure. Hydrogen atoms have been omitted for clarity. (c) Sodalite topology of MUV-3. (d) Two single crystals of MUV-3 showing the characteristic truncated rhombic dodecahedron morphology of ZIF-8 emphasizing the (100) and (110) faces.

ization unambiguously reveals the formation of the desired material. The good quality of the crystals permitted crystal structure determination by single-crystal X-ray diffraction despite the fact that the synthesis is carried out in the absence of solvents (Figure 1).

Single-crystal X-ray diffraction analysis of the as-synthesized material reveals that the yellow crystals are isostructural with ZIF-8 ($a = 17.1656(2)$ Å; space group $I\bar{4}3m$). The structure solution shows that each iron atom is connected to four nitrogen atoms from four imidazolate ligands (Fe–N distance of 2.032(1) Å and Fe...Fe distances of 6.069(1) Å), with voids of 2580 Å³ in size, which are accessible through windows of 3.3 Å, similar to the case for ZIF-8. Magnetic measurements indicate the presence of strong antiferromagnetic metal–metal interactions between the Fe(II) centers occurring through the imidazolate bridges (see section S1.6). The pores of the as-synthesized single crystals contain residual electron density in the voids (estimated to be 494 electrons), which can be

attributed to starting material, template, and/or cyclopentadiene resulting from the reaction.

In fact, the as-synthesized bulk material presents different peak intensities in the experimental X-ray powder diffraction (XRPD) pattern in comparison with the theoretical pattern (Figure S2), and also thermogravimetric analysis (TGA) reveals a 4% weight loss at 200 °C (Figure S7). A thorough activation process was therefore performed, which consisted of washing several times with dry acetonitrile for 48 h and subsequent overnight heating at 150 °C under vacuum. This yields an activated form of MUV-3, as demonstrated by XRPD (Figure S2).

In contrast to ZIF-8, ZIF-67, and CdIF-1, MUV-3 is quite sensitive to humidity in air (Figure S3), as has also been observed in Mg-ZIF-8⁸ and Mn-ZIF-8.⁹ Nevertheless, a time-resolved XRPD study indicates that MUV-3 is stable for a few hours in air before it starts to decompose. The stability in dry air drastically improves, pointing out humidity as the main stability issue (Figure S4). Despite this moisture sensitivity, the compound is stable for months under an inert (N₂ or Ar) atmosphere.

Remarkably, the use of 4,4'-bipyridine as template is essential for the exclusive formation of MUV-3; in its absence, the dense coordination polymer Fe(Meim)₂·0.13FeCp₂ is instead obtained (Figure S5).^{17d} The importance of a template in other types of solvent-free reactions (specifically mechanochemical reactions) was established by Friščić and co-workers, who showed that the presence of NH₄⁺ affects the thermodynamic/kinetic product in Zn-based ZIFs.¹⁸ We hypothesize that the presence of 4,4'-bipyridine blocks some of the coordination positions of the iron centers, thus affecting the kinetics of the crystal growth. We have screened an extensive number of templates, primarily based on pyridines, in order to examine the importance of pK_{HA} , the physical state of the template under the reaction conditions, the steric hindrance of the template and its coordination ability, establishing the importance of the last two (see section S1.3 in the Supporting Information). In fact, the structure-directing role of a pyridine derivative was previously observed for the formation, in solution, of ZIF-7. This MOF required the presence of 2,2'-bipyridine in order to obtain single crystals,¹⁹ although an alternative synthetic protocol was later described without the need for such a template.⁵ The role of the template in modifying the kinetics of the crystal growth is consistent with SEM images, which show the formation of truncated rhombohedral crystals with well-defined shapes and variable sizes that can be controlled with the reaction time (Figure S9). Indeed, the observed crystal shapes are significantly distorted in comparison with the characteristic ZIF-8 structure.²⁰ Such a distortion could be an effect of the template on the growth mechanism, which is currently being investigated.

Generalization of the Solvent-Free Synthesis. The solvent-free approach described here can be expanded to the preparation of other metal analogues isostructural with MUV-3 (Figure 2). Thus, using other metal sources compatible with chemical vapor deposition (CVD) techniques such as Zn(TMHD)₂ (TMHD = bis(2,2,6,6-tetramethyl-3,5-heptanedionato)), ZnO, and cobaltocene, we could also obtain ZIF-8 and ZIF-67 (see section S2.1). However, in contrast to the preparation of MUV-3, no template is required for the formation of ZIF-8 or ZIF-67, which opens the door to reach a variety of mixed-metal structures (see section S2).

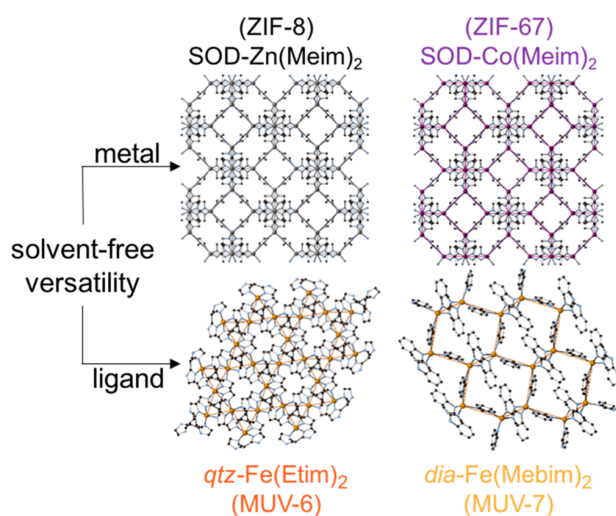


Figure 2. Expansion of the solvent-free methodology to prepare metal analogues isostructural with MUV-3, ZIF-8 (shown in black) and ZIF-67 (shown in purple), represented with the *sod* topology, and different topologies of other iron(II)-ZIFs obtained with the same solvent-free methodology (MUV-6 and MUV-7, shown in dark orange and light orange, respectively).

Furthermore, the use of different imidazolate ligands allows the preparation of other unprecedented iron(II)-ZIFs with different topologies, such as Fe(Etim)₂ (EtimH = 2-ethylimidazole), with *qtz* topology (denoted MUV-6), and Fe(Mebim)₂ (MebimH = 2-methylbenzylimidazole), with *dia* topology (denoted MUV-7). This highlights the relevance of the methodology described here (see section S2).

Gas Sorption in MUV-3. The porous nature of MUV-3 was assessed by N₂ sorption at 77 K. Activation of MUV-3 prior to measurement was achieved by treating the washed material at 150 °C under vacuum overnight. Figure 3a displays

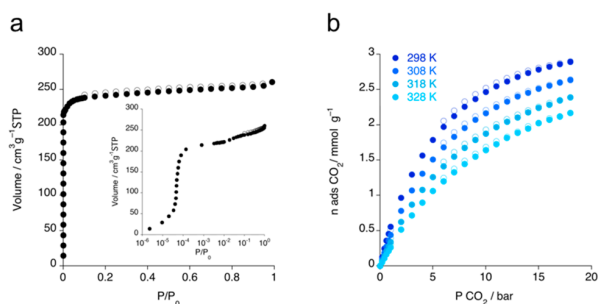


Figure 3. (a) N₂ sorption (solid circles) and desorption (open circles) of MUV-3 at 77 K. Inset: semilog plot revealing the two-step adsorption resulting from the flexibility of MUV-3. (b) CO₂ sorption (solid circles) and desorption (open circles) isotherms at different temperatures.

a characteristic two-step N₂ adsorption isotherm, with a plateau at 260 cm³ g⁻¹, which is reminiscent of that of the analogous ZIF-8 and ZIF-67 materials. Such a similar structural response upon sorption is attributed to the flexibility of the ligands.²¹ The obtained accessible surface area was calculated using the Brunauer–Emmett–Teller (BET) model, giving a value of 960 m² g⁻¹, which is significantly lower than that of ZIF-8 (ca. 1400 m² g⁻¹) likely due to the presence of organic

molecules remaining in the pores. The CO₂ sorption at 298 K, shown in Figure 3b, reveals a total uptake of 2.9 mmol g⁻¹ at 18 bar, whereas an isosteric heat of adsorption, q_{st} is found to be 20 kJ mol⁻¹ (Figure S16).

Furthermore, we examined the sorption capacity of MUV-3 toward the biologically active NO gas. MUV-3 material was subjected to NO volumetric adsorption at 273 K, presenting a total uptake of 2.1 mmol g⁻¹ at 1 bar (Figure 4a), which

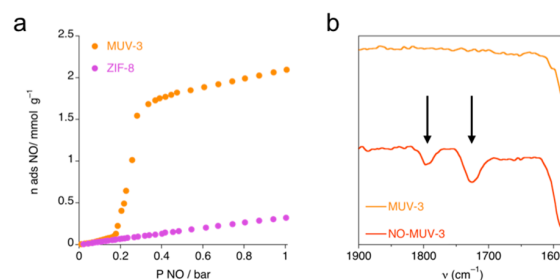


Figure 4. (a) NO sorption of MUV-3 (orange) and ZIF-8 (violet) at 273 K. (b) Infrared spectra of MUV-3 before (light orange) and after (dark orange) exposure to NO at room temperature and ambient pressure (the analogous spectrum for ZIF-8 is shown in Figure S21). The arrows indicate the appearance of characteristic vibrations of coordinated NO species.

corresponds to ca. 0.45 NO molecules per Fe²⁺ site. This suggests an incomplete NO loading, which is in agreement with the absence of a saturated plateau at 1 bar. This sorption value is lower than the exceptional storage capacity of the M-MOF-74 materials (up to 7 mmol g⁻¹)^{12,22} and is similar to that of HKUST-1 (3 mmol g⁻¹),²³ both of them presenting a high density of open metal sites. However, in sharp contrast to M-MOF-74, which shows a similar NO sorption regardless of the metal center,^{12,22} MUV-3 has a behavior significantly different from that of its isostructural Zn analogue (i.e., ZIF-8). As shown in Figure 4a, the behavior of both MUV-3 and ZIF-8 is analogous at low pressures (<0.15 bar), with a slow progressive loading of NO, which can be attributed to physisorption. Upon further pressure increase, the amount of NO adsorbed by MUV-3 rises sharply between 0.15 and 0.23 bar, which is not observed for ZIF-8. This is attributed to a “gate-opening” effect caused by the chemisorption of NO molecules to the Fe(II) centers that is unprecedented in MOFs, which typically show a constant NO sorption, even when flexible MOFs such as MIL-88 and MIL-53 are used.^{12a,24} The NO chemisorption is evidenced by IR spectroscopy, which reveals the appearance of characteristic vibrations of coordinated NO species¹² (ν_{N-O} 1720 and 1790 cm⁻¹, see Figure 4b) after MUV-3 is exposed to NO, which are absent in ZIF-8 (Figure S20). In addition, upon vacuum treatment of the NO-loaded MUV-3 and re-exposure to NO, we observe only a small sorption that can be attributed exclusively to physisorption (Figure S18), indicating that the coordinated NO molecules are retained in the structure. Interestingly, at low pressures (<0.2 bar) the amount of adsorbed NO is larger than that observed in the first sorption cycle, indicating that NO-MUV-3 (i.e., MUV-3 with chemisorbed NO) remains in the open form.

Synthesis of NC-MUV-3. Despite their typical low conductivity and relatively poor stability, which limit their use in energy storage devices, MOFs have been demonstrated as suitable precursors for fabricating heteroatom-doped

nanocarbon materials that exhibit excellent electrocatalytic activities for energy-related applications.²⁵ In fact, ZIFs have been successfully used as templates and precursors to create N-doped nanocarbons due to their highly ordered nanoporous structure and the use of nitrogen-rich organic ligands,²⁶ resulting in an abundance of nitrogen incorporation which significantly enhances the electrocatalytic performance toward oxygen reduction (ORR) and oxygen evolution (OER) reactions. In addition, as the catalytic activity of the nanocomposites resulting from the pyrolysis of a given ZIF can be increased by iron loading in the ZIFs,¹⁶ we investigated the electrocatalytic activity of the nanocomposite resulting from the controlled thermal treatment of MUV-3. In this sense, the Co analogue of MUV-3, ZIF-67, has been proved to be an excellent precursor of N-doped carbon nanotubes with outstanding ORR and OER performance,²⁷ as well as bimetallic $\text{Co}_x\text{Zn}_{100-x}$ -ZIF-8²⁸ and core-shell ZIF-67@ZIF-8 and ZIF-8@ZIF-67.^{29,30}

The low-temperature processing of MUV-3 in a CVD oven (700 °C for 3.5 h under an N_2 atmosphere) yields a black powdered carbon material, which is subsequently treated in 0.5 M H_2SO_4 solution for 6 h in order to remove residual metals, thoroughly washed with ethanol, and dried at 80 °C (see details in section S4). This nanocomposite (NC), denoted as NC-MUV-3, has been exhaustively characterized (see section S5). The formation of these nanostructures is related to the in situ formation of catalytically active metallic Fe nanoparticles (NPs), detected by XRPD (Figure S23), which originate from the presence of iron in the structure of the precursors.³¹ In fact, residual Fe NPs (0.78% according to ICP-OES analysis; Table S7) of ca. 10–30 nm in size that remained intact after acid leaching can be observed embedded in the carbon matrix, as shown in Figure 5a,b and as previously observed for Co.¹⁸ PXRD and XPS analyses of NC-MUV-3 confirm the formation of N-doped graphitic carbon (Figure 5c). Field-emission scanning electron microscopy (FESEM) analysis shows that the previously observed defined morphology is completely lost after the thermal treatment, giving a meso-/microporous crumpled material (Figure S25). High-resolution transmission electron microscopy (HRTEM) studies support the formation of graphitic carbon. In fact, the morphology of the sample consists of a carbon matrix composed of several graphene layers endowed with a marked corrugation, as can be observed in Figure 5. In addition, statistical Raman spectroscopy (>7000 single point spectra) shows average values of I_D/I_G ratios of ca. 0.85, suggesting a low density of disorder and carbon defects (Figure 5d).

Oxygen Evolution Reaction of NC-MUV-3. The electrocatalytic performance of NC-MUV-3 toward the oxygen evolution reaction (OER) was repeatedly tested in two different basic mediums (1 and 0.1 M KOH) in a standard three-electrode cell. For comparative purposes, we prepared working electrodes consisting of NC-MUV-3 and other materials, including other ZIF-derived electrocatalysts and commercial catalysts. NC-MUV-3 was investigated by linear sweep voltammetry (LSV), showing an excellent electrochemical performance. The polarization curves, depicted in Figure 6a, show low onset potentials of 1.588 and 1.541 V vs the reversible hydrogen electrode (RHE) for 1 and 0.1 M KOH, respectively (see also Figure S34). Overpotentials of 316 mV (1.542 V vs RHE) and 335 mV (1.561 V vs RHE) are required at $j = 10 \text{ mA cm}^{-2}$ for NC-MUV-3 in 1 and 0.1 M KOH, respectively. These values are much lower than those of

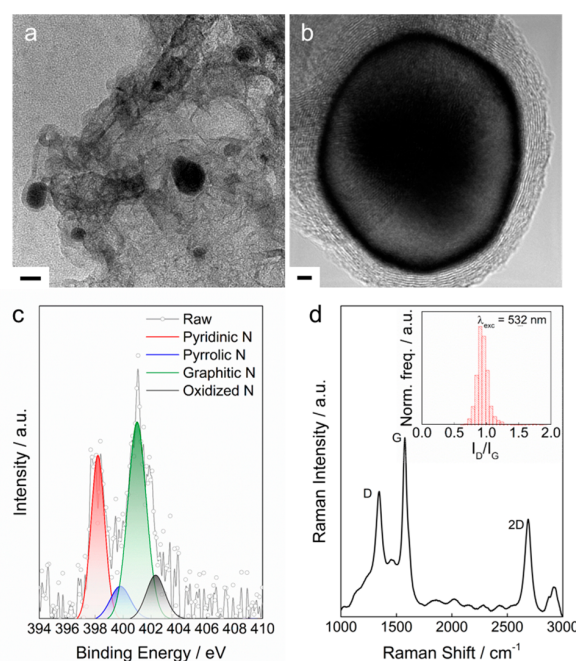


Figure 5. (a) HRTEM of NC-MUV-3 (general overview), showing the presence of the carbon matrix with embedded encapsulated Fe NPs. The scale bar is 20 nm. (b) High-magnification HRTEM of one Fe NP of ca. 30 nm surrounded by a carbon shell consisting of ca. 10 graphene layers. The scale bar is 2 nm. (c) XPS high-resolution N 1s spectrum. (d) Averaged Raman spectra of NC-MUV-3 (~7600 single-point spectra). The inset shows the corresponding I_D/I_G ratio distribution histogram ($\lambda_{\text{exc}} = 532 \text{ nm}$).

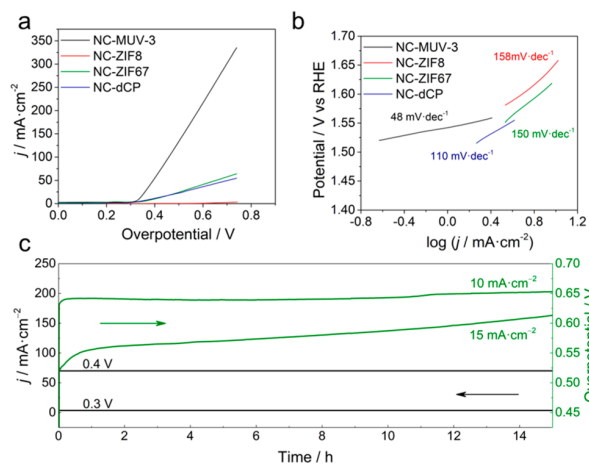


Figure 6. (a) Polarization curves of NC-MUV-3, NC-ZIF-8, NC-ZIF-67, and NC-dense-CP measured in 0.1 M KOH. Values for different conditions of pyrolysis, and comparison with benchmark catalysts can be found in the section S6 in the Supporting Information. (b) Tafel plots highlighting the corresponding values of Tafel slopes. (c) Potentiostatic (in green) and galvanostatic (in black) stability tests under a certain potential or current density of NC-MUV-3 in 0.1 M KOH.

other of ZIF-derived electrocatalysts (see Tables S9 and S10 for a complete list of MOF-derived nanocomposites and other relevant materials). A current density of 331 mA cm^{-2} at 0.74 V (2.0 V vs RHE) is obtained in 0.1 M KOH, a value over 500% better than that for the analogous NC-ZIF-67 (Figure

6a),³² also surpassing the values obtained for the benchmark electrocatalyst in basic medium, NiFe-based oxyhydroxides (NiFeOOH; see Figure S34).³³ In addition, a maximum current density of 710 mA cm⁻² is found in 1 M KOH, a great value when the large values of current density required for the development of oxygen evolution electrodes (>500 mA·cm⁻²) are taken into account,³⁴ which is of the order of magnitude of NiFeOOH. The excellent catalytic activity of NC-MUV-3 is also reflected in the Tafel slopes (Figure 6b), showing values in the range of 37 and 48 mV per decade in 1 and 0.1 M KOH, respectively, extremely low values that are much smaller than those for NiFeOOH (71 and 91 mV per decade in 1 and 0.1 M KOH, respectively) and related MOF-derived nanocarbon-based electrocatalysts, indicative of superior kinetics for the OER (see Tables S9 and S10). Finally, Figure 6c shows a high stability and durability of NC-MUV-3 at constant current densities j of 10 and 15 mA cm⁻² and with constant overpotentials, η , of 300 and 400 mV for 15 h (see Figure S37 for further information). The remarkable electrochemical OER performance is mainly attributed to the synergistic effect from chemical composition and the robust porous structure composed of micro- and mesopores as well as crystalline nitrogen-doped few-layer graphene.

CONCLUSIONS

In summary, we have presented the solvent-free synthesis of the highly interesting iron(II) analogue of ZIF-8, MUV-3, inaccessible through conventional preparation routes, thus paving the way for its exploration in many applications. The presence of a template is crucial for the facile synthesis of phase-pure single crystals of MUV-3, which show a gate-opening behavior analogous to that of ZIF-8. However, its behavior toward NO sorption is completely different due to the presence of Fe(II) centers, revealing a chemisorption of the NO molecules to the metal centers. The synthetic procedure presented here, using ferrocene as the source of iron, is also compatible with the chemical vapor deposition (CVD) techniques commonly used in microelectronics and recently shown to be effective with MOFs,³⁵ thus facilitating its applicability. Finally, upon controlled pyrolysis at 700 °C, the synergistic effect of the highly ordered nanoporous structure, the use of nitrogen-rich organic ligands, and the presence of Fe(II) causes the formation of a nanocomposite that shows an extraordinary performance in electrocatalytic water splitting. The low-cost materials used here, together with the low-temperature methodology and the facile processing, opens the possibility of using this novel material as a cheap alternative to current electrocatalysts.

EXPERIMENTAL SECTION

All reagents were commercially available and were used without further purification.

Synthesis of MUV-3. Ferrocene (30 mg, 0.16 mmol), 4,4-bipyridine (50 mg, 0.32 mmol, or an alternative template; see section S1.3 in the Supporting Information), and 2-methylimidazole (25 mg, 0.30 mmol) were combined and sealed under vacuum in a layering tube (4 mm diameter). The mixture was heated at 150 °C for 4 days to obtain yellow crystals suitable for X-ray single-crystal diffraction. The product was cooled to room temperature, and the layering tube was then opened. The unreacted precursors were extracted with acetonitrile and benzene, and MUV-3 was isolated as yellow crystals (yield 20%). Phase purity was established by X-ray powder diffraction. Details on the thermogravimetric, SEM, and magnetic analyses can be found in the Supporting Information.

ZIF-8, ZIF-67, MUV-6, and MUV-7 were synthesized in an analogous manner by adapting the previous procedure (see section S2 in the Supporting Information).

Single-Crystal Diffraction. Single crystals of MUV-3, MUV-6, and MUV-7 were mounted on cryoloops using a viscous hydrocarbon oil to coat the crystals. X-ray data were collected at 120 K on a Supernova diffractometer equipped with a graphite-monochromated Enhance (Mo) X-ray source ($\lambda = 0.71073$ Å). The program CrysAlisPro (Oxford Diffraction Ltd.) was used for unit cell determinations and data reduction. Empirical absorption correction was performed using spherical harmonics, implemented in the SCALE3 ABSPACK scaling algorithm. Crystal structures were solved and refined against all F^2 values by using the SHELXTL and Olex2 suite of programs.³⁶ Non-hydrogen atoms were refined anisotropically, and hydrogen atoms were placed at calculated positions (riding model). The solvent mask protocol in Olex 2 was implemented to account with the remaining electron density corresponding to disordered molecules of the starting material in MUV-3. In all, 494 electrons were found to be unaccounted for in the model (in a cavity of 2580 Å³ in size). A summary of the data collection and structure refinement is provided in Tables S1 and S3. CCDC-1825894 (MUV-3), -1899778 (MUV-6) and -1899779 (MUV-7) contain supplementary crystallographic data for this paper. These data can be obtained free of charge from The Cambridge Crystallographic Data Centre via www.ccdc.cam.ac.uk/data_request/cif (or from the Cambridge Crystallographic Data Centre, 12 Union Road, Cambridge CB21EZ, U.K.; fax (+44)1223-336-033; deposit@ccdc.cam.ac.uk).

Gas Sorption. Nitrogen isotherms were measured using a TRIFLEX apparatus (Micromeritics) at -196 °C. The sample was transferred from a sealed ampule to the sample holder inside a glovebox. Before the analysis, 50 mg of the thoroughly washed MUV-3 was degassed at 150 °C and $\sim 5 \times 10^{-6}$ bar overnight. The BET surface area was calculated by using the Brunauer–Emmett–Teller equation, and the micropore volume was calculated by the t -plot method.

The high-pressure CO₂ adsorption isotherms were measured in an IGA-100 gravimetric sorption analyzer (Hidden Isochema). A 50 mg portion of adsorbent was placed in a sample holder, and before measurement, the sample was degassed for 3 h at 100 °C under vacuum. CO₂ adsorption isotherms were acquired at 25, 35, 45 and 55 °C.

The NO adsorption isotherms were collected in a Micromeritics ASAP 2010 apparatus. In the first experiment, 200 mg of fresh MUV-3 was placed in the sample holder and activated at 100 °C under vacuum overnight. Then, the isotherm was measured at 0 °C up to 1 bar. In order to distinguish between physisorption and chemisorption, a second isotherm was measured on the same sample but with degassing at room temperature, assuming that only the physisorbed molecules were removed.

Infrared Spectra. IR spectra were recorded in a Platinum-ATR diamond Bruker spectrometer in the 4000–350 cm⁻¹ range using powdered samples.

Synthesis of NC-MUV-3. The controlled thermal treatment of MUV-3 was carried out in a CVD oven at a low temperature of 700 °C under a nitrogen atmosphere (ramp rate of 2 °C min⁻¹), and the material was kept at that temperature for 3.5 h. This process yielded a black powdered carbon material, which was subsequently treated in 0.5 M H₂SO₄ solution for 6 h in order to remove residual metals. The resulting sample was thoroughly washed with ethanol and dried at 80 °C, giving a nanocomposite (NC) denoted as NC-MUV-3. This reaction was carried out three times with similar electrocatalyst values for the three different batches. Details on the structural characterization of the NC can be found in section S5 in the Supporting Information.

Electrochemical Characterization of NC-MUV-3. The electrochemical experiments were performed using an Autolab electrochemical workstation (PGSTAT-128N potentiostat/galvanostat) connected to a personal computer that uses Nova 2.1 electrochemical software. The powdered materials were mixed with acetylene black and PVDF in a mass ratio of 80:10:10 in ethanol and deposited on a

nickel foam or carbon felt electrode. The as-prepared electrodes were dried overnight at 80 °C and pressed. Each working electrode contained about 0.20–0.30 mg cm⁻² of electroactive material and had a geometrical surface area of about 0.2 cm². A typical three-electrode experimental cell equipped with a stainless-steel plate having 4 cm² of surface area as the counter electrode, and a Metrohm Ag/AgCl (3 M KCl) as the reference electrode was used for the electrochemical characterization of the working electrodes. All measurements were carried out with magnetic agitation and nitrogen bubbling. In addition, chronoamperometric studies were performed at constant overpotentials ($j = 0.3$ and 0.4 V) and chronopotentiometric studies at constant current densities of 10 and 15 mA cm⁻². All potentials reported in this paper were converted to the RHE reference scale using $E(\text{RHE}) = E(\text{NHE}) + (0.059 \times \text{pH}) = E^\circ(\text{Ag}/\text{AgCl}) + 0.197 \text{ V} + (0.059 \times \text{pH})$ and to the OP reference scale using $\text{OP} = E(\text{NHE}) - 0.4 \text{ V}$, where $E(\text{NHE}) = E(\text{Ag}/\text{AgCl}) + 0.197 \text{ V}$.

■ ASSOCIATED CONTENT

Supporting Information

The Supporting Information is available free of charge on the ACS Publications website at DOI: 10.1021/jacs.9b02686.

General methods and materials, synthesis and characterization of MUV-3, MUV-6, MUV-7, ZIF-8, ZIF-67, and NC-MUV-3, and electrochemical measurements (PDF)
Crystallographic data for MUV-3 (CIF)
Crystallographic data for MUV-6 (CIF)
Crystallographic data for MUV-7 (CIF)

■ AUTHOR INFORMATION

Corresponding Author

*E-mail for G.M.E.: guillermo.minguez@uv.es.

ORCID

Gonzalo Abellán: 0000-0003-1564-6210

Mónica Giménez-Marqués: 0000-0002-4931-5711

Fernando Rey: 0000-0003-3227-5669

Guillermo Mínguez Espallargas: 0000-0001-7855-1003

Author Contributions

[†]J.L.-C. and J.R. contributed equally.

Notes

The authors declare no competing financial interest.

■ ACKNOWLEDGMENTS

The work has been supported by the European Union (ERC-2016-CoG 724681-S-CAGE and ERC-2018-StG 804110-2D-PnictoChem) and the Spanish MINECO (Structures of Excellence María de Maeztu MDM-2015-0538 and Severo Ochoa SEV-2016-0683; projects CTQ2014-59209-P, CTQ2017-89528-P, and MAT2015-71842-P). G.M.E. and M.G.-M. thank the MICINN for “Ramón y Cajal” and “Juan de la Cierva – Incorporación” fellowships, respectively. J.L.-C. acknowledges the Universitat de València for an “Atracció de Talent” grant. G.A. acknowledges support by the Generalitat Valenciana (CIDEGENT/2018/001) and the Deutsche Forschungsgemeinschaft (DFG; FLAG-ERA AB694/2-1). Dr. F. Hauke and Prof. A. Hirsch are acknowledged for their kind support with the Raman equipment.

■ REFERENCES

- (1) Maurin, G.; Serre, C.; Cooper, A.; Férey, G. The new age of MOFs and of their porous-related solids. *Chem. Soc. Rev.* **2017**, *46*, 3104–3107.
- (2) Wang, L. J.; Deng, H.; Furukawa, H.; Gándara, F.; Cordova, K. E.; Peri, D.; Yaghi, O. M. Synthesis and characterization of metal-

organic framework-74 containing 2, 4, 6, 8, and 10 different metals. *Inorg. Chem.* **2014**, *53*, 5881–5883.

- (3) Caskey, S. R.; Wong-Foy, A. G.; Matzger, A. J. Dramatic tuning of carbon dioxide uptake via metal substitution in a coordination polymer with cylindrical pores. *J. Am. Chem. Soc.* **2008**, *130*, 10870–10871.

- (4) (a) Bloch, E. D.; Queen, W. L.; Krishna, R.; Zdrozny, J. M.; Brown, C. M.; Long, J. R. Hydrocarbon separations in a metal-organic framework with open iron(II) coordination sites. *Science* **2012**, *335*, 1606–1610. (b) Queen, W. L.; Hudson, M. R.; Bloch, E. D.; Mason, J. A.; Gonzalez, M. I.; Lee, J. S.; Gygi, D.; Howe, J. D.; Lee, K.; Darwish, T. A.; James, M.; Peterson, V. K.; Teat, S. J.; Smit, B.; Neaton, J. B.; Long, J. R.; Brown, C. M. Comprehensive study of carbon dioxide adsorption in the metal-organic frameworks M₂(dobdc) (M = Mg, Mn, Fe, Co, Ni, Cu, Zn). *Chem. Sci.* **2014**, *5*, 4569–4581.

- (5) Park, K. S.; Ni, Z.; Côté, A. P.; Choi, J. Y.; Huang, R.; Uribe-Romo, F. J.; Chae, H. K.; O’Keeffe, M.; Yaghi, O. M. Exceptional chemical and thermal stability of zeolitic imidazolate frameworks. *Proc. Natl. Acad. Sci. U. S. A.* **2006**, *103*, 10186–10191.

- (6) Huang, X.-C.; Lin, Y.-Y.; Zhang, J.-P.; Chen, X.-M. Ligand-directed strategy for zeolite-type metal-organic frameworks: zinc(II) imidazolates with unusual zeolitic topologies. *Angew. Chem., Int. Ed.* **2006**, *45*, 1557–1559.

- (7) Banerjee, R.; Phan, A.; Wang, B.; Knobler, C.; Furukawa, H.; O’Keeffe, M.; Yaghi, O. M. High-throughput synthesis of zeolitic imidazolate frameworks and application to CO₂ capture. *Science* **2008**, *319*, 939–943.

- (8) Tian, Y.-Q.; Yao, S.-Y.; Gu, D.; Cui, K.-H.; Guo, D.-W.; Zhang, G.; Chen, Z.-X.; Zhao, D.-Y. Cadmium imidazolate frameworks with polymorphism, high thermal stability, and a large surface area. *Chem. - Eur. J.* **2010**, *16*, 1137–1141.

- (9) Horike, S.; Kadota, K.; Itakura, T.; Inukai, M.; Kitagawa, S. Synthesis of magnesium ZIF-8 from Mg(BH₄)₂. *Dalton Trans.* **2015**, *44*, 15107–15110.

- (10) Kadota, K.; Sivaniah, E.; Bureekaew, S.; Kitagawa, S.; Horike, S. Synthesis of manganese ZIF-8 from [Mn(BH₄)₂·3THF]·NaBH₄. *Inorg. Chem.* **2017**, *56*, 8744–8747.

- (11) (a) Brozek, C. K.; Miller, J. T.; Stoian, S. A.; Dinca, M. NO Disproportionation at a mononuclear site-isolated Fe²⁺ center in Fe²⁺-MOF-5. *J. Am. Chem. Soc.* **2015**, *137*, 7495–7501. (b) Liu, X.; Zhou, Y.; Zhang, J.; Tang, L.; Luo, L.; Zeng, G. Iron containing metal-organic frameworks: structure, synthesis, and applications in environmental remediation. *ACS Appl. Mater. Interfaces* **2017**, *9*, 20255–20275. (c) Osadchii, D. Y.; Olivos-Suarez, A. I.; Szécsényi, A.; Li, G.; Nasalevich, M. A.; Dugulan, I. A.; Crespo, P. S.; Hensen, E. J. M.; Veber, S. L.; Fedin, M. V.; Sankar, G.; Pidko, E. A.; Gascon, J. Isolated Fe sites in metal organic frameworks catalyze the direct conversion of methane to methanol. *ACS Catal.* **2018**, *8*, 5542–5548.

- (12) (a) McKinlay, A. C.; Eubank, J. F.; Wuttke, S.; Xiao, B.; Wheatley, P. S.; Bazin, P.; Lavalley, J.-C.; Daturi, M.; Vimont, A.; De Weireld, G.; Horcajada, P.; Serre, C.; Morris, R. E. Nitric oxide adsorption and delivery in flexible MIL-88(Fe) metal-organic frameworks. *Chem. Mater.* **2013**, *25*, 1592–1599. (b) Bloch, E. D.; Queen, W. L.; Chavan, S.; Wheatley, P. S.; Zdrozny, J. M.; Morris, R.; Brown, C. M.; Lamberti, C.; Bordiga, S.; Long, J. R. Gradual release of strongly bound nitric oxide from Fe₂(NO)₂(dobdc). *J. Am. Chem. Soc.* **2015**, *137*, 3466–3469. (c) Brozek, C. K.; Miller, J. T.; Stoian, S. A.; Dinca, M. NO disproportionation at a mononuclear site-isolated Fe²⁺ center in Fe²⁺-MOF-5. *J. Am. Chem. Soc.* **2015**, *137*, 7495–7501.

- (13) Phan, A.; Doonan, C. J.; Uribe-Romo, F. J.; Knobler, C. B.; O’Keeffe, M.; Yaghi, O. M. Synthesis, structure, and carbon dioxide capture properties of zeolitic imidazolate frameworks. *Acc. Chem. Res.* **2010**, *43*, 58–67.

- (14) (a) Liu, B.; Shioyama, H.; Akita, T.; Xu, Q. Metal-organic framework as a template for porous carbon synthesis. *J. Am. Chem. Soc.* **2008**, *130*, 5390–5391. (b) Santos, V. P.; Wezendonk, T. A.; Jaén, J. J. D.; Dugulan, A. I.; Nasalevich, M. A.; Islam, H.-U.;

- Chojceki, A.; Sartipi, S.; Sun, X.; Hakeem, A. A.; Koeken, A. C. J.; Ruitenbeek, M.; Davidian, T.; Meima, G. R.; Sankar, G.; Kapteijn, F.; Makkee, M.; Gascon, J. Metal organic framework-mediated synthesis of highly active and stable Fischer–Tropsch catalysts. *Nat. Commun.* **2015**, *6*, 6451. (c) Cao, X.; Tan, C.; Sindoro, M.; Zhang, H. Hybrid micro-/nano-structures derived from metal–organic frameworks: preparation and applications in energy storage and conversion. *Chem. Soc. Rev.* **2017**, *46*, 2660–2677. (d) Dang, S.; Zhu, Q.-L.; Xu, Q. Nanomaterials derived from metal–organic frameworks. *Nat. Rev. Mater.* **2017**, *3*, 17075. (e) Zhang, H.; Liu, X.; Wu, Y.; Guan, C.; Cheetham, A. K.; Wang, J. MOF-derived nanohybrids for electrocatalysis and energy storage: current status and perspectives. *Chem. Commun.* **2018**, *54*, 5268.
- (15) Zhao, D.; Shui, J. L.; Grabstanowicz, L. R.; Chen, C.; Commet, S. M.; Xu, T.; Lu, J.; Liu, D. J. Highly efficient non-precious metal electrocatalysts prepared from one-pot synthesized zeolitic imidazolate frameworks. *Adv. Mater.* **2014**, *26*, 1093–1097.
- (16) (a) Zhao, D.; Shui, J.-L.; Chen, C.; Chen, X.; Reprogel, B. M.; Wang, D.; Liu, D.-J. Iron imidazolate framework as precursor for electrocatalysts in polymer electrolyte membrane fuel cells. *Chem. Sci.* **2012**, *3*, 3200. (b) Zheng, R.; Liao, S.; Hou, S.; Qiao, X.; Wang, G.; Liu, L.; Shu, T.; Du, L. A hollow spherical doped carbon catalyst derived from zeolitic imidazolate framework nanocrystals impregnated/covered with iron phthalocyanines. *J. Mater. Chem. A* **2016**, *4*, 7859–7868. (c) Chen, Y.; Ji, S.; Wang, Y.; Dong, J.; Chen, W.; Li, Z.; Shen, R.; Zheng, L.; Zhuang, Z.; Wang, D.; Li, Y. Isolated single iron atoms anchored on N-doped porous carbon as an efficient electrocatalyst for the Oxygen Reduction Reaction. *Angew. Chem., Int. Ed.* **2017**, *56*, 6937–6941.
- (17) (a) Seel, F.; Wende, P.; Marcolin, H. E.; Trautwein, A. T.; Maeda, Y. Iron(II) compounds of imidazoles. *Z. Anorg. Allg. Chem.* **1976**, *426*, 198–204. (b) Spek, A. L.; Duisenberg, A. J. M.; Feiters, M. C. The structure of the three-dimensional polymer poly[μ -hexakis(2-methylimidazolato-N,N')-triiron(II)], $[\text{Fe}_3(\text{C}_4\text{H}_5\text{N}_2)_6]_n$. *Acta Crystallogr., Sect. C: Cryst. Struct. Commun.* **1983**, *39*, 1212–1214. (c) Rettig, S. J.; Storr, A.; Summers, D. A.; Thompson, R. C.; Trotter, J. Transition metal azolates from metallocenes. 2. Synthesis, X-ray structure, and magnetic properties of a three-dimensional polymetallic iron(II) imidazolate complex, a low-temperature weak ferromagnet. *J. Am. Chem. Soc.* **1997**, *119*, 8675–8680. (d) Rettig, S. J.; Storr, A.; Summers, D. A.; Thompson, R. C.; Trotter, J. Iron(II) 2-methylimidazolate and copper(II) 1,2,4-triazolate complexes: systems exhibiting long-range ferromagnetic ordering at low temperatures. *Can. J. Chem.* **1999**, *77*, 425–433. (e) López-Cabrelles, J.; Mañas-Valero, S.; Vitórica-Yrezábal, I. J.; Bereciartua, P. J.; Rodríguez-Velamazán, J. A.; Waerenborgh, J. C.; Vieira, B. J. C.; Davidovikj, D.; Steeneken, P. G.; van der Zant, H. S. J.; Mínguez Espallargas, G.; Coronado, E. Isorecticular two-dimensional magnetic coordination polymers prepared through pre-synthetic ligand functionalization. *Nat. Chem.* **2018**, *10*, 1001–1007.
- (18) Beldon, P. J.; Fábíán, L.; Stein, R. S.; Thirumurugan, A.; Cheetham, A. K.; Frišćić, T. Rapid room-temperature synthesis of zeolitic imidazolate frameworks by using mechanochemistry. *Angew. Chem., Int. Ed.* **2010**, *49*, 9640–9643.
- (19) Huang, X.; Zhang, J.; Chen, X. $[\text{Zn}(\text{Bim})_2] \cdot (\text{H}_2\text{O})_{1.67}$: A metal-organic open-framework with sodalite topology. *Chin. Sci. Bull.* **2003**, *48*, 1531.
- (20) Avci, C.; Ariñez-Soriano, J.; Carné-Sánchez, A.; Guillerm, V.; Carbonell, C.; Imaz, I.; MasPOCH, D. Post-synthetic anisotropic wet-chemical etching of colloidal sodalite ZIF crystals. *Angew. Chem., Int. Ed.* **2015**, *54*, 14417–14421.
- (21) Fairen-Jimenez, D.; Moggach, S. A.; Wharmby, M. T.; Wright, P. A.; Parsons, S.; Düren, T. Opening the gate: framework flexibility in ZIF-8 explored by experiments and simulations. *J. Am. Chem. Soc.* **2011**, *133*, 8900–8902.
- (22) McKinlay, A. C.; Xiao, B.; Wragg, D. S.; Wheatley, P. S.; Megson, I. L.; Morris, R. E. Exceptional behavior over the whole adsorption–storage–delivery cycle for NO in porous metal organic frameworks. *J. Am. Chem. Soc.* **2008**, *130*, 10440–10444.
- (23) Xiao, B.; Wheatley, P. S.; Zhao, X.; Fletcher, A. J.; Fox, S.; Rossi, A. G.; Megson, I. L.; Bordiga, S.; Regli, L.; Thomas, K. M.; Morris, R. E. High-capacity hydrogen and nitric oxide adsorption and storage in a metal–organic framework. *J. Am. Chem. Soc.* **2007**, *129*, 1203–1209.
- (24) Hinks, N. J.; McKinlay, A. C.; Xiao, B.; Wheatley, P. S.; Morris, R. E. Metal organic frameworks as NO delivery materials for biological applications. *Microporous Mesoporous Mater.* **2010**, *129*, 330–334.
- (25) (a) Mai, H. D.; Rafiq, K.; Yoo, H. Nano metal-organic framework-derived inorganic hybrid nanomaterials: synthetic strategies and applications. *Chem. - Eur. J.* **2017**, *23*, 5631–5651. (b) Kaneti, Y. V.; Tang, J.; Salunkhe, R. R.; Jiang, X.; Yu, A.; Wu, K. C. W.; Yamauchi, Y. Nanoarchitected design of porous materials and nanocomposites from metal-organic frameworks. *Adv. Mater.* **2017**, *29*, 1604898. (c) Xia, W.; Mahmood, A.; Zou, R.; Xu, Q. Metal–organic frameworks and their derived nanostructures for electrochemical energy storage and conversion. *Energy Environ. Sci.* **2015**, *8*, 1837–1866. (d) Liu, J.; Zhu, D.; Guo, C.; Vasileff, A.; Qiao, S. Z. Design strategies toward advanced MOF-derived electrocatalysts for energy-conversion reactions. *Adv. Energy Mater.* **2017**, *7*, 1700518. (e) Liang, Z.; Qu, C.; Guo, W.; Zou, R.; Xu, Q. Pristine metal-organic frameworks and their composites for energy storage and conversion. *Adv. Mater.* **2018**, *30*, 1702891. (f) Guan, B. Y.; Yu, X. Y.; Wu, H. B.; Lou, X. W. D. Complex nanostructures from materials based on metal–organic frameworks for electrochemical energy storage and conversion. *Adv. Mater.* **2017**, *29*, 1703614. (g) Shen, K.; Chen, X.; Chen, J.; Li, Y. Development of MOF-derived carbon-based nanomaterials for efficient catalysis. *ACS Catal.* **2016**, *6*, 5887–5903. (h) Sun, J.-K.; Xu, Q. Functional materials derived from open framework templates/precursors: synthesis and applications. *Energy Environ. Sci.* **2014**, *7*, 2071–2100. (i) Wu, H. B.; Lou, X. W. Metal-organic frameworks and their derived materials for electrochemical energy storage and conversion: promises and challenges. *Sci. Adv.* **2017**, *3*, eaap9252. (j) Qian, Y.; Khan, I. A.; Zhao, D. Electrocatalysts derived from metal-organic frameworks for oxygen reduction and evolution reactions in aqueous media. *Small* **2017**, *13*, 1701143. (k) Wang, W.; Xu, X.; Zhou, W.; Shao, Z. Recent progress in metal-organic frameworks for applications in electrocatalytic and photocatalytic water splitting. *Adv. Sci.* **2017**, *4*, 1600371. (l) Wang, H.; Zhu, Q.-L.; Zou, R.; Xu, Q. Metal-organic frameworks for energy applications. *Chem.* **2017**, *2*, 52–80. (m) Barkholtz, H. M.; Liu, D.-J. Advancements in rationally designed PGM-free fuel cell catalysts derived from metal–organic frameworks. *Mater. Horiz.* **2017**, *4*, 20–37.
- (26) Chaikittisilp, W.; Hu, M.; Wang, H.; Huang, H.-S.; Fujita, T.; Wu, K. C.-W.; Chen, L.-C.; Yamauchi, Y.; Ariga, K. Nanoporous carbons through direct carbonization of a zeolitic imidazolate framework for supercapacitor electrodes. *Chem. Commun.* **2012**, *48*, 7259.
- (27) Xia, B. Y.; Yan, Y.; Li, N.; Wu, H. B.; Lou, X. W.; Wang, X. A Metal–organic framework-derived bifunctional oxygen electrocatalyst. *Nat. Ener.* **2016**, *1*, 15006.
- (28) Gadipelli, S.; Zhao, T.; Shevlin, S. A.; Guo, Z. Switching effective oxygen reduction and evolution performance by controlled graphitization of a cobalt–nitrogen–carbon framework system. *Energy Environ. Sci.* **2016**, *9*, 1661–1667.
- (29) Wang, Z.; Lu, Y.; Yan, Y.; Larissa, T. Y. P.; Zhang, X.; Wu, D.; Zhang, H.; Yang, Y.; Wang, X. Core-shell carbon materials derived from metal-organic frameworks as an efficient oxygen bifunctional electrocatalyst. *Nano Energy* **2016**, *30*, 368–378.
- (30) Zhao, J.; Quan, X.; Chen, S.; Liu, Y.; Yu, H. Cobalt nanoparticles encapsulated in porous carbons derived from core-shell ZIF67@ZIF8 as efficient electrocatalysts for Oxygen Evolution Reaction. *ACS Appl. Mater. Interfaces* **2017**, *9*, 28685–28694.
- (31) Romero, J.; Rodríguez-San-Miguel, D.; Ribera, A.; Mas-Ballesté, R.; Otero, T. F.; Manet, I.; Licio, F.; Abellán, G.; Zamora, F.; Coronado, E. Metal-functionalized covalent organic frameworks as

precursors of supercapacitive porous N-doped graphene. *J. Mater. Chem. A* **2017**, *5*, 4343–4351.

(32) Dou, S.; Li, X.; Tao, L.; Huo, J.; Wang, S. Cobalt nanoparticle-embedded carbon nanotube/porous carbon hybrid derived from MOF-encapsulated Co_3O_4 for oxygen electrocatalysis. *Chem. Commun.* **2016**, *52*, 9727–9730.

(33) Dionigi, F.; Strasser, P. NiFe-based (oxy)hydroxide catalysts for Oxygen Evolution Reaction in non-acidic electrolytes. *Adv. Energy Mater.* **2016**, *6*, 1600621.

(34) Lu, X.; Zhao, C. Electrodeposition of hierarchically structured three-dimensional nickel–iron electrodes for efficient oxygen evolution at high current densities. *Nat. Commun.* **2015**, *6*, 6616.

(35) Stassen, I.; Styles, M.; Greci, G.; Van Gorp, H.; Vanderlinden, W.; De Feyter, S.; Falcaro, P.; De Vos, D.; Vereecken, P.; Ameloot, R. Chemical vapour deposition of zeolitic imidazolate framework thin films. *Nat. Mater.* **2016**, *15*, 304–310.

(36) (a) Sheldrick, G. M. Crystal structure refinement with SHELXL. *Acta Crystallogr., Sect. C: Struct. Chem.* **2015**, *71*, 3–8.

(b) Dolomanov, O. V.; Bourhis, L. J.; Gildea, R. J.; Howard, J. A. K.; Puschmann, H. OLEX2: a complete structure solution, refinement and analysis program. *J. Appl. Crystallogr.* **2009**, *42*, 339–341.

Solvent-free synthesis of ZIFs: a route towards the elusive Fe(II) analogue of ZIF-8

Javier López-Cabrelles,^{a,†} Jorge Romero,^{a,†} Gonzalo Abellán,^{a,b} Mónica Giménez-Marqués,^a Miguel Palomino,^c Susana Valencia,^c Fernando Rey,^c Guillermo Mínguez Espallargas^{a,*}

^a Instituto de Ciencia Molecular (ICMol), Universitat de València, c/Catedrático José Beltrán, 2, 46980 Paterna, Spain.

^b Department of Chemistry and Pharmacy & Joint Institute of Advanced Materials and Processes (ZMP), Friedrich-Alexander-Universität Erlangen-Nürnberg (FAU), Henkestr. 42, 91054 Erlangen and Dr.-Mack Str. 81, 90762 Fürth, Germany.

^c Instituto de Tecnología Química (UPV-CSIC), Universitat Politècnica de València–Consejo Superior de Investigaciones Av. de los Naranjos s/n, 46022 Valencia, Spain.

Supporting Information

Contents

S1. Characterization of MUV-3	3
S1.1 Single crystal diffraction.....	3
S1.2 X-Ray powder diffraction.....	4
S1.3 Template effect	7
S1.4 Thermogravimetric analysis	9
S1.5 Scanning electronic microscopy	10
S1.6 Magnetic properties	11
S2 Solvent-free synthesis and characterization of others ZIFs: ZIF-8, ZIF-67, qtz-[Fe(etim) ₂] (MUV-6), dia-[Fe(mebim) ₂] (MUV-7)	13
S2.1 Synthesis	13
S2.2 Characterization	14
S2.2.1 Single crystal diffraction.....	14
S2.2.2 X-Ray powder diffraction.....	15
S2.2.3 Thermogravimetric analysis	17
S3 Gas sorption measurements	18
S3.1 Nitrogen and CO ₂ adsorption.....	18
S3.2 Nitric oxide adsorption	21
S3.2.1 Infrared study of NO sorption.....	22
S3.2.2 X-Ray powder diffraction.....	24
S4 Synthesis of NC-MUV-3	25
S5 Characterization of NC-MUV-3	26
S5.1 X-ray powder diffraction	26
S5.2 Field-emission scanning electron microscopy	28
S5.3 High-resolution transmission electron microscopy	30

S5.4 XPS characterization	31
S5.5 Inductively Coupled-Plasma Optical Emission	33
S5.6 Raman Spectroscopy	34
S5.7 Textural characterization of NC-MUV-3.	35
S6 Electrochemical characterization of NC-MUV-3	37
S6.1 Polarization curves for Oxygen Evolution Reaction	38
S6.2 Current densities for Oxygen Evolution Reaction.....	41
S6.3 Stability testings	42
S7 References.....	45

S1. Characterization of MUV-3

S1.1 Single crystal diffraction

Table S1. Crystallographic information for MUV-3

	MUV-3
Crystal colour	Yellow
Crystal size (mm)	0.18 × 0.16 × 0.15
Crystal system	Cubic
Space group, <i>Z</i>	<i>I</i> -43 <i>m</i> , 12
<i>a</i> (Å)	17.1656(2)
<i>V</i> (Å ³)	5057.98(18)
Density (Mg.m ⁻³)	0.859
Wavelength (Å)	0.71073
Temperature (K)	120
μ(Mo-Kα) (mm ⁻¹)	0.870
2θ range (°)	6.714 to 50.08
Reflns collected	60287
Independent reflns (<i>R</i> _{int})	867 (0.1164)
Reflns used in refinement, <i>n</i>	867
L.S. parameters, <i>p</i>	34
No. of restraints, <i>r</i>	0
<i>R</i> 1 (<i>F</i>) ^a <i>I</i> > 2.0σ(<i>I</i>)	0.0482
<i>wR</i> 2(<i>F</i> ²), ^b all data	0.1456
<i>S</i> (<i>F</i> ²), ^c all data	1.507
Flack parameter	0.04(2)

[a] $R1(F) = \sum(|F_o| - |F_c|) / \sum|F_o|$; [b] $wR2(F^2) = [\sum w(F_o^2 - F_c^2)^2 / \sum wF_o^4]^{1/2}$; [c] $S(F^2) = [\sum w(F_o^2 - F_c^2)^2 / (n + r - p)]^{1/2}$

S1.2 X-Ray powder diffraction

A polycrystalline sample of **MUV-3** was lightly ground in an agate mortar and pestle and used to fill a 0.5 mm borosilicate capillary that was mounted and aligned on an Empyrean PANalytical powder diffractometer, using Cu K α radiation ($\lambda = 1.54056 \text{ \AA}$). Two repeated measurements were collected at room temperature ($2\theta = 2\text{--}40^\circ$) and merged in a single diffractogram, with sharp and intense peaks denoting the high crystallinity of the material (Figure S1). Pawley refinements^[1] were performed using the TOPAS computer program^[2] and revealed an excellent fit to a one-phase model for compound **MUV-3**, indicating the absence of any other detectable crystalline phases ($R_{wp} = 0.0169$, GOF = 1.539).

Figure S2 shows the comparison of the peaks intensity between the theoretical, as-synthesized and activated **MUV-3**. In Figures S3 and S4 the powder diffraction pattern shows the stability of **MUV-3** in air.

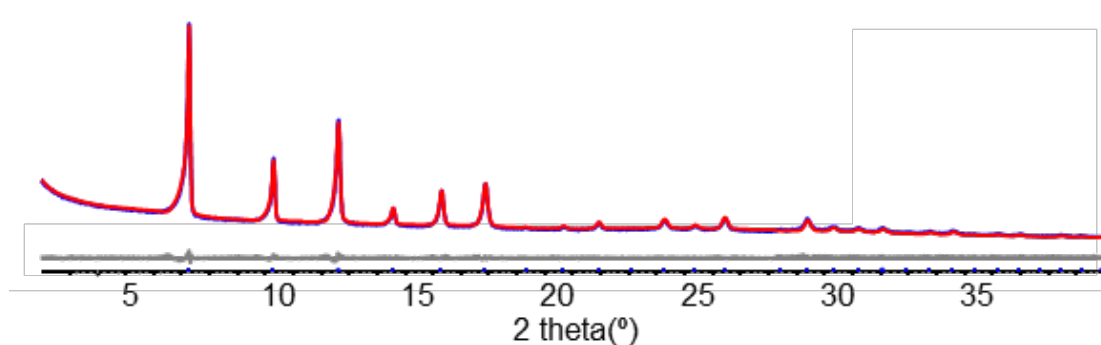


Figure S1. Observed (blue) and calculated (red) profiles and difference plot $[(I_{obs} - I_{calcd})]$ (gray) of the Pawley refinement of **MUV-3** (2θ range $4.0\text{--}40.0^\circ$).

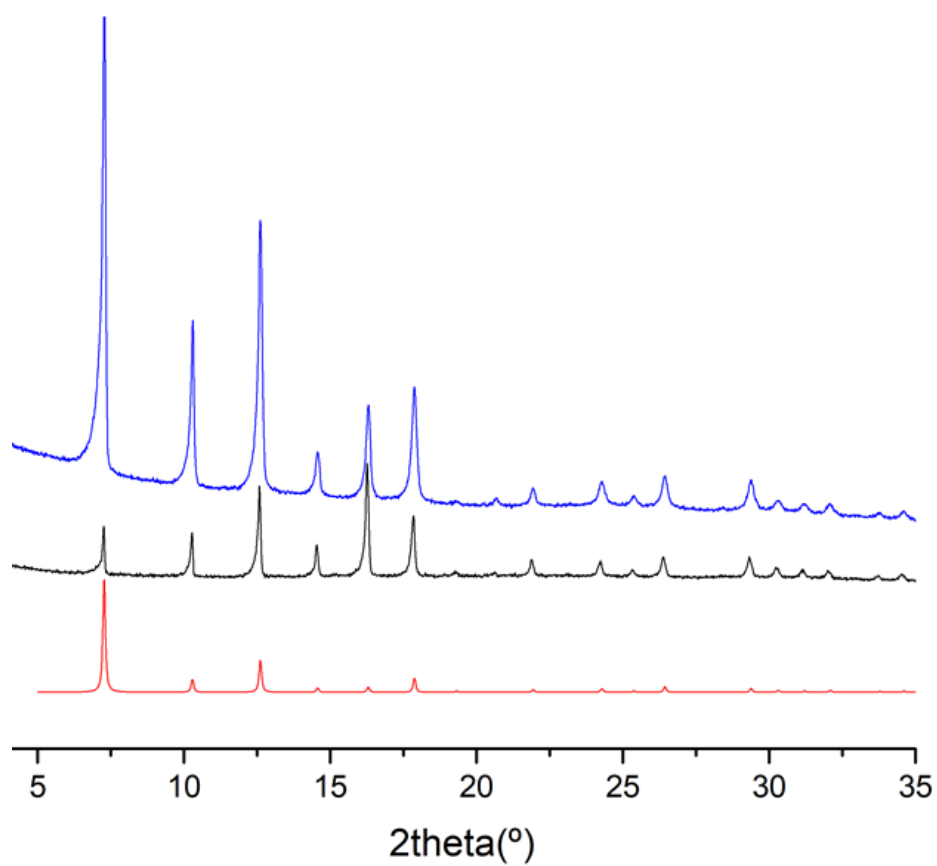


Figure S2. X-ray powder diffraction of **MUV-3** to check the activation process. In red, theoretical powder pattern of **MUV-3**; in black, as-synthesized; and in blue, the activated material. Note the change in the intensity of the peaks upon activation.

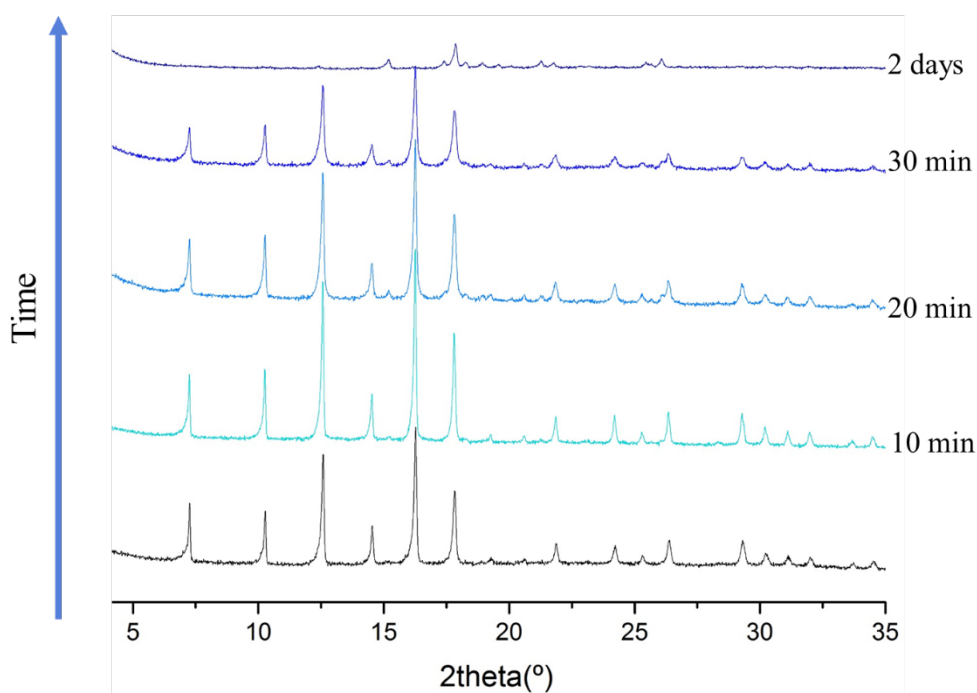


Figure S3. Test of stability in air with X-ray powder diffraction of **MUV-3** at different times in air atmosphere.

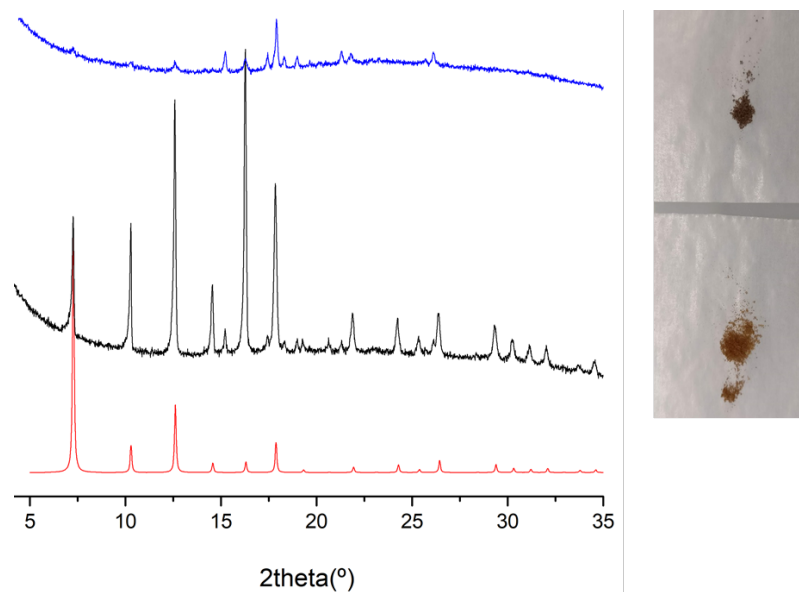


Figure S4. Test of stability in air with X-ray powder diffraction of **MUV-3** under dry air and vapour water atmosphere. In red, theoretical powder pattern of **MUV-3**; in black, **MUV-3** after 4 hours exposure at dry air atmosphere; in blue, **MUV-3** after 1 hour exposure to humid air atmosphere.

S1.3 Template effect

Figure S5 shows the template effect and the impurity of the **MUV-3** synthesis without the presence of 4,4-bipyridine. In order to elucidate the possible mechanism of the reaction, we chose a family of pyridines with diverse characteristics, like physical state at the reaction, pK_{HA} , steric hindrance of the nitrogen of the pyridine ring and substitution of the pyridine ring. We observe that pyridine and 4-aminopyridine do not act as template, resulting in the formation of both porous **MUV-3** and the dense coordination polymer $Fe(Meim)_2 \cdot 0.13(FeCp_2)$. We hypothesize that the nitrogen atom of the pyridine interacts with the iron blocking the coordination and directing the structure formation to the porous material. If the pyridine has a small substituted group (or none), it does not block the coordination of the iron and does not act as a template (as observed with pyridine and 4-aminopyridine). If a bulky group is used in the 2 position, it blocks the interaction of the pyridine nitrogen with the iron, also therefore it does not act either as a template (as observed with 2-bromopyridine).

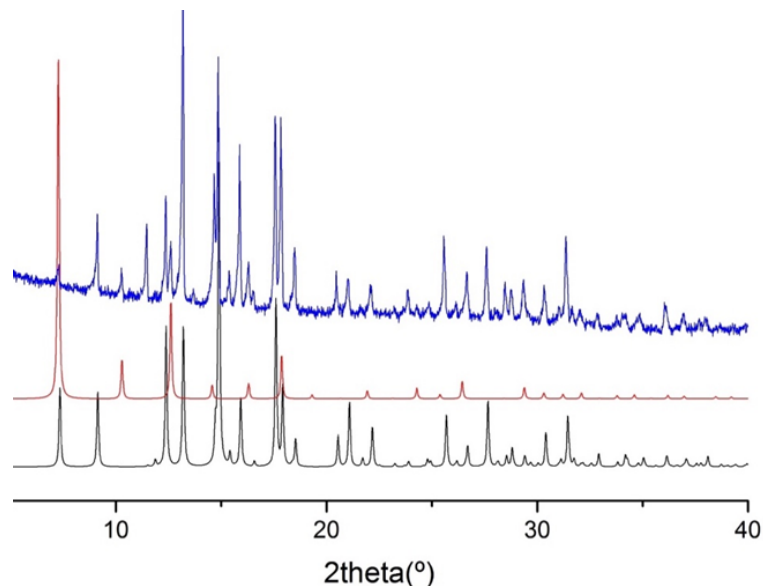
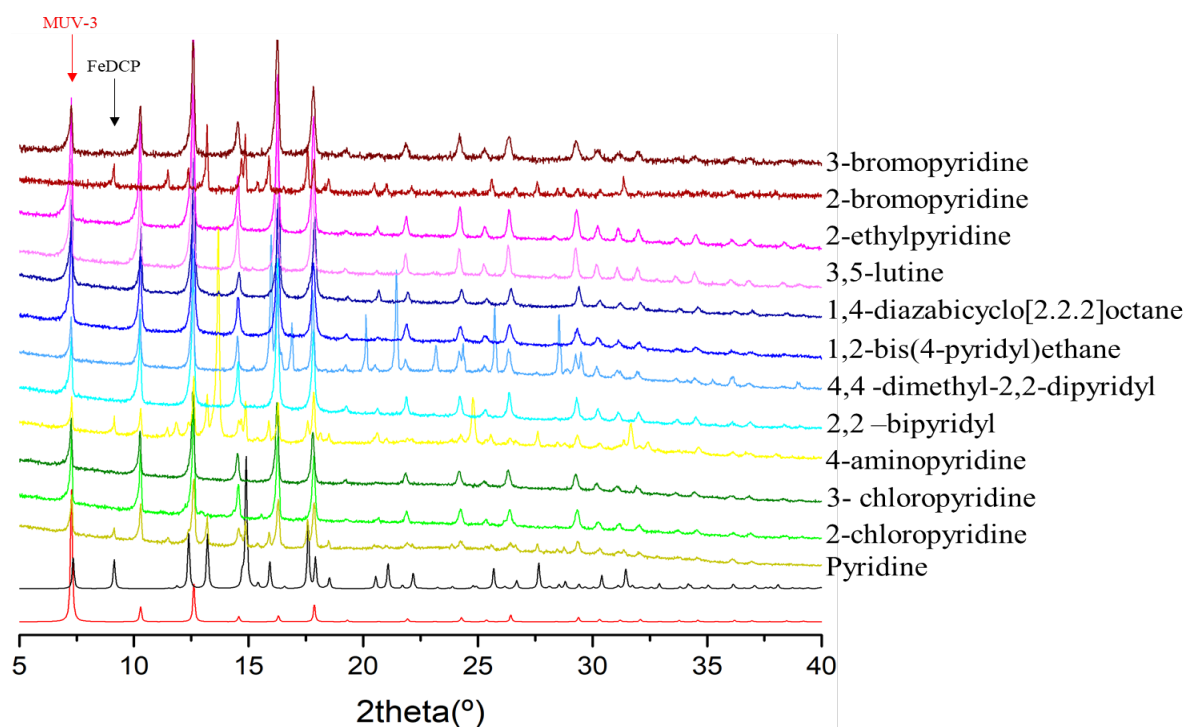


Figure S5. Template effect of 4,4-bipyridine in the solvent free synthesis of **MUV-3**. In black, theoretical pattern of the dense coordination polymer $Fe(Meim)_2 \cdot 0.13(FeCp_2)$; ^[3] in red the theoretical pattern of **MUV-3**; and in blue for the mixture of compounds obtained without presence of template.

Table S2. List of different molecules used as templates in the solvent-free synthesis of **MUV-3**.

Template	Physical state at the reaction	pK _{HA}	Exclusive formation of MUV-3
pyridine	Gas	5.14	No
2-chloropyridine	Gas-liquid	0.72	Yes
3- chloropyridine	Gas	2.84	Yes
4-aminopyridine	Liquid	8.96	No
2,2-bipyridyl	Liquid	4.3	Yes
4,4-dimethyl-2,2-dipyridyl	Liquid	-	Yes
1,2-bis(4-pyridyl)ethane	Liquid	-	Yes
1,4-diazabicyclo[2.2.2]octane	Liquid	8.8	Yes
3,5-lutidine	Gas-liquid	-	Yes
2-ethylpyridine	Gas	5.83	Yes
2-bromopyridine	Liquid	0.9	No
3-bromopyridine	Liquid	2.84	Yes

**Figure S6.** Template effect in the solvent free synthesis of **MUV-3** with different molecules. In red, the theoretical pattern of **MUV-3**; in black, theoretical pattern of dense coordination polymer $\text{Fe}(\text{MeIm})_2 \cdot 0.13(\text{FeCp}_2)$. From green to garnet the experimental XRPD patterns after the synthesis using different the different templates (each indicated on the right). The arrows at the top indicate the most characteristic peaks for **MUV-3** and the iron dense coordination polymer (FeDCP) and serve to analyse the effect of the template. In the case of 4,4-dimethyl-2,2-dipyridyl we can also observe the diffraction peaks corresponding to the template.

S1.4 Thermogravimetric analysis

Thermogravimetric analysis of **MUV-3** was carried out with a TA instruments TGA 550 apparatus in the 25–500 °C temperature range under a 5°C·min⁻¹ scan rate and a N₂ flow of 40 mL·min⁻¹. The results are shown in Figures S7 and S8.

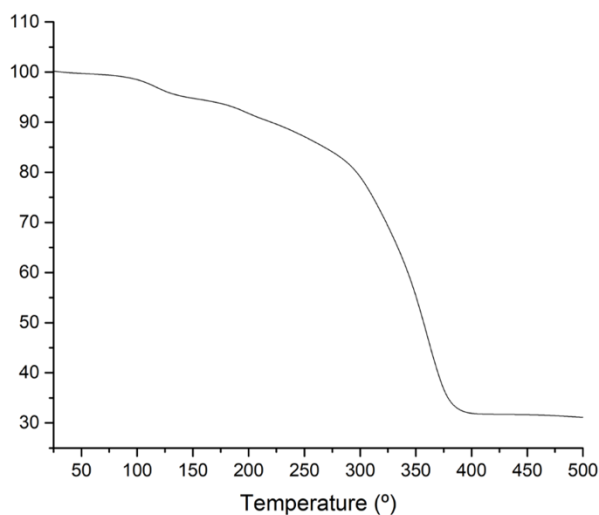


Figure S7. Thermal gravimetric analysis (TGA) of as-synthesized bulk crystals of **MUV-3** at a heating rate of 5 °C min⁻¹.

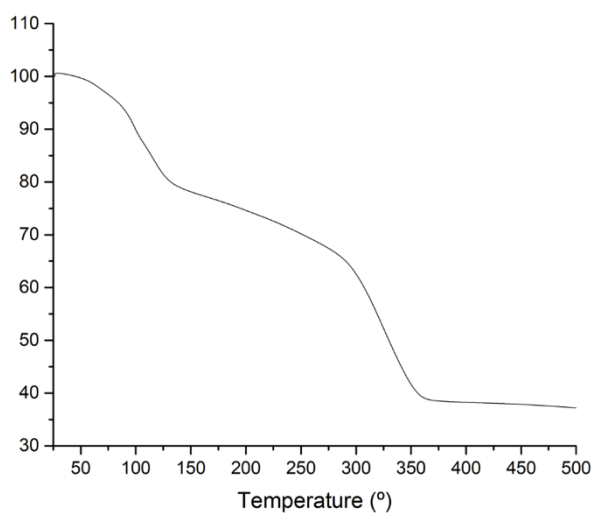


Figure S8. Thermal gravimetric analysis (TGA) of activated bulk crystals of **MUV-3** at a heating rate of 5 °C min⁻¹.

S1.5 Scanning electronic microscopy

Scanning Electronic Micrographs images were recorded in a Hitachi S-4800 at different times of reaction. Synthesis length below 12 hours yields crystals of around 50 μm , whereas synthesis length longer than 12 hours yields crystals of around 100 μm size (Figure S9).

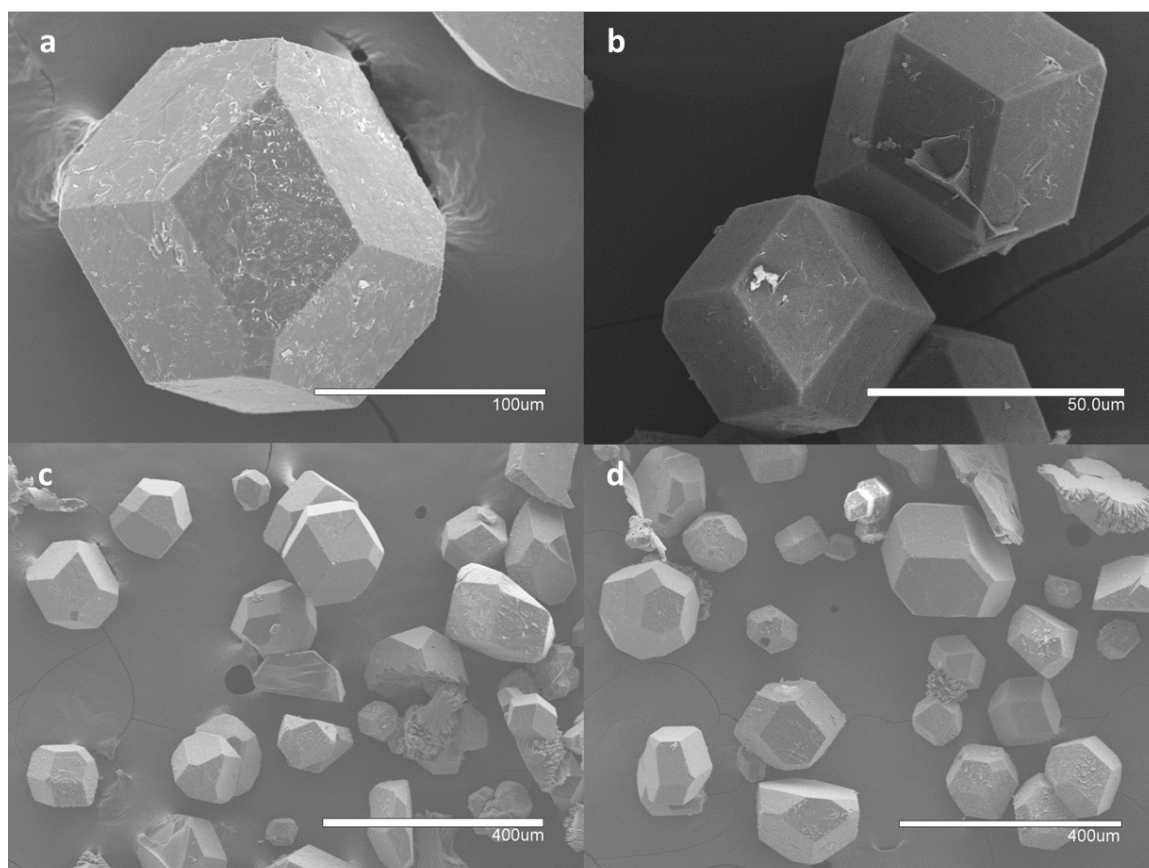


Figure S9. SEM image of the as-synthesized material, showing the morphology of **MUV-3**. Figures S9a, S9c and S9d show images of crystals from 72 hours of reaction revealing a crystal size of aprox. 100 μm . Figure S9b shows an image of crystals from 8 h reaction, revealing a crystal size of aprox. 50 μm .

S1.6 Magnetic properties

The magnetic structure and the presence of Fe(II) was characterized by magnetic measurements. Variable-temperature (2–300 K) direct current (dc) magnetic susceptibility measurements were carried out in applied fields of 0.1 T and variable field magnetization measurements up to 5 T at 2 K. Figure S10a depicts the variable temperature magnetic susceptibility measurements above 2 K of polycrystalline **MUV-3** in an applied dc field of 0.1 T. The product of the molar magnetic susceptibility and temperature, $\chi_m T$, has a value of 4.0 $\text{emu}\cdot\text{mol}^{-1}\cdot\text{K}$ at room temperature, which is slightly larger than expected for an $S = 2$ system. As the system is cooled, the $\chi_m T$ product continuously decreases, indicating the presence of strong antiferromagnetic Fe–Fe interactions occurring through the imidazolate bridges. The temperature dependence of the magnetic susceptibility in the high temperature range ($T > 130$ K) can be fitted by the Curie-Weiss law, $\chi_m = C/(T-\Theta)$, with a Curie constant $C = 5.8 \text{ emu}\cdot\text{mol}^{-1}\cdot\text{K}$ and a negative Curie-Weiss temperature $\Theta = -160$ K (Figure S9c). At lower temperatures, a maximum value of 0.038 $\text{emu}\cdot\text{mol}^{-1}$ is observed at 23.3 K in the χ_m vs. T plot, indicative of antiferromagnetic ordering. The $\partial(\chi_m T)/\partial T$ vs. T curve shows a maximum value at 20.8 K, which serves to accurately establish the Neel temperature (T_N) of the material. The strong antiferromagnetic nature **MUV-3** is confirmed by the weak M vs. H linear signal, which is much below the expected saturation value ($M_{\text{sat}} = 4 \mu\text{B}$) for an isolated spin $S = 2$ (Figure S10b).

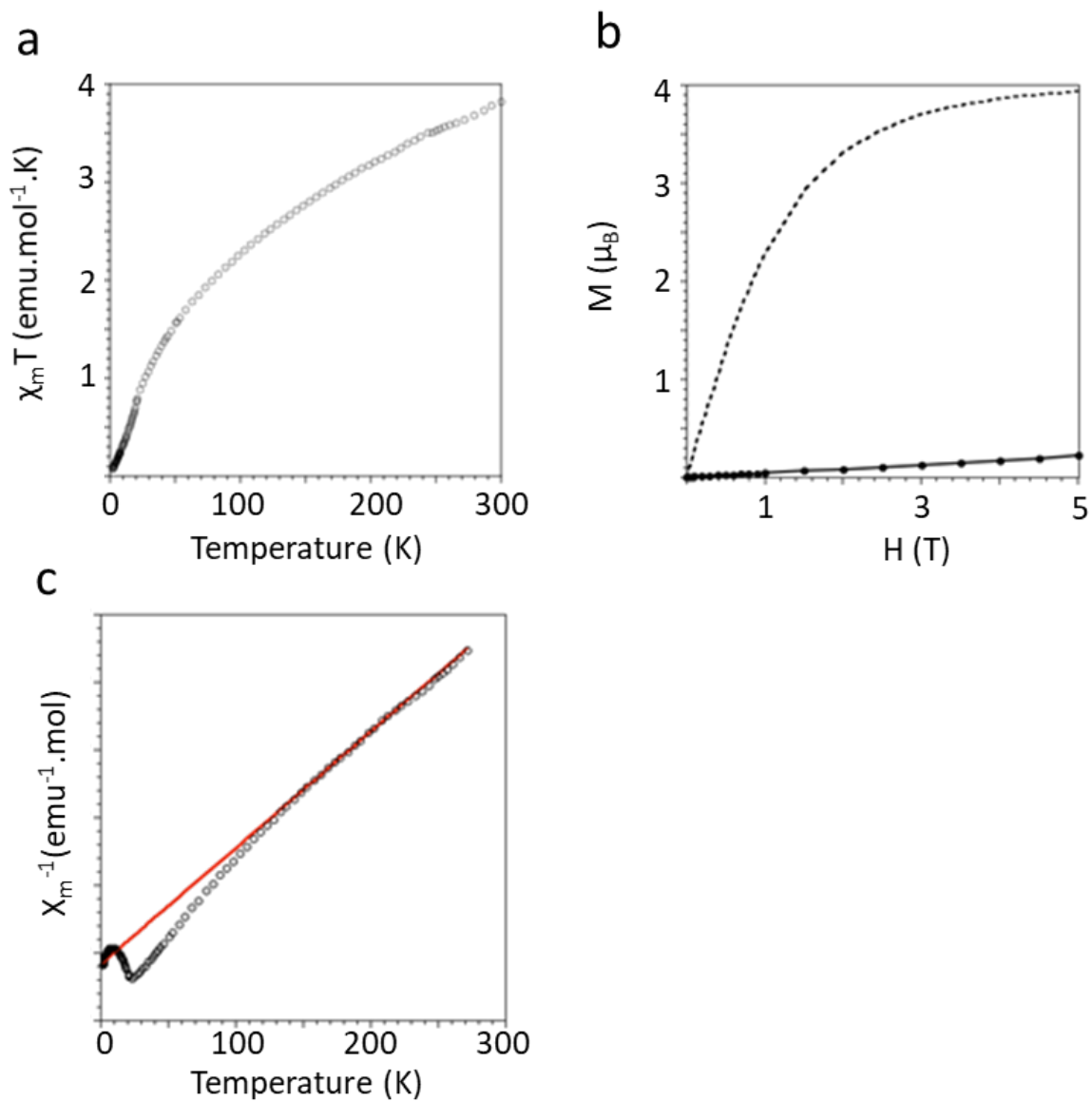


Figure S10. a) Thermal dependence of the product of the molar magnetic susceptibility and temperature, $\chi_m T$, of **MUV-3**. b) Magnetization at 2 K of **MUV-3**; the dotted line represents the Brillouin function for $S = 2$. c) The temperature dependence of the magnetic susceptibility in the high temperature range. The red line represents the fit to the Curie-Weiss law.

S2 Solvent-free synthesis and characterization of others ZIFs: ZIF-8, ZIF-67, qtz-[Fe(etim)₂] (MUV-6), dia-[Fe(mebim)₂] (MUV-7)

S2.1 Synthesis

All reagents were commercially available and used without further purification.

Cobaltocene (for ZIF-67, 30 mg, 0.16 mmol), ZnO (for ZIF-8, 13 mg, 0.16 mmol) or bis(2,2,6,6-tetramethyl-3,5-heptanedionato) zinc(II) (for ZIF-8, 69 mg, 0.16 mmol) and 2-methylimidazole (25 mg, 0.30 mmol) were combined and sealed under vacuum in a layering tube (4 mm diameter). The mixtures were heated at 150 °C for 4 days to obtain purple powder (ZIF-67) or white powder (ZIF-8). The products were allowed to cool to room temperature, and the layering tubes were then opened. The unreacted precursors were extracted with acetonitrile and benzene. Phase purity was established by X-ray powder diffraction.

Ferrocene (30 mg, 0.16 mmol), 2-ethylimidazole (29 mg, 0.30 mmol, for the preparation of qtz-[Fe(etim)₂], **MUV-6**) or 2-methylbenzimidazole (40 mg, 0.30 mmol, for the preparation of dia-[Fe(mebim)₂], **MUV-7**) were combined and sealed under vacuum in a layering tube (4 mm diameter). The mixtures were heated at 150 °C for 4 days to obtain pale yellow crystals suitable for X-ray single-crystal diffraction. The products were allowed to cool to room temperature, and the layering tube were then opened. The unreacted precursors were extracted with acetonitrile and benzene, and **MUV-6** or **MUV-7** were isolated as pale yellow crystals. Phase purity was established by X-ray powder diffraction.

S2.2 Characterization

S2.2.1 Single crystal diffraction

Table S3. Crystallographic information for **MUV-6** and **MUV-7**

	MUV-6	MUV-7
Crystal colour	Yellow	Yellow
Crystal size (mm)	0.13 × 0.13 × 0.09	0.13 × 0.10 × 0.07
Crystal system	Trigonal	orthorhombic
Space group, <i>Z</i>	<i>P</i> 3 ₁ 21	<i>P</i> 2 ₁ 2 ₁ 2 ₁
<i>a</i> (Å)	8.4206(2)	9.2434(14)
<i>b</i> (Å)	8.4206(2)	9.3503(13)
<i>c</i> (Å)	13.1696(3)	15.9876(18)
<i>V</i> (Å ³)	808.70(4)	1381.8(3)
Density (Mg.m ⁻³)	1.516	1.529
Wavelength (Å)	0.71073	0.71073
Temperature (K)	120	120
μ(Mo-Kα) (mm ⁻¹)	1.370	1.089
2θ range (°)	8.34 to 55.744	6.702 to 50.064
Reflns collected	3392	4359
Independent reflns (<i>R</i> _{int})	1123 (0.0316)	2426 (0.0362)
Reflns used in refinement, <i>n</i>	1123	2426
L.S. parameters, <i>p</i>	70	193
No. of restraints, <i>r</i>	0	0
<i>R</i> 1 (<i>F</i>) ^a <i>I</i> > 2.0σ(<i>I</i>)	0.0265	0.0554
<i>wR</i> 2(<i>F</i> ²), ^b all data	0.0510	0.1369
<i>S</i> (<i>F</i> ²), ^c all data	1.101	1.069
Flack parameter	0.020(16)	-0.09(2)

[a] $RI(F) = \Sigma(|F_o| - |F_c|) / \Sigma|F_o|$; [b] $wR2(F^2) = [\Sigma w(F_o^2 - F_c^2)^2 / \Sigma wF_o^4]^{1/2}$; [c] $S(F^2) = [\Sigma w(F_o^2 - F_c^2)^2 / (n + r - p)]^{1/2}$

S2.2.2 X-Ray powder diffraction

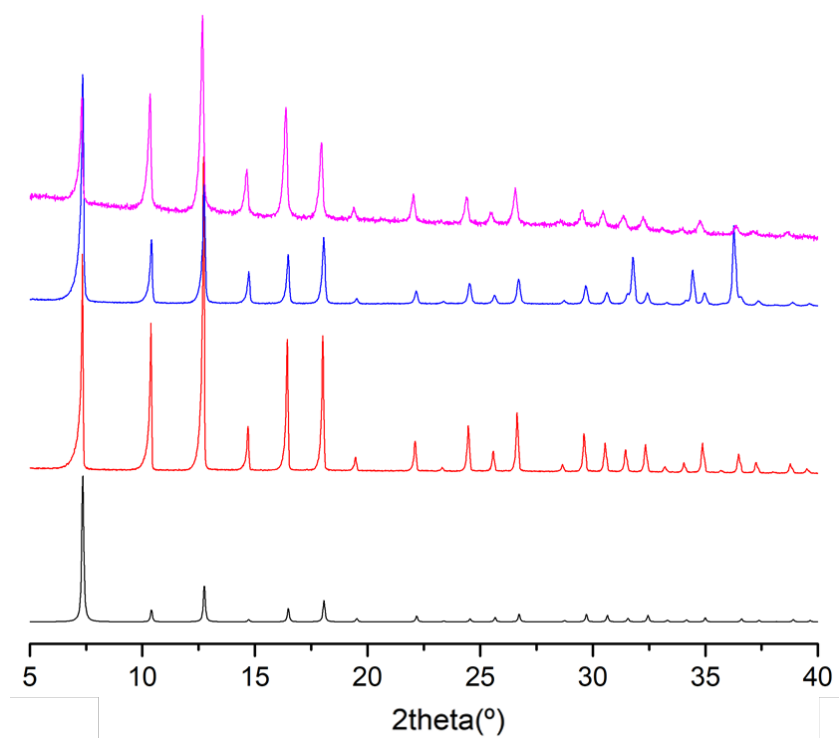


Figure S11. X-ray powder diffraction of ZIF-8 and ZIF-67 synthesized by solvent-free method. In black, theoretical powder pattern of ZIF-8; in red, ZIF-8 synthesized using bis(2,2,6,6-tetramethyl-3,5-heptanedionato) zinc(II); in blue, ZIF-8 synthesized using ZnO; in pink, ZIF-67 synthesized using cobaltocene.

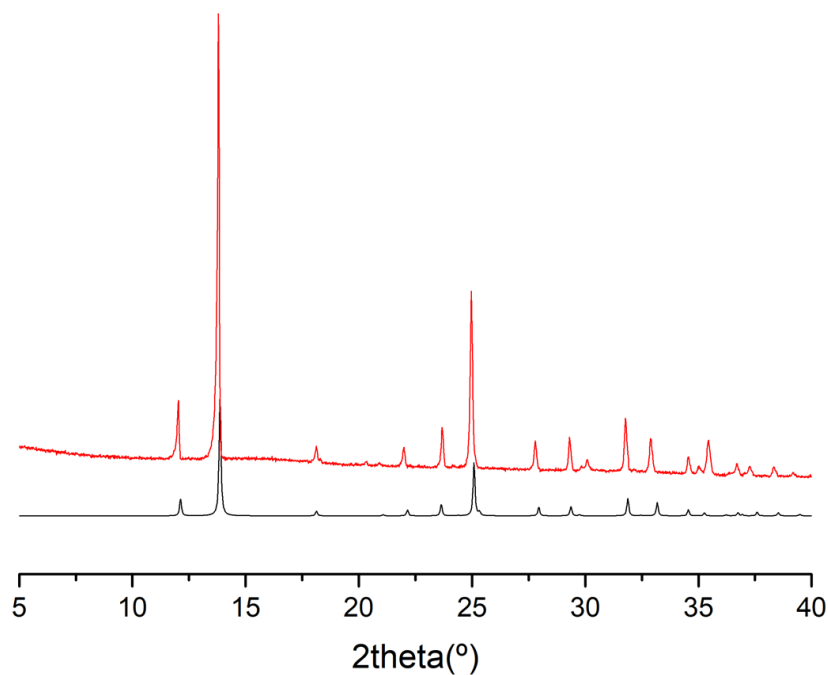


Figure S12. X-ray powder diffraction of **MUV-6** synthesized by solvent-free method (in red) and the theoretical powder pattern of **MUV-6** (in black).

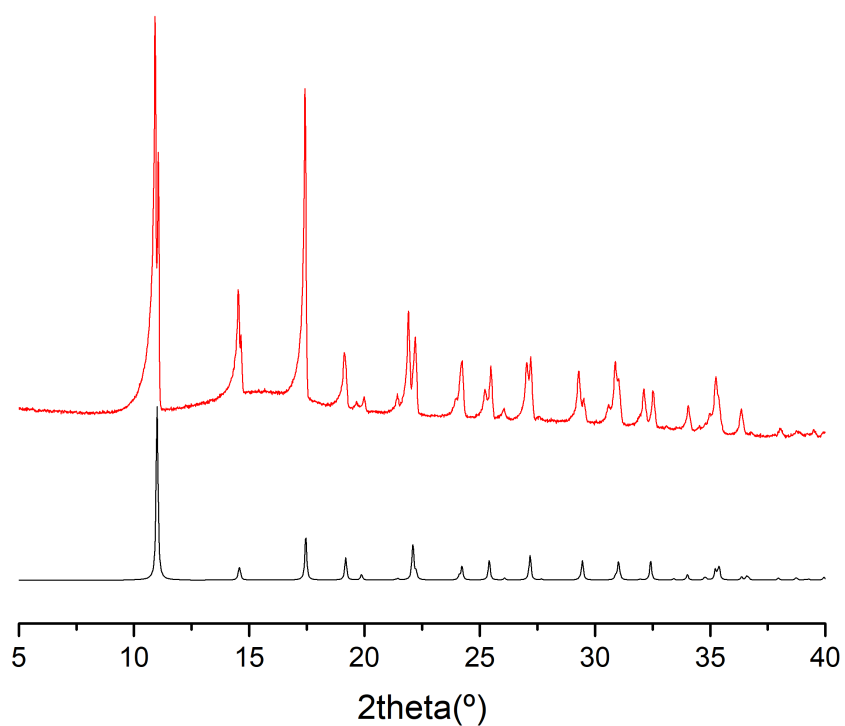


Figure S13. X-ray powder diffraction of **MUV-7** synthesized by solvent-free method (in red) and the theoretical powder pattern of **MUV-7** (in black).

S2.2.3 Thermogravimetric analysis

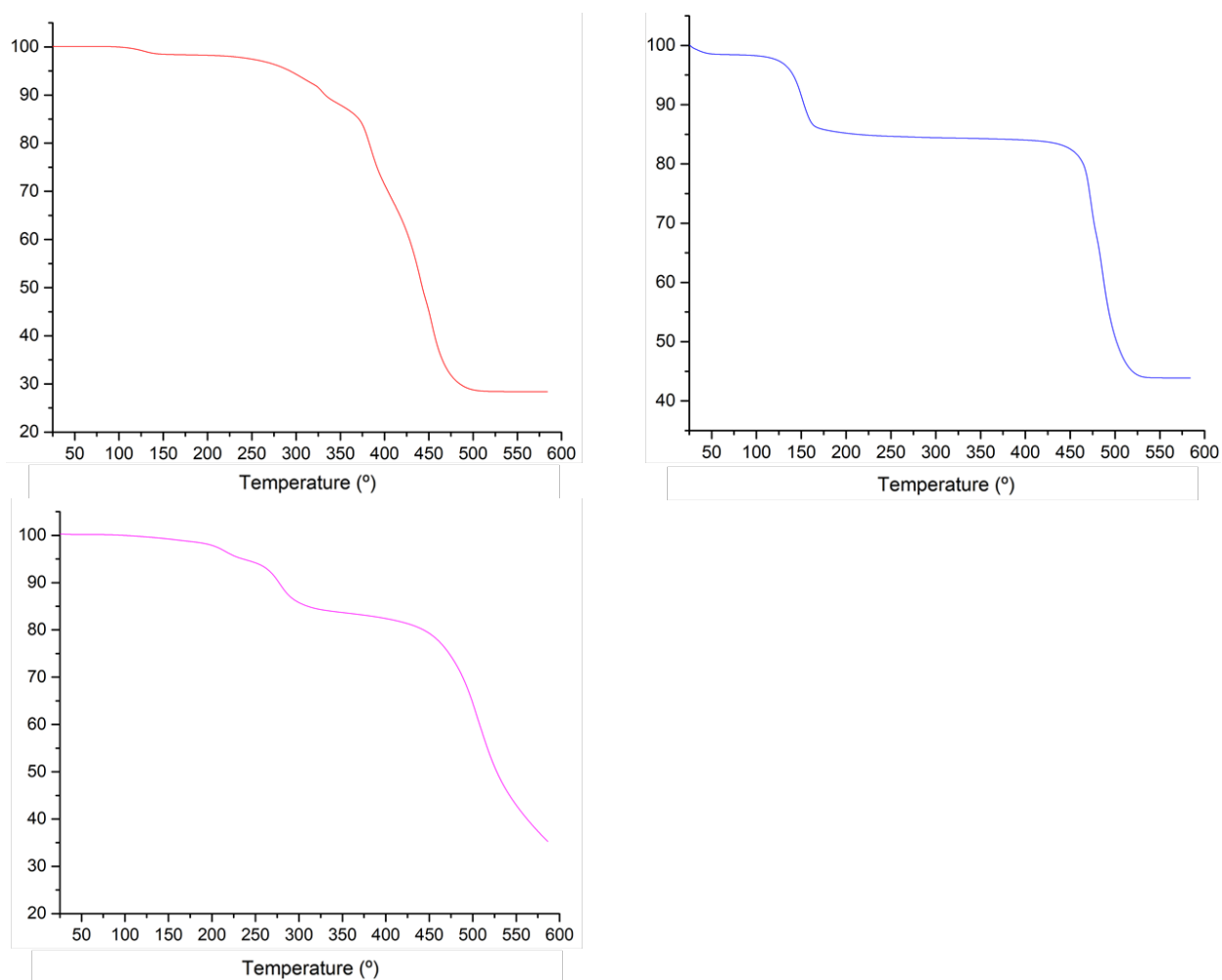


Figure S14. Thermal gravimetric analysis (TGA) of ZIF-8 and ZIF-67 synthesized by solvent-free method. In red, using bis(2,2,6,6-tetramethyl-3,5-heptanedionato) zinc(II); in blue, ZIF-8 synthesized using ZnO; in pink, ZIF-67 synthesized using cobaltocene.

Heating rates of $10\text{ }^{\circ}\text{C min}^{-1}$.

S3 Gas sorption measurements

S3.1 Nitrogen and CO₂ adsorption

Nitrogen isotherms were measured using an TRIFLEX apparatus (Micromeritics) at $-196\text{ }^{\circ}\text{C}$. The sample was transferred from a sealed ampoule to the sample holder inside a glove box. Before the analysis, 50 mg of the thoroughly washed **MUV-3** material were degassed at $150\text{ }^{\circ}\text{C}$ overnight. The BET surface area was calculated by using the Brunauer–Emmett–Teller equation.

The CO₂ adsorption isotherms (high pressure, up to 18 bar) were measured in a gravimetric sorption analyzer IGA-100 (Hiden Isochema). 50 mg of adsorbent were placed in a sample holder and before measurement, the sample was degassed 3 hours at $100\text{ }^{\circ}\text{C}$ under vacuum. CO₂ adsorption isotherms were acquired at 10, 25, 35 and $55\text{ }^{\circ}\text{C}$.

The CO₂ adsorption isotherms (low pressure, up to 1 bar) were measured in a Micromeritics ASAP 2010 instrument using approximately 200 mg of adsorbent placed in a sample holder that was immersed into a liquid circulation thermostatic bath for precise temperature control. Before each measurement, the sample was degassed overnight at $100\text{ }^{\circ}\text{C}$ under vacuum. CO₂ adsorption isotherms were then acquired at 0, 10, 25, 40 and $60\text{ }^{\circ}\text{C}$.

The experimental data was fitted with a fourth grade virial equation:

$$P = \frac{Q}{K_H} \cdot \exp(A_1 \cdot Q + A_2 \cdot Q^2 + A_3 \cdot Q^3 + A_4 \cdot Q^4)$$

Where K_H is the Henry constant, A_i are the virial coefficients, and P y Q are the experimental values of the isotherms.

The isosteric heat of adsorption can be determined from a set of isotherms at different temperatures according to the Clausius-Clapeyron equation^[4] :

$$q_{st} = R \cdot T^2 \cdot \left[\frac{\partial(\ln P)}{\partial T} \right]_{Q=cte} \equiv R \cdot \left[- \frac{\partial(\ln P)}{\partial \left(\frac{1}{T} \right)} \right]_{Q=cte}$$

A set of CO₂ isotherms at different temperatures were measured on **MUV-3**. The experimental values were fitted with a fourth-grade virial equation. The results are given in Figure S15.

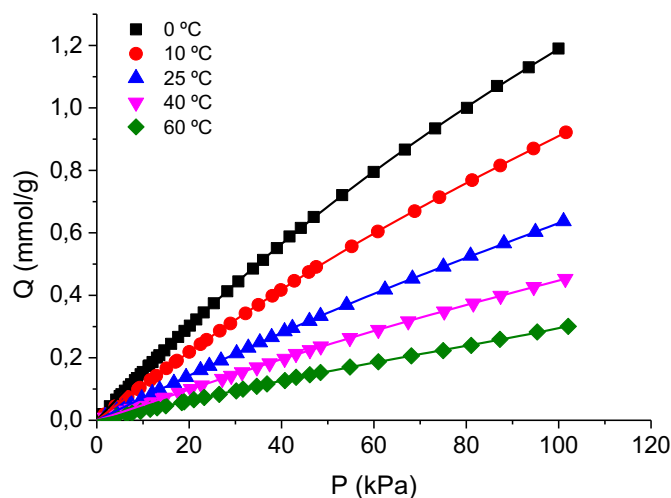


Figure S15. CO₂ adsorption isotherms measured at 0, 10, 25, 40 and 60 °C on **MUV-3**.

The isosteric heat of CO₂ adsorption on **MUV-3** is shown in Figure S16.

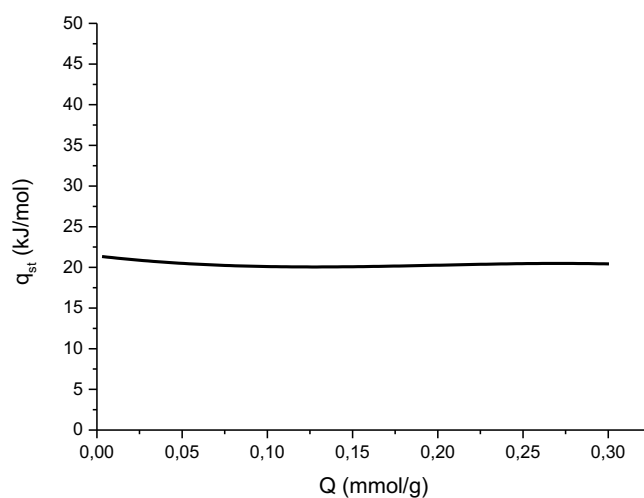


Figure S16. Isosteric heat of adsorption (q_{st}) vs CO₂ loading (Q) obtained on **MUV-3**.

The specific surface area of the **MUV-3** was also determined through the monolayer capacity of CO₂ at 0 °C by applying the linearized Dubinin-Astakhov equation.⁵

$$\log(V) = \log(V_0) - \left[\frac{RT}{\beta E_0} \right]^n \left[\log \left(\frac{p_0}{p} \right) \right]^n$$

where V₀, R, T, β, E₀, n, p₀ and p are the monolayer capacity, the gas constant, the analysis temperature, the CO₂ affinity coefficient, the characteristic energy, the Astakhov exponent, the saturation vapour pressure of the CO₂ at the analysis temperature, and the equilibrium pressure respectively. The application of the linearized Dubinin-Astakhov equation is shown in Figure S17.

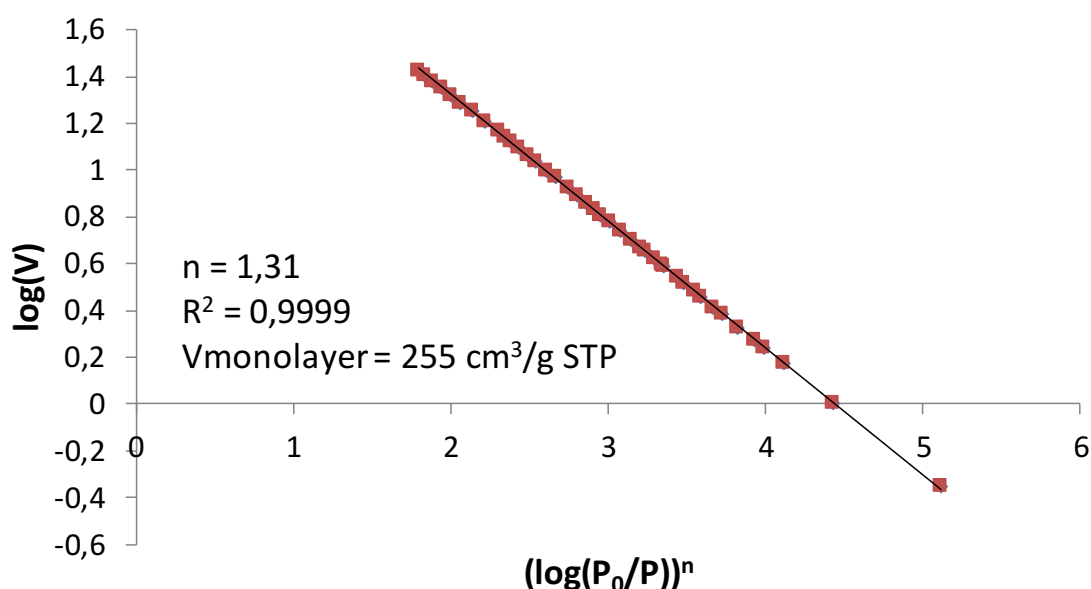


Figure S17. Dubinin-Astakhov plot for CO₂ adsorption at 0 °C on **MUV-3**.

The monolayer capacity V₀ was obtained from the fitting of the linearized Dubinin-Astakhov equation and used to estimate the specific surface area of the MUV-3 according to the expression

$$S(\text{m}^2/\text{g}) = \frac{6.022 \cdot 10^{23} (\text{molecule/mol}) \cdot \sigma (\text{nm}^2/\text{molecule}) \cdot V_0 (\text{cm}^3/\text{g})}{22414 (\text{cm}^3/\text{mol}) \cdot 10^{18} (\text{nm}^2/\text{m}^2)}$$

being σ the molecular sectional area of CO_2 at 0°C , with a value of 0.187 nm^2 .⁶ According to this equation, the calculated surface area of MUV-3 is $1820\text{ m}^2/\text{g}$. This value is larger than the corresponding obtained with N_2 at -196°C and the BET model, due to the fact that CO_2 at 0°C is able to access to a different porosity that is not accessible for N_2 at -196°C , as it was also reported in the literature for other solid adsorbents.⁷

S3.2 Nitric oxide adsorption

The NO adsorption isotherms were also collected in a Micromeritics ASAP 2010 apparatus. In the first experiment, 200 mg of fresh MUV-3 were placed in the sample holder and activated at 100°C under vacuum overnight. Then, the isotherm was measured at 0°C up to 1 bar. In order to distinguish between physisorption and chemisorption, a second isotherm was measured on the same sample but degassing at room temperature, assuming that only the physisorbed molecules were removed.

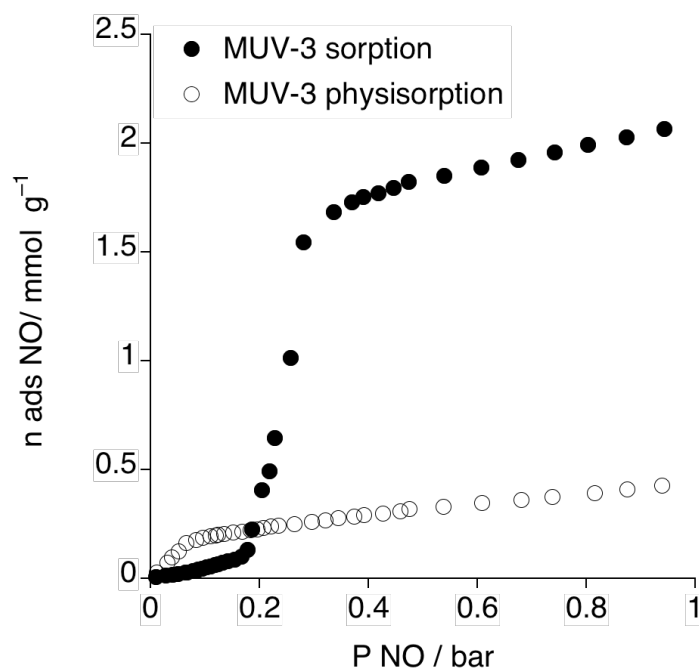


Figure S18. NO sorption of MUV-3 at 273 K, showing the first cycle of sorption (filled circles) and the second cycle of sorption (empty circles).

S3.2.1 Infrared study of NO sorption

In Figure S19, the infrared spectra of bulk crystals of **MUV-3**, **MUV-3_NO**, ZIF-8 and ZIF-8_NO are presented. Figure S20 shows the characteristic peaks corresponding to the vibration of coordinated NO species, at 1725 cm^{-1} and 1795 cm^{-1} , which are absent when using ZIF-8 (Figure S21).

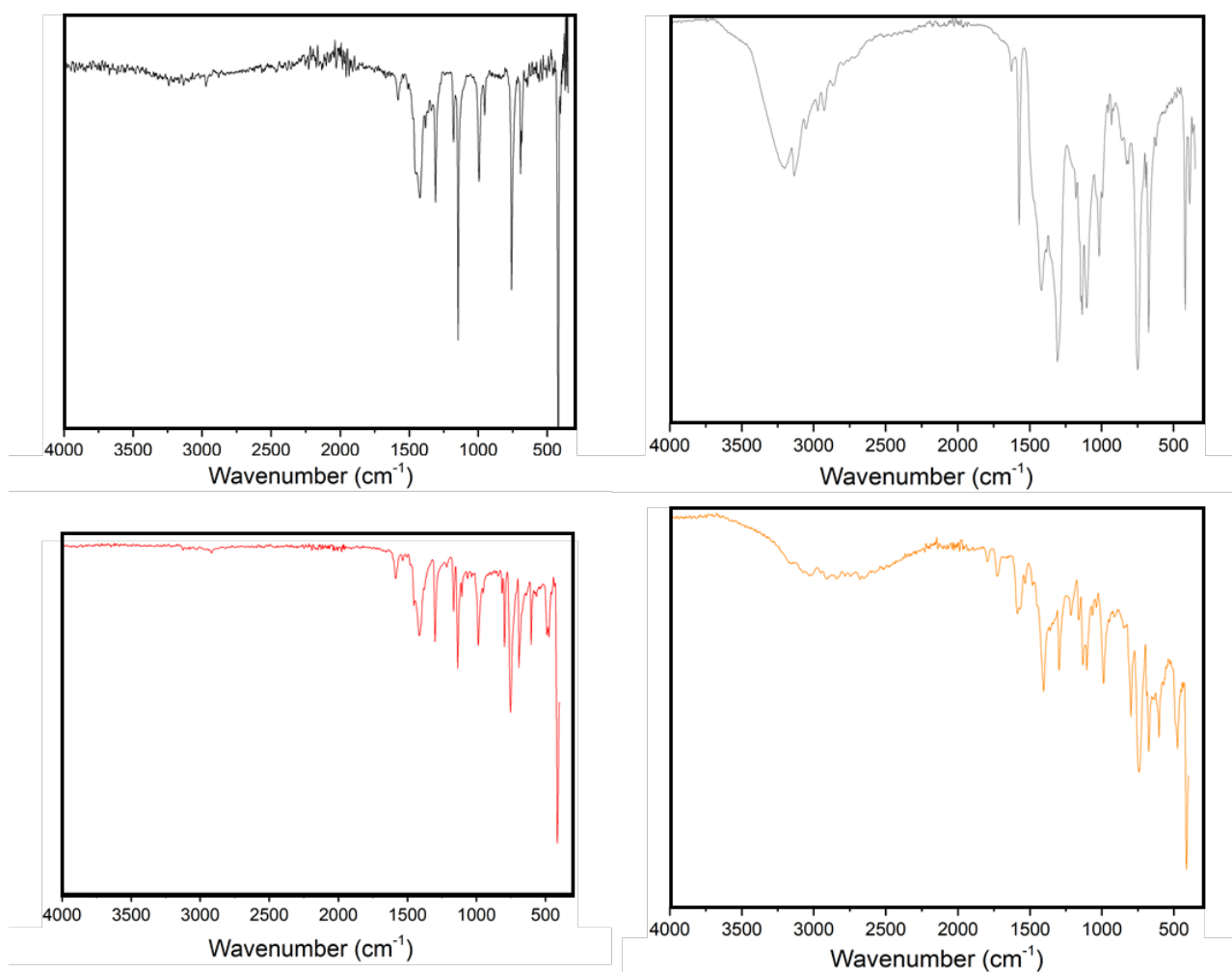


Figure S19. Infrared spectra of **ZIF-8** (black curve), **ZIF-8** exposed to NO gas (grey curve), bulk crystals of **MUV-3** (red curve) and **MUV-3_NO** (orange curve),

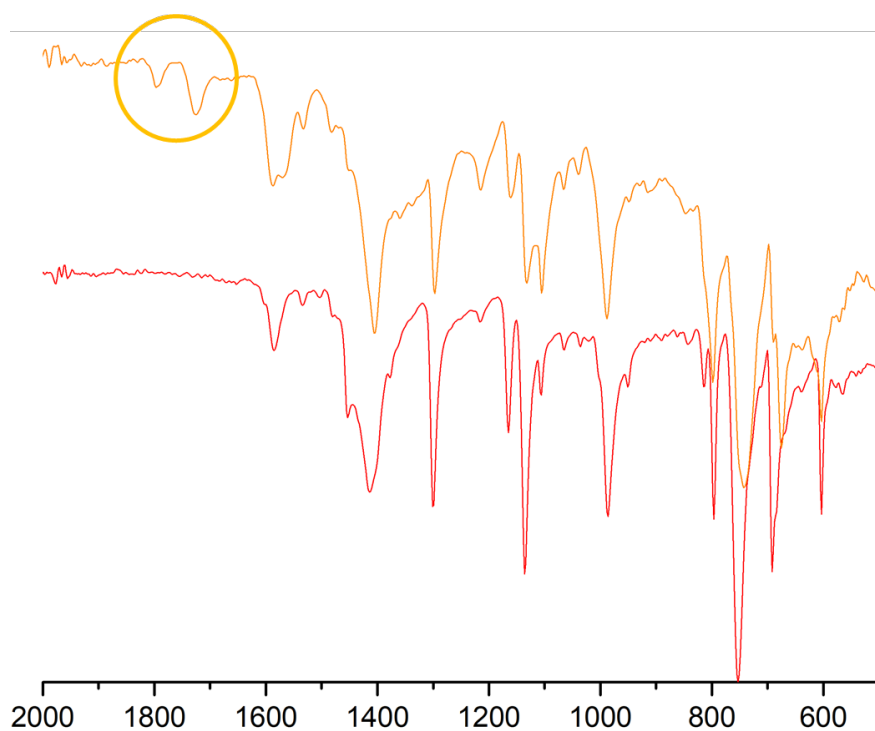


Figure S20. Infrared spectra of **MUV-3** before (red) and after (orange) exposure to NO. The orange circle highlights the peaks corresponding to coordinated NO species.

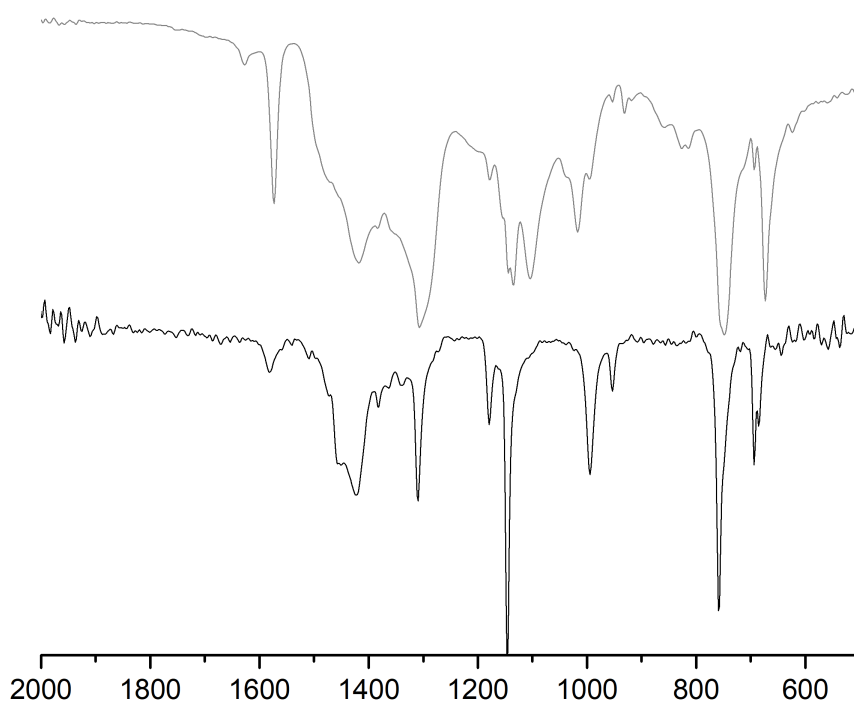


Figure S21. Infrared spectra of **ZIF-8** before (black) and after (gray) exposure to NO.

S3.2.2 X-Ray powder diffraction

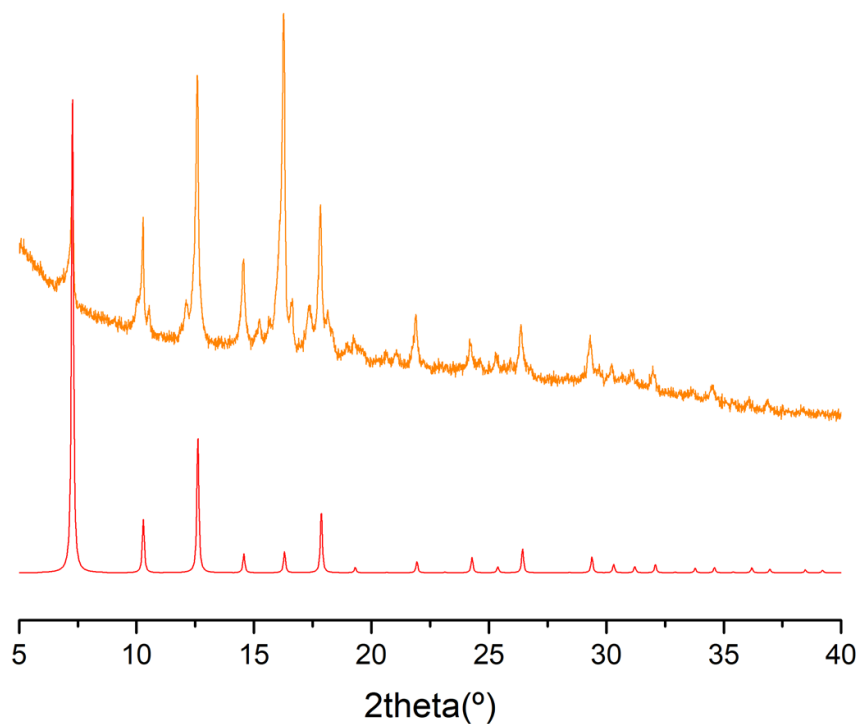


Figure S22. X-ray powder diffraction of **MUV-3_NO** (orange) and theoretical powder pattern of **MUV-3** (red).

S4 Synthesis of NC-MUV-3

For comparative purposes, we prepared working electrodes consisting of **NC-MUV-3**, NC-ZIF-8, NC-ZIF-67, NC-d-CP, Ni-FeOOH and a commercial IrO₂ catalyst as references. The two latter are considered two of the most efficient OER catalyst for water splitting.

The others NC were synthesized with the same controlled thermal treatment, using as precursor the ZIF-8, ZIF-67, a dense coordination polymer previously reported and the original precursors of **MUV-3**.^[3,8,9]

The synthesis of NiFeOOH was carried out following a reported procedure.^[10] Specifically, solutions of 0.1 M Ni(NO₃)₂·6H₂O and 0.1 M Fe(acac)₃ in a ratio of 1:1 with additions of 10 mM 1,2-benzenediol were mixed in benzyl alcohol affording a final concentration of 22 mM of Ni and Fe precursors in a volume of 20 mL. The mixture was sealed in special autoclave vials and heated to 190 °C for 15 min. After immediate cooling to room temperature the solid products were collected by washing five times with absolute ethanol and recollected by repetitive centrifugation at 7500 rpm for 15 min. The collected material was freeze-dried and stored as powders under inert atmosphere until use.

S5 Characterization of NC-MUV-3

The nanocomposite **NC-MUV-3** is exhaustively characterized by XRPD, field-emission scanning electron microscopy (FESEM), high-resolution transmission electron microscopy (HRTEM), X-ray photoelectron spectroscopy (XPS), inductively coupled plasma-optical emission spectroscopy (ICP-OES), Raman spectroscopy, and gas sorption isotherms, which in global provide a real overview of the synthesized material.

S5.1 X-ray powder diffraction

A polycrystalline sample of **NC-MUV-3** was lightly ground in an agate mortar and pestle and used to fill a 0.5 mm borosilicate capillary that was mounted and aligned on an Empyrean PANalytical powder diffractometer, using Cu K α radiation ($\lambda = 1.54056 \text{ \AA}$). Two repeated measurements were collected at room temperature ($2\theta = 10\text{--}90^\circ$) and merged in a single diffractogram. Figures S23 and S24 show the diffraction patterns of the nanocomposite before and after the cleaning method. Figure S23 shows the characteristic peaks of metallic iron corresponding to (110), (200) and (211) planes. The absence of these peaks in the diffractogram after acid treatment (Figure S24) confirms the disappearance of the majority of metallic iron.

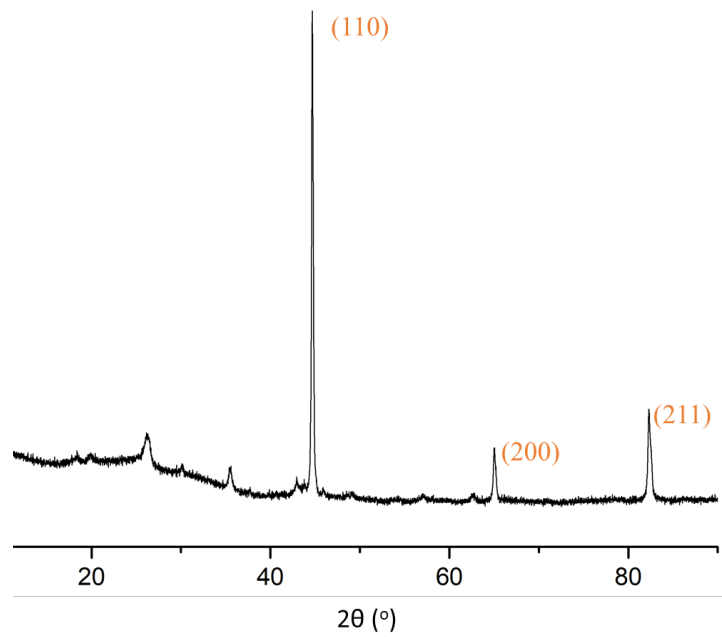


Figure S23. X-ray powder diffraction of NC-MUV-3 before acid leaching. The characteristic peaks of iron are indicated.

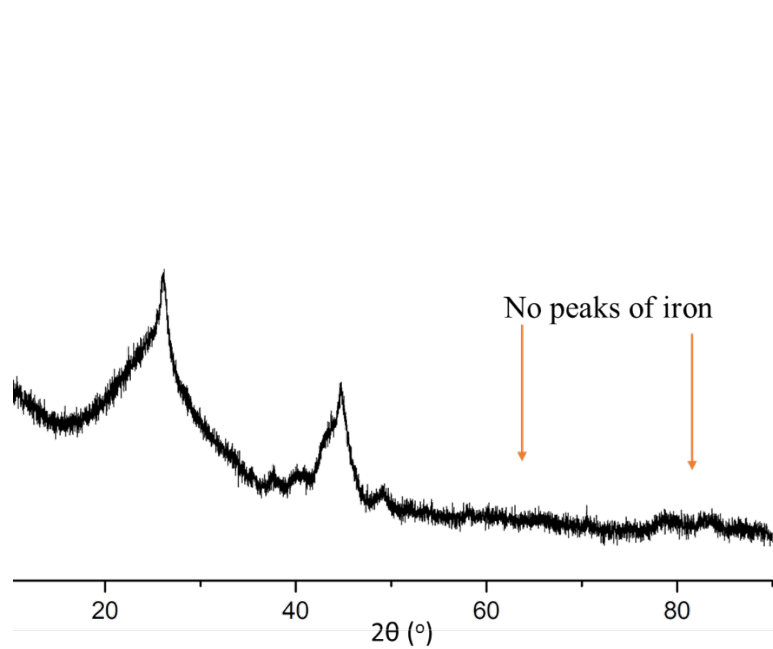


Figure S24. X-ray powder diffraction of NC-MUV-3 after acid leaching. Iron is not detected.

S5.2 Field-emission scanning electron microscopy

Field-emission scanning electron microscopy (FESEM) studies were performed on a Hitachi S-4800 microscope operating at an accelerating voltage of 20 kV and without metallization of the samples. Field-emission scanning electron microscopy (FESEM) analysis shows that the previously observed defined morphology is completely lost after the thermal treatment, originating a crumpled material (Figure S25).

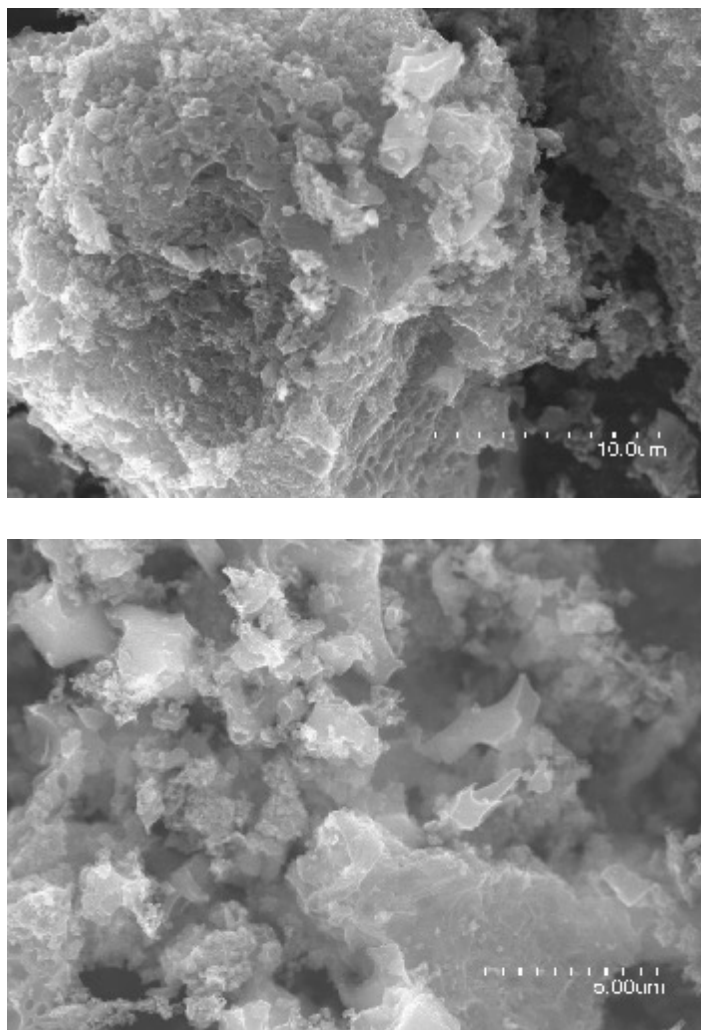


Figure S25. Field-emission scanning electron microscopy (FESEM) image of NC-MUV-3.

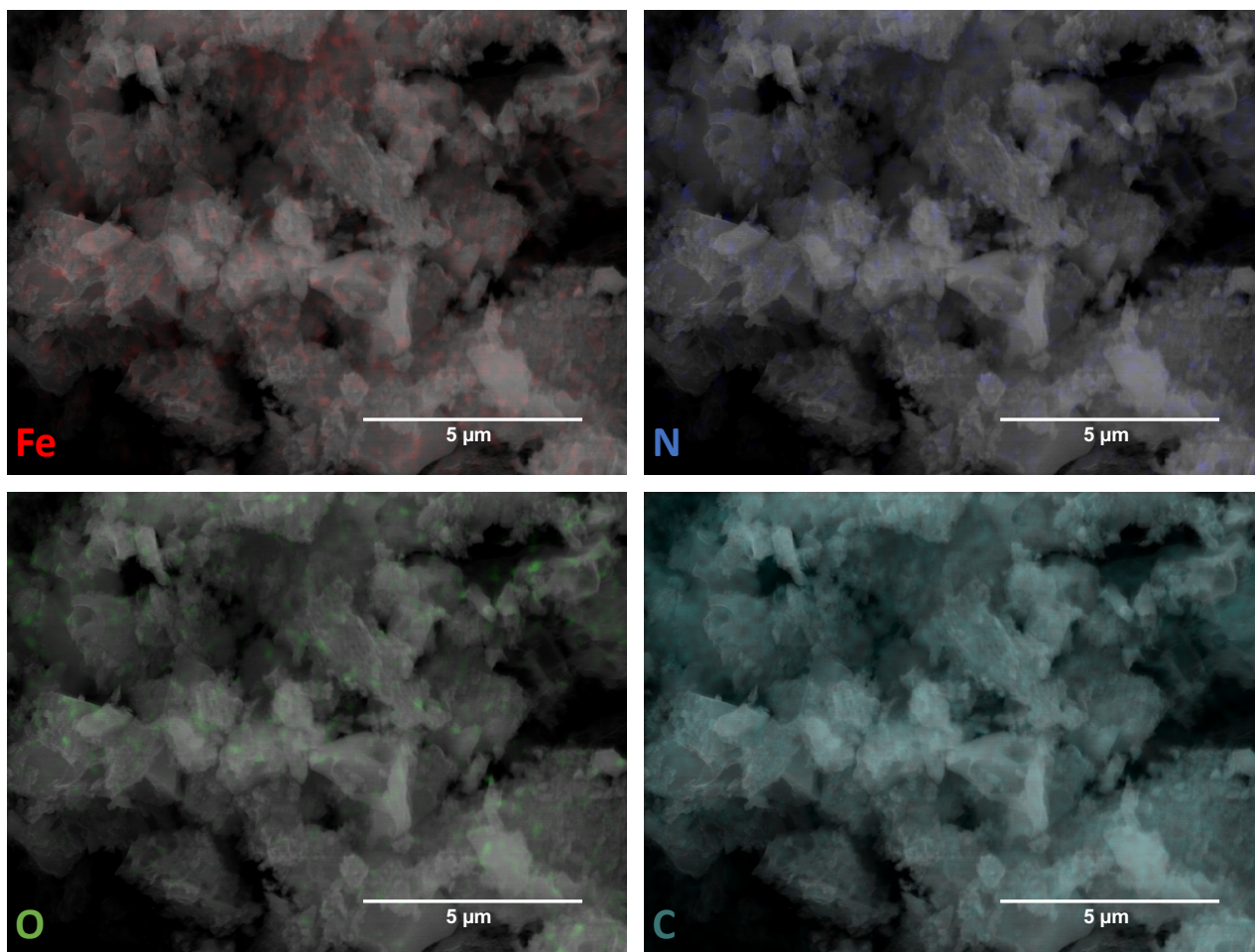


Figure S26. NC-MUV-3 FESEM mapping of Fe, N, O, C.

S5.3 High-resolution transmission electron microscopy

High Resolution Transmission Electron Microscopy (HRTEM) studies of NC-MUV-3 were carried out on a JEM-2010 microscope (JEOL, Japan) operating at 200kV. Samples were prepared by dropping a sonicated suspension of the material in ethanol on a carbon-coated copper grid. The digital analysis of the HRTEM images was done using Digital Micrograph 1.80.70 for GMS 1.8.0 by Gatan. High-resolution transmission electron microscopy (HRTEM) revealed the formation of graphitic carbon. In fact, the morphology of the sample consists of carbon nanocages composed of several graphene layers endowed with a marked corrugation, as can be observed in Figure S27. The formation of these nanostructures is related to the *in-situ* formation of metallic Fe nanoparticles (NP), detected by XRPD (Figure S23), which are originated from the presence of iron in the structure of the precursors. In addition, Fe NPs of *ca.* 10–30 nm in size that remained intact after acid leaching can be observed embedded in the carbon matrix, as highlighted in Figure S27a-b.

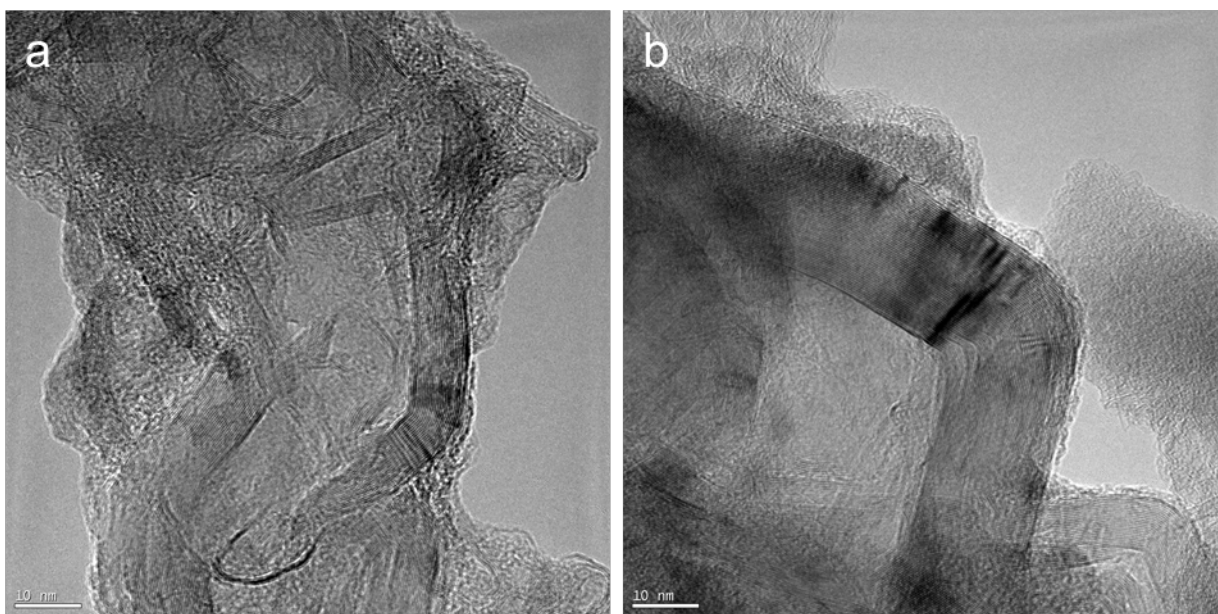


Figure S27. HRTEM of NC-MUV-3. Higher magnifications of two different regions of the graphitic carbon structures.

S5.4 XPS characterization.

X-ray Photoelectron Spectroscopy (XPS) was performed *ex situ* at the X-ray Spectroscopy Service at the Universidad de Alicante using a K-Alpha X-ray photoelectron spectrometer system (Thermo Scientific). All spectra were collected using Al K α radiation (1486.6 eV), monochromatized by a twin crystal monochromator, yielding a focused X-ray spot (elliptical in shape with a major axis length of 400 μm) at 3 mA·C and 12 kV. The alpha hemispherical analyzer was operated in the constant energy mode with survey scan pass energies of 200 eV to measure the whole energy band and 50 eV in a narrow scan to selectively measure the particular elements. XPS data were analyzed with Avantage software). The predominant sp^2 character of the graphitic sample is confirmed, highlighting the almost absence of catalytic metal, and a moderate nitrogen doping (Figure S28). The high-resolution N1s spectra peaking at *ca.* 400 eV shows the presence of nitrogen as a dopant, with values of 1.10 % (Figure S28b). It is worth to remark here that nitrogen could be incorporated as “lattice N” within the carbon network or “chemical N” in the form of functional groups at the periphery of the graphene plane. The deconvoluted peak reveals four different N types, *i.e.* pyridinic-N, pyrrolic-N, graphitic-N and pyridine-N-oxide groups, being predominant the graphitic-type nitrogen (49.1%). Furthermore, the residual amount of Fe NPs in **NC-MUV-3** has been determined by inductively coupled plasma-optical emission spectroscopy (ICP-OES) analysis, showing that the metal content is 0.79%.

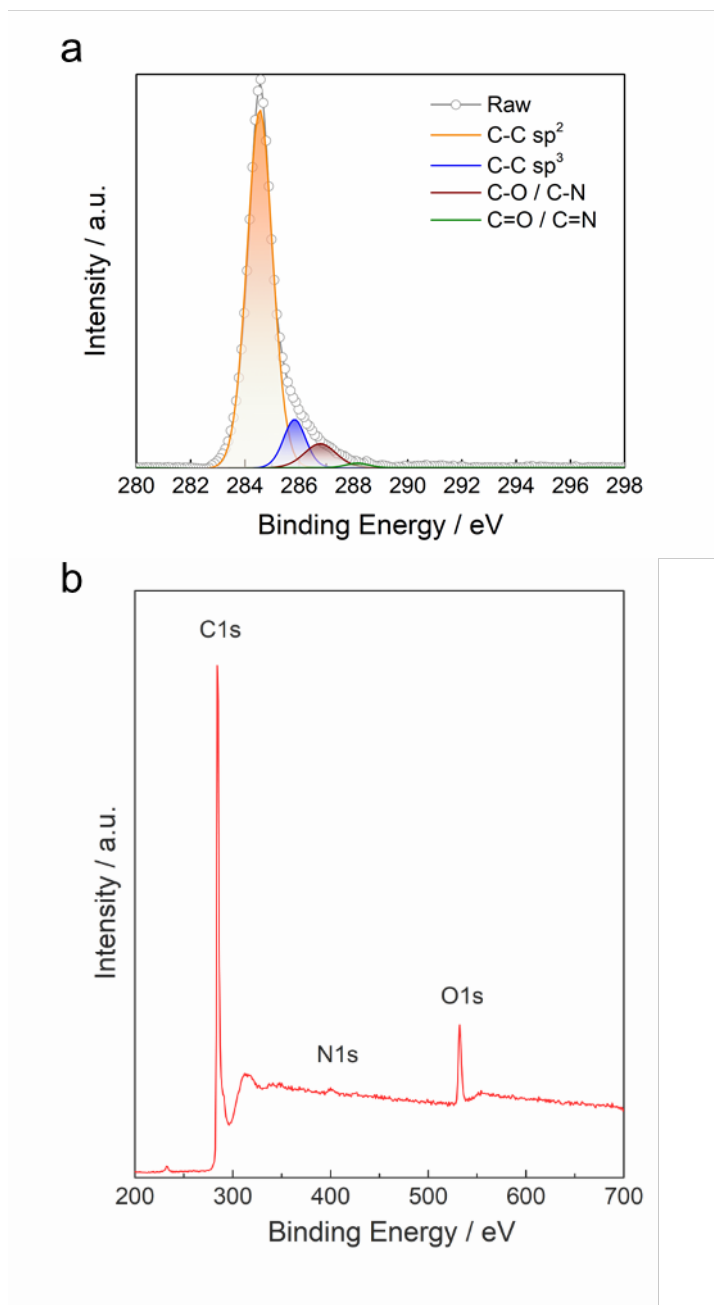


Figure S28. XPS high-resolution a) C1s and b) survey spectrum for **NC-MUV-3**.

Table S4. Atomic composition (expressed as atomic percentage) of **NC- MUV-3** as determined by XPS analysis.

	C	N	O
at. %	90.71	1.10	8.19

Table S5. Relative content of different C species to total C of **NC-MUV-3**.

	C-C sp ²	C-C sp ³	C-O / C-N	C=O / C=N
%	82.61	9.62	6.85	0.92

Table S6. Relative content of different N species to total N of **NC-MUV-3**.

N1	N2	N3	N4	(N1+N3)/N _{total}
0.31	0.09	0.49	0.11	0.80

*N1 (pyridinic-N); N2 (pyrrolic-N); N3 (graphitic-N); N4 (pyridine-N-oxide).

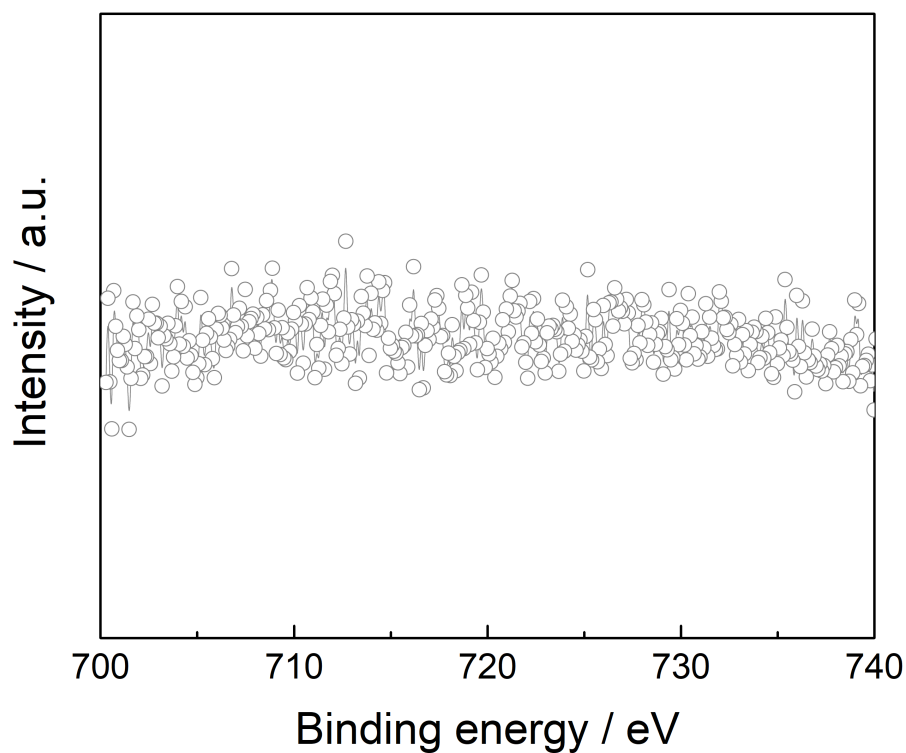


Figure S29. XPS high-resolution Fe2p survey spectrum for **NC-MUV-3** shows the absence of iron.

S5.5 Inductively Coupled-Plasma Optical Emission

Inductively Coupled-Plasma Optical Emission Spectrometry (ICP-OES) analysis was conducted at the Universidad Complutense de Madrid (CAI de Técnicas Geológicas). Samples were digested in a mixture of hydrochloric and nitric acids using a high- pressure microwave oven.

Table S7. ICP-OES values.

	Fe (%)
NC-MUV-3	0.79 ± 0.08

S5.6 Raman Spectroscopy

Raman spectroscopy was performed using a Horiba Jobin Yvon LabRAM Aramis confocal Raman spectrometer equipped with a microscope and an automated XYZ-table (excitation wavelength 532 nm) with a laser spot size of $\sim 1 \mu\text{m}$ (Olympus LMPlanFl 100x, NA 0.80). The incident laser power was kept as low as possible to avoid structural sample damage: $< 240 \mu\text{W}$ (532 nm), and the grating was $1800 \text{ g}\cdot\text{mm}^{-1}$. Maps were recorded with a step size of $2 \mu\text{m}$. The homogeneity of the samples over wide areas of more than $85 \times 85 \mu\text{m}^2$ was also evaluated by I_D/I_G ratio Raman mappings (see Figure S30), showing rather uniform spatial I_D/I_G ratio distributions, and providing a real overview of the synthesized nanocomposite.

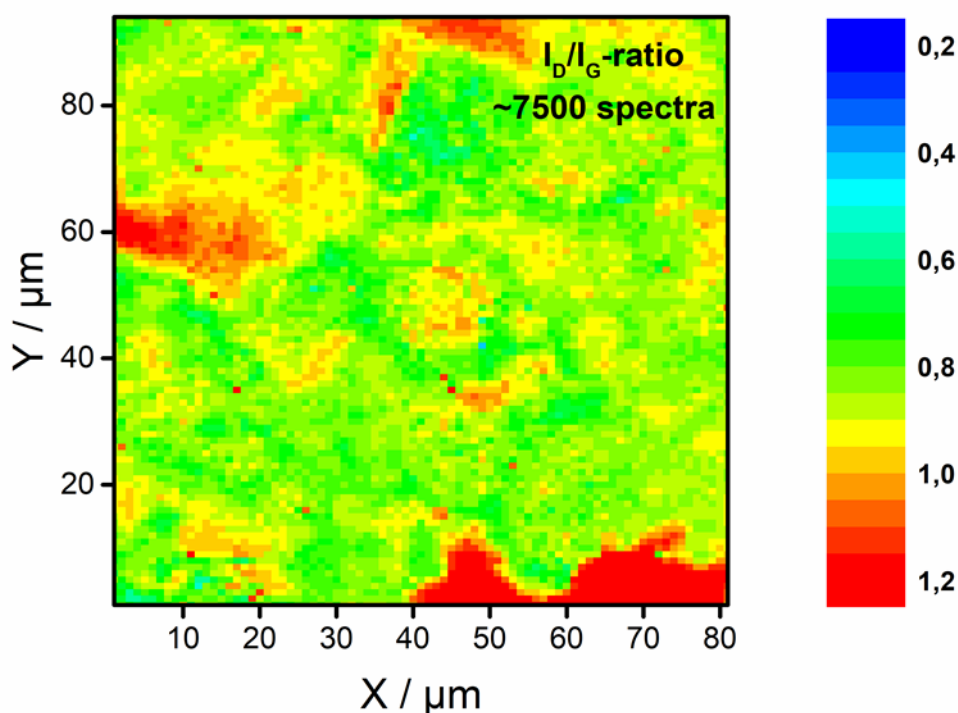


Figure S30. NC-MUV-3 I_D/I_G ratio Raman mapping over a wide area of $94 \times 81 \mu\text{m}^2$, using a step size of $2 \mu\text{m}$, $\lambda_{\text{exc}} = 532 \text{ nm}$.

S5.7 Textural characterization of NC-MUV-3.

The porous texture of all the materials prepared was characterized by N₂ adsorption at 77 K and CO₂ at 273 K using an AUTOSORB-6 apparatus. Samples were degassed for 8 h at 523 K and 5×10⁻⁵ bar prior to analysis. Surface areas were estimated according to the BET model, and pore size dimensions were calculated by the solid density functional theory (QSDFT) for the adsorption branch assuming a cylindrical pore model. The micropore volumes were determined by applying t-plot and DR methods to the N₂ and CO₂ adsorption data. The N₂ isotherm reveals a characteristic type IV isotherm, with a specific Brunauer–Emmett–Teller (BET) surface area of 463 m²·g⁻¹. The pore size distribution (PSD) was analysed by quenched solid density functional theory (QSDFT), showing a total pore volume of 0.960 cm³·g⁻¹ likely related with the nanocavities originated by the corrugation of graphene (in agreement with the HRTEM observations). CO₂ adsorption at 0 °C was used to evaluate the presence of narrow micropores (<0.7 nm) not accessible for N₂, a matter of utmost importance in electrochemical redox reactions, revealing a value of 0.120 cm³·g⁻¹, with a narrow micropores contribution of *ca.* 12 % of the total pore volume of the material.

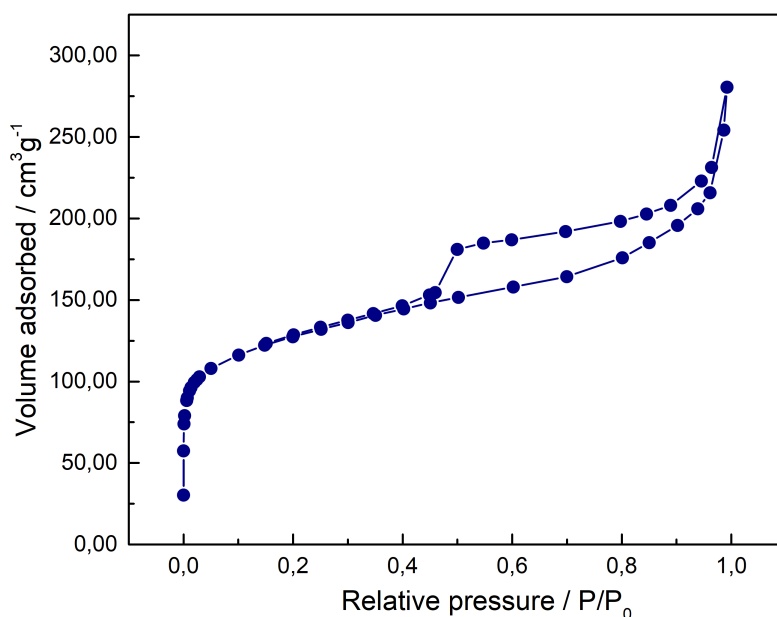


Figure S31. N₂ adsorption/desorption isotherms at 77 K of NC-MUV-3.

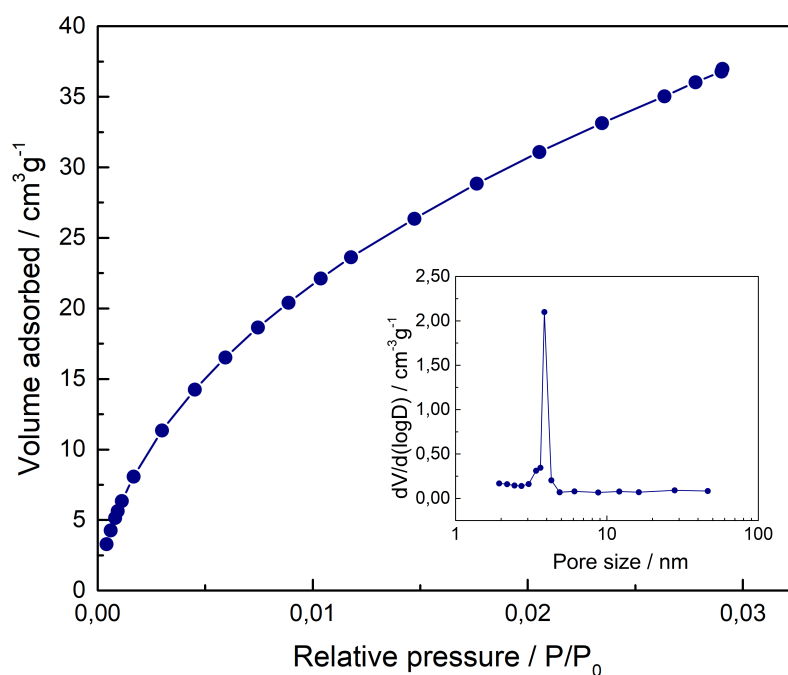


Figure S32. CO₂ adsorption/desorption isotherms at 273 K of **NC-MUV-3**. The inset shows the pore size distribution.

Table S8. Textural characterization values.

$S_{\text{BET}}^{[a]}$	t-plot		$V_t^{[b]}$	$V_{\mu(<0.7 \text{ nm})}^{[c]}$	$V_{\mu\text{DR}}^{[d]}$	$V_{\text{meso}}^{[e]}$	$V_{\text{meso}}^{[f]}$ ($P/P_0=0.7$)
($\text{m}^2 \text{g}^{-1}$)	$S_{\mu}^{[a]}$ ($\text{m}^2 \text{g}^{-1}$)	$S_T^{[a]}$ ($\text{m}^2 \text{g}^{-1}$)	($\text{cm}^3 \text{g}^{-1}$)	($\text{cm}^3 \text{g}^{-1}$)	($\text{cm}^3 \text{g}^{-1}$)	($\text{cm}^3 \text{g}^{-1}$)	($\text{cm}^3 \text{g}^{-1}$)
462.71	363.39	99.33	0.96	0.121	0.181	0.780	0.297

[a] Data obtained from N₂-adsorption. Specific surface area calculated by BET method. Microporous surface contribution S_{μ} and external surface S_T calculated using t-plot. [b] Total pore volume at $P/P_0=0.96$. [c] Data obtained from CO₂-adsorption. Volume of narrow micropores (<0.7 nm) calculated according to the DR method. [d] Micropore volume calculated from N₂-adsorption using DR method. [e] Mesopore volume was calculated according to: $V_{\text{meso}} = V_{\text{Total}} - V_{\mu\text{DR}}$ [f] Mesopore volume ($V_{\text{meso}}(P/P_0=0.7)$) was calculated as the difference of total (V_t) at $P/P_0 = 0.7$ and micropore volume (V_{micro}). [g] Pore size distribution was analysed by using the solid density functional theory (QSDFT) for the adsorption branch assuming a cylindrical pore model.

S6 Electrochemical characterization of NC-MUV-3

The electrochemical experiments were performed using an Autolab electrochemical workstation (PGSTAT-128N potentiostat/galvanostat) connected to a personal computer that uses Nova 2.1 electrochemical software. The powdered materials were mixed with acetylene black and PVDF in a mass ratio of 80:10:10 in ethanol and deposited on a nickel foam or carbon felt electrode. The as-prepared electrodes were dried overnight at 80 °C and pressed. Each working electrode contained about 0.20–0.30 mg·cm⁻² of electroactive material and had a geometric surface area of about 0.2 cm². A typical three-electrode experimental cell equipped with a stainless steel plate having 4 cm² of surface area as the counter electrode, and a Metrohm Ag/AgCl (3 M KCl) as the reference electrode was used for the electrochemical characterization of the working electrodes. All measurements were carried out with magnetic agitation and nitrogen bubbling.

The electrochemical properties were studied measuring the LSV in 1 and 0.1 M KOH. In addition, chronoamperometric studies were performed at a constant overpotential ($j = 0.3$ and 0.4 V), and chronopotentiometric studies at constant current densities of 10 and 15 mA·cm⁻². All potentials reported in this manuscript were converted to the RHE reference scale using $E_{\text{RHE}} = E_{\text{NHE}} + 0.059 \cdot \text{pH} = E_{\text{Ag/AgCl}}^{\circ} + 0.197 \text{ V} + 0.059 \cdot \text{pH}$; and to the OP reference scale using $\text{OP} = 1.229 - 0.059 \cdot \text{pH}$ V (vs. NHE), where $E_{\text{NHE}} = E_{\text{Ag/AgCl}} + 0.197 \text{ V}$.

S6.1 Polarization curves for Oxygen Evolution Reaction

S6.1.1 Comparative with different NCs.

In order to optimize the catalytic properties of the final NC, different studies were made modifying the pyrolysis process, the porosity and the metal of the precursor. To compare different pyrolysis processes, we changed the temperature and the atmosphere, using two temperatures (700 and 900 °C) and two different atmospheres, an inert atmosphere (N₂) and a reducing atmosphere (H₂/Ar 1:9). To analyse the importance of the precursor's porosity, we compare the use of **MUV-3** with a dense coordination polymer formed by the same components as precursors.⁴ And finally, we compare the effect of the metal in the precursor' structure using Fe (**MUV-3**), Zn (ZIF-8) and Co (ZIF-67).

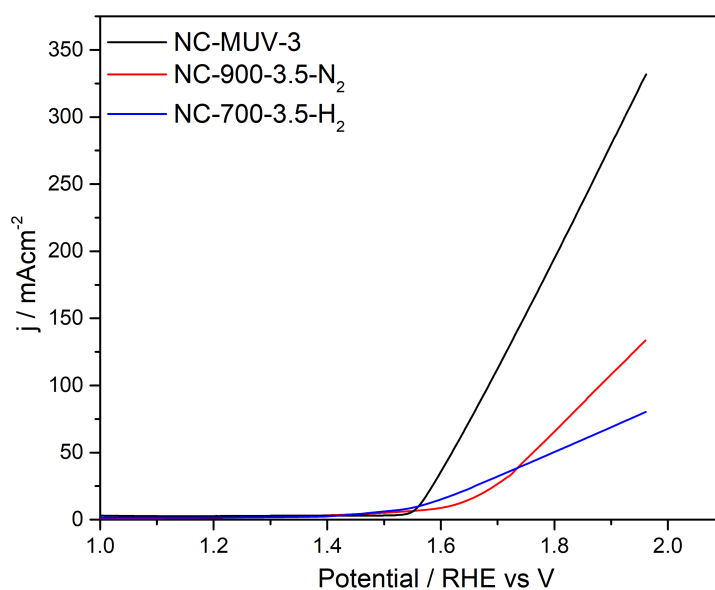


Figure S33. Oxygen Evolution Reaction polarization curves in KOH 0.1 M of different derived **MUV-3** NCs by different calcination process, changing the temperature and atmosphere. **NC-MUV-3** was calcinated using a ramp of 2 °C·min⁻¹, at 700 °C for 3.5 h under nitrogen atmosphere; **NC-900-3.5-N₂** was calcinated using a ramp of 2 °C·min⁻¹, at 900°C for 3.5 h under nitrogen atmosphere; and **NC-700-3.5-H₂** was calcinated using a ramp of 2 °C·min⁻¹, at 700 °C for 3.5 h under hydrogen/argon (1:9) atmosphere.

S6.1.2 Comparative with different commercial catalyst.

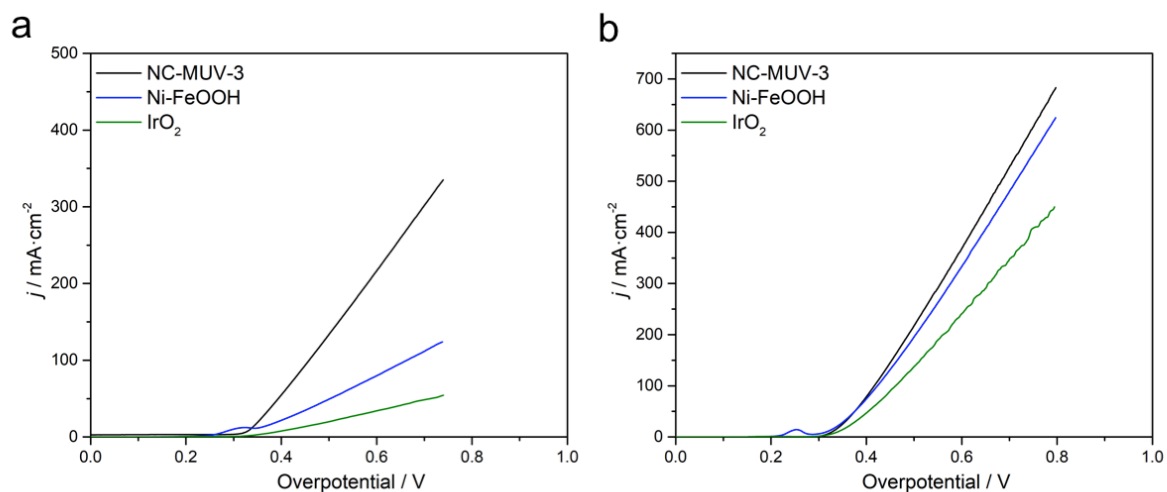


Figure S34. Oxygen Evolution Reaction polarization curves of NC-MUV-3 compared with commercial catalysts (IrO₂ and NiFeOOH) in (a) 0.1 M KOH and (b) 1 M KOH.

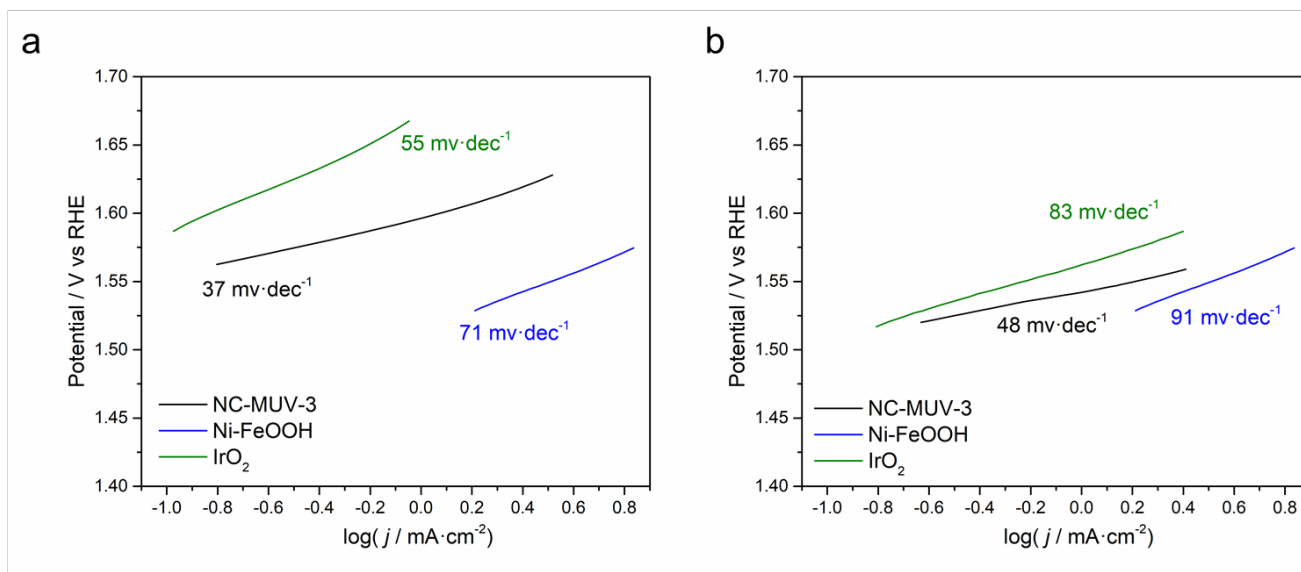


Figure S35. Tafel plots highlighting the corresponding values of Tafel slopes of NC-MUV-3 compared with commercial catalysts (IrO₂ and Ni-FeOOH) (a) 1 M KOH and (b) 0.1 M KOH .

Table S9. Comparison of electrocatalytic values of selected MOF-derived structure materials measured in 0.1M KOH.

Composite	Onset	Tafel Slope	Potential @10 mA·cm ⁻²	η @10 mA·cm ⁻²	η @15 mA·cm ⁻²
	V vs RHE	mV per decade	V vs RHE	mV	mV
NC-MUV-3	1.541	48	1.561	335	344
NC-ZIF-8	1.595	151	1.699	473	529
NC-ZIF-67	1.582	71	1.626	400	438
NC-dense-Fe-CP	1.547	110	1.614	388	434

S6.2 Current densities for Oxygen Evolution Reaction

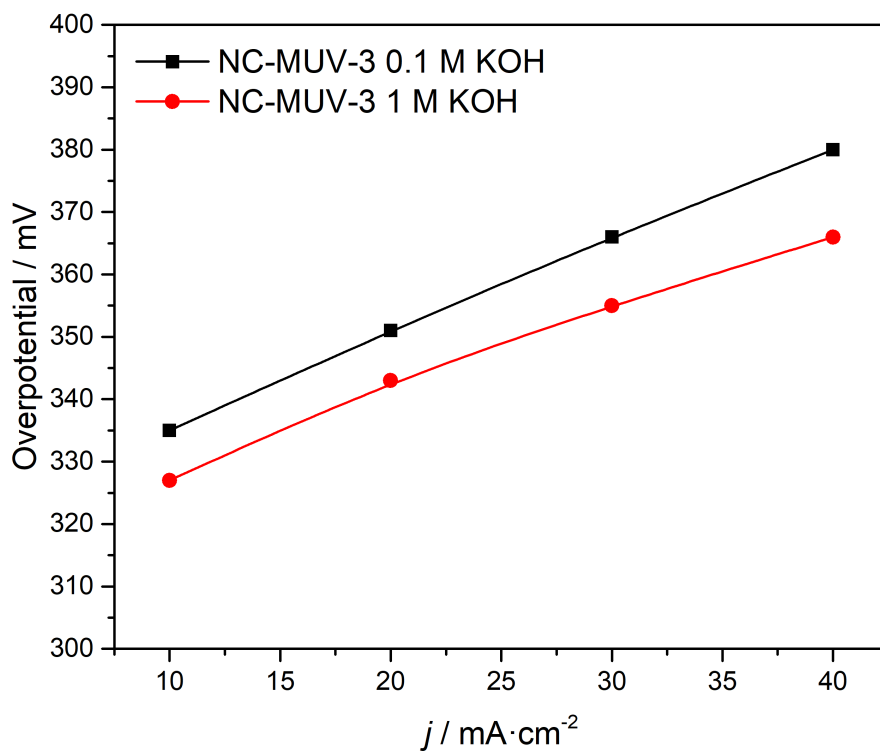


Figure S36. Overpotential at different current densities of NC-MUV-3 in 1 and 0.1 M KOH.

S6.3 Stability testings

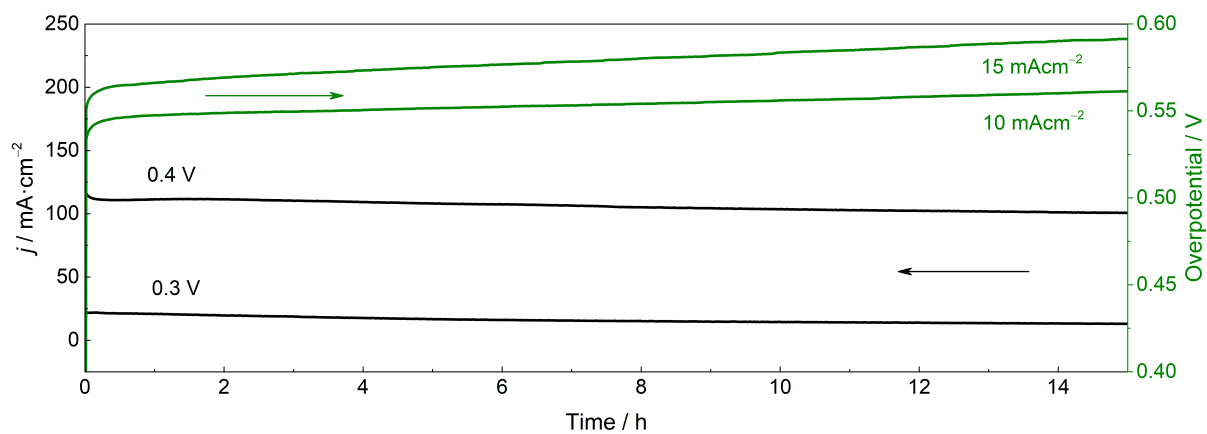


Figure S37. Amperometric (in green) and galvanostatic (in black) stability testings under a certain potential or current density of **NC-MUV-3** in 1 M KOH.

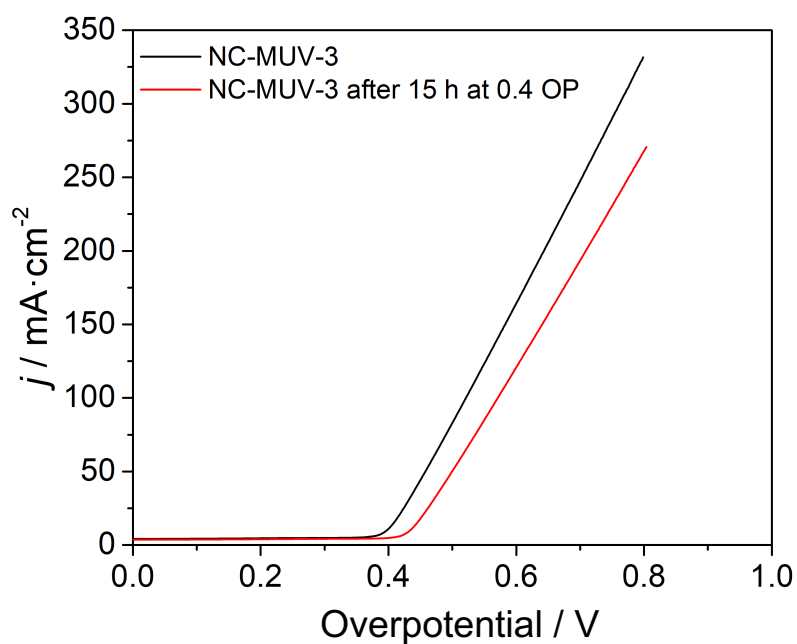


Figure S38. Oxygen Evolution Reaction polarization curves of **NC-MUV-3** in 0.1 M KOH, before and after stability test under a constant current of 15 mA·cm⁻² during 15 h, showing an onset potential of 1.607 V vs. RHE (440 mV of overpotential). This represents an increase of only 66 mV in the overpotential value compared to the pristine material.

Table S10. Comparison of all literature materials.

Composite	MOF precursor	Medium	Onset	Tafel slope	Potential @10 mA·cm ⁻²	OP @10 mA·cm ⁻²	OP @15 mA·cm ⁻²	Loading	S BET	Ref
			V vs RHE	mV per decade	V vs RHE	mV	mV	mV	mg·cm ⁻²	
NC-MUV-3	MUV-3	1 M KOH	1.588	37	1.542	316	324	0.25	463	This work
	NC-MUV-3	0.1 M KOH	1.541	48	1.561	335	344	0.25	463	This work
MO2	-	1 M KOH	1.605	55	1.565	339	352	0.25	-	This work
	MO2	0.1 M KOH	1.587	83	1.647	421	463	0.25	-	This work
NC-ZIF-67	ZIF-67	0.1 M KOH	-	71	1.626	400	438	0.25	-	This work
	ZIF-8 @ Ni/foam	0.1 M KOH	-	-	1.630	463	-	-	960	Angew. Chem. Int. Ed. 2013, 52, 52
Co3O4@C-MWCNTs from ZIF-9	ZIF-9	1 M KOH	1.496	62	1.546	320	-	0.27	-	J. Mater. Chem. A 2015, 3, 17392
	ZIF-67	1 M KOH	-	93	1.600	370	-	0.2	-	Nat. Energy, 2016, 1, 1506
N-doped carbon nanotube from ZIF-67	ZIF-67	0.1 M KOH	-	-	1.750	583	-	0.36	375	Adv. Funct. Mater. 2015, 25, 872
	ZIF-derived carbon	0.1 M KOH	-	-	1.660	493	-	0.36	46	Adv. Funct. Mater. 2015, 52, 5248
N/Co-doped MOF derived carbon/NRGO	ZIF-67	0.1 M KOH	1.58	89	1.617	450	-	0.35	48	J. Power Sources 2015, 294, 103
	Co3-O4-300x	0.1 M KOH	1.52	72	1.557	390	-	0.35	97	Nano Energy 2015, 12, 1
Co3O4@N-PC	ZIF-67	0.1 M KOH	-	51	1.464	238	-	1	185	Adv. Energy Mater. 2017, 7, 160264
	Co3O4@COO	1 M KOH	-	81	1.536	310	-	-	226	J. Am. Chem. Soc. 2016, 138, 10226
Co4N/CNW/CC	ZIF-67	1 M KOH	-	88	1.566	340	-	1	46	J. Am. Chem. Soc. 2015, 137, 5590
	ZIF-67	1 M KOH	1.53	52	1.545	319	-	-	-	Chem. Mater. 2015, 27, 7636.
CoPy NPs @ N-doped carbon matrices	ZIF-67	1 M KOH	-	76	1.596	370	-	-	-	J. Mater. Chem. A 2016, 4, 3204
	ZIF-67	0.1 M KOH	-	54	1.577	410	-	-	-	Angew. Chem. Int. Ed. 2016, 55, 408
Co3O4@CNT-graphitic N-doped carbon	ZIF-67	1 M KOH	-	66	1.566	340	-	-	-	Chem. Sci. 2016, 7, 1690.
	Layer CoP/GO composite	1 M KOH	-	51	1.464	238	-	-	-	Adv. Energy Mater. 2017, 1602643
Co3O4@CoP from ZIF-67	ZIF-67	1 M KOH	-	64	1.447	280	-	0.2	-	J. Power Sources 2016, 334, 112.
	NiCo4S@C-1000 from ZIF-67	ZIF-67	1.367	57	1.626	400	-	0.3	-	ACS Appl. Mater. Interfaces 2016, 8,
CoP hollow polyhedrons from ZIF-67	ZIF-67	1 M KOH	1.526	74	1.482	315	-	0.26	-	Chem. Commun. 2016, 52, 9727
	Co-CNT-PC from ZIF-67	1 M KOH	1.427	74	1.482	315	-	-	-	Chem. Sci. 2016, 7, 1690
CoP/GO-400 from ZIF-67	ZIF-67	1 M KOH	-	66	1.566	340	-	-	209	Nat. Energy 2016, 1, 16184
	NiCo-UMOFNs	1 M KOH	1.42	42	1.476	250	-	0.2	235	Nanoscale 2015, 8, 1033
MOF/Fe1-Co3/550N	MOF/Fe1-Co3/550N	0.1 M KOH	1.52	73	1.557	390	-	0.14	31	Adv. Mater. 2016, 28, 4601.
	Ni-Co mixed oxide cages	1 M KOH	-	50	1.606	380	-	-	31	Adv. Mater. 2016, 28, 4601.
NF@NC-CoFe2O4/C NRAs	MOF-derived PBA	1 M KOH	1.45	45	1.466	240	-	1.03	76	Adv. Mater. 2016, 29, 1604437
	MOF-74	1 M KOH	1.52	52	1.628	402	-	0.14	128	J. Phys. Chem. C 2015, 120, 517
Ni/Fe3-xO4	Co-Fe-PBA	1 M KOH	1.52	70	1.457	290	-	-	251	J. Am. Chem. Soc. 2014, 136, 13925.
	Co-naphthalenedicarboxylate MOF	0.1 M KOH	-	88	1.582	356	-	-	-	ACS Appl. Mater. Interfaces 2016, 8,
Co3O4@NiA	Co-MOF	1 M KOH	-	73	1.557	390	-	-	-	Nanoscale 2016, 8, 1033
	Co-doped NH2-MIL-53(Fe)	0.1 M KOH	-	73	1.550	324	-	-	-	Nano Res. 2016, 9, 1856.
CoNi hydroxide ultrathin nanosheets	Co-acetate MOF	1 M KOH	-	33	1.650	483	-	0.36	25	Energy Environ. Sci. 2014, 7, 609
	-	0.1 M KOH	-	-	1.640	473	-	0.21	-	Angew. Chem. Int. Ed. 2014, 53, 85
Zn-doped CoSe2/CrC from Zn-Co-ZIF	-	0.1 M KOH	-	-	1.700	533	-	0.28	-	ACS Appl. Mater. Inter. 2013, 5, 506
	-	0.1 M KOH	-	-	1.630	463	-	0.24	813	Small 2014, 10, 2251
NiCo2S4@N/S-GO	-	0.1 M KOH	-	-	1.600	433	-	0.2	149	Angew. Chem. Int. Ed. 2014, 53, 72.
	-	0.1 M KOH	-	-	1.610	443	-	0.2	560	Nat Commun. 2013, 4, 2390
N-doped carbons	-	0.1 M KOH	-	-	1.800	633	-	1.75	208	Adv. Funct. Mater. 2014, 26, 2925
	-	1 M KOH	-	48	1.526	300	-	-	122	ACS Appl. Mater. Inter-faces 2016, 8,
FeNi@N-CNT from ZIF/Ni-ZIF	-	1 M KOH	-	-	1.800	633	-	-	-	ACS Appl. Mater. Inter-faces 2016, 8,
	-	1 M KOH	-	-	1.526	300	-	-	-	ACS Appl. Mater. Inter-faces 2016, 8,

S7 References

- [1] Pawley, G. S. *J. Appl. Crystallogr.* **1981**, *14*, 357–361.
- [2] Coelho, A. A. *TOPAS-Academic*, version 4.1. 2007. See: <http://www.topas-academic.net>
- [3] S. J. Rettig, A. Storr, D. A. Summers, R. C. Thompson and J. Trotter, *J. Can. J. Chem.* **1999**, *433*, 425–433.
- [4] T. L. Hill, *J. Chem. Phys.* **1949**, *17*, 520–535
- [5] M.M. Dubinin. *Physical Adsorption of Gases and Vapors in Micropores*, Elsevier, **1975**, *9*, 1-70
- [6] M. Iley, H. Marsh, and F. R. Reinoso, *Carbon N. Y.*, **1973**, *11*, 633–638.
- [7] a) F. Carrasco-Marin, M. V. Lopez-Ramon, C. Moreno-Castilla, *Langmuir*, **1993**, *11*, 2758–2760, 1993. b) J. Garrido, A. Linares-Solano, J. M. Martin-Martinez, M. Molina-Sabio, F. Rodriguez-Reinoso, R. Torregrosa, *Langmuir*, **1987**, *3*, 76–81
- [8] J. Tang, R. R. Salunkhe, J. Liu, N. L. Torad, M. Imura, S. Furukawa, Y. Yamauchi. *J. Am. Chem. Soc.* **2015**, *137*, 1572–1580
- [9] Xia, B. Y.; Yan, Y.; Li, N.; Wu, H. Bin; Lou, X. W.; Wang, X. *Nat. Energy* **2016**, *1* (1), 15006.
- [10] M. Görlin, P. Chernev, J. Ferreira de Araújo, T. Reier, S. Dresch, B. Paul, R. Krähnert, H. Dau, P. Strasser *J. Am. Chem. Soc.*, **2016**, *138*, (17), 5603-5614

Appendix: Chapter 5

Material scaling and supercapacitive device assembly

5.1 Introduction

The scaling-up in chemical engineering is the increase in mass or volume of a chemical reaction or process with the appropriate use of chemical apparatus and equipment necessary to accomplish it. For this, a first laboratory scaling study is required, where the different reactions and chemical mechanisms are studied. Once studied in the laboratory, a new investigation has to be done in order to increase the mass or volume of the same reaction. To carry it out, it is necessary with chemical engineering to study the modification of some variables, such as the total volume of reaction, reagent concentration, physical conditions, *etc.* to obtain a final product equal to that obtained in laboratory¹. Chemical engineering is a branch of engineering that uses principles of chemistry, physics, mathematics, *etc.*, to efficiently use, produce, design, transport and transform energy and materials. The work of chemical engineers can range from the utilisation of nanotechnology and nanomaterials in the laboratory to large scale industrial processes that convert chemicals into useful forms and products.

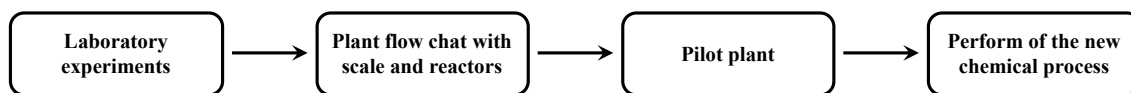


Figure 5.1. Overview of a typical scale-up procedure.

The scale process or scaling follows a procedures consisting of different steps procedure (Figure 5.1). Starting point is a lab experiments directly, a publication or a patent document. With this lab study we know all the steps and quantities used on the laboratory scale. This information is then used to elaborate the second point: design a simple plant flow diagram. Such a diagram should include all the steps involved as well as the scale, reactors, apparatus and main equipment. The next stage consists of the use of a pilot plant, which is one of the most common ways in chemical engineering to carry out chemical scaling. A pilot plant is a pre-commercial production system that employs new production technology and/or produces small volumes of new technology-based products, mainly for the purpose of learning about the new technology. In addition, the knowledge obtained in a pilot plant can be used to design full-scale production systems and commercial products, as well as for identification of further research objectives and

support of investment decisions. The final step, deals with the use of the pilot plant to obtain the desired materials/chemicals in order to use them in the industry.

Recent research developed in our laboratory has led to some patents of different materials, with very good supercapacitive and electrocatalytic properties, and therefore, different companies have been interested in these patents. In order to work with companies, we must move from a laboratory scale to a higher Technology Readiness Levels (TRL) that is from TRL-X to TRL-5/6 (see Figure 5.2). Typically, research laboratories are in a TRL-1/2, but if you want to reach higher levels it is necessary to assemble commercial like prototypes and study the behaviour in these prototypes of materials. For this reason, it has been very important to set up a laboratory or pilot plant to obtain enough quantities for industrial tests, with synthesis close to kilograms of material, as well as the study of different battery-type devices, in order to reach a TRL6.

Once we obtained enough material for industrial tests, something not trivial, it was necessary to study these materials in systems closer to commercial batteries/capacitors. That is why a severe study was also carried out on commercial battery prototypes of different materials, evaluating their properties as closely to their systems.

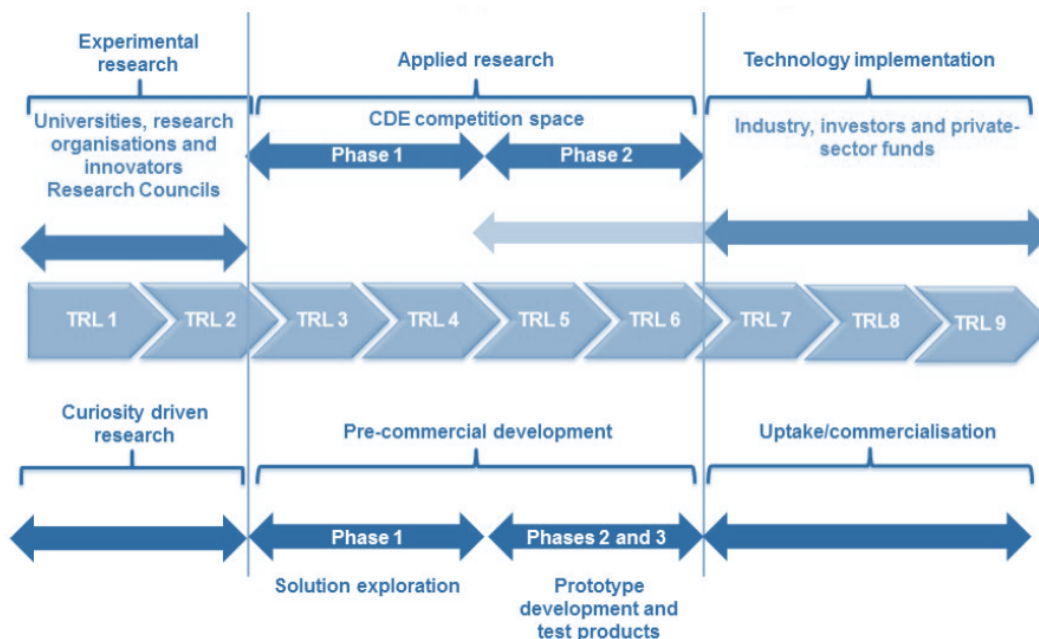


Figure 5.2. Scheme of the different TRL levels.

5.2 Scaling of FeNi₃-Graphene nanocomposite

As we can see in Chapter 2, FeNi₃-Graphene NC has an exceptional supercapacitive behaviour. For this reason, many companies like *Maxwell Technologies*, *3M*, *Itelcond*, *Industrial Química del Nalón*, etc., were interested in the material and the patent (WO2018011445A1). The main problem of this is that companies required hundreds of grams for their tests, and the production of the precursor for this material (NiFe-LDH-Seb) in the laboratory-scale is only *ca.* 5 g per synthesis, therefore, we had to make a production scaling to afford the demands of the companies.

The FeNi₃-Graphene is obtained by a controlled thermal treatment in an inert atmosphere, using as precursor a NiFe-LDH with sebacate molecules in the interlaminar space²⁻⁷. The scaling process of the precursor was carried out in a 20 l reactor, in cooperation with Instituto Tecnológico del Plástico (Aimplas). After control tests in the laboratory, it was decided to make some changes to the original synthesis described in our group previously⁵. The precursor NiFe-LDH-Seb was prepared by a coprecipitation system, adding at the same time by using peristaltic pumps a solution with the salts of nickel and iron dissolved keeping the stoichiometric coefficient $x = M^{III} / (M^{II} + M^{III})$ at the value of $x = 0.20$, and another one with sodium sebacate. In addition, pH was monitored throughout the metals/sebacate addition, using a 2.5 M NaOH solution to keep pH at 8, as we can see in Figure 5.3. Subsequently, the slurry was heated up to 80 °C, with temperature checks inside the reactor to confirm that the temperature was correct, under constant stirring (300 revolutions per minute), and kept at this temperature for 7 days at nitrogen atmosphere.

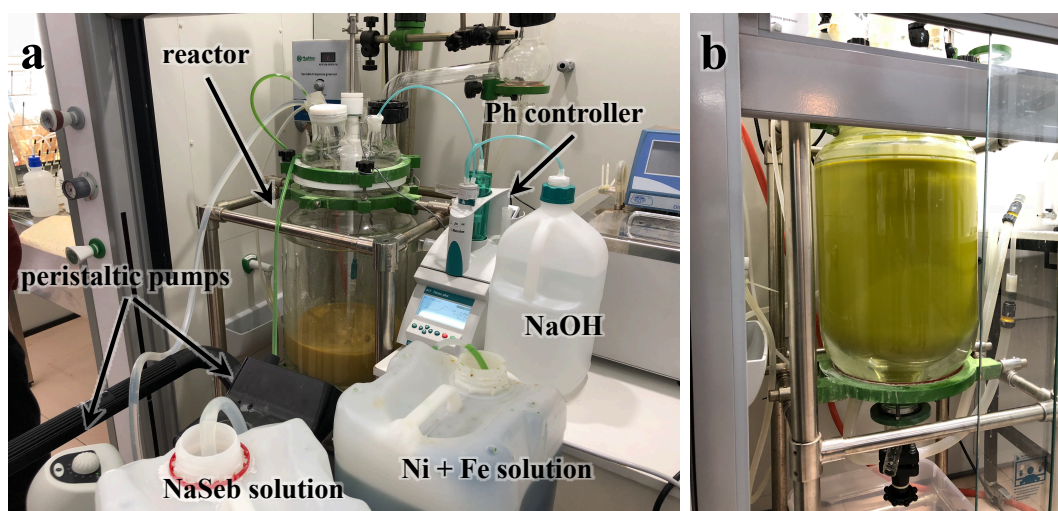


Figure 5.3. NiFe-LDH-Seb scaling process. (a) Addition of the different solutions in the 20 l reactor with all the different components used. (b) Full reactor by heating the slurry at 80 °C.

After the 7 days, the solid was filtered, washed with deionized water and ethanol, and dried at 80 °C for several days (Figure 5.4 a-b). After the first wash, XRPD showed a contamination of the metal salts used, as we can see in Figure 5.3. To remove them, a series of intensive washes with deionized water were performed, confirming later by XRPD and elemental analysis a precursor with free-metal salts, a LDH structure and the presence of sebacete. The final mass obtained was more than half a kilogram, two orders of magnitude higher than using conventional synthetic method.

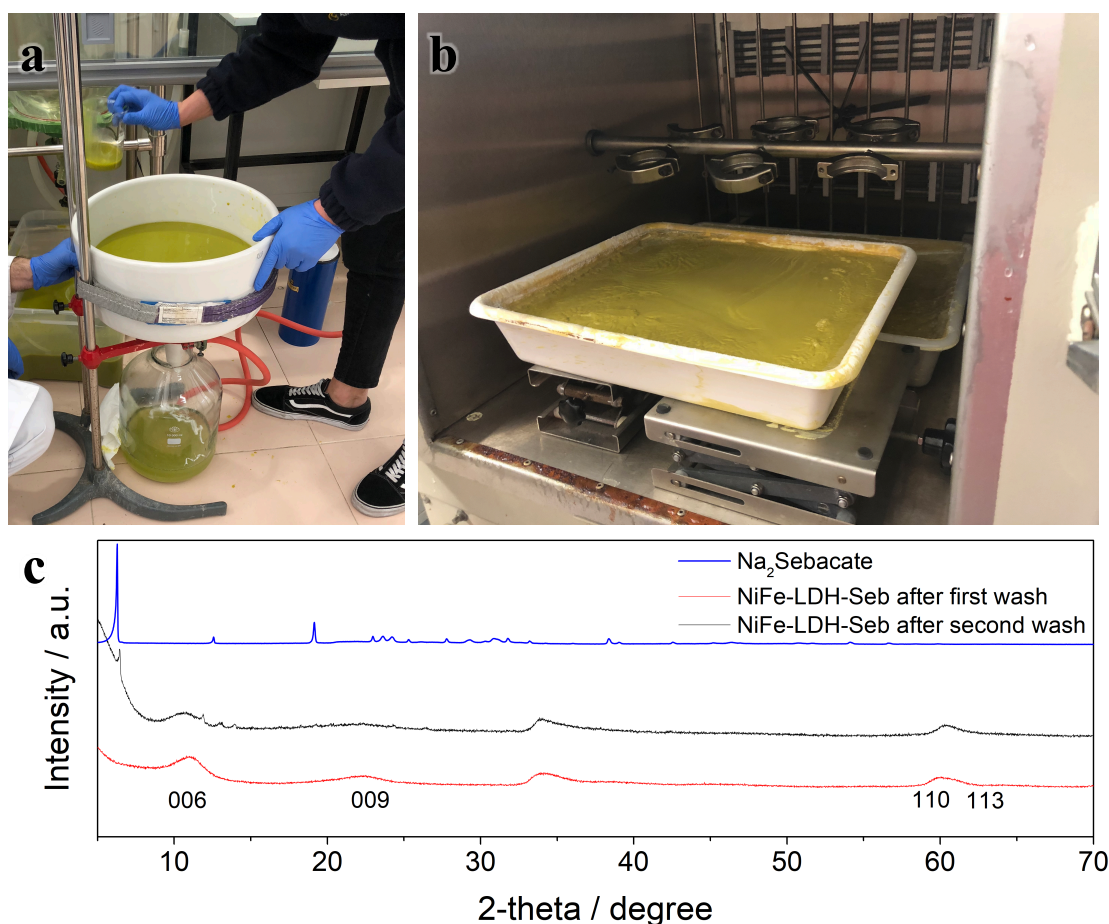


Figure 5.4. (a) Filtration of the NiFe-LDH-Seb synthesized and (b) dried in an oven at 80 °C. (c) XRPD pattern of the NiFe-LDH-Seb obtained by the scaling method, before and after the second wash.

Once the precursor was obtained, a calcination process was carried out to obtain the final NC of FeNi₃-Graphene. Using a classic CVD oven, it is not possible to calcine more than 2 g of the precursor at the same time, so it was necessary to use a much larger type of oven and extrapolate the calcination process. To do that, we used an MTI three zone tubular furnace, with a much larger quartz tube, where we were able to calcine more than 50 g of precursor each run. As we can see in Figure 5.5-a, the precursor was deposited in ceramic racks, and subsequently placed inside the oven. To remove all oxygen trace from the tube, several vacuum purge cycles with nitrogen were performed. The calcination process was carried out at 900 °C for 2 hours, in an inert atmosphere with a continuous flow of 500 ml·min⁻¹, and with a heating and cooling ramp of 2 °C·min⁻¹.

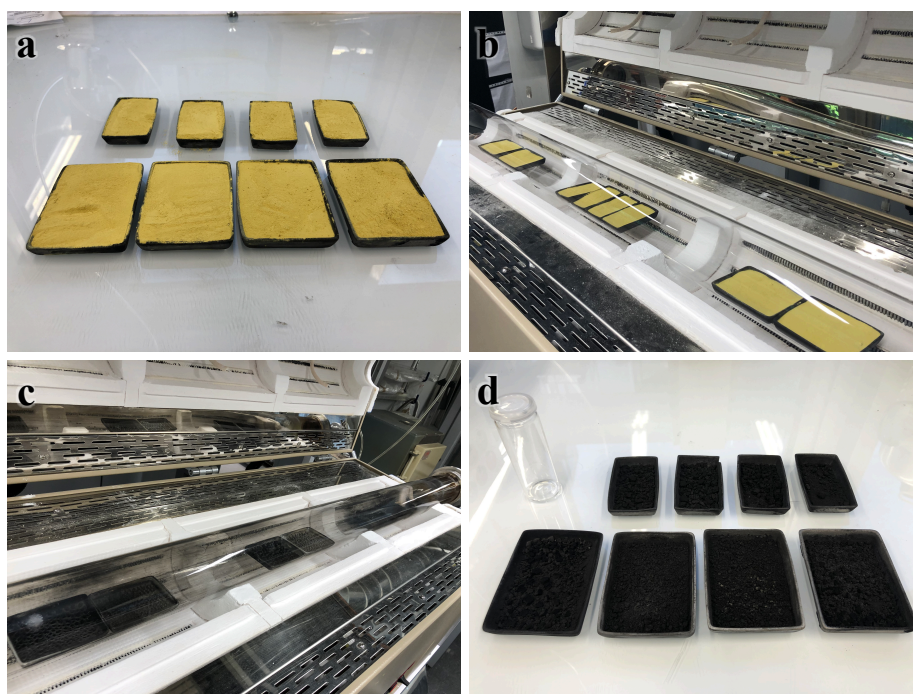


Figure 5.5. (a) Precursor of NiFe-LDH-Seb in porcelain racks. (b) Porcelain racks with the precursor inside the oven quartz tube. (c) Result after calcination process at 900 °C. (d) NC of FeNi₃-Graphene obtained in a calcination batch.

Finally, the resulting black powder was characterized. The XRPD patterns confirmed the crystalline structure of FeNi₃, and the high resolution TEM images showed the presence of graphitic carbon surrounding the metallic NP (Figure 5.6). This morphology is very similar than the NC obtained by the traditional method, with the same size of NP and a little less carbon matrix. In addition, in order to confirm its capacitive behaviour, electrochemical measurements were performed in a three-electrode cell, observing in the

galvanostatic charge/discharge cycles values practically equal to those previously obtained in Chapter 2 (Figure 5.7).

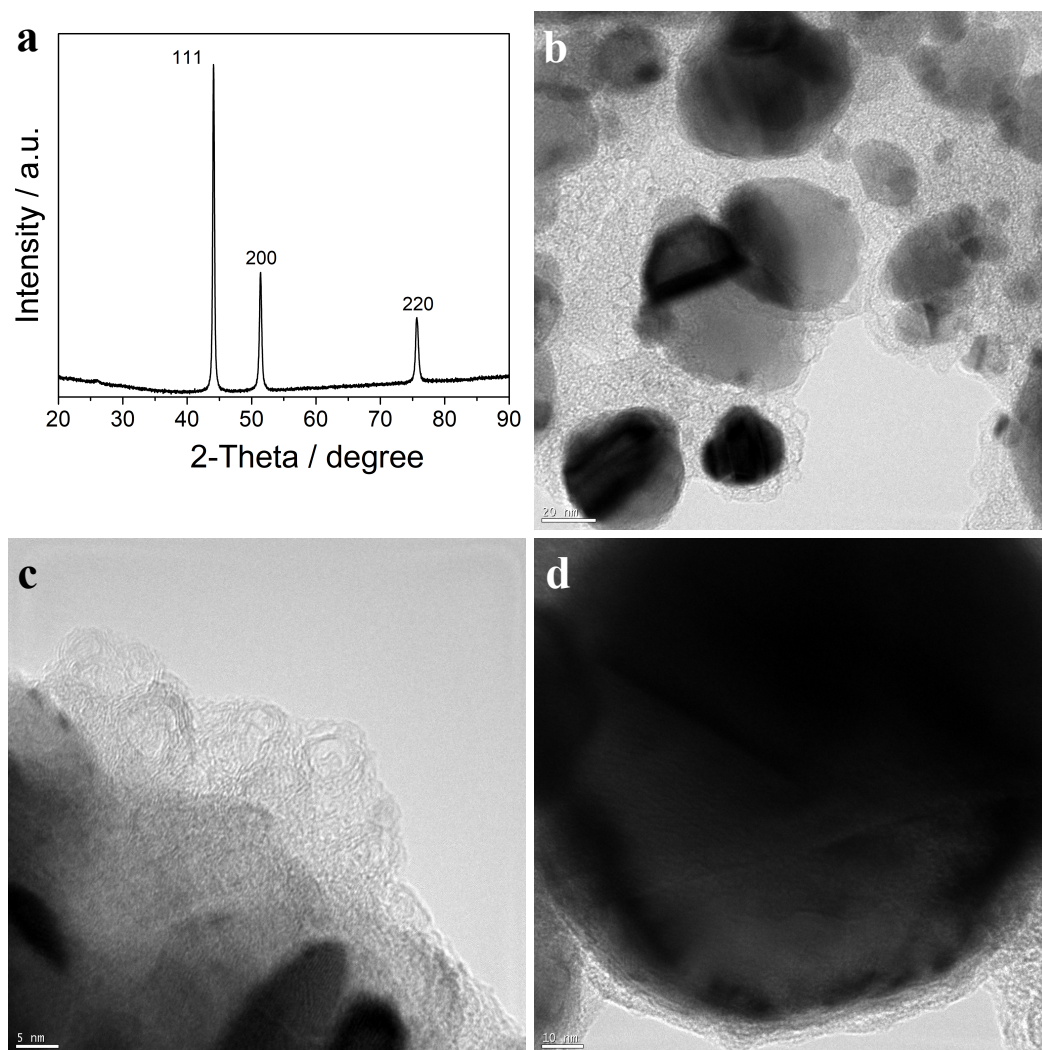


Figure 5.6. (a) XRPD pattern and (b-d) high resolution TEM images of the FeNi₃-Graphene obtained after the scaled calcination process.

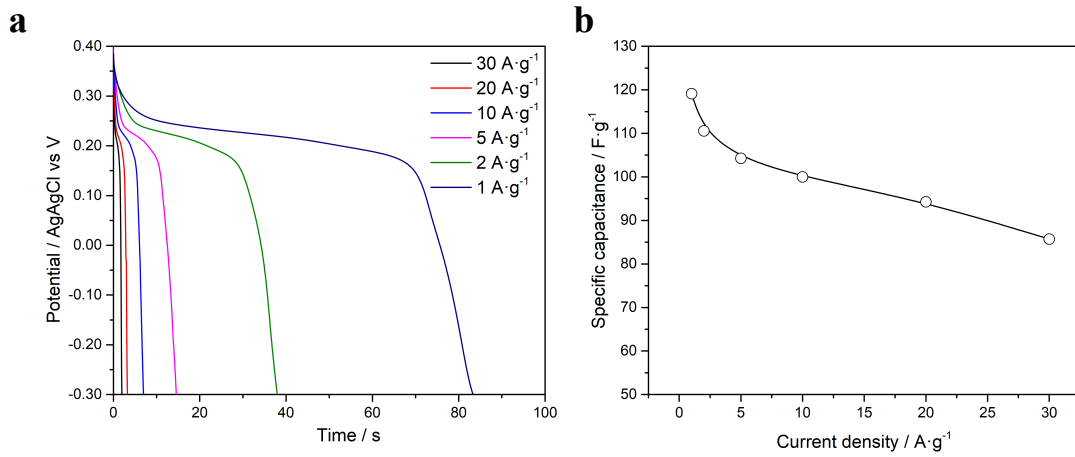


Figure 5.7. Electrochemical measurements in a three-electrode cell configuration using 6M KOH aqueous solution of the FeNi₃-Graphene obtained after the scaling calcination process. (a) Galvanostatic discharge curves at different discharge current densities. (b) Specific capacitance at different discharge current densities.

5.3 Scaling of the FeNi₃-Graphene-NiFoam electrodes

Another demand of companies was the assembly of NiFoam electrodes with the NC deposited or directly growth on them and already activated magnetically as we see in Chapter 2⁷. These electrodes had to have dimensions of minimum 10 x 10 cm to be able to punch circles to use them in coin cells as working electrode. The maximum dimensions that we could use in a three-electrode cell was 2.5 x 2.5 cm, so we had to design a new cell, in which it was possible to use 10x10 cm electrodes and to apply galvanostatic charge and discharge cycles in the presence of an external magnetic field.

As we can see in Figure 5.8, we designed a cell formed by two clamping plates, with a working and a counter electrode in the middle, separated by a plastic net to avoid the short circuit. For both electrodes, a connector protrudes from the top to be able to connect them to a potentiostat. In addition, it has two liquid inlets, to be able to fill it with the desired electrolyte and to evacuate bubbles produced by possible water splitting.

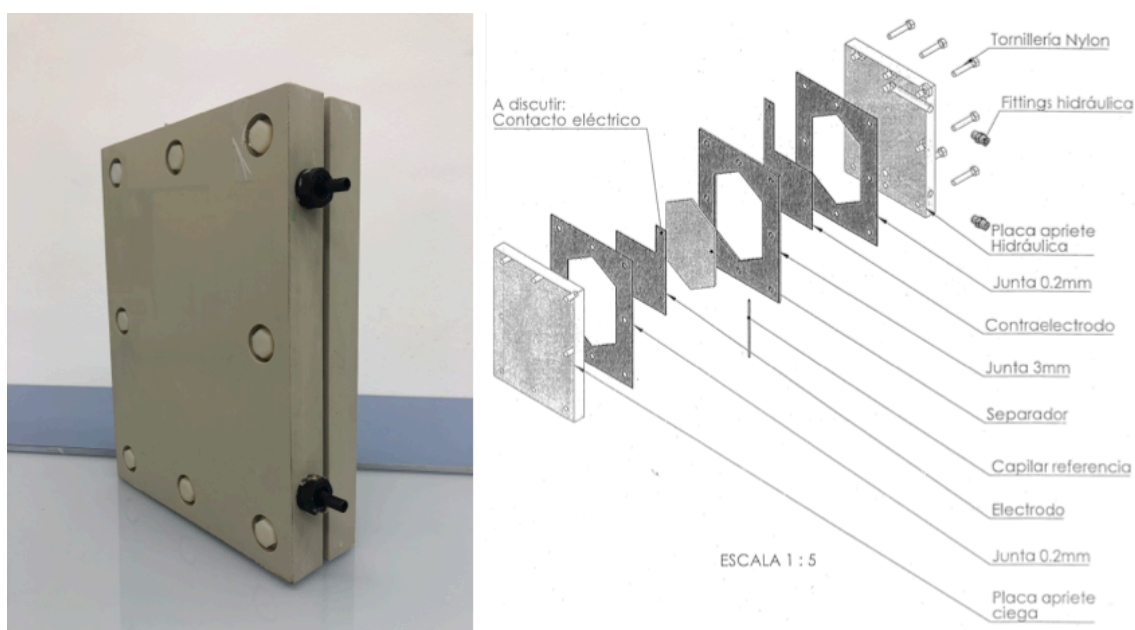


Figure 5.8. (a) Cell used to activate 10x10 cm NiFoam electrodes. (b) Exploded view of the cell.

To prepare the working electrode, a mixture of acetylene black and PVDF in ethanol in a mass ratio of 80 : 10 : 10 was prepared and deposited on a Ni foam 10 x 10 cm electrode (Figure 5.9). The as-prepared nickel foam electrodes were dried overnight at 80

°C and pressed. Each working electrode contained about $0.5 \text{ mg}\cdot\text{cm}^{-2}$ of electroactive material.

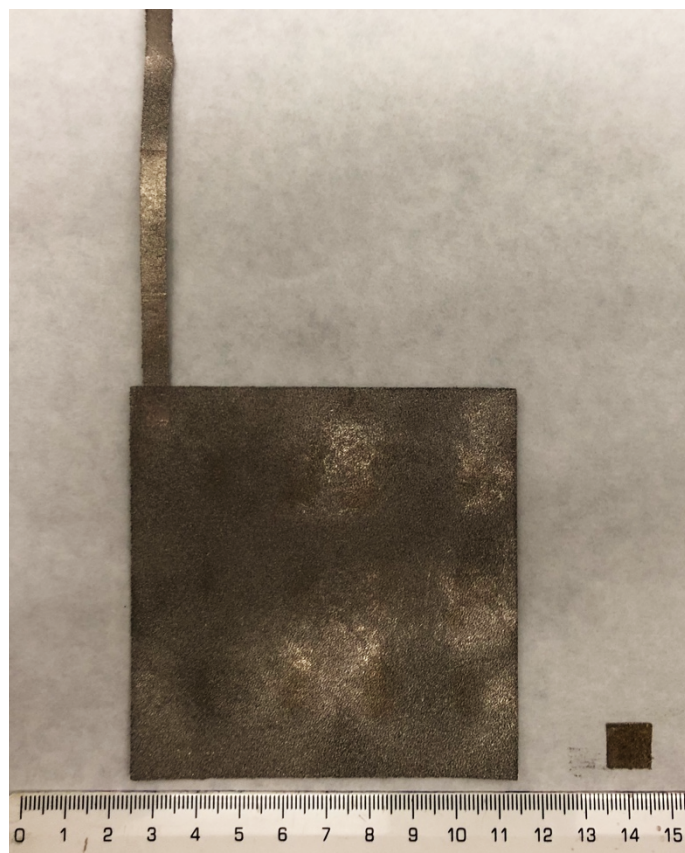


Figure 5.9. Comparative size of a 10 x 10 cm electrode vs a normal electrode of 1 cm².

Using KOH 6 M as electrolyte, CV show the typical redox picks, where we can perfectly see the oxidation peaks of Ni (Figure 5.9-a). Also, in galvanostatic charge/discharge curves at different current densities we obtained a slightly lower values than using a typical three-electrode cell. In order to produce the metal segregation and increase the specific capacitance, the new cell was placed in the middle of an electromagnet Bruker ELEXYS E580, applying a magnetic field of 4,000 Oe and galvanostatic charge/discharge cycles at the same time.

The increase of capacitance was lower than that produced in a 1 cm^{-2} electrode, possibly due to the inhomogeneous applied magnetic field throughout all the electrode, and being in a much more compact space. Observing Figure 5.9-b, we can see the increase of the capacitance, showing a maximum of ca. 540%.

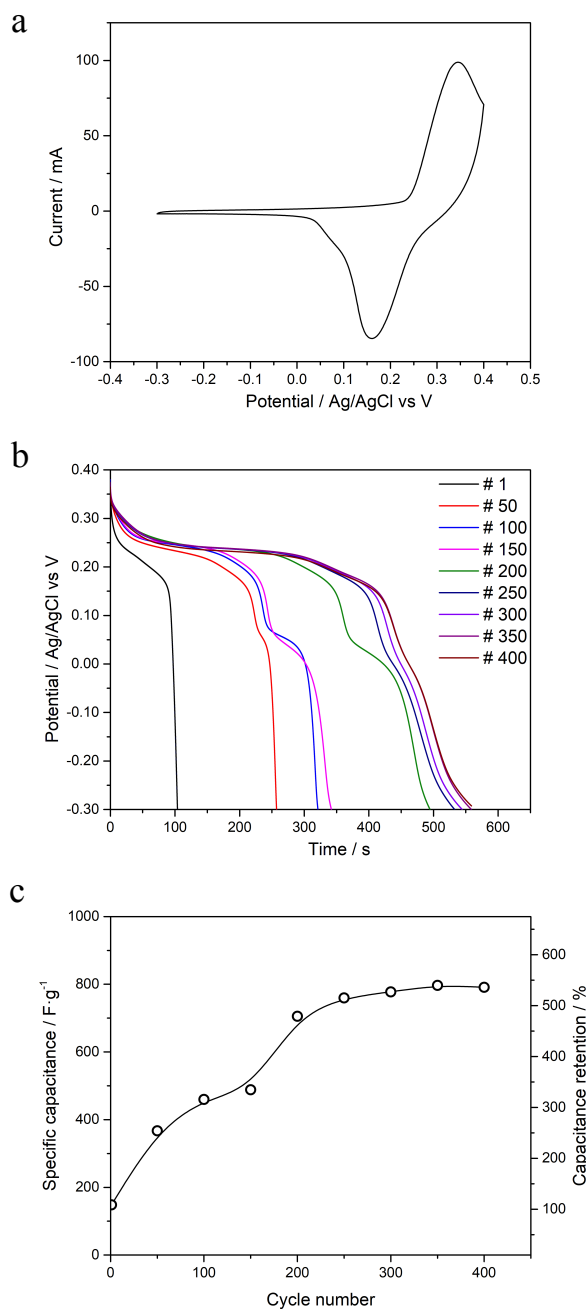


Figure 5.10. Electrochemical measurements of the 10 x 10 cm electrode in the special cell using 6 M KOH as electrolyte and Ag/AgCl as reference electrode. (a) Cyclic voltamperometry at 100 mV·s⁻¹ scan rate. (b) Galvanostatic discharges at 1 A·g⁻¹ current density in presence of an external magnetic field, with (c) the corresponding capacity retention per cycles.

There is currently an optimization process, changing variables such as the density of active material per square centimetre, to try to obtain a capacitance similar to that obtained in Chapter 2.

5.4 Assembly and study of two-electrode batteries

One of the main objectives during the development of PhD has been the application of different nano materials as supercapacitors. A very important point to consider is the study of this materials in two-electrode cell configurations, which is much closer to real state of commercial batteries/capacitors^{8,9}. This cells are comprised of two electrodes that are isolated from electrical contact by a porous separator. The separator and electrodes are impregnated with an electrolyte, which allows ionic current to flow between the electrodes while preventing a short circuit in the cell. The main problem of these types of cells is that there is not reference electrode, the reference is the counter electrode itself, so the cell voltage is the difference voltage between the counter and the working electrode. This means that we do not know where exactly the potential of each electrode is, and we do not know if it is in an optimum or harmful potential window for the material.

To solve this, we use a “false” two-electrode cell, where with special potentiostats, we can create a two-electrode configuration, but having a fixed reference, such as Ag/AgCl, monitoring the potential all the time of both electrodes. As we can see in Figure 5.11, with a *Swagelok*[®] T-cell we can put the materials with the typical configuration of two-electrode cell, and also a reference electrode to know the potential in both electrodes. This way of being able to know the exact potential of each electrodes is very important, since it gives you the possibility of changing the working potential window to an optimized window by mass modifications in the electrodes, to a more optimal window, increasing its specific capacitance, and avoiding electrode degradation¹⁰⁻¹³.

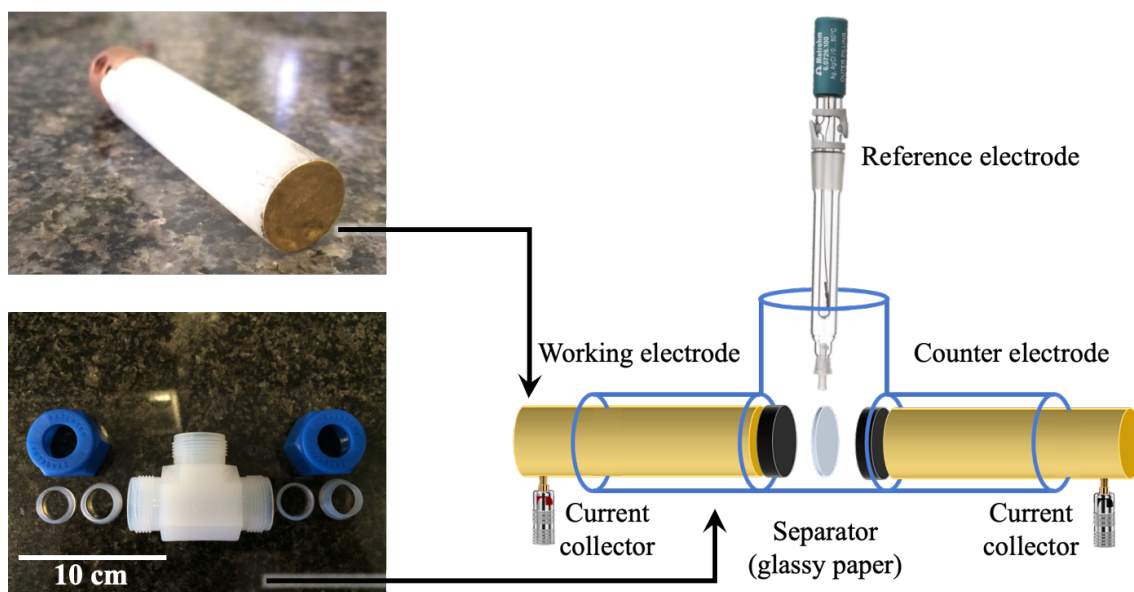


Figure 5.11. Scheme of a Swagelok® T-cell with the different components. Top a gold connector and bottom the disassembled Swagelok® T-cell.

There are many possible combinations for two-electrode cells, but they can be classified into two main groups: I) symmetric cells, where the composition, the material and the mass of working and counter electrode are exactly the same; II) asymmetric, where working and counter electrode are different. Mainly, they are used to make hybrids with the two possible types of capacity, being generally a working electrode with a pseudocapacitive material (faradic capacitance) and a counter electrode with EDLC. In the present work, we studied both combinations in order to understand how different types of capacitances behave in these systems.

5.4.1 Symmetric two-electrode cell supercapacitor

As we have seen in Chapter 3, we used N-doped graphene from the calcination of COF-1-Fe as active material in a two-electrode symmetric cell. Since the material is porous and allows easy access of the electrolyte, the electrodes were assembled as a pellet form, mixing about 5 mg of active material and Teflon (9 : 1 proportion). The electrolyte employed was aqueous 6 M KOH, and a cellulose membrane as separator. The test

voltage range was optimized with a T-two-electrodes using Ag/AgCl as reference electrode.

In symmetrical two-electrode cell configurations, as the counter and working electrode are exactly the same, the potential differences applied to each electrode are equal to each other and are one-half of the cell potential. As we can see in Figure 5.12, the optimal voltage for the cell with this material in a two-electrode cell was 1 V. The reason why this voltage is optimal is that T-cell showed that the potential of the working and the counter electrode always remain in the optimum potential range for carbon materials in basic media, about 0 to -1 V vs Ag/AgCl^{14–17}. If we increase the cell voltage, the working electrode potential would reach to positive potentials vs. Ag/AgCl, where this N-doped graphene does not have EDLC, as we show in our work⁹. At the same time, the potential of the counter electrode would fall to potentials below -1 V vs. Ag/AgCl, taking place the reduction of the carbon and therefore the degradation of the battery. In addition, the typical ohmic drop can be seen in all different current densities, occurring at the beginning of the discharge and charge, typical in EDLC capacitors.

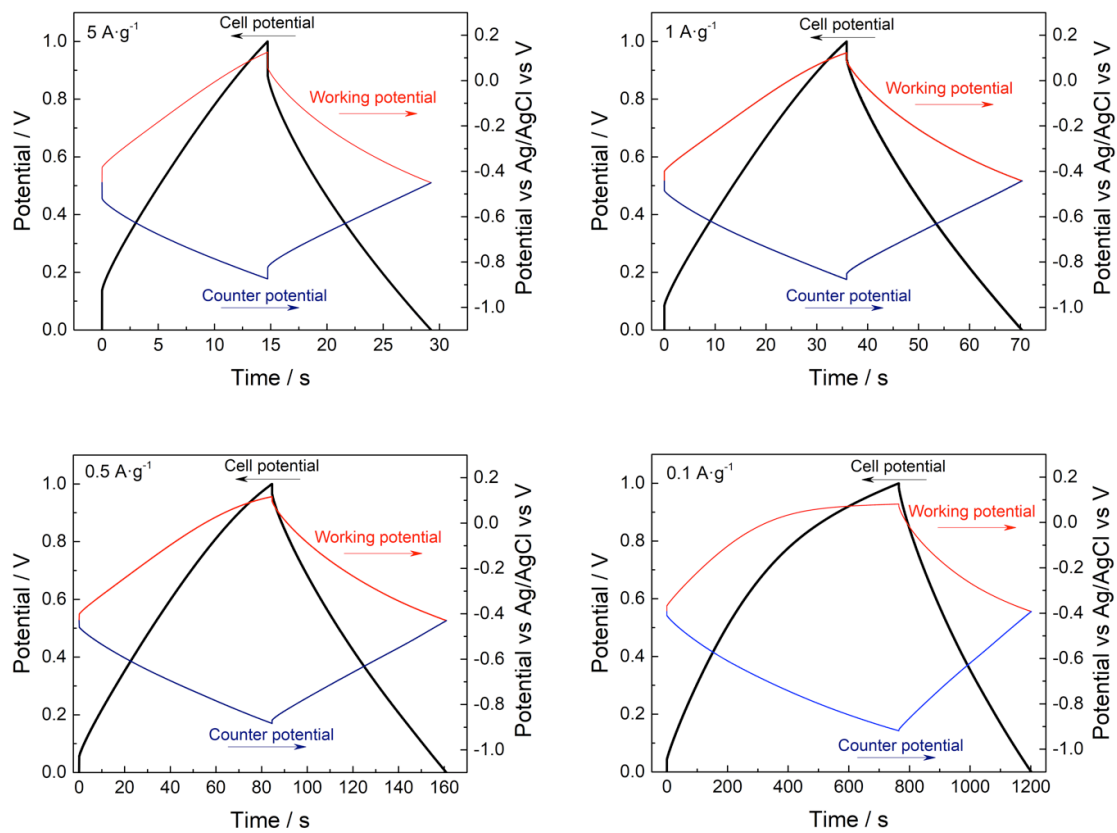


Figure 5.12. Electrochemistry measurements of the N-doped graphene in a T-two-electrode cell in 6 M KOH and Ag/AgCl as reference electrode. Galvanostatic charge

and discharges curves at different current densities, using 1 V as potential window of the cell and showing the potential of both electrodes vs Ag/AgCl.

5.4.2 Asymmetric two-electrode cell supercapacitor

In order to study asymmetric supercapacitors, we used the FeNi₃-graphene NC of Chapter 2, and their respective carbon matrix without NP, removing them by an acid leaching. For working electrode we used the FeNi₃-graphene in order to obtain the pseudocapacitance of the metallic NP, and for the counter electrode, as we need a high specific area with EDLC, we used the porous graphene carbon matrix (obtained from acid leaching of the NC). As with the symmetric two-electrode cell, the electrolyte was aqueous 6 M KOH, a cellulose membrane as separator and the test voltage range was optimized with a T-two-electrodes using Ag/AgCl as reference electrode.

For counter electrodes preparation, the same procedure was performed as for the symmetric supercapacitors, using a pellet mixing the active material and Teflon (9 : 1 proportion). However, for working electrodes, the NPs of the FeNi₃-graphene formed an impermeable film when we applied pressure, preventing that the electrolyte soak all electrode. For this reason, we looked for another approach, using a carbon felt (previously calcined under nitrogen atmosphere at 1000 °C for 2 h) as a support that provides good conductivity and facilitates the access of the electrolyte. To make these electrodes, the active material was mixed with acetylene black and PVDF in ethanol, in a mass ratio of 80 : 10 : 10, and deposited on the carbon felt electrode, dried overnight at 80 °C. As we can see in Figure 5.13, FE-SEM images show a good distribution of the NC and a good contact on the carbon felt.

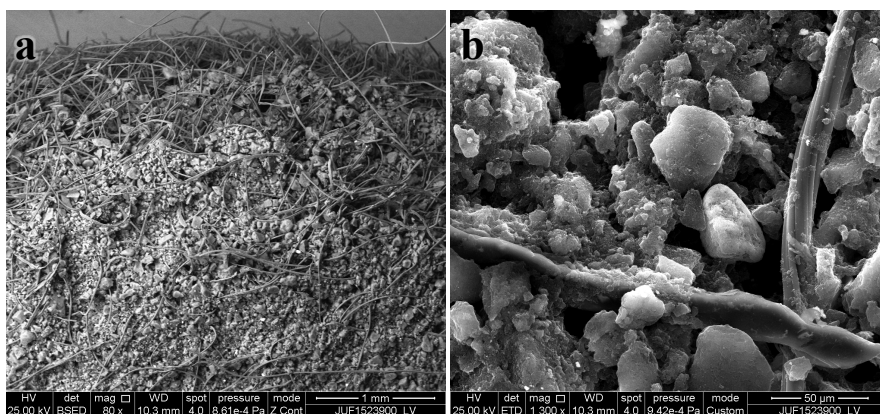


Figure 5.13. FE-SEM images of the carbon felt with the NC at (a) low and (b) high magnifications.

Once assembled the device with the different electrodes, charge/discharge test were performed. The optimal current density of this configuration was $2 \text{ A} \cdot \text{g}^{-1}$, since it was the minimum current density at which water splitting did not occur and degraded the device. Different cell potential windows were tested in order to find the most optimal. As we can see in Figure 5.14a, with a potential window of 1 V the counter electrode was in the optimal range for carbon materials, over -1 V vs Ag/AgCl as it mentioned above. Conversely, the working electrode potential is too low for a complete oxidation of the metallic NPs, doing a low specific capacitance value, as we can see in Table 6.1. Increasing the potential window to 1.2 V, we see in Figure 5.14b that the same thing happens, but if we increase it to 1.4 V it is when we can obtain the best values from this device. With that cell potential window, as can be seen in Figure 5.14c, the potential of the counter electrode reaches up to -1 V vs. Ag/AgCl, with the typical triangle-like curve of the EDLC and being the maximum potential it can be reached without degrading. In addition, the working electrode potential reaches values where practically all the metallic NPs are oxidized, showing a large pseudocapacitance curve. As a consequence of this optimization we get the maximum specific capacity value of *ca.* $19 \text{ F} \cdot \text{g}^{-1}$. Figure 5.14d shows the Ragone plot, with a maximum energy density of $5.14 \text{ W} \cdot \text{h} \cdot \text{kg}^{-1}$ and a corresponding power density of $1447 \text{ W} \cdot \text{kg}^{-1}$, intermediate values between double-layer capacitors and ultra- capacitors.

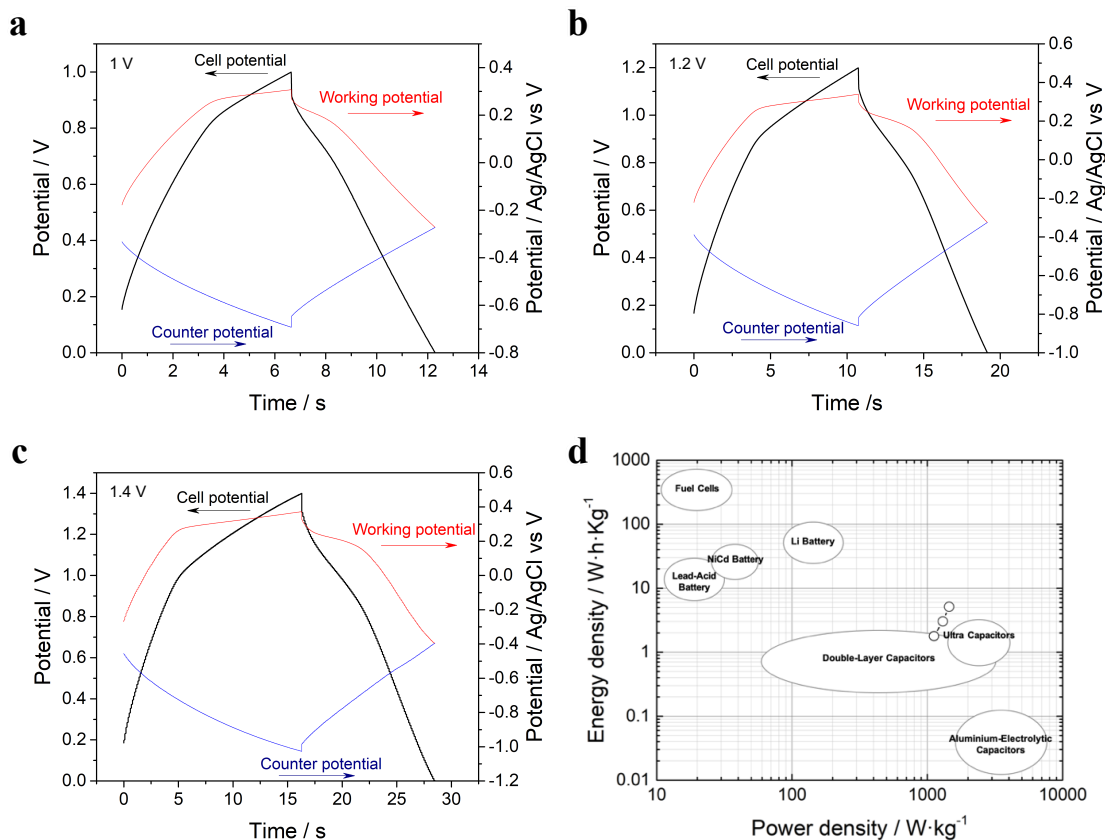


Figure 5.14. (a-c) Electrochemistry measurements of the FeNi₃-graphene / graphene in a T-two-electrode cell in 6 M KOH and Ag/AgCl as reference electrode. Galvanostatic charge and discharges curves at 2 A·g⁻¹ with different potential windows. (d) Ragone plot of the supercapacitive devices among various commercial energy-storage devices (source data from US Defense Logistics Agency).

Table 5.1. Energy values of the supercapacitive devices

<i>Electrodes</i>	FeNi ₃ -G // Graphene	FeNi ₃ -G // Graphene	FeNi ₃ -G // Graphene
Operating V	<i>1 V</i>	<i>1.2 V</i>	<i>1.4 V</i>
Specific Capacitance	<i>12,6 F·g⁻¹</i>	<i>15,2 F·g⁻¹</i>	<i>18,9 F·g⁻¹</i>
Energy density	<i>1.75 W·h·kg⁻¹</i>	<i>3.04 W·h·kg⁻¹</i>	<i>5.14 W·h·kg⁻¹</i>
Power density	<i>1115 W·kg⁻¹</i>	<i>1302 W·kg⁻¹</i>	<i>1447 W·kg⁻¹</i>

Finally, we can state that we have been able to assemble different devices of two-electrodes cell, with values that compare favorably with other recently reported symmetric and asymmetric supercapacitors working in alkaline solutions^{18–22}. In addition, with the T-two-electrode cell we have been able to perform more accurate studies in this type of cell configuration, being able to know the optimal current density and potential windows values more precisely. All this facilitates that in the near future we can make easier and optimal assemblies of real and commercial devices, like for example coin or pouch cells.

6.5 References

1. Piccinno, F., Hischier, R., Seeger, S. & Som, C. From laboratory to industrial scale: a scale-up framework for chemical processes in life cycle assessment studies. *J. Clean. Prod.* **135**, 1085–1097 (2016).
2. Lewis, N. S. & Nocera, D. G. Powering the planet: Chemical challenges in solar energy utilization. *Proc. Natl. Acad. Sci.* **103**, 15729–15735 (2006).
3. Abellán, G. *et al.* Unifying Principles of the Reductive Covalent Graphene Functionalization. *J. Am. Chem. Soc.* **139**, 5175–5182 (2017).
4. Nicolosi, V., Chhowalla, M., Kanatzidis, M. G., Strano, M. S. & Coleman, J. N. Liquid Exfoliation of Layered Materials. *Science* **340**, 1226419 (2013).
5. Coronado, E. *et al.* Spontaneous Magnetization in Ni–Al and Ni–Fe Layered Double Hydroxides. *Inorg. Chem.* **47**, 9103–9110 (2008).
6. Abellán, G., Coronado, E., Martí-Gastaldo, C., Ribera, A. & F. Sánchez-Royo, J. Layered double hydroxide (LDH)–organic hybrids as precursors for low-temperature chemical synthesis of carbon nanoforms. *Chem. Sci.* **3**, 1481–1485 (2012).
7. Romero, J. *et al.* Giant Enhancement in the Supercapacitance of NiFe–Graphene Nanocomposites Induced by a Magnetic Field. *Adv. Mater.* **31**, 1900189 (2019).
8. Stoller, M. D. & Ruoff, R. S. Best practice methods for determining an electrode material’s performance for ultracapacitors. *Energy Environ. Sci.* **3**, 1294–1301 (2010).
9. Romero, J. *et al.* Metal-functionalized covalent organic frameworks as precursors of supercapacitive porous N-doped graphene. *J. Mater. Chem. A* **5**, 4343–4351 (2017).
10. González, Z., Vizireanu, S., Dinescu, G., Blanco, C. & Santamaría, R. Carbon nanowalls thin films as nanostructured electrode materials in vanadium redox flow batteries. *Nano Energy* **1**, 833–839 (2012).
11. Diez, N. *et al.* Activated carbon fibers prepared directly from stabilized fibers for use as electrodes in supercapacitors. *Mater. Lett.* **136**, 214–217 (2014).
12. Roldán, S. *et al.* Redox-active electrolyte for carbon nanotube-based electric double

layer capacitors. *Electrochimica Acta* **56**, 3401–3405 (2011).

13. Roldán, S., Blanco, C., Granda, M., Menéndez, R. & Santamaría, R. Towards a Further Generation of High-Energy Carbon-Based Capacitors by Using Redox-Active Electrolytes. *Angew. Chem. Int. Ed.* **50**, 1699–1701 (2011).

14. Gamby, J., Taberna, P. L., Simon, P., Fauvarque, J. F. & Chesneau, M. Studies and characterisations of various activated carbons used for carbon/carbon supercapacitors. *J. Power Sources* **101**, 109–116 (2001).

15. Frackowiak, E., Abbas, Q. & Béguin, F. Carbon/carbon supercapacitors. *J. Energy Chem.* **22**, 226–240 (2013).

16. Zhi, M., Xiang, C., Li, J., Li, M. & Wu, N. Nanostructured carbon–metal oxide composite electrodes for supercapacitors: a review. *Nanoscale* **5**, 72–88 (2013).

17. Vangari Manisha, Pryor Tonya & Jiang Li. Supercapacitors: Review of Materials and Fabrication Methods. *J. Energy Eng.* **139**, 72–79 (2013).

18. Patiño, J. *et al.* Phosphorus-doped carbon–carbon nanotube hierarchical monoliths as true three-dimensional electrodes in supercapacitor cells. *J. Mater. Chem. A* **4**, 1251–1263 (2016).

19. Wang, D.-W., Li, F., Liu, M., Lu, G. Q. & Cheng, H.-M. 3D Aperiodic Hierarchical Porous Graphitic Carbon Material for High-Rate Electrochemical Capacitive Energy Storage. *Angew. Chem. Int. Ed.* **47**, 373–376 (2008).

20. Lei, Z. *et al.* A high-energy-density supercapacitor with graphene –CMK-5 as the electrode and ionic liquid as the electrolyte. *J. Mater. Chem. A* **1**, 2313–2321 (2013).

21. Huang, X., Wang, Q., Chen, X. Y. & Zhang, Z. J. N-doped nanoporous carbons for the supercapacitor application by the template carbonization of glucose: The systematic comparison of different nitridation agents. *J. Electroanal. Chem.* **748**, 23–33 (2015).

22. Li, Y. & Zhao, D. Preparation of reduced graphite oxide with high volumetric capacitance in supercapacitors. *Chem. Commun.* **51**, 5598–5601 (2015).

Resumen de la Tesis Doctoral

Introducción

La escasez de energía está siendo uno de los desafíos globales más serios actualmente. El consumo mundial de energía está aumentando dramáticamente debido al rápido crecimiento de la población y el desarrollo económico, lo que resulta en mayores emisiones de gases de efecto invernadero y el cambio climático. Se estima que las demandas mundiales de energía se dupliquen para 2050 y se tripliquen para el año 2100. Para evitar problemas ambientales debido a las energías contaminantes y satisfacer la creciente demanda de energía, es necesaria una nueva revolución tecnológica de energía limpia y sostenible. Para ello, la comunidad científica está desarrollando una intensa investigación en áreas de tecnologías avanzadas para el almacenamiento de energía (por ejemplo, supercondensadores y baterías) y conversión (por ejemplo, celdas fotovoltaicas y electrocatalíticas). Como resultado, se ha impulsado una investigación en sistemas más eficientes y limpios para diferentes aplicaciones.

Hoy en día, la energía solar, eólica, hidrotermal, geotérmica, nuclear, biomasa, celdas de combustible, baterías de alta densidad de energía y supercondensadores están siendo más demandados. Entre éstos, las pilas de combustible, las baterías y los supercondensadores se denominan tecnologías de energía electroquímica, ya que dependen de un principio electroquímico común, que transforma la energía química directamente en energía eléctrica con poca o ninguna contaminación. Sin embargo, aún no es posible hacer una comercialización de la mayoría de las tecnologías de energía electroquímica, debido principalmente a problemas de alto costo, durabilidad y operabilidad, que a su vez están vinculados al uso de materiales innovadores.

Es por todo esto que el objetivo principal hoy en día es el diseño y desarrollo de nuevos materiales que puedan aumentar la eficiencia, mejorar la durabilidad y reducir los costos, haciendo que estas tecnologías sean comercialmente viables. En este sentido, la nanotecnología y los materiales nanoestructurados son una gran promesa debido a las propiedades inusuales de sus bajas dimensiones. En este sentido, la exploración de diferentes enfoques sintéticos y procesos innovadores juega un papel crítico en el rendimiento general, obteniendo el control de la composición, el tamaño, la morfología y las propiedades electroquímicas.

Almacenamiento de energía

En la actualidad, ha aumentado el interés en sistemas de almacenamiento de alta potencia y alta densidad de energía, debido al aumento de la demanda de las energías renovables. Los sistemas de almacenamiento de energía son la clave para lidiar con la naturaleza intermitente de las fuentes de energía renovables y aumentar la potencia transmitida a la red desde sistemas como la energía eólica y solar. Además, la aparición de los vehículos eléctricos requiere que la energía cinética de los éstos se almacene en algún lugar cada vez que el vehículo desacelera o se detiene. Aunque se ha logrado con éxito con baterías de baja potencia, si se desea mejorar la eficiencia, se requerirán grandes cantidades de energía que solo pueden proporcionar otras tecnologías de almacenamiento de energía, como los supercondensadores o supercapacitores. Por esta razón, los supercapacitores han llamado la atención significativamente, debido a su alta potencia y larga vida útil, lo que hace ser una muy buena opción para construir sistemas de almacenamiento híbridos más avanzados.

Los supercapacitores son dispositivos con altos valores de potencia en comparación con las baterías comunes. Aunque los supercapacitores pueden proporcionar una potencia miles de veces con un mismo volumen, no pueden almacenar la misma cantidad de carga que las baterías (de 3 a 30 veces menos). Esto hace que los supercapacitores sean adecuados para aplicaciones donde se necesitan una gran cantidad de energía en un corto periodo de tiempo, pero no se requiere una gran capacidad de almacenamiento de energía. Una gran ventaja que ofrecen los supercondensadores es su ciclo de vida, con millones de ciclos gracias a su mecanismo de almacenamiento de carga, que no implica reacciones químicas irreversibles para un condensador eléctrico puro de doble capa. Por otro lado, la principal desventaja relacionada con el mecanismo de almacenamiento de carga es el voltaje de funcionamiento de una celda de supercondensador, que debe mantenerse bajo para evitar la descomposición química de los electrolitos.

Una celda de supercapacitor está formada por un electrodo de trabajo y un contraelectrodo, con un separador permeable entre ellos. Los electrodos pueden ser idénticos (configuración simétrica) o diferentes (configuración asimétrica). Los electrolitos más utilizados son los acuosos y orgánicos. Los electrolitos acuosos generalmente tienen un voltaje de ruptura bajo, alrededor de 1 V, que es significativamente menor que con los electrolitos orgánicos (alrededor de 3 V), pero la

conductividad de los electrolitos acuosos es mayor que la de los electrolitos orgánicos, lo cual es deseable para dispositivos de alta potencia.

Dependiendo del mecanismo de almacenamiento, se pueden distinguir supercapacitores de doble capa eléctrica, pseudocapacitores o supercapacitores faradaicos y capacitores híbridos (combinación de ambos). Los supercapacitores de doble capa eléctrica se basan en materiales nanoporosos con un área superficial específica muy alta ($> 1000 \text{ m}^2 \cdot \text{g}^{-1}$) como materiales activo. Los electrodos generalmente están hechos de materiales carbonosos nanoporosos gracias a su disponibilidad, producción industrial y bajo costo. Los pseudocapacitores generalmente están hechos de polímeros conductores, óxidos metálicos y, a veces, en carbonos porosos funcionalizados, que combinan mecanismos de almacenamiento electrostático y pseudocapacitivo. Estos materiales pueden obtener valores de capacitancia específicos mucho más altos que en los de doble capa, con un mecanismo de almacenamiento que depende de las rápidas reacciones redox que ocurren en la superficie del electrodo. Sin embargo, estas reacciones redox pueden hacer que los electrodos se hinchen, dando lugar a una estabilidad mecánica mucho más baja y una menor vida de ciclo útil en materiales pseudocapacitivos. Finalmente, los condensadores híbridos son la combinación de un electrodo del tipo doble capa eléctrica y pseudocapacitivo, que combina las propiedades de ambos sistemas y ofrece rendimientos intermedios en algunos casos.

El factor más significativos para evaluar el comportamiento supercapacitivo de un material es la capacitancia específica, cuya unidad es el faradio por gramo ($\text{F} \cdot \text{g}^{-1}$). Dicho valor se calcula de forma diferente para cada tipo de supercapacitor (capacitores de doble capa eléctrica y pseudocapacitores), y la forma más común para obtenerlo en ambos casos es mediante los ciclos de carga/descarga galvanostática. A partir de la capacidad específica también se puede calcular la energía y la densidad de potencia, dándose la densidad de energía en vatios hora por kilogramo ($\text{W} \cdot \text{h} \cdot \text{kg}^{-1}$), y la densidad de potencia en vatios por kilogramo ($\text{W} \cdot \text{kg}^{-1}$).

Conversión de energía

La conversión de energía se ha considerado como una posible solución para reducir significativamente la dependencia de los combustibles fósiles. Entre los diversos sistemas de energía a través de reacciones electroquímicas, las pilas de combustible, la división del agua y las baterías metal-aire son los sistemas más eficientes y confiables.

La reacción de oxidación del agua o reacción de evolución de oxígeno (OER del inglés oxygen evolution reaction) es la reacción central de todos estos sistemas. Esta reacción puede darse en condiciones ácidas, donde a través de la oxidación de dos moléculas de agua (H_2O) da cuatro protones (H^+), una molécula de oxígeno (O_2) y cuatro electrones, y en condiciones básicas, donde la oxidación de los grupos hidroxilo (OH^-) se transforman en H_2O y O_2 con la misma cantidad de electrones. Para tener un voltaje de referencia fijo sin que influya el pH del medio, se toma como referencia el electrodo reversible de hidrógeno (RHE en inglés), donde se tiene en cuenta el cambio de pH mediante la ecuación de Nernst.

En la actualidad, los materiales basados en metales nobles son los más usados para OER por su estabilidad en todos los valores de pH, a pesar de su alto precio y la escasez de dichos metales. Es por esta razón que se están dedicando considerables esfuerzos para obtener materiales alternativos para OER. Como los óxidos de metales no nobles no son estables en condiciones ácidas, se están buscando alternativas para la electrocatálisis OER en condiciones alcalinas, en donde son químicamente estables. Algunas de estas alternativas son materiales basados en carbono (por ejemplo, grafeno y óxido de grafeno, nanotubos de carbono, carbono dopado con nitrógeno, *etc.*), aleaciones, óxidos, hidróxidos y oxihidróxidos de metales abundantes en la tierra (por ejemplo, Mn, Co, Ni y Fe, *etc.*) y su combinación con carbono. Aunque se han desarrollado muchos catalizadores de alto rendimiento basados en metales no nobles, todavía no ha podido encontrar un material que sea competitivo y reemplace a los catalizadores basados en metales nobles de la industria. Esto es debido a que estos materiales deben tener un bajo sobrepotencial, baja pendiente de Tafel, alta estabilidad/durabilidad, buena actividad catalítica, bajo costo, alta abundancia de tierra, escalabilidad, *etc.*

Los soportes para los electros electrocatalizadores se dividen en dos categorías: electrodo de superficie plana y electrodo 3D. Los electrodos de superficie plana más

comunes son carbono vítreo, lámina de Cu/Ti y sustrato de óxido de estaño dopado con indio (ITO en inglés), que permiten la penetración unidireccional del electrolito, que limita la catálisis solo en la superficie del catalizador; mientras, los sustratos 3,D como el papel de carbono y la espuma de níquel, permiten múltiples vías para la penetración de electrolitos desde todos los lados del catalizador e involucran a todo el material en la reacción catalítica.

El electrolito para la reacción OER influye extremadamente en el rendimiento del material catalítico del electrodo. La reacción OER se produce favorablemente en medios básicos y alcanza un rendimiento muy bajo en solución ácida. Actualmente, la mayor parte de la investigación se centra en materiales estables en condiciones alcalinas, pero muchos de estos materiales no lo son en condiciones ácidas, por lo que un material para OER que sea capaz de funcionar bajo un rango completo de pH (0–14) es altamente demandado.

El factor más significativo para evaluar el rendimiento como OER es su potencial de inicio, pero es difícil observar el valor exacto. Por esta razón se usan otros factores, como el valor del sobrepotencial a una densidad de corriente de $10 \text{ mA}\cdot\text{cm}^{-2}$, siendo un excelente catalizador cuando se encuentra comprendido entre 300 - 400 mV. También se pueden usar otros factores, como el análisis de Tafel, que proporciona conocimientos de la cinética y el mecanismo de reacción, la estabilidad a un potencial o densidad de corriente constante durante un determinado tiempo y la frecuencia de rotación (TOF en inglés) para determinar la actividad catalítica del material.

La aplicación de la reacción OER para la generación de hidrogeno a partir de una electrólisis es una de las principales aplicaciones, dado que el uso de hidrógeno como combustible en vez de los combustibles fósiles está cobrando fuerza. También se utiliza en el almacenamiento de energía electroquímica, como para la baterías de metal-aire y pilas de combustible.

Motivación

Esta tesis está motivada por los recientes avances en almacenamiento y conversión de energía. Inspirados por la rápida demanda de energía que demanda la sociedad, los diferentes materiales aplicados al sector energético, en almacenamiento y conversión, han ganado una atención significativa en toda la comunidad científica. En este contexto, los nuevos nanocompuestos basados en carbono y los hidróxidos dobles laminares mostraron recientemente resultados excepcionales en aplicaciones como supercondensadores y electrocatalizadores, siendo más baratos que los materiales utilizados actualmente. Además, la posibilidad de escalar estos materiales es una parte vital para futuras aplicaciones en la industria.

Se ha desarrollado una extensa investigación sobre el procesamiento de síntesis y la aplicación de nanocompuestos basados en carbono e hidróxidos laminares utilizando enfoques innovadores. Los aspectos fundamentales de los nanomateriales basados en grafeno como supercondensadores, como un nanocompuesto híbrido que consiste en FeNi₃-grafeno (Capítulo 2) o grafeno dopado con nitrógeno (Capítulo 3) se han estudiado y evaluado a fondo. Además, el estudio de los nanocompuestos de hierro y carbono (Capítulo 4) como electrocatalizadores nos permitieron proponer nuevas alternativas eficientes para establecer electrocatalizadores de referencia. Por último, un gran estudio en la ampliación y creación de prototipos (Anexo/Capítulo 5) nos ayudó a acercar a la aplicación estos materiales energéticos sostenibles y prometedores.

Respecto a los artículos adjuntos a esta tesis, fueron seleccionados en función de su tema principal. El Capítulo 2 incluye dos documentos centrados en un nanocompuesto de FeNi₃-grafeno con propiedades magnéticas y comportamiento supercondensativo: “Insights into formation of metal carbon nanocomposites using hybrid NiFe layered double hydroxides as precursors” Romero, J., Assebban, M., Jorda, J. L., Varela, M., Coronado, E. & Abellán, G (*submitted*); “Giant Enhancement in the Supercapacitance of NiFe–Graphene Nanocomposites Induced by a Magnetic Field” Romero, J., Prima-Garcia, H., Varela, M., Miralles, S. G., Oestreicher, V., Abellán, G., & Coronado, E. *Adv. Mater.* 31, 1970200 (2019). El Capítulo 3 enfoca el grafeno dopado con nitrógeno como excelente supercondensador: “Metal-functionalized covalent organic frameworks as precursors of supercondensative porous N-doped graphene” Romero, J., Rodríguez-San-Miguel, D., Ribera, A., Mas-Ballesté, R., Otero, T. O., Manet, I., Licio, F., Abellán, G., Zamora, F.

& Coronado, E. *J. Mater. Chem. A* 5, 4343–4351 (2017). El Capítulo 4 apunta a las excelentes propiedades electrocatalíticas para OER de un nanocompuesto de hierro-carbono sin precedentes: “Solvent-Free Synthesis of ZIFs: A Route toward the Elusive Fe(II) Analogue of ZIF-8” López-Cabrelles, J., Romero, J., Abellán, G., Giménez-Marqués, M., Palomino, M., Valencia, S., Rey, F. & Mínguez Espallargas, G. *J. Am. Chem. Soc.* 141, 7173–7180 (2019). Finalmente, el Anexo/Capítulo 5 se enfoca en el estudio del proceso de escalado de materiales y su ensamblaje en celdas prototipo de supercapacitores comerciales.

Nanocompuestos para supercapacitores

Por la necesidad de reducir el calentamiento global y el fin de los combustibles fósiles, la búsqueda de fuentes alternativas de energía se ha intensificado dramáticamente durante los últimos años. Como resultado, recientemente ha habido un creciente interés en los sistemas de almacenamiento de alta potencia y alta densidad de energía. Los materiales 2D como el grafeno y sus análogos inorgánicos, como los dicalcogenuros de metales de transición o los hidróxidos dobles laminares, han tomado gran importancia en el diseño de nanomateriales avanzados debido a su rendimiento electroquímico, como para su aplicación en supercapacitores. Los supercapacitores son elementos clave entre dispositivos de almacenamiento de energía y se utilizan principalmente para aplicaciones industriales fijas, transporte automotriz y aplicaciones electrónicas portátiles. En dispositivos supercapacitivos, todos los esfuerzos que intentan mejorar la energía y las densidades de potencia se han dedicado a modificar la configuración interna del condensador. Esto incluye nuevos enfoques sintéticos para materiales de electrodos, configuraciones novedosas de condensadores o jerarquías porosas personalizadas.

En este contexto, un enfoque poco investigado para alcanzar este desafío consiste en la aplicación de un estímulo externo, como por ejemplo un campo magnético. Para este tipo de aplicación, los mejores tipos de supercapacitores son los híbridos, debido a su combinación de pseudocapacidad y doble capa eléctrica. Estos supercapacitores híbridos combinan la presencia de nanopartículas de óxidos metálicos, con propiedades magnéticas, y una matriz de carbono que proporciona una mejor conductividad y una disposición homogénea de las nanopartículas. En principio, los campos magnéticos pueden afectar las resistencias internas del capacitor, ya que se espera que induzcan fenómenos magnetohidrodinámicos complejos en los electrolitos, ofreciendo una nueva herramienta para ajustar el rendimiento de los supercapacitores, pero desafortunadamente este efecto siempre ha sido pequeño.

En este estudio presentamos un enfoque para superar esta limitación, que consiste en incorporar nanopartículas magnéticas en el material electroquímicamente activo, que puede ser fácilmente magnetizado por un campo magnético. El objetivo principal es sintetizar un nanocompuesto que tiene un comportamiento supercapacitivo y propiedades magnéticas para realizar estímulos externos a través de un campo magnético.

Para obtener dicho material híbrido, se utilizó un procedimiento de calcinación a 900 °C en una atmósfera de nitrógeno, utilizando un hidróxido doble laminar (LDH en inglés) de NiFe con cadenas de sebacato en el espacio interlaminar como precursor, donde el NiFe-LDH proporciona los metales para las nanopartículas y las cadenas de sebacato la parte orgánica para formar la matriz de carbono. Se estudió la formación del nanocompuesto mediante difracción de rayos X en polvo *in-situ*, donde pudimos observar los cambios estructurales dependientes de la temperatura, observando un colapso de la estructura LDH a 250 °C, mientras al mismo tiempo aparecía un nuevo pico asignado al plano (111) de una estructura fcc, lo que sugiere el inicio de la formación de pequeñas nanopartículas de FeNi₃. Cuando la temperatura aumenta hasta 350 °C, todos los picos asociados con la estructura LDH desaparecen y aparecen todas las líneas de reflexión que forman la estructura fcc. Además, empleando la ecuación de Scherrer, pudimos determinar el crecimiento de las nanopartículas, empezando en 5 nm hasta 30 nm en menos de 150 °C.

Para ver los cambios químicos durante la formación del nanocompuesto, se realizó un análisis termogravimétrico acoplado a un espectrómetro de masas mostrando una primera pérdida de masa correspondiente al agua interlamelar, seguida a temperaturas superiores por dos señales atribuidas a agua y dióxido de carbono, atribuidas a una dihidroxilación y descomposición de la LDH y las cadenas orgánicas, siendo la mismo rango de temperatura que el observado con rayos X. Además, a temperaturas próximas a 400 °C se apreciaron señales de benceno, lo que confirma el inicio de la formación de la matriz de grafito. Complementario a esto, se hizo un estudio Raman *in-situ*, revelando al las bandas características de cadenas de alquilo, atribuidas a las moléculas de sebacato, que confirmaron la conversión de las cadenas de sebacato a matriz de carbono debido a su desaparición al incrementar la temperatura y la aparición de las bandas D y G características del carbón grafitico.

Finalmente, gracias la microscopía electrónica de transmisión de escaneo corregida con resolución atómica y espectroscopía de pérdida de energía electrónica (STEM-EELS en inglés) y un chip de calentamiento, se observó mediante imágenes la formación del nanocomposite *in-situ*. Se vieron variaciones en la estructura de las laminas de los LDHs, donde la estructura laminar de los LDHs comenzaba a cambiar a nuevas estructuras de nanocristales perfectos con tamaños en el rango de pocos nm a 350 °C, y viendo claramente la formación de las nanopartículas a 400 °C.

Realizado el estudio *in-situ* del nanocomposite compuesto por nanopartículas de FeNi₃ enbebidas en una matriz de carbono, y que éste presentaba un excelente comportamiento como supercapacitor y al mismo tiempo poseía propiedades magnéticas, se estudió cómo afecta la combinación de ambas propiedades. Para evaluar el rendimiento, aplicamos un campo magnético externo durante ciclos de carga/descarga galvanostáticos, presentamos un aumento drástico de la retención de capacitancia y la contribución de pseudocapacitiva/Faradaica. Esta capacidad específica, después de 1000 ciclos de carga/descarga alcanza $1850 \pm 180 \text{ F}\cdot\text{g}^{-1}$ ($360 \text{ mA}\cdot\text{h}\cdot\text{g}^{-1}$), un aumento en la supercapacidad de aproximadamente un 1100% con respecto al valor inicial, y con excelentes valores de energía y densidad de potencia ($71.31 \text{ W}\cdot\text{h}\cdot\text{kg}^{-1}$ y $9450 \text{ W}\cdot\text{kg}^{-1}$).

Para comprender mejor el comportamiento fundamental de los nanocompuestos de FeNi₃-grafeno magneto-capacitivos, se realizaron diferentes estudios. La espectroscopía de impedancia electroquímica potenciostática mostró variaciones en la resistencia del electrodo, lo que indica que es responsable de la mejora en el rendimiento de almacenamiento de energía. Respecto al grado de grafitización y homogeneidad del material, la espectroscopía estadística Raman mostró una ligera disminución en la funcionalización del material, resultado en concordancia con las medidas de espectroscopia de fotoelectrones emitidos por rayos X (XPS en inglés), donde los espectros de alta resolución de C1s mostraron una disminución en la contribución de C-O. Además, los espectros de Ni 2p mostraron un aumento del NiO y Ni(OH)₂. Adicionalmente, las mediciones de conductividad mostraron un aumento en la resistencia de un orden de magnitud, pasando del comportamiento de un conductor de metal a un semiconductor, confirmando, como las caracterizaciones anteriores, que los procesos de oxidación en la superficie de las nanopartículas de metal se mejoran por el campo magnético.

Como se ha dicho, todas estas técnicas apuntan hacia un crecimiento preferencial de las capas de óxido electroactivo y una mejor resistencia estructural de la matriz de grafeno cuando los ciclos de carga/descarga tienen lugar en presencia de un campo magnético, y para una corroboración del mecanismo que ocurre, se realizaron medidas de STEM-EELS. Después de los ciclos galvanostáticos en presencia de un campo magnético, las imágenes de microscopía revelaron la amplia formación de pequeños precipitados. Las partículas más pequeñas tendían a exhibir una estructura tipo núcleo-corteza, racimos cristalinos en forma de aguja y otras partículas pequeñas cristalinas (<5 nm). El análisis

de EELS demostró que todos los precipitados aparecidos consistían en Ni, Fe y O, mostrando una fuerte segregación de Ni-Fe, con una separación total de Ni-Fe, siendo los grupos ricos en Fe fuertemente oxidados, mientras que los grupos ricos en Ni permanecían metálicos y solo se oxidaba la superficie.

Para aclarar si la segregación de metales por campo magnético requiere un proceso electroquímico o no, realizamos un análisis STEM-EELS *in-situ* de vanguardia bajo el campo magnético de la lente objetivo del microscopio (del orden de 2 T) y temperaturas entre temperatura ambiente y 400 ° C. Pasadas 15 h de exposición al campo magnético a temperatura ambiente, se produjo cierta segregación de la superficie de grupos de nanopartículas con una composición no homogénea. Después de ser calentados *in-situ* a 400 ° C durante 30 minutos, nanopartículas segregadas aumentaron de tamaño, casi duplicando su volumen, con una oxidación no homogénea que recordaba a la morfología núcleo-corteza. Estos resultados confirman el proceso de segregación inducido por el campo magnético, lo que demuestra la importancia de proporcionar energía al sistema, ya sea en forma de agitación térmica o potencial electroquímico.

Grafeno dopado con nitrógeno supercapacitivo

Los materiales basados en carbono se consideran como algunos de los materiales más adecuados para supercapacitores, debido a su alta superficie específica, buena conductividad electrónica, excelente estabilidad química, procesamiento sencillo, bajo costo y amplio rango de temperatura de operación. Estos materiales exhiben alta capacitancia debido a un comportamiento predominante de la doble capa eléctrica. A lo largo del tiempo se han utilizado una gran variedad de materiales de carbono como supercapacitores, tales como carbonos activos, aerogeles de carbono, nanotubos de carbono, nanofibras de carbono, *etc.*

Gran parte de la investigación actual se centra en sintetizar nanomateriales de carbono resistentes con distribuciones de tamaño de poro adecuadas y valores altos de área de superficie específica. Recientemente, se ha descubierto que las laminas de grafeo son un material ideal para electrodos de supercapacitores, debido a sus propiedades únicas, como su excelente conductividad eléctrica y térmica y resistencia mecánica. Tradicionalmente, el grafeno se obtiene por exfoliación mecánica del grafito, exfoliación en fase líquida y por deposición química de vapor usando superficies catalíticas, obteniendo un grafeno no poroso que típicamente no excede de $200\text{F}\cdot\text{g}^{-1}$ a $1\cdot\text{A}\cdot\text{g}^{-1}$. Para evitar esta limitación, se han desarrollado varias rutas sintéticas para obtener grafeno altamente corrugado con porosidad mejorada, pero el desarrollo de métodos sintéticos escalables y rentables de grafeno poroso sigue siendo un desafío.

En nuestro grupo se han utilizado LDHs híbridos orgánico-inorgánicos como precursores catalíticos de un material de carbono poroso grafitizado que exhibe altos valores de capacitancia específica, como hemos visto en la parte anterior. Usando un enfoque parecido, se ha incorporado iones catalíticos a un precursor orgánico laminar en lugar de formar una estructura catalítica laminar como en el caso de los LDH. Para ello, usamos un marco orgánico covalente (COF en inglés) que consisten en estructuras ordenadas con alto contenido de carbono y átomos de nitrógeno. Todo esto hace que los COF sean un precursor ideal de grafeno.

Nuestro enfoque sintético fue el uso del COF-1 con la incorporación de iones metálicos catalíticos en la estructura (Fe, Co, Ni). Mediante un tratamiento térmico a $900\text{ }^{\circ}\text{C}$ en atmósfera inerte se obtuvieron diferentes formas grafiticas corrugadas. En obtenido

usando hierro como metal catalítico fue el que exhibió una estructura jerárquica más definida, demostrando el papel que desempeña el hierro en los procesos de grafitización catalítica, de acuerdo con la literatura actual. Al mismo tiempo, mediante XPS, confirmamos que el derivado de hierro fue la muestra más grafitica, confirmado también por la espectrometría Raman. Además, los espectros de N1s reveló cuatro tipos diferentes de N, es decir, grupos piridínico-N, pirrólico-N, grafitico-N y piridina-N-óxido, siendo especialmente interesante que el derivado de hierro poseía la mayor cantidad de piridínico-N y pirrólico-N, generalmente relacionado con un aumento en la contribución capacitiva. Finalmente, mediante isothermas de adsorción de N₂ a 77 K y CO₂ a 273 K de se confirmó un área superficial más alta (1147 m²·g⁻¹), volumen de poro y microporos para la muestra derivada de hierro.

Para ilustrar la aplicación de estos materiales como supercapacitores, se evaluaron sus propiedades electroquímicas en un medio acuoso básico (KOH 6 M) mediante cronovoltamperogramas y cronopotenciogramas. Las medidas electroquímicas mostraron un comportamiento claro de doble capa eléctrica, obteniendo un máximo de capacidad específica de 460 F·g⁻¹ a 10 A·g⁻¹, un valor entre los más altos en comparación con los carbones similares recientes. Además, se verificó la estabilidad con 10,000 ciclos de carga/descarga con una retención superior al 90%.

Finalmente, se estudió su rendimiento en un prototipo de celda de dos electrodos comercial, usando una configuración simétrica (misma cantidad y material en el ánodo y el cátodo) en un rango de potencial de 1 V en KOH 6 M. Los valores de capacitancia específica máxima fueron de 175 F·g⁻¹ a una densidad de corriente de 0.2 A·g⁻¹, con una densidad de energía de 6,1 W·h·kg⁻¹ y una densidad de potencia máxima de 5000 W·kg⁻¹. Dichos valores son comparables con otros supercapacitores simétricos basados en carbono en soluciones alcalinas reportados recientemente en la literatura.

Nanocompuesto para catálisis OER

La oxidación del agua o electrocatálisis OER han recibido mucha atención en los últimos años debido a su papel principal en la división del agua, las baterías recargables de metal-aire y las celdas de combustible. Actualmente, los nanocompuestos basados en carbono con metales no nobles representa una familia prometedora de materiales con excelente rendimiento como materiales de electrodo para OER. Existen muchos métodos que pueden emplearse para preparar estos materiales, pero recientemente el la gran flexibilidad sintética que ofrecen los marcos organometálicos (MOF en inglés) hace que se estén comenzando a usar como precursores para nanocompuestos. A pesar de su baja conductividad y su poca estabilidad limita su uso en dispositivos de almacenamiento o conversión de energía, se ha demostrado que pueden ser buenos precursores para fabricar materiales carbonosos dopados con heteroátomos a través de procesos de calcinación, que exhiben excelentes actividades electrocatalíticas. Tras la pirólisis, los componentes metálicos proporcionan una fuente metálica intrínseca para derivar nanoestructuras de metales u óxidos metálicos, y por otro lado, proporcionan una fuente de carbono para preparar carbonos nanoporosos.

Recientemente, los marcos de imidazolatos zeolíticos (ZIF en inglés), una subfamilia de los MOF que consta de centros metálicos tetraédricos conectados por enlaces orgánicos basados en imidazolatos con una estructura cristalina análoga a las de las zeolitas, se han utilizado con éxito como precursores para crear nanocarbones dopados con nitrógeno. Esto se debe a su estructura nanoporosa altamente ordenada y al uso de ligandos orgánicos ricos en nitrógeno, lo que resulta en una abundante incorporación de nitrógeno que mejora significativamente el rendimiento electrocatalítico para OER. Paralelo a esto, se ha demostrado recientemente que la inclusión de hierro antes de la pirolisis mejora significativamente la eficiencia electrocatalítica del nanocompuesto resultante.

El miembro más destacado de la familia ZIF es ZIF-8, cuyo metal es el zinc, ha sido estudiado como precursor de carbono dopado con nitrógeno, con un buen rendimiento para OER. Su análogo de cobalto, también conocido como ZIF-67, también se ha utilizado como el precursor de compuestos de carbono dopados de nitrógeno con un excelente rendimiento electrocatalítico. Sin embargo, el análogo de hierro formado exclusivamente por centros de Fe (II), es altamente inestable, siendo especialmente un

gran candidato como precursor de nanomateriales para OER al contener hierro en su estructura. Es por ello que nosotros diseñamos por primera vez una síntesis libre de disolventes compatible con Fe (II) para obtener el MUV-3 (MUV: Materiales de la Universidad de Valencia), el análogo de hierro de ZIF-8.

La síntesis del precursor se realizó mediante una síntesis libre de disolventes en un tubo a vacío a 150 °C, obteniendo el análogo de hierro del ZIF-8, el MUV-3. Después de eso, un se le realizó un tratamiento térmico a baja temperatura en un horno tubular a 700 ° C durante 3,5 h bajo atmósfera de nitrógeno, obteniendo así el nanocompuesto de carbono, que posteriormente se trata con una lixiviación ácida para eliminar los metales residuales. La microscopía de transmisión de electrones de alta resolución confirmó la formación del nanocompuesto, con una matriz de carbono corrugado de varias capas de grafeno y nanopartículas de Fe residual de aproximadamente 10-30 nm embebidas en la matriz de carbono.

Mediante espectroscopía de fotoelectrones de rayos X corroboramos el carácter predominante de carbono grafitico y un dopaje de nitrógeno (aprox. 1.10%), donde el espectro de alta resolución del N1s mostraba la presencia de N-piridínico, N-pirrónico, N-grafito y óxido de N-piridina, siendo predominante el nitrógeno de tipo grafitico. Junto con esto, Además, la espectroscopía estadística Raman mostró las bandas características G y D, así como una banda 2D marcada, indicando también un alto grado de grafitización. Finalmente la caracterización textural mediante isothermas de adsorción de N₂ y CO₂ a 77 K y 273 K respectivamente, mostraron una superficie específica de 463 m²·g⁻¹ y un volumen total de poros de 0.960 cm³·g⁻¹.

Todas las caracterizaciones realizadas indicaban que el nanocompuesto obtenido era un excelente candidato como catalizador electroquímico para OER, por lo que se estudió como electrocatalizador en dos medios básicos (1 y 0.1 M KOH) en una celda estándar de tres electrodos. Las mediciones de LSV mostraron un excelente rendimiento electroquímico, con bajos potenciales de inicio de 1.588 y 1.541 V frente al electrodo de hidrógeno reversible (RHE) para KOH 1 y 0.1 M, respectivamente. Además de esto, observamos que se requerían sobrepotenciales (η) de 316 mV (1.542 V vs RHE) y 335 mV (1.561 V vs RHE) a una densidad de corriente $j = 10 \text{ mA} \cdot \text{cm}^{-2}$ en 1 y 0.1 M KOH, respectivamente, valores mejores que los electrocatalizadores derivados de otros ZIFs y del catalizador comercial de IrO₂ y NiFeOOH. Además, su excelente actividad catalítica

se vio refleja con una pendiente de Tafel de 37 y 48 mV por década en KOH 1 y 0.1 M, respectivamente. Para terminar, la estabilidad y durabilidad del catalizador se probó aplicando densidades de corriente constantes de $j = 10$ y $15 \text{ mA} \cdot \text{cm}^{-2}$ y sobrepotenciales constantes de $\eta = 300$ y 400 mV durante 15 h, mostrando una excelente estabilidad en todos los casos. Tal actividad sorprendente, que supera a la mayoría de los electrocatalizadores libres de metales nobles actuales, es el resultado de la combinación de capas de carbono grafito ultrafinas y conductoras ricas en defectos, un dopaje de nitrógeno uniforme con micro y mesoporos que facilitan la difusión del electrolito, y la presencia de nanopartículas de Fe encapsulado. Vale la pena destacar que los resultados obtenidos con este nanocompuesto se encuentran entre los mejores reportados hasta ahora en la literatura para cualquier nanocompuesto basado en carbono.

Escalado de material y ensamblaje de dispositivo supercapacitivo

La ingeniería química es una rama de la ingeniería que utiliza principios de química, física, matemáticas, etc., para usar, producir, diseñar, transportar y transformar de manera eficiente la energía y los materiales. El trabajo de los ingenieros químicos puede variar desde la utilización de nanotecnología y nanomateriales en el laboratorio hasta procesos industriales a gran escala que convierten productos químicos en formas y productos útiles.

El proceso de escalado es un procedimiento que consiste en un procedimiento de diferentes pasos. El punto de partida es un laboratorio de experimental clásico, donde se estudian todos los pasos para obtener los compuestos deseados. El siguiente paso a seguir es diseñar un diagrama de flujo en el que se debe incluir todos los pasos involucrados, así como la escala, los reactores y el equipo principal que se usarán para realizar el proceso de escalado. La siguiente etapa consiste en el uso de una planta piloto, que es una de las formas más comunes en la ingeniería química para llevar a cabo el escalado químico. Y finalmente, el paso final es el uso de la planta piloto para obtener los materiales/productos químicos deseados para poder ser usados en la industria.

Investigaciones recientes desarrolladas en nuestro laboratorio de nuevos materiales han dado lugar a algunas patentes de diferentes materiales, con muy buenas propiedades supercapacitivas y electrocatalíticas, y diferentes empresas se están interesado en estas patentes. Para trabajar con empresas, debemos pasar de una escala de laboratorio a niveles de preparación tecnológica (TRL en inglés) más altos. Por lo general, los laboratorios de investigación están en un TRL-1/2, pero si desea alcanzar niveles más altos, es necesario ensamblar prototipos comerciales y estudiar el comportamiento en estos prototipos de materiales. Por esta razón, ha sido muy importante establecer un laboratorio o una planta piloto para obtener cantidades suficientes para pruebas industriales, con síntesis cercanas a kilogramos de material, así como el estudio de diferentes dispositivos de tipo batería, para alcanzar un TRL6.

El primer material escalado fue el nanocompuesto de FeNi₃-grafeno con altas propiedades supercapacitivas. Para ello se realizó una colaboración con el Instituto Tecnológico del Plástico (Aimplas). Después de diferentes pruebas de control en el laboratorio, se decidió realizar algunos cambios en la síntesis original descrita en nuestro grupo anteriormente. El precursor NiFe-LDH-Seb se preparó mediante un sistema de

coprecipitación, añadiendo al mismo tiempo usando bombas peristálticas una disolución con las sales de níquel y hierro y otra con sebacato de sodio. Además, se monitoreó el pH en toda la adición de metales y sebacato, usando una solución de NaOH 2.5 M para mantener el pH a 8. Posteriormente, la suspensión se calentó hasta 80 ° C, con controles de temperatura dentro del reactor para confirmar que la temperatura era correcta, bajo agitación constante (300 revoluciones por minuto), y se mantuvo a esta temperatura y atmósfera inerte durante 7 días. Pasados los días se filtró, se lavó con agua desionizada y etanol, y se secó confirmando por difracción de rayos X y análisis elemental la formación del precursor deseado, obteniendo aproximadamente medio kilo de material.

Posteriormente el precursor se calcinó en un horno tubular a 900 °C durante 2 horas, en una atmósfera inerte, obteniendo el nanocompuesto final de FeNi₃-grafeno. La caracterización del nanocompuesto obtenido mediante difracción de rayos X y microscopia de transmisión de electrones de alta resolución confirmó la formación de un nanocompuesto prácticamente idéntico al que se obtenía en el laboratorio. Además, para confirmar su comportamiento capacitivo, se realizaron medidas electroquímicas en una celda de tres electrodos, observando en los ciclos de carga/descarga galvanostática valores similares a los obtenidos previamente.

Para solventar la demanda de diferentes empresas de electrodos de espuma de níquel de 10 x 10 cm con el nanocompuesto depositado y activado magnéticamente se tuvo que diseñar una celda electroquímica especial donde se pudieran introducir y activar dichos electrodos. La celda diseñada constaba de dos placas de sujeción, con el electrodo de trabajo y un contraelectrodo en el medio, separados por una red de plástico para evitar el cortocircuito. Además, tenía dos entradas de líquido, para poder llenarlo con el electrolito deseado y evacuar las burbujas producidas por la posible descomposición del agua. Usando KOH 6 M como electrolito, se realizaron las diferentes pruebas electroquímicas con la celda puesta en medio de un electroimán Bruker ELEXYS E580, aplicando un campo magnético de 4,000 Oe. Se le realizaron los ciclos de carga/descarga galvanostática de la misma manera que realizábamos con los electrodos clásicos, observando un aumento de la capacidad específica de aproximadamente 540%, menos de la mitad que cuando lo hacíamos con electrodos tradicionales. Este aumento menor posiblemente fue debido a que el campo magnético aplicado no era del todo homogéneo en todo el electrodo debido a sus dimensiones y al estar en un espacio mucho más compacto, impidiendo una fácil difusibilidad.

Finalmente en este capítulo, uno de los principales objetivos durante el desarrollo del doctorado ha sido la aplicación de diferentes nano materiales como supercapacitores. Un punto muy importante a considerar es el estudio de estos materiales en configuraciones de celdas de dos electrodos, que está mucho más cerca de las baterías/capacitores comerciales. Este tipo de celdas están compuestas por dos electrodos que están aislados del contacto eléctrico por un separador poroso. El principal problema de este tipo de celdas es que no hay un electrodo de referencia, la referencia es el contraelectrodo en sí, lo que significa que no sabemos en ningún momento dónde está exactamente el potencial de cada electrodo, y no sabemos si está en una ventana de potencial óptimo o perjudicial para el material.

Para solventar esto, utilizamos una celda de dos electrodos "falsa", donde con potenciostatos especiales, podemos crear una configuración de dos electrodos, pero con una referencia fija, como Ag/AgCl. Usando una caelda *Swagelok*® en forma de T podemos colocar los materiales con la configuración típica de una celda de dos electrodos, y a la vez un electrodo de referencia en la parte superior para conocer el potencial en ambos electrodos. Gracias a este sistema tenemos la posibilidad de conocer si los electrodos están en su ventana de potencial óptima, siendo posible mediante cambios internos, modificar dichos potenciales si se encuentran en ventanas que degraden el material del electrodo.

Existen muchas combinaciones posibles para las celdas de dos electrodos, pero se pueden clasificar en dos grupos principales: I) celdas simétricas, donde la composición, el material y la masa del electrodo trabajo y el contraelectrodo son exactamente iguales; II) asimétrico, donde el electrodo de trabajo y el contraelectrodo son diferentes. En el presente trabajo, estudiamos ambas combinaciones para comprender cómo se comportan los diferentes tipos de capacitancias en estos sistemas.

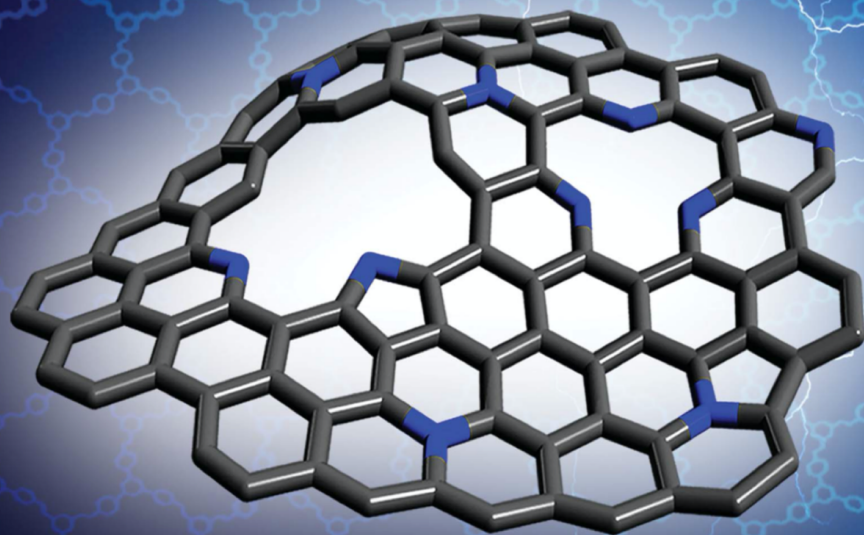
En el caso de celdas simétricas de dos electrodos usamos el grafeno dopado con nitrógeno obtenido de la calcinación del COF-1-Fe comentado anteriormente. Como el material es poroso y permite un fácil acceso al electrolito, los electrodos se ensamblaron en forma pellet, usando KOH 6 M como electrolito acuoso y una membrana de celulosa como separador. En configuraciones simétricas de celdas de dos electrodos, dado que el contador y el electrodo de trabajo son exactamente iguales, las diferencias de potencial aplicadas a cada electrodo son iguales entre sí y son la mitad del potencial de la celda.

Con el sistema de celda en T pudimos observar que el voltaje óptimo para la celda con este material era de 1 V. La razón por la cual este voltaje es óptimo es que la celda T mostró que el potencial del electrodo de trabajo y contraelectrodo siempre permanecían en un rango de potencial óptimo para materiales carbonosos en medios básicos, y si sobrepasábamos 1 V en la celda comenzaban a estar en ventanas de potencial que degradan el carbón. En los diferentes ciclos de carga/descarga se pudo observar un clásico comportamiento de doble capa eléctrica, con formas de triángulos.

Por otro lado, respecto a la configuración de electrodo asimétrico, usamos el nanocompuesto de FeNi₃-grafeno escalado como electrodo de trabajo, y su respectiva matriz de carbono sin nanopartículas metálicas como contraelectrodo. Al igual que con la configuración simétrica, el electrolito fue KOH 6 M en medio acuoso, una membrana de celulosa como separador y el rango de voltaje de prueba se optimizó con un la celda en T usando un Ag/AgCl como electrodo de referencia. Dado que en este caso el nanocompuesto tiene nanopartículas metálicas no se pudieron hacer electrodos en forma de pellet, por lo que se tubo que depositar en un fieltro de carbono previamente tratado térmicamente a 1,000 °C en atmosfera inerte. El material activo se mezcló con negro de humo y PVDF en etanol, en una relación de masa de 80: 10: 10, y se depositó la suspensión obtenida sobre el fieltro de carbono de forma homogénea, secándose a 80 °C toda la noche. Una vez ensamblado el dispositivo con los diferentes electrodos, se realizaron pruebas de carga/descarga galvanostaticas. Se probaron diferentes ventanas de potencial para encontrar la más óptima, dando como resultado que la ventana más optima era de 1.4 V. Aunque la ventana de potencial del contraelectrodo siempre estaba en una ventana optima para el carbono (superior a -1 V vs Ag/AgCl) el electrodo de trabajo no llegaba a estar a un potencial necesario para que se produjera la oxidación completa de las nanopartículas, lo que daba una muy baja contribución farádica. Con esa ventana de potencial optimizada obtuvimos una capacidad específica máxima de aprox. 19 F·g⁻¹, con una densidad de energía máxima de 5,14 W · h · kg⁻¹ y una densidad de potencia correspondiente de 1,447 W·kg⁻¹, valores intermedios entre capacitores de doble capa y ultracapacitores.

Finalmente, podemos afirmar que hemos podido ensamblar diferentes dispositivos de celda de dos electrodos, con valores que se comparan favorablemente con otros supercapacitores simétricos y asimétricos recientemente reportados que trabajan en medios alcalinos. Además, con la celda de dos electrodos en forma de T, hemos podido

realizar estudios más precisos en este tipo de configuración de celda, pudiendo conocer la densidad de corriente óptima y los valores de ventanas potenciales con mayor precisión. Todo esto facilita que en un futuro cercano podamos hacer ensamblajes más fáciles y óptimos de dispositivos reales y comerciales, como por ejemplo, celdas tipo botón o pouch.



The shortage of energy is one of the most serious global challenges of our time. The main objective today is the design and development of new materials that can increase efficiency, improve durability and reduce cost, making these technologies commercially viable. In this regard, nanotechnology and nanostructured materials make a great promise due to the unusual properties endowed by their low dimensions and the combination of bulk and surface properties to the overall behaviour. This dissertation is focused on new nanomaterials for energy storage and conversion, from its synthesis and characterization to its assembly in industrial prototypes.



VNIVERSITAT
DE VALÈNCIA

ICM^QL

Institut de Ciència Molecular